



HAL
open science

Study of Vector-Boson Scattering with the ATLAS detector and design of the High Granularity Timing Detector for HL-HLC

Oleksii Kurdysh

► **To cite this version:**

Oleksii Kurdysh. Study of Vector-Boson Scattering with the ATLAS detector and design of the High Granularity Timing Detector for HL-HLC. High Energy Physics - Experiment [hep-ex]. Université Paris-Saclay, 2024. English. NNT : 2024UPASP096 . tel-04790271

HAL Id: tel-04790271

<https://theses.hal.science/tel-04790271v1>

Submitted on 19 Nov 2024

HAL is a multi-disciplinary open access archive for the deposit and dissemination of scientific research documents, whether they are published or not. The documents may come from teaching and research institutions in France or abroad, or from public or private research centers.

L'archive ouverte pluridisciplinaire **HAL**, est destinée au dépôt et à la diffusion de documents scientifiques de niveau recherche, publiés ou non, émanant des établissements d'enseignement et de recherche français ou étrangers, des laboratoires publics ou privés.

Study of Vector-Boson Scattering with
the ATLAS detector and design of the
High Granularity Timing Detector for
HL-LHC

*Etude des diffusions de bosons vecteurs avec le détecteur
ATLAS et conception du High Granularity Timing
Detector pour HL-LHC*

Thèse de doctorat de l'université Paris-Saclay

École doctorale n° 576 Particules, Hadrons, Energie et noyau : instrumentation,
imagerie, cosmos et simulation (PHENIICS)
Spécialité de doctorat: Physique des Particules
Graduate School : Physique. Référent : Faculté des sciences d'Orsay

Thèse préparée dans l'unité de recherche **IJCLab** (Université Paris-Saclay, CNRS), sous la
direction de **Nikola MAKOVEC**, Chargé de recherche

Thèse soutenue à Paris-Saclay, le 27 Septembre 2024, par

Oleksii KURDYSH

Composition du jury

Membres du jury avec voix délibérative

| | |
|---|------------------------|
| Fabien CAVALIER Directeur de recherche (HDR), Université Paris-Saclay & IJCLab | Président |
| Emmanuel MONNIER Directeur de recherche (HDR), Aix-Marseille Université & CPPM | Rapporteur & Examineur |
| Christophe OCHANDO Chargé de recherche (HDR), École polytechnique & LLR | Rapporteur & Examineur |
| Reina CAMACHO TORO Chargée de recherche (HDR), Sorbonne Université & LPNHE | Examinatrice |
| Caroline COLLARD Directrice de recherche (HDR), Université de Strasbourg & IPHC | Examinatrice |

Titre: Etude des diffusions de bosons vecteurs avec le détecteur ATLAS et conception du High Granularity Timing Detector pour HL-LHC

Mots clés: Front-end électronique, High Granularity Timing Detector, Rejection de l'empilement, Interaction électrofaible, Au-delà du Modèle Standard

Résumé: Le Modèle Standard (SM) est connu pour être incomplet, et l'approche de la Théorie Effective des Champs (TEF) permet de paramétrer des déviations potentielles subtiles du SM. L'EFT pertinente pour cette thèse implique la description des couplages de jauge quartiques anormaux (aQGC) à travers les opérateurs d'Eboli. J'ai participé à la première combinaison statistique complète de l'analyse de la diffusion vectorielle du boson (VBS) d'ATLAS qui contraint ces opérateurs. En particulier, j'ai estimé l'importance des termes croisés dans les simulations, démontrant qu'ils ne peuvent pas être ignorés lorsque les deux membres de la paire appartiennent à la même famille d'opérateurs, mais de nombreuses analyses ne les incluaient pas initialement. J'ai développé une méthode pour insérer les termes croisés manquants en tirant parti de la dégénérescence expérimentale entre certains opérateurs. Une méthode similaire est utilisée si un seul opérateur est manquant. La méthode d'insertion a été validée, montrant généralement moins de 10% de non-fermeture. Une autre partie de cette thèse se concentre sur la migration du fJVT (forward jet vertex tagger) d'ATLAS vers le logiciel ATLAS mis à jour, ce qui a initialement entraîné une dégradation des performances de l'ordre de 15%. De plus, j'ai calibré le fJVT en utilisant les données du Run-2, Run-3 (2022-2023) : les différences d'efficacité du fJVT entre les simulations et les données réelles ont été quantifiées (typiquement en dessous de 5%) via un ensemble de facteurs d'échelle (SF), ainsi

que l'incertitude du SF composée de facteurs statistiques et de plusieurs facteurs systématiques. Le SF dépend du moment transverse du jet et du nombre d'interactions proton-proton simultanées (appelé pileup) dans l'événement. Les résultats sont maintenant disponibles pour l'ensemble de la collaboration. Trois points de travail sont fournis. Une autre partie de cette thèse porte sur la mise à niveau d'ATLAS pour le LHC à haute luminosité (HL-LHC): le pileup atteindrait 200, ce qui poserait des problèmes importants pour la reconstruction des objets. Pour résoudre ce problème, les informations sur la chronologie de la trajectoire seront fournies par le High Granularity Timing Detector (HGTD). Pour ce faire, il faut une électronique frontale dotée d'excellentes performances temporelles, appelée ALTIROC. J'ai analysé les données du faisceau d'essai pour ALTIROC1, démontrant une résolution temporelle de 45 ps. J'ai contribué au développement du logiciel ALTIROC2 et mené de multiples évaluations, en particulier de l'étape de discrétisation du temps d'arrivée (TOA), du seuil le plus bas possible et de l'analyse du faisceau d'essai. En outre, j'ai analysé les données des faisceaux d'essai pour ALTIROC3, montrant que l'étalonnage effectué en laboratoire ne pouvait pas être directement appliqué à l'environnement des faisceaux d'essai. J'ai identifié une méthode permettant de surmonter cette erreur d'étalonnage et d'obtenir une résolution temporelle moyenne de 44 ps sur de nombreux pixels.

Title: Study of Vector-Boson Scattering with the ATLAS detector and design of the High Granularity Timing Detector for HL-LHC

Keywords: Front-end Electronics, High Granularity Timing Detector, Electroweak interaction, Beyond the Standard Model

Abstract: The Standard Model (SM) is known to be incomplete, and the Effective Field Theory (EFT) approach enables the parametrization of potential subtle deviations from the SM. The EFT relevant to this thesis involves describing anomalous Quartic Gauge Couplings (aQGC) through Ebboli operators. I have participated in the first comprehensive statistical combination of ATLAS Vector Boson Scattering (VBS) analysis constraining those operators. In particular, I have estimated the significance of cross-terms in simulations, demonstrating that they cannot be ignored when both pair members belong to the same operator family, but many analyses did not initially include them. I developed a method to insert missing cross-terms by leveraging experimental degeneracy between certain operators. A similar method is utilized if single operators are missing. The insertion method was validated, typically showing less than 10% non-closure. Another part of this thesis focuses on the migration of the ATLAS forward jet vertex tagger (fJVT) to the updated ATLAS software, which initially resulted in up to 15% performance degradation. Additionally, I calibrated the fJVT using Run-2, Run-3 (2022-2023) data: differences in fJVT efficiency between simulations and real data quantified (typically below 5%) via a set of scale factors (SF), together with

SF uncertainty composed of statistical and several systematic ones. SF depends on jet transverse momentum and the number of simultaneous proton-proton interactions (so-called pileup) in the event. Results are now available for use by the entire collaboration. Three working points are provided. Yet another part of this thesis focuses on the ATLAS Upgrade for the High Luminosity LHC (HL-LHC): pileup would reach 200, creating significant challenges for object reconstruction. To address this, track timing information would be provided by the High Granularity Timing Detector (HGTD). Achieving this requires front-end electronics with excellent time performance called ALTIROC. I analyzed test beam data for ALTIROC1, demonstrating a time resolution of 45 ps. I contributed to the development of ALTIROC2 software and conducted multiple evaluations particularly of the Time of Arrival (TOA) discretization step, the lowest possible threshold, and test beam analysis. Furthermore, I analyzed test beam data for ALTIROC3, showing that calibration performed in the laboratory could not be directly applied to the test beam environment. I identified a method to overcome this miscalibration, achieving an average time resolution of 44 ps across many pixels.

AP Photo/Libkos. Source: apnews.com



In memory of Ukrainians (civilians and military) killed by russian occupants in 2014-2022, 2022-...

Contents

| | |
|--|-----------|
| Acknowledgements | 9 |
| Introduction | 11 |
| 1 Theoretical context | 15 |
| 1.1 The Standard Model | 15 |
| 1.1.1 Particle content | 15 |
| 1.1.2 Lagrangian and underlying symmetries | 16 |
| 1.1.3 EWK symmetry breaking | 17 |
| 1.1.4 Experimental results | 17 |
| 1.2 Vector Boson Scattering within the SM | 18 |
| 1.2.1 Process definition | 18 |
| 1.2.2 Vertices | 18 |
| 1.2.3 Diagrams | 20 |
| 1.2.4 Unitarity restoration | 23 |
| 1.3 VBS measurements at the LHC | 23 |
| 1.3.1 Motivation | 23 |
| 1.3.2 Experimental features | 24 |
| 1.3.3 Experimental status | 25 |
| 1.4 Beyond the Standard Model motivation | 26 |
| 1.5 Effective Field Theory | 28 |
| 2 Experimental context | 31 |
| 2.1 Historical overview | 31 |
| 2.2 Accelerator complex | 31 |
| 2.2.1 Overview | 31 |
| 2.2.2 Injector chain | 31 |
| 2.2.3 LHC | 33 |
| 2.2.4 Luminosity | 34 |
| 2.3 ATLAS | 34 |
| 2.3.1 From proto-collaborations to Higgs discovery | 34 |
| 2.3.2 Run-3 detector configuration | 36 |
| 2.3.3 Object reconstruction | 40 |
| 3 aQGC EFT VBS Run-2 combination | 47 |
| 3.1 Analyses involved | 47 |
| 3.2 Eboli operators | 47 |
| 3.3 Expectation from the combination | 49 |
| 3.4 EFT samples generation | 49 |

| | | |
|----------|--|-----------|
| 3.5 | EFT cross-sections | 50 |
| 3.6 | SM and EFT distributions | 51 |
| 3.7 | Unitarity bound | 51 |
| 3.8 | Clipping | 52 |
| 3.9 | Cross-term size | 56 |
| 3.10 | Operator replacement | 60 |
| 3.10.1 | $Z(\rightarrow \bar{\nu}\nu)\gamma$ analysis | 61 |
| 3.10.2 | $W^\pm Z$ analysis | 64 |
| 3.10.3 | Other analyses | 65 |
| 3.11 | Preliminary results | 68 |
| 3.11.1 | 1-D limits | 68 |
| 3.11.2 | 2-D limits | 68 |
| 3.12 | Outlook | 71 |
| 3.12.1 | Inputs | 71 |
| 3.12.2 | 1-D limits | 71 |
| 3.12.3 | n-D limits | 71 |
| 3.13 | Conclusion | 72 |
| 4 | Forward Jet Vertex Tagger | 79 |
| 4.1 | Principle of operation | 79 |
| 4.2 | Release 22 update | 82 |
| 4.3 | fJVT calibration | 84 |
| 4.3.1 | Methodology | 84 |
| 4.3.2 | $Z \rightarrow \ell\bar{\ell} + jets$ samples and validation | 85 |
| 4.3.3 | Binning and working points | 85 |
| 4.3.4 | Uncertainties | 86 |
| 4.3.5 | Run-2 R22 calibration | 88 |
| 4.3.6 | Run-3 R22 calibration | 88 |
| 4.4 | Potential improvement | 93 |
| 4.4.1 | Shape information | 93 |
| 4.4.2 | Targeting specific type of pile-up | 93 |
| 4.4.3 | Detector upgrades | 94 |
| 4.5 | Conclusion | 95 |
| 5 | HL-LHC | 97 |
| 5.1 | Project overview | 97 |
| 5.2 | Accelerator upgrades | 97 |
| 5.3 | ATLAS Phase-II upgrades | 99 |
| 5.3.1 | Trigger and Data Acquisition | 100 |
| 5.3.2 | Inner Tracker | 100 |
| 5.3.3 | Calorimeters | 101 |
| 5.3.4 | Muon | 101 |
| 5.3.5 | High Granularity Timing Detector | 101 |

| | | |
|----------|--|------------|
| 5.3.6 | Computing | 101 |
| 5.4 | Physics case - VBS | 103 |
| 5.4.1 | $W^\pm W^\pm$ analysis | 103 |
| 5.4.2 | ZZ analysis | 104 |
| 5.4.3 | $W^\pm Z$ analysis | 105 |
| 5.5 | HGTD | 107 |
| 5.5.1 | Detector overview | 108 |
| 5.5.2 | Sensor | 111 |
| 5.5.3 | Time resolution components | 113 |
| 5.5.4 | Front-end electronics | 114 |
| 5.5.5 | ASIC characterization aspects | 117 |
| 6 | ALTIROC1 testbeam | 121 |
| 6.1 | Campaign overview | 121 |
| 6.2 | Method of time resolution extraction | 123 |
| 6.3 | SiPM time reconstruction and it's matching with hybrid | 124 |
| 6.4 | Resolution obtained with TZ preamplifier | 125 |
| 6.4.1 | TOA-TOT coupling caveat | 125 |
| 6.4.2 | Event selections | 125 |
| 6.4.3 | Uncorrected resolution | 126 |
| 6.4.4 | Timewalk correction variables | 126 |
| 6.4.5 | Amplitude dependence | 137 |
| 6.4.6 | Impact of TDC DNL | 139 |
| 6.5 | Resolution obtained with VPA preamplifier | 139 |
| 7 | ALTIROC2 testbench | 143 |
| 7.1 | LSB calibration | 143 |
| 7.1.1 | Methodology | 143 |
| 7.1.2 | General trends observed | 144 |
| 7.1.3 | More on LSB dependence on injection | 145 |
| 7.2 | Lowest detectable charge and associated jitter | 150 |
| 7.3 | TID test | 154 |
| 7.4 | Low temperature test | 158 |
| 8 | ALTIROC2/3 testbeam | 163 |
| 8.1 | Setup | 163 |
| 8.2 | ALTIROC2 timing | 165 |
| 8.3 | Tracking, efficiency and interpad | 168 |
| 8.4 | ALTIROC3 timing | 171 |
| 8.4.1 | LSBs from resolution minimization | 171 |
| 8.4.2 | LSBs from $t_{MCP} : TOA$ fit | 173 |
| 8.4.3 | Correction for DNL | 174 |
| 8.4.4 | TOT-inclusive timewalk correction | 175 |

| | | |
|---------------------|--|------------|
| 8.4.5 | Summary of different configurations | 179 |
| Conclusion | | 181 |
| A | $Z(\rightarrow \bar{\nu}\nu)\gamma$ replacements | 183 |
| B | $Z(\rightarrow \bar{\nu}\nu)\gamma$ replacements validation fits | 191 |
| C | $Z \rightarrow \ell\bar{\ell} + \text{jets}$ basic distributions | 195 |
| D | ε_{HS} , SF , σ_{SF} for Tighter WP | 199 |
| E | ε_{HS} , SF , σ_{SF} for Loose WP | 201 |
| F | Synthèse en français | 203 |
| | F.1 Les couplages de jauge quartiques anormaux | 203 |
| | F.2 Forward jet vertex tagger | 203 |
| | F.3 High Granularity Timing Detector | 204 |
| Bibliography | | 211 |

Acknowledgements

I want to start by expressing my gratitude to the jury members: Fabien Cavalier, Caroline Collard, Emmanuel Monnier, Christophe Ochando, Reina Toro for kindly accepting the role. Particularly to Emmanuel and Christophe for reading the text and particularly to Christophe for providing a set of useful comments.

Finishing the work I did (and documenting it) within the time allocated (strictly 3 years) would be impossible without several people. First of all, Nikola Makovec, who was a professional supervisor (probably was not easy with me sometimes) throughout the whole period: somehow always finding time to talk to me about scientific, administrative, or whatever the type of question/concern I had and happy to share knowledge and experience. I'm unreasonably lucky that I had a supervisor like you and hopefully, we'll meet again.

For the VBS part, I've been closely working with Nicolas Morange, whom I would like to greatly thank for the countless discussions we had on the subject (and not only), guiding me through the project and reading part of the manuscript. A big thank also goes to Laurent Serin for his valuable feedback on my HGTD work and reading part of the manuscript. Michael Holzbock introduced me to fJVT, technical aspects but not only - I very much appreciate all your "inline answers". Thanks to Robert Les I was able to quickly start on MC generation, would be so much harder without your quick Skype replies. It was great to work with Mathieu Markovitch on VBS, you're a great teammate and hopefully timescale will allow to include the full combination in your thesis. Was great to work with all of you and hope to see you later.

Of course, I still remember what I learned a long time ago during my studies in Ukraine from my supervisors Oleg Bezshyyko and Sergey Barsuk, without your support I will likely never start the scientific path. I am also grateful to Bora Akgün and Pieter Everaerts, who were wonderful supervisors for me during CERN Summer School, which was a turning point towards a decision to do a PhD.

I'm keeping this as a scientific acknowledgment. But I cannot not mention my parents for their continuous love and support, even if I'm doing something honestly stupid, despite my hometown, where they live, being attacked by various types of drones, ballistic and cruise missiles launched by russian occupants roughly once a week for almost three years.

I also want to say thanks to my friends for being my friends (rest is beer discussion).

Introduction

The Standard Model (SM) is known to be incomplete, and the Effective Field Theory (EFT) approach enables the parametrization of potential subtle deviations from the SM. The EFT relevant to this thesis involves describing anomalous Quartic Gauge Couplings (aQGC) through Eboli operators. They are best constrained in Vector Boson Scattering (VBS).

Thesis starts with presentation of theoretical (Chapter 1) an experimental (Chapter 2) context. Theoretical part includes relevant parts of the SM, VBS within the SM and summary of experimental results obtained thus far at the LHC, followed by motivation for Beyond the Standard Model (BSM) physics and one of the BSM approaches, EFT. The introduction includes a brief overview of the Large Hadron Collider and a rather historical introduction to ATLAS, tracing why it is the way it is. The introduction concludes with object reconstruction in ATLAS, with emphasis on jets, as an introduction to Chapter 4.

The first part of my thesis (Chapter 3) focuses on the first comprehensive statistical combination of ATLAS Run-2 VBS analyses. Many are finished already or close to being finished, covering different production and decay channels, which in turn allows to constrain different operators. As a specific introduction, a review of analyses involved, combination strategy, Eboli operators, EFT kinematics, different EFT terms (of series expansion), unitarity violation (of EFT) and remedies to it (clipping technique) are presented. One of the goals of combination is to provide two- and n-dimensional limits on operators, where EFT cross-terms cannot be neglected, as opposed to one-dimensional constraints. However, as many analyses were only doing one-dimensional limits, they did not have cross-terms. Also, some operators are completely missing in some analyses, but for combination, it's desirable that all the analyses have all the operators. The method developed allowed post-factum augmentation of the analysis with missing EFT terms. Its validation is also presented. Partial combination (not all the building blocks were available at the time of writing) results are shown: one-dimensional combined limits. Also, two-dimensional limits are shown, obtaining which was only possible because of previous work done on completing the missing EFT terms.

VBS topology feature is the presence of two forward ($|\eta| > 2.5$) jets. In analysis, one is typically interested in Hard Scatter (HS) jets. To improve forward jet performance for Run-3 analyses and beyond, I worked on jets performance (Run-3) and one of ATLAS High Luminosity Large Hardon Collider (HL-LHC) upgrade projects: High Granularity Timing Detector (HGTD).

In ATLAS currently forward HS jets are selected with forward Jet Vertex Tagger (fJVT). Chapter 4 presents my work on integrating the algorithm into updated ATLAS software and fJVT data/MC calibration with Run-3 2022, 2023 data: scale factors are derived, taking into account the statistical and systematic uncertainties. fJVT chapter concludes with potential ways of improving forward pileup tagging, where one of the ways is including timing information provided by the HGTD.

HGTD is introduced in Chapter 5, starting from HL-LHC project overview, and ATLAS upgrades apart from HGTD (also mentioning computing). VBS perspectives at HL-LHC are shown. Within HGTD, the focus is on front-end electronics, named ALTIROC. ALTIROC performance is crucial to the success of the project overall and it's characterization is the subject of following three chapters.

I participated in the testing of several ALTIROC prototypes, from small-scale to full-size chip. Time resolution measurement with particles (in testbeam) of ALTIROC1 (having 25 pixels, small-scale) is shown in Chapter 6. The goal was to check the accordance of time resolution obtained with the requirement from the Technical Design Report (TDR). Testbeam setup is described, together

with the methodology of time resolution measurements and data analysis strategy and results. When the test was happening ¹, two architectures for preamplifiers were considered: Voltage Preamplifier (VPA) and Trans Impedance (TZ), therefore results are shown for both.

Characterizing small-scale prototypes, I then moved on to full-scale prototypes (225 pixels) testing: ALTIROC2 (not fully radiation-hard) and ALTIROC3 (fully radiation-hard).

ALTIROC2 was the first large chip and I characterized its performance in terms of Time of Arrival (TOA) discretization step or Least Significant Bit (LSB), lowest detectable charge, performance stability against Total Ionizing Dose (TID) and temperature - all in testbench, as described in Chapter 7. LSB is of great importance as its mismeasurement (if any) translates into time resolution misperformance and results of extensive LSB tests are shown. To be compatible with charge sensor provides (before and after irradiation), ALTIROC should be able to reach certain lowest detectable charge and time resolution at this charge - results of measurements in various configurations are shown. During HGTD operation, electronics will be irradiated, and therefore it's important to check potential degradation of performance depending on the dose received: important quantities are monitored during TID test and results are shown. ALTIROC will be operated at cold, but measurements are often done (e.g. LSB) at room temperature. To check that the performance we see at room temperature is still the same at low temperatures, important quantities (e.g. time resolution) were measured at different temperatures.

When the behavior of the new large chip was understood in the testbench, more realistic tests were done in testbeam - subject of Chapter 8. Results of ALTIROC2 time resolution measurements are shown where similarly to ALTIROC1 only one pixel was measured. Also, the hit efficiency of the ALTIROC2+sensor was measured, relying on tracking information provided by the MIMOSA telescope. With ALTIROC3, the time resolution is measured in many pixels. LSB non-uniformity is observed and a method is developed to correct for it. A summary of average time resolution across many pixels in different configurations is given.

¹In which I participated (installation and data-taking) roughly two weeks after the start of my thesis

$$\begin{aligned}\mathcal{L} = & -\frac{1}{4} F_{\mu\nu} F^{\mu\nu} \\ & + i\bar{\Psi}\not{D}\Psi \\ & + \chi_i Y_{ij} \chi_j \phi + \text{h.c.} \\ & + |D_m \phi|^2 - V(\phi)\end{aligned}$$

1 - Theoretical context

1.1 The Standard Model

The Standard Model (SM) embodies particles with no known (at the time) substructure, called fundamental particles, and interactions between them: strong, weak and electromagnetic force. The SM is founded on principles of QFT, developed in early 1970's and withstood all the experimental tests done since then, including, notably, Higgs boson discovery in 2012.

1.1.1 Particle content

Fundamental particles included in the SM are summarized on Fig. 1.1. Depending on the spin there are two types of particles in the SM: bosons (integer spin) and fermions (half-integer spin). All "matter" particles are fermions, further divided into quarks and leptons where only quarks are participating in strong interactions. Both quarks and leptons are organized into three generations where each generation properties are the same except the mass (third generation has the highest mass). Each generation includes two pairs of particles. For quarks, each pair members has electric charges $+2/3$ (in units of e) and $-1/3$, for leptons pair includes particle with charge -1 and neutral one. All force carriers are bosons: in the SM there are four vector bosons (spin-1) and one scalar (spin-0) boson. Names, masses, charges, spins can be read-off from the figure. For each particle, there is an anti-particle with opposite quantum numbers and same mass.

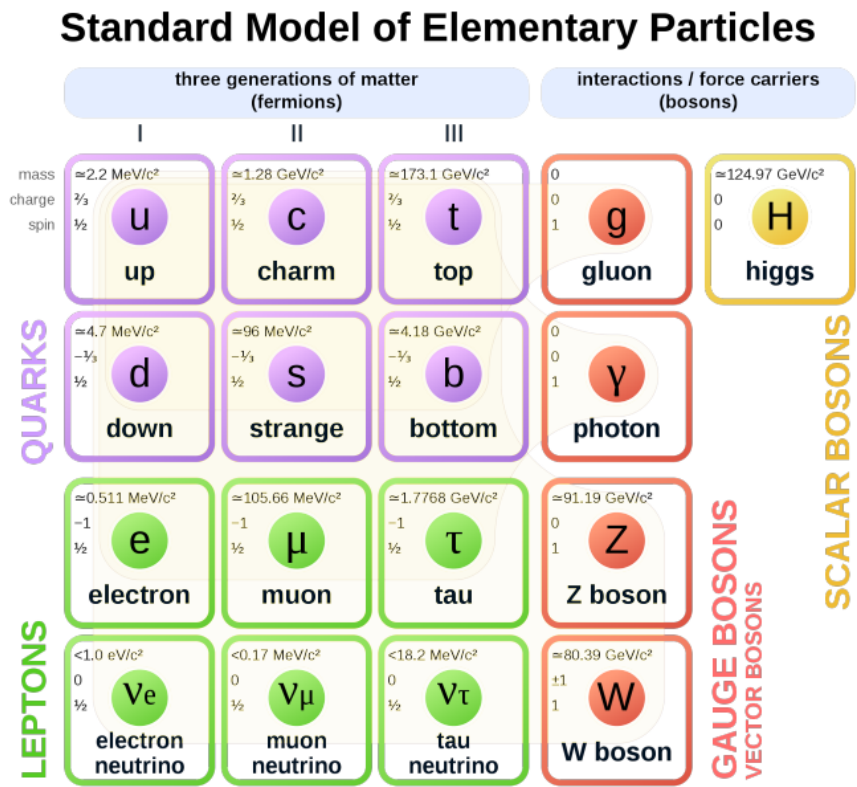


Figure 1.1: Particle content of the Standard Model.

1.1.2 Lagrangian and underlying symmetries

The main model building tool in SM is the Lagrangian density (word density is often dropped) \mathcal{L} . Equations of motion follows from Lagrangian via the least action principle. In SM \mathcal{L} is designed to be invariant under local symmetries of $SU(3)_C \times SU(2)_{I(Left)} \times U(1)_Y$ group. Conservation of corresponding charges follow from symmetry: color C, weak isospin I and hypercharge Y. The SM Lagrangian can be separated into Quantum Chromodynamics (QCD) and electroweak (EWK) non-broken parts, described in the two following subsections. Another contribution, subject of Sec. 1.1.3, is from EWK symmetry breaking.

QCD Lagrangian

QCD part of the Lagrangian is given by

$$\mathcal{L}_{QCD} = \bar{\psi}_i \left(i(\gamma^\mu D_\mu)_{i,j} - m\delta_{i,j} \right) \psi_j - \frac{1}{4} G_{\mu\nu}^a G_a^{\mu\nu} \quad (1.1)$$

where

$$D_\mu = \partial_\mu - \frac{1}{2} i g_s \sum_{a=1}^8 \lambda_a G_\mu^a \quad (1.2)$$

$$G_{\mu\nu}^a = \partial_\mu G_\nu^a - \partial_\nu G_\mu^a + g_s f^{abc} G_\mu^b G_\nu^c \quad (1.3)$$

in which D_μ is a covariant derivative and index a runs over 8 gluon fields G_μ . λ are the Gell-Mann matrices. g_s is the coupling constant of SU(3) color group. f^{abc} are the structure constants of $SU(3)_C$ group.

Consequences of such Lagrangian is that all interactions are given in terms of a single strong coupling constant. Strength of coupling depends on energy and at low energy it becomes too large bringing QCD into non-perturbative regime. There are self-interactions among the gauge fields and these self-interactions give rise to color confinement (starting point to formation of jets, see Sec. 2.3.3).

EWK Lagrangian

Gluons was mentioned above. Other vector bosons mentioned in Fig. 1.1 are obtained from the $B_\mu, W_\mu^1, W_\mu^2, W_\mu^3$ fields of $SU(2)_L \times U(1)_Y$ symmetry by

$$W_\mu^\pm = \frac{1}{\sqrt{2}} (W_\mu^1 \mp iW_\mu^2) \quad (1.4)$$

$$\begin{pmatrix} A_\mu \\ Z_\mu \end{pmatrix} = \begin{pmatrix} \cos \theta_W & \sin \theta_W \\ -\sin \theta_W & \cos \theta_W \end{pmatrix} \begin{pmatrix} B_\mu \\ W_\mu^3 \end{pmatrix} \quad (1.5)$$

where θ_W is the Weinberg angle.

Three lepton families under EWK group are organized as doublets, e.g. left-handed electron together with electron neutrino. For quarks up- and down-type form doublets. Right-handed fields are singlets: quarks and leptons, except that there no right-handed neutrino is SM. Description of interactions between fermions and fields of Eq. 1.5 and Eq. 1.4 lies in

$$\mathcal{L}_{EWK}^{non-broken} = i\bar{\psi}_L \gamma^\mu D_\mu \psi_L + i\bar{\psi}_R \gamma^\mu D_\mu \psi_R - \frac{1}{4} W_{\mu\nu}^a W_a^{\mu\nu} - \frac{1}{4} B_{\mu\nu}^a B_a^{\mu\nu} \quad (1.6)$$

where covariant derivative contains both W and B fields.

In above considerations, masses of W and Z bosons are not allowed as mass term would break gauge invariance¹. This is resolved by EWK symmetry breaking.

¹Also fermion masses are forbidden - they acquire masses through Yukawa coupling.

1.1.3 EWK symmetry breaking

To explain the missing masses, following F. Englert and R. Brout [67], P. Higgs [79] and G. Guralnik, C. Hagen, T. Kibble [77] one might add the following term to SM Lagrangian

$$\mathcal{L}_{\text{Higgs}} = (D^\mu \phi)^\dagger (D_\mu \phi) - V(\phi) \quad (1.7)$$

with ϕ being complex scalar doublet and

$$V(\phi) = \mu^2 \phi^\dagger \phi + \lambda (\phi^\dagger \phi)^2 \quad (1.8)$$

being the Higgs potential that depends on two parameters Λ, μ , and its shape is illustrated on Fig. 1.2 for the case $\mu^2 < 0$. It's visible that there is not one but multiple possible minima of potential but multiple of them, choosing one of them breaks EW symmetry spontaneously. One can arbitrarily choose minimum

$$\phi_0 = \frac{1}{\sqrt{2}} \begin{pmatrix} 0 \\ v \end{pmatrix} \quad (1.9)$$

with v being vacuum expectation and expand $\phi(x)$ around the that minimum

$$\phi(x) = \frac{1}{\sqrt{2}} \begin{pmatrix} 0 \\ v + h(x) \end{pmatrix} \quad (1.10)$$

It will lead to $(D^\mu \phi)^\dagger (D_\mu \phi)$ term in Eq. 1.7 containing desired mass terms for W, Z² with masses

$$\begin{aligned} M_W &= \frac{1}{2} g v \\ M_Z &= \frac{1}{2} (g^2 + g'^2) v \end{aligned} \quad (1.11)$$

photons, as desired, are massless and mass of newly-appeared particle, Higgs boson, should have mass $M_H = \sqrt{2\lambda}v$. Coupling of Higgs to W pair at vertex should be $ig^2/2$ and $i(g^2 + g'^2)/2$ between Higgs and Z pair.

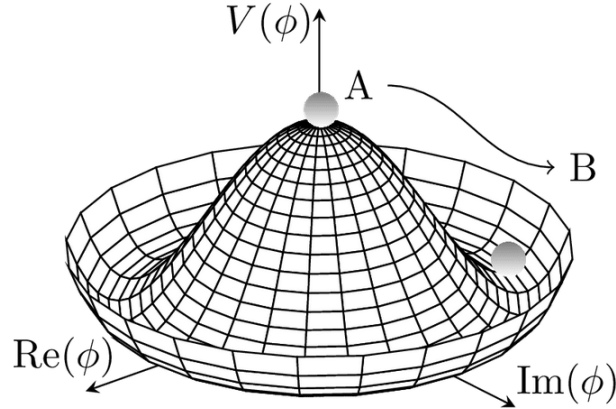


Figure 1.2: Illustration of Higgs potential.

1.1.4 Experimental results

Extensive experimental test of the Standard Model were performed and one facet of them is shown on Fig. 1.3: ATLAS “dinosaur” plot displaying production cross-sections, measured and predicted by SM. For a wide array of different processes spanning 14 orders of magnitude in cross-section, data is consistent with the Standard Model which is a remarkable achievement! Electroweak Vector Boson Scattering processes, subject of Sec. 1.2 and Chapter 3, are denoted as “ $V\gamma jj$ ” and “ $VVjj$ ”.

²Mechanism also generates masses for fermions.

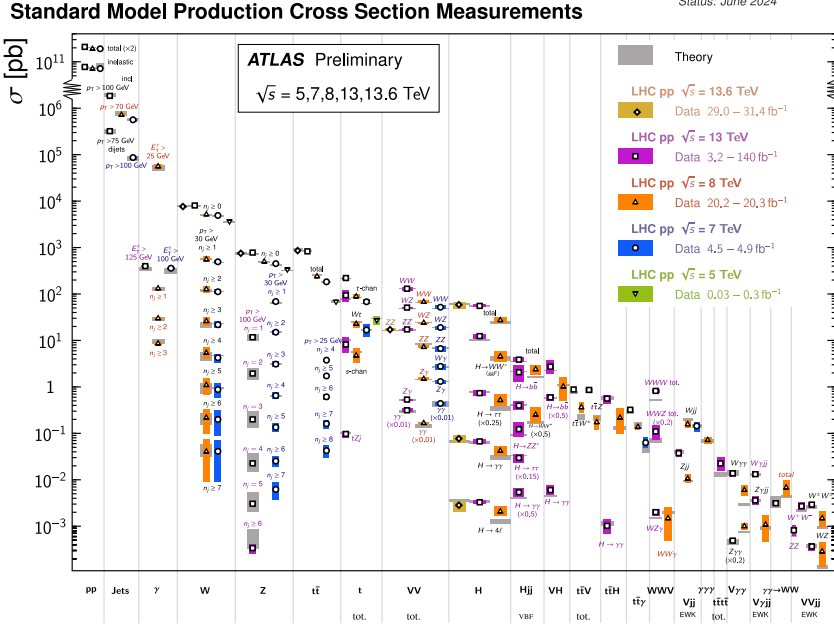


Figure 1.3: Summary of several Standard Model total and fiducial production cross-section measurements where total cross sections are reported, the measurements are corrected for branching fractions and compared to the corresponding theoretical expectations. In some cases, the fiducial selection is different between measurements in the same final state for different centre-of-mass energies \sqrt{s} , resulting in lower cross section values at higher \sqrt{s} [29].

1.2 Vector Boson Scattering within the SM

1.2.1 Process definition

Example of what is referred by “Electroweak VBS“, as shown on Fig. 1.4, is a process where two incoming partons each radiate a vector boson $V \equiv W/Z/\gamma$ (not necessary the same from each parton) that scatter of each other. Scattering options (not all of them are available to all di-boson combinations) are shown on Fig. 1.5, from left to right: quartic self-interaction, s-channel with intermediate V , t-channel with intermediate V (u is not drawn), s- and t-channel (u is not drawn) involving Higgs.

Including the decays of V , if both V are not photons, one arrives at a process (at tree-level) of type

$$qq' \rightarrow f_V \bar{f}'_V f''_V \bar{f}'''_V q'' q''' \quad (1.12)$$

or if a photon is involved

$$qq' \rightarrow f_V \bar{f}'_V \gamma q'' q''' \quad (1.13)$$

where q denote initial (anti)quark, f_V is (anti)fermion appeared from decay of scattered vector boson and γ is a photon.

1.2.2 Vertices

Let’s see how vertices participating in Fig. 1.5 arise within SM. Pure kinetic term of gauge fields B_μ, \vec{W}_μ can be separated from Eq. 1.6

$$\mathcal{L}_G = -\frac{1}{4} F_{\mu\nu} F^{\mu\nu} - \frac{1}{4} \vec{W}_{\mu\nu} \cdot \vec{W}^{\mu\nu} \quad (1.14)$$

where

$$F_{\mu\nu} \equiv \partial_\mu B_\nu - \partial_\nu B_\mu \quad (1.15)$$

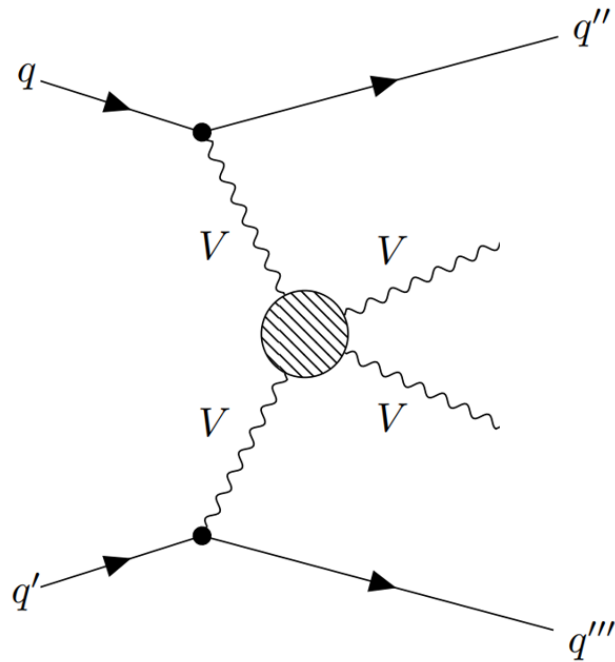


Figure 1.4: Feynman diagram illustrating collection of VBS processes allowed by SM. Content of “blob“ is shown on Fig. 1.5.

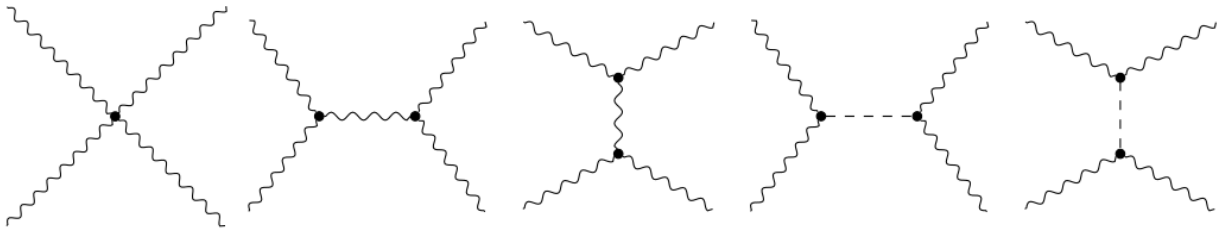


Figure 1.5: Feynman diagrams contributing to “blob“ of Fig. 1.4 at Leading Order.

$$\vec{W}_{\mu\nu} \equiv \partial_\mu \vec{W}_\nu - \partial_\nu \vec{W}_\mu - g_2 \vec{W}_\mu \times \vec{W}_\nu \quad (1.16)$$

Then quadrilinear gauge bosons vertices (main interest for VBS) can be obtained from the Lagrangian Eq. 1.14 . Substituting definitions Eq. 1.15, Eq. 1.16 resulting expression one would get will contain

$$\begin{aligned} \mathcal{L}_4 = -\frac{g_2^2}{4} [& 2W_\mu^+ W^{-\mu} W_\nu^+ W^{-\nu} - 2W_\mu^+ W^{+\mu} W_\nu^- W^{-\nu} \\ & + 4W_\mu^+ W^{-\mu} W_{3\nu} W^{3\nu} - 4W_\mu^+ W_3^\mu W_\nu^- W^{3\nu}] \end{aligned} \quad (1.17)$$

Inverting Eq. 1.5 to eliminate B, W^3 in favour of A, Z one would obtain expression in terms of W^-, W^+, Z, A leading vertices allowed by SM with four gauge bosons participating

$$W^+ W^- W^+ W^-, W^+ W^- Z Z, W^+ W^- Z \gamma, W^+ W^- \gamma \gamma \quad (1.18)$$

Similarly one would obtain allowed tri-linear vertices (which will constitute a background for aQGC), there are only two

$$W^+ W^- \gamma, W^+ W^- Z \quad (1.19)$$

1.2.3 Diagrams

Currently Next to Leading Order (NLO) simulations for VBS are available only for Standard Model processes and not for anomalous Quartic Gauge Coupling Effective Field Theory (aQGC EFT) which is the subject of Chapter 3. Therefore, discussion will be focused on Leading Order (LO).

There are different ways to transition from initial to final states mentioned in Eq. 1.12 and Eq. 1.13, they can be classified into

1. Pure electroweak vector boson scattering diagrams with quartic gauge (named EW VBS for brevity), in turn divided into cases with quartic or triple gauge couplings
2. Pure EW diagrams with Higgs
3. Pure EW non-VBS case
4. QCD-induced production - gluon or quark initiated

Specific examples of diagrams of each case are shown below.

LO EW

EW diagrams contributing to WZjj process is as a concrete example of case where both bosons are massive. EW QGC VBS diagram at LO is shown on Fig. 1.6, it is of order α_{EW}^6 . EW TGC VBS diagrams without Higgs are shown on Fig. 1.7. Higgs exchange diagram, of particular importance for the reasons that will be mentioned in Sec. 1.2.4 , is shown on Fig. 1.8. Both Fig. 1.7 and Fig. 1.8 are also of order α_{EW}^6 .

For a class of EW diagrams where photons are involved, one can consider $Z\gamma jj$ case. Here at LO, there are no diagrams with Higgs. EW VBS, QGC and Triple Gauge Coupling (TGC) are shown on Fig. 1.9. QGC is forbidden in the SM but can be induced by BSM physics, for example aQGC EFT (see Sec. 3.2). EW non-VBS diagram is shown on Fig. 1.10. Both Fig. 1.9 and Fig. 1.10 are of order α_{EW}^4 .

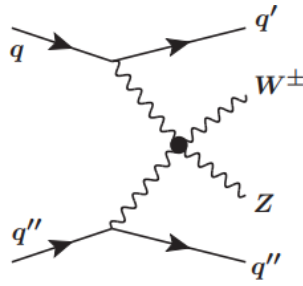


Figure 1.6: EW quartic gauge coupling VBS WZ.

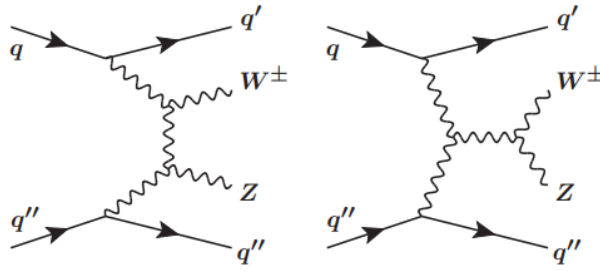


Figure 1.7: EW VBS triple gauge coupling WZ.

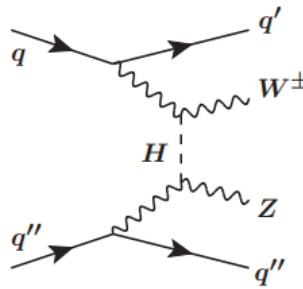


Figure 1.8: EW VBS with Higgs exchange WZ.

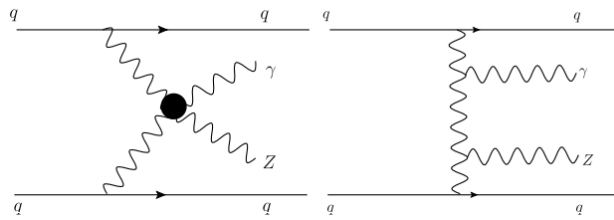


Figure 1.9: EW VBS quartic and triple gauge coupling $Z\gamma$.

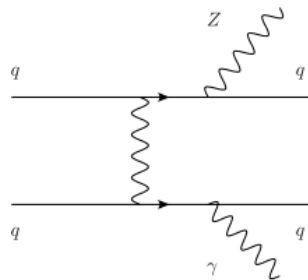


Figure 1.10: EW non-VBS $Z\gamma$.

LO QCD diagrams

Major background to EW VBS is QCD-induced VVjj production mode. There are kinematic differences between the two, allowing to separate EW and QCD, as will be discussed in Sec. 1.3.2. Examples of such diagrams are shown for $W^\pm Z$ on Fig. 1.11a (quark-initiated) and on Fig. 1.11b (gluon-initiated) - they are of order $\alpha_{EW}^4 \alpha_S^2$. Similarly, for $Z\gamma$ QCD diagrams are shown on Fig. 1.12, they are of order $\alpha_{EW}^2 \alpha_S^2$.

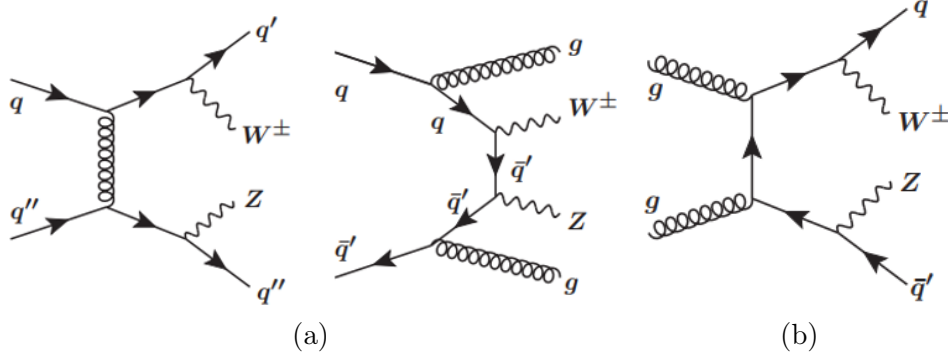


Figure 1.11: QCD WZ (a) quark-initiated (b) gluon-initiated.

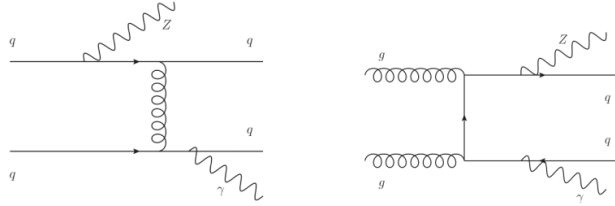


Figure 1.12: QCD $Z\gamma$ (left) quark-initiated (right) gluon-initiated.

Comparison of EW and QCD effects

For the case where all bosons are massive, like $W^\pm Z$ above, cross-section (being proportional to squared amplitude) receives contributions from both pure EW (power 6 in α_{EW} and denoted as VVjj-EW6) and EW-QCD components (power 4 in α_{EW} and denoted as VVjj-EW4) as follows

$$\begin{aligned}
 \sigma_{VVjj} &\sim |\mathcal{M}_{VVjj-EW6} + \mathcal{M}_{VVjj-EW4}|^2, \\
 &\sim |\mathcal{M}_{VVjj-EW6}|^2 + |\mathcal{M}_{VVjj-EW4}|^2 + 2 \operatorname{Re} (\mathcal{M}_{VVjj-EW6} \mathcal{M}_{VVjj-EW4}^*) \\
 &\equiv \sigma_{EW6} + \sigma_{EW4} + \sigma_{INT}
 \end{aligned} \tag{1.20}$$

giving, apart from pure VVjj-EW6 and VVjj-EW4 terms, rise also to the interference term, denoted as σ_{INT} , of order $\alpha_{EW}^5 \alpha_S$. Interference contribution is color suppressed. For example in the case of W^+W^+ , as shown in [24], it's contribution at LO is within few percent.

Depending on process, contributions from VVjj-EW6 and VVjj-EW4 may be different. Summary of cross-sections, for the case where all bosons are massive and are decaying leptonically, is given in Table 1.1. It can be seen that contribution from QCD differs per process but never dominating (this would mean $\frac{\sigma_{EW6}}{\sigma_{EW4}} \ll 1$). Among three cases shown ($W^\pm W^\pm$, $W^\pm Z$, ZZ) a special place is taken by $W^\pm W^\pm$ where QCD background is small, but for the other two processes QCD is a major background.

Table 1.1: Pure EW and EW with contributions from QCD cross-sections for different processes, predicted by SHERPA [76].

| Process | $\sigma_{EW6}[\text{fb}]$ | $\sigma_{EW4}[\text{fb}]$ | $\frac{\sigma_{EW6}}{\sigma_{EW4}}$ |
|------------------|---------------------------|---------------------------|-------------------------------------|
| $W^\pm W^\pm jj$ | 3.97 | 0.346 | 11.5 |
| $W^\pm Zjj$ | 2.34 | 4.38 | 0.53 |
| $ZZjj$ | 0.098 | 0.100 | 0.98 |

1.2.4 Unitarity restoration

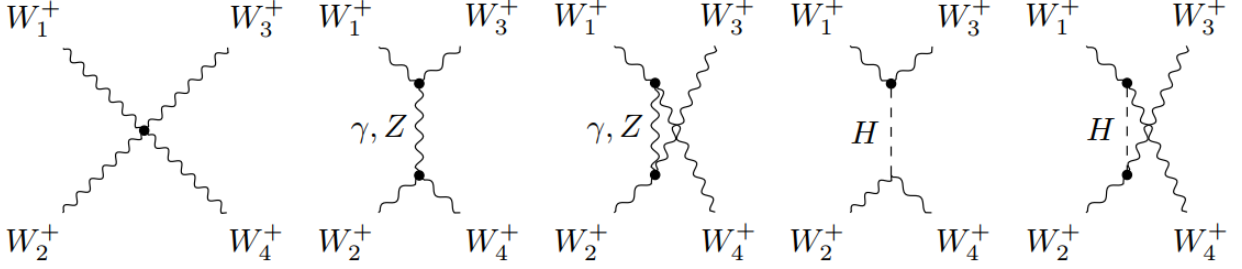


Figure 1.13: $W^\pm W^\pm$ LO diagrams.

Diagrams with Higgs, like the one that was shown on Fig. 1.8 for $W^\pm Z$ case, are the ones without which VBS cross-section would diverge at high energy. This can be demonstrated, following [101], via $W^\pm W^\pm$ example. All the LO diagrams contributing are shown on Fig. 1.13, involving quartic and triple gauge vertex (the ones with Z, γ) and Higgs exchange diagrams. Then amplitude is

$$\mathcal{M} = \mathcal{M}^{QGC} + \mathcal{M}^{TGC} + \mathcal{M}^H \quad (1.21)$$

Calculation shows, making an assumption that energies involved are much higher than bosons mass, that

$$\begin{aligned} \text{i } \mathcal{M}^{QGC} &= g_W^2 \left[\frac{E^4}{m_W^4} (6 - 2 \cos^4 \theta^*) - 4 \frac{E^2}{m_W^2} \right] \\ \text{i } \mathcal{M}^{TGC} &= g_W^2 \left[-\frac{E^4}{m_W^4} (6 - 2 \cos^4 \theta^*) + 3 \frac{E^2}{m_W^2} \right] \\ \text{i } \mathcal{M}^H &= g_W^2 \left[\frac{E^2}{m_W^2} \right] \end{aligned} \quad (1.22)$$

Individually all (QGC, TGC, H) cross-sections grow $\propto E^4$, however adding them all together cancels exactly such dependence.

Behaviour of cross-section depending on energy, for $W^+ W^-$ process, gives the dependence shown on Fig. 1.14 - only the inclusion of Higgs prevents the divergence with energy. Similar results for more boson pairs are shown on Fig. 1.15 with same conclusion. It thus said that Higgs boson restores unitarity in VBS: more specifically tree unitarity, stating that for any given $2 \rightarrow 2$ process its amplitude with respect to increasing energy cannot grow indefinitely.

1.3 VBS measurements at the LHC

1.3.1 Motivation

Interest to VBS experimental test is two-fold. On one hand, this process provides opportunity to test self-couplings of gauge bosons via QGC and TGC couplings. Couplings arise from underlying

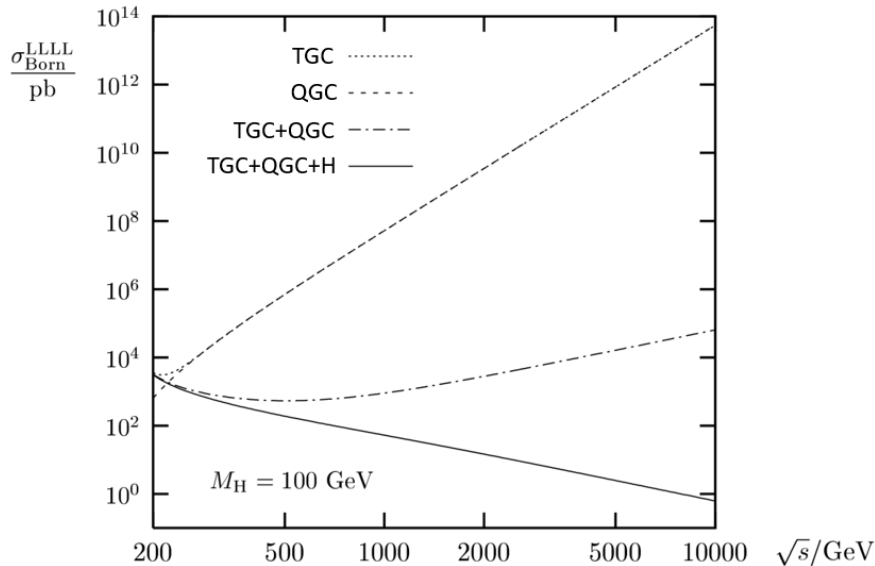


Figure 1.14: The cross-sections for longitudinal W^+W^- gauge-boson scattering resulting from subsets of the tree-level diagrams. Adapted from [63].

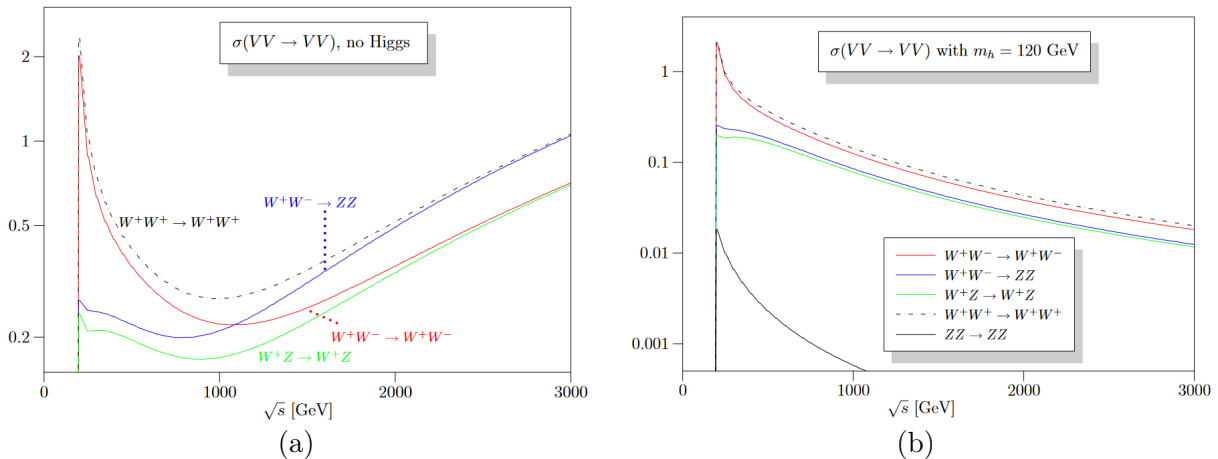


Figure 1.15: Cross-sections for longitudinal component of the electroweak $VVjj$ production depending on energy [18] (a) without Higgs (b) with Higgs.

EW symmetry group $SU(2)_L \times U(1)_Y$. Particularly some vertices are forbidden in SM, like neutral Quartic Gauge Couplings (nQGC), and provide a stringent test of the SM. On the other hand, W and Z bosons acquire masses through Higgs mechanism and therefore longitudinal polarisation mode. $V_L V_L$ cross-section is not diverging due to a delicate cancellation mechanism necessarily involving QGC, TGC, Higgs diagrams together. It would only work if Higgs boson's coupling to weak bosons doesn't deviate from SM prediction. Thus, VBS is an indirect probe of Electroweak Symmetry breaking.

1.3.2 Experimental features

First of all EW VBS process is very rare, as already can be seen from powers of coupling constant counting giving α_{EW}^6 for $VVjj$ where $V=W,Z$ and α_{EW}^4 for $V\gamma jj$. Also process has a specific topology that one might want to target:

- Two jets that radiated vector bosons (called tagging jets) are expected to have large m_{jj}

and large rapidity separation. m_{jj} selection is often used to reduce contamination from TGC processes

- Bosons are expected to be emitted centrally and jet activity in central is expected to be small and this is often quantified by Zeppenfeld variable ³

$$\xi_X = \left| \left(y_X - \frac{(y_{j_1} + y_{j_2})}{2} \right) / (y_{j_1} - y_{j_2}) \right| \quad (1.23)$$

where $y_{j_1}(y_{j_2})$ are leading (second-leading) p_T jet's rapidity. X is an object or collection of objects centrality of which, with respect to VBS tagging jets, one wants to define. For example third-leading p_T jet or $\ell\gamma$ system. Smaller values correspond to more centrality and selection is often applied to obtain separation from QCD VBS

As a concrete example of two points above, Fig. 1.16 shows illustration of an expected EW $W^\pm Z$ event if both bosons are decaying leptonically.

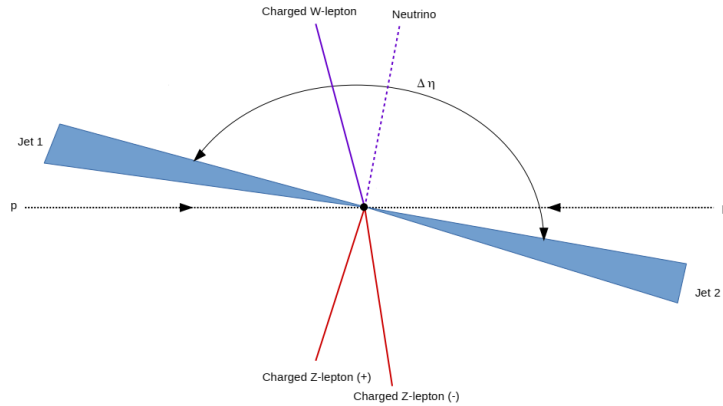


Figure 1.16: Schematic representation of a WZjj-EW event from a pp collision [96].

Depending on how massive bosons decay, one might obtain final states which are fully hadronic (when both bosons are decaying into quarks), semileptonic (when one boson decays leptonically and second one - into quarks) or fully leptonic. Branching fraction of leptonic decay is smaller, however configuration is “cleaner“ to measure. Multiple of the analyses that will be shown below are of this type. On the other hand, fully hadronic final state is dominated by multi-jet background and was never measured. There are also analyses with photon, their final state is photon together with either lepton or neutrino pair.

1.3.3 Experimental status

Despite long-standing interest (first experimental projections for not-cancelled-yet SSC were published in 80s), because of small cross-sections and rather challenging background of other di-boson processes, searches for VBS only started with Run-1 LHC data, that would typically result in seeing 5σ later with Run-2 data. Particularly, ATLAS ⁴ reported

- Evidence [35] and later observation [10] of $W^\pm W^\pm$
- $Z\gamma$ significance of 2σ [36] and later observation in [13]
- Observation of $W^\pm Z$ in [11]

³Sometimes also confusingly called centrality.

⁴There are CMS counter-parts to most analyses.

Table 1.2: Summary of non-hadronic input analyses to combination.

| Production | Boson Decay | Ref. | σ_{EW}^{fid} [fb] |
|--------------|----------------|-----------|--------------------------------|
| $Z\gamma$ | $\nu\nu\gamma$ | [48] | $0.77^{+0.34}_{-0.3}$ |
| ZZ | $llll$ | [50],[52] | 1.27 ± 0.14 |
| same-sign WW | $l\nu l\nu$ | [55] | 2.92 ± 0.29 |
| $W^\pm Z$ | $l\nu ll$ | [56] | 0.368 ± 0.07 per lep. mode |
| $W\gamma$ | $l\nu\gamma$ | [31] | 13.2 ± 2.5 |

- ZZ observation in [50]

With observation being made, people started to measure cross-sections, particularly differentially. Resulting analyses are summarized in Table 1.2 and they constitute inputs to EFT aQGC combination discussed in Chapter 3.

In light of Sec. 1.3.2, Table 1.3 summarizes “common VBS“ selections applied by those analysis. On top of them, depending on background specific per analysis, listed in “major non-EW4 bkg“ column (QCD is background for everyone so removed from this list), each team optimizes the selection specifically. Major systematic uncertainties, listed in “major syst“ column, often involve theoretical and jet (experimental) ones.

In tables there is no analysis with hadronic or semi-leptonic final state. ATLAS VV semileptonic analysis ⁵ is not yet published (team is close though) and I’m not able to discuss internal results here. However, VV semileptonic is also an input to combination.

Measurements discussed are already a part of ATLAS Standard Model compilation previously shown on Fig. 1.3 - they occupy the right-bottom corner of plot as one of rarest processes measured so far at the LHC. Additionally, VBS measurements together with Vector Boson Fusion and tri-boson fiducial production cross-sections are compared to SM prediction in Fig. 1.17. Unfortunately, no deviation from the Standard Model is seen. However, motivation for Beyond the Standard Model physics arises elsewhere.

1.4 Beyond the Standard Model motivation

Thus far no deviations from the Standard Model were seen in VBS measurements (Fig. 1.17), but also in other SM tests (Fig. 1.3). Nevertheless, it’s clear that SM is not a complete theory of Nature:

- Gravity, which is fourth fundamental force, is not included in the SM
- Neutrino masses (much smaller than other ones but non-zero), following from observation of neutrino oscillations, are not included
- Dark Matter, evidence for which is provided from astronomical and cosmological data, is not included in the SM
- Asymmetry between matter and anti-matter is not following from the SM

1.5 Effective Field Theory

⁵ATLAS internal code ANA-STDM-2018-27: https://atlas-glance.cern.ch/atlas/analysis/analyses/details.php?ref_code=ANA-STDM-2018-27

Table 1.3: Summary of SR selections, backgrounds and systematics of Table 1.2 analyses

| Analysis | m_{jj} sel. | ΔY sel. | Zeppenfeld sel. | major non-EW4 bkg. | major syst. |
|--|---------------|---------------------------------|------------------------|---|---|
| $Z\gamma \rightarrow \nu\nu\gamma$ | > 300 | - | $\xi_{4\ell} < 0.4$ | $W(\ell\nu)\gamma jj$ QCD and EWK $t\bar{t}\gamma jj$ w/ semilep., lep. dec. | $Z(\rightarrow \bar{\nu}\nu)\gamma jj$ EWK, QCD model. exp. jet, E_T^{miss} |
| $ZZ \rightarrow \ell\ell\ell$ | > 300 | $\Delta\eta_{jj} > 2.0$ | $\xi_{4\ell} < 0.4$ | Non-prompt leptons $t\bar{t}Z, WWZ, WZZ$ | Jets Unfolding Backgrounds |
| $W^\pm W^\pm \rightarrow \ell\nu\ell\nu$ | > 500 | $\Delta y_{jj} > 2.0$ | - | $WZ/\gamma^* jj$ | bkg. misid. leptons QCD $W^\pm W^\pm$ theor. model. EW $W^\pm W^\pm$, QCD corrections JES&JER, Luminosity |
| $W^\pm Z \rightarrow \ell\nu\ell\ell$ | > 500 | $\eta_{j1} \cdot \eta_{j2} < 0$ | - | $ZZ, t\bar{t}Z, t\bar{t}W$ | EW theor.model QCD theor. model. PDFs |
| $W\gamma \rightarrow \ell\nu\gamma$ | > 1000 | $\Delta y_{jj} > 2.0$ | $\xi_{W\gamma} < 0.35$ | $W\gamma jj, t(1+\gamma)$ misid. $W+\text{jet}$ | exp. jets exp. lepton, photon, pile-up Strong, EW $W\gamma jj$ model. |

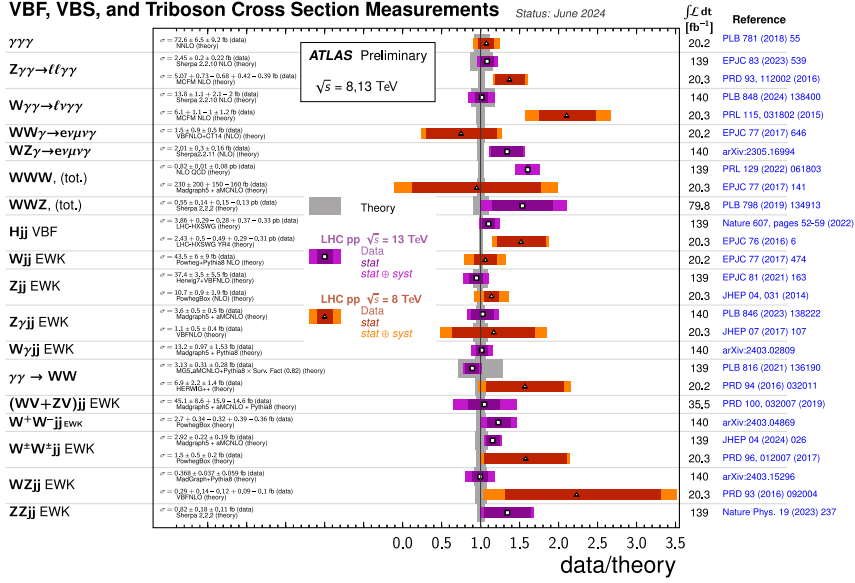


Figure 1.17: The data/theory ratio for several vector boson fusion, vector boson scattering, and triboson fiducial production cross-section measurements [29].

We know that SM is not complete, however there is no particularly striking theory to start searching for at the LHC, like it was with SM before Higgs discovery. At the same time, there are way too many other models published on arXiv and searching for each of them is practically undoable. Therefore, it is desirable to formulate a model-independent approach which gives “complete set of possibilities“. Working within such framework allows to find a “direction“ where New Physics more likely lies.

One such model-independent approach is an Effective Field Theory (EFT). EFT also allows to probe energy scales currently unreachable: underlying assumption that SM is low energy limit of some other theory that we don’t know yet and typical scale Λ of this theory is well above the EW scale. Higher-scale theory should have symmetries and field content as the SM. In this case one organizes NP is Taylor series of form

$$\mathcal{L}_{\text{EFT}} = \mathcal{L}_{\text{SM}} + \sum_i \frac{c_i}{\Lambda^2} \mathcal{O}_i^{(d=6)} + \sum_i \frac{c_i}{\Lambda^4} \mathcal{O}_i^{(d=8)} + \dots \quad (1.24)$$

i.e. SM Lagrangian is extended with new non-SM operators \mathcal{O}_i entering together with coefficients (called Wilson coefficients) c_i . Each next term is suppressed by $1/\Lambda^{d-4}$. Dimension-5 and dimension-7 are excluded as they violate lepton number conservation. Dimension-6 and dimension-8 are the largest terms left. Here series is truncated at dimension-8 as it’s the smallest dimension exclusively modifying quartic gauge couplings. The corresponding operators will be introduced in Sec. 3.2.



2 - Experimental context

2.1 Historical overview

LHC as we know it today is a result of decades of work by many people - key events and dates are summarized in Table 2.1. Already in 1979 (before LEP approval), its construction was foreseen, as discussed in LEP White Book [104]: “Tunnel with 27 km circumference and a diameter of 5 m, with a view to the replacement of LEP at the end of its activities by a proton-proton Collider using cryogenic magnets“.

2.2 Accelerator complex

2.2.1 Overview

For ATLAS, colliding beams are provided by the Large Hadron Collider (LHC). Beams are colliding instead of one beam impinging on a fixed target as it a more efficient way to reach a higher center-of-mass (CM) energy. The LHC is the largest particle accelerator in the world (27 km ring), at the moment of writing, operating at $\sqrt{s} = 13.6$ TeV CM energy (another category where LHC is the most powerful in the world). To reach that energy, a whole chain of accelerators is used, partially re-using pre-LHC components. Proton-proton specific part of the accelerator chain is shown on Fig. 2.1.

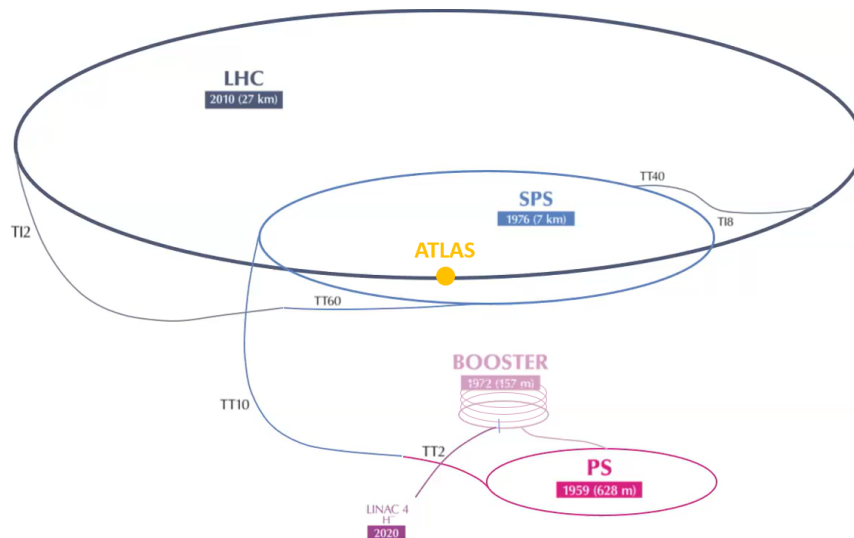


Figure 2.1: LHC chain, proton-proton injector path only. Adapted from [93]. Only the ATLAS experiment is located.

2.2.2 Injector chain

It all starts with a hydrogen bottle, a clone of which one can buy in a CERN souvenir shop.

H^- ions then enter the LINAC4¹ which accelerates them up to 160 MeV energy and forms bunches thanks to Radio Frequency (RF) cavities, as illustrated on Fig. 2.2a. They feature an alternating voltage, and particles passing through them will gain different amounts of energy depending on their phase: particles falling behind will be accelerated more, and the ones leading can be decelerated. RF cavities are used in all parts of the whole chain.

¹LINAC3 is a starting point for heavy ions.

| | |
|------|--|
| 1984 | Workshop on a Large Hadron Collider in the LEP tunnel, Lausanne, Switzerland where the feasibility of hadron collider in future LEP tunnel was discussed |
| 1987 | Workshop on the Physics at Future Accelerators, La Thuile, Italy. The Rubbia “Long-Range Planning Committee“ recommends the Large Hadron Collider as the right choice for CERN’s future. |
| 1990 | LHC Workshop, Aachen, Germany (discussion of physics, technologies, and detector design concepts, including the first realistic MC studies). |
| 1992 | General Meeting on LHC Physics and Detectors, Evian-les-Bains, France (with four general-purpose experiment Expressions of Interest presented). |
| 1993 | Three Letters of Intent were evaluated by the CERN peer review committee LHCC. ATLAS and CMS were selected to proceed to a detailed technical proposal. |
| 1994 | The LHC accelerator was approved for construction, initially in two stages. |
| 1995 | LHC Conceptual Design Report. |
| 1996 | ATLAS and CMS Technical Proposals approved. |
| 1996 | Approval for the construction of the 14 TeV LHC , to be completed in 2005. |
| 1997 | Formal approval for ATLAS and CMS to move to construction. |
| 1997 | Construction of the experiments commences (after approval of detailed Technical Design Reports of detector subsystems). |
| 2000 | Assembly of experiments commences at CERN. The LEP accelerator is closed down to make way for the LHC . |
| 2008 | LHC experiments ready for pp collisions. LHC starts operation. An incident stops the LHC operation. |
| 2009 | LHC restarts operation, first pp collisions at 900 GeV recorded by the LHC detectors. |
| 2010 | LHC collides protons at high energy (center of mass energy of 7 TeV). |
| 2012 | LHC operates at 8 TeV: announcement of the discovery of a Higgs-like boson. |
| 2015 | After a shutdown in 2013-2014, the LHC operates at 13 TeV for Run-2 until 2018. |
| 2022 | Start of Run-3. |

Table 2.1: Some key dates of the LHC project. Adapted from [9].

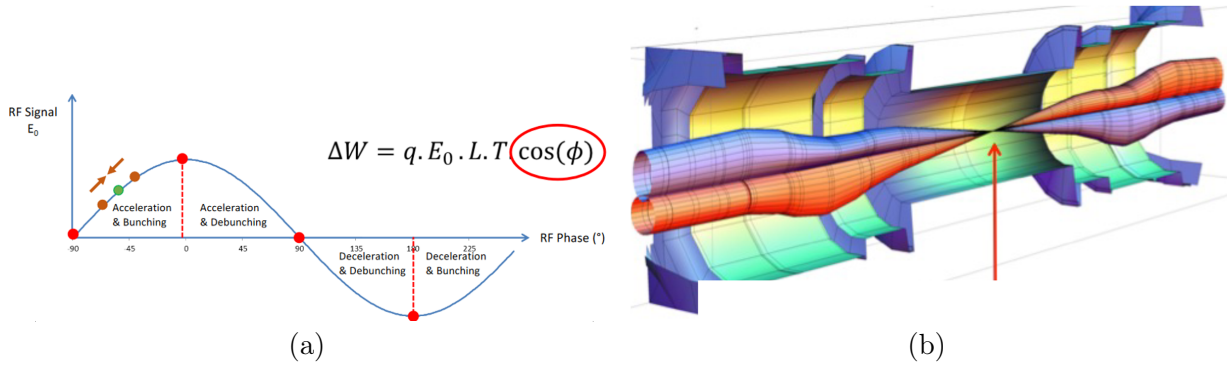


Figure 2.2: (a) RF cavity principle of operation illustration [102] (b) beam squeezing at IP illustration.

The next stage after LINAC4 is the Proton Synchrotron Booster (PSB), which is, in fact, not a single ring but four independent rings, each with a circumference of 157 m. PSB is the place where H^- gets converted to protons. The output of the PSB is a proton beam with 2 GeV energy. Some experiments use this beam already, e.g. ISOLDE studies atomic nuclei, including the most exotic species.

The next stage after the PSB is the Proton Synchrotron (PS) - the oldest operating synchrotron at CERN with a circumference of 628 m. The PS raises the proton energy to 26 GeV. The PS is the most flexible regarding “RF gymnastics“. Particularly, it’s the only stage in the accelerator chain that has combined-function magnets: not just dipoles bending the trajectory followed by the quadrupoles for focusing but a hybrid of the two. Among notable experiments happening at the PS is AD-ELENA, anti-proton deceleration facility, where recently measurement was done showing that antihydrogen atoms, released from magnetic confinement in the ALPHA-g apparatus, behave in a way consistent with gravitational attraction to the Earth [66].

Last pre-LHC stage is the Super Proton Synchrotron (having a ring of 6.9 km length), accelerating the protons from the PS up to 450 GeV. It’s the first CERN accelerator underground. Separate dipole and quadrupole magnets are used (unlike PS). In the 80s it was operated as a proton-antiproton collider ($S\bar{p}\bar{p}S$ project), leading to the Nobel Prize for the discovery of the W and Z bosons ² by the UA1 ³ and UA2 ⁴ experiments [69, 71]. The SPS is particularly relevant for this thesis as it delivers the beam to the test area (H6A) where ALTIROC tests were performed (see Chapters 6 and 8).

2.2.3 LHC

The LHC is the first and only accelerator in the chain with two beams circulating in it (in opposite directions, going through cold mass 19.4 cm apart) before collision. Each beam is accelerated up to 6.8 TeV energy through a series of RF cavities. Keeping those beams on the trajectory requires usage of innovative, at the time of construction, superconducting magnets. The main magnets are immersed in superfluid helium and operate at a temperature of 1.9 K (RF cavities are also superconducting and operated at 4.5 K). LHC magnets are not only dipoles (main dipoles having a field of 8.33 T, 1232 of them) and quadrupoles (833 used) but also corrector magnets (6000 are used) for beam quality. Once LHC beams reach their top energy, they are focused to four Interaction Points (IP), ATLAS being one of them. At the IP beam size reaches transverse size of $\approx 10 \mu\text{m}$.

²Providing, among other things, belief that a “dirty“ hadron collider can do great discoveries.

³First hermetic hadron collider detector, like ATLAS.

⁴Fine (by its time) calorimeter cells, operated in phases - like ATLAS.

Squeezing is illustrated on Fig. 2.2b. However, one cannot squeeze at IP infinitely as β^* will then explode away from the IP and the beam may hit the accelerator.

LHC nominal cycle is shown on Fig. 2.3. By design, LHC can collide up to 2800 bunches. There are 1.6×10^{11} protons in each bunch. Spacing between bunches is 25 ns, coming from the extraction from the PS - injection to SPS, done via kicker whose rise-time is not instantaneous but 25 ns. Similarly, the SPS-LHC interface is done via another kicker, which also introduces spacing between groups of batches.

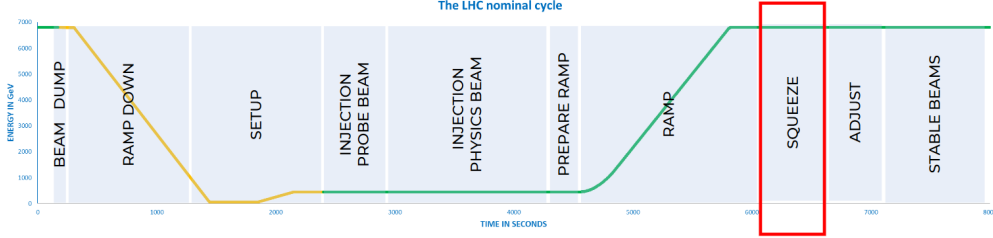


Figure 2.3: The LHC nominal cycle [102].

2.2.4 Luminosity

The instantaneous luminosity can be written as

$$L = \frac{N_b^2 n_b f_{rev} \gamma}{4\pi \varepsilon_n \beta^*} F = \frac{c}{4\pi} \times \underbrace{\frac{\gamma}{l}}_{\text{accelerator features}} \times \underbrace{N_b^2 n_b}_{\text{beam intensity features}} \times \underbrace{\frac{1}{\varepsilon_n \beta^*}}_{\text{beam geometry features}} F \quad (2.1)$$

where γ and l are the “energy“ and length of the machine, respectively. n_b and N_b are the number of bunches and particles in a bunch, respectively. The size of the beam at IP is controlled by ε_n (normalized emittance) and β^* (beta function) and a geometry reduction factor (0.55) taking into account that beams are rotated and not head-on at IP.

The integrated delivered by the LHC and collected per day in 2024 (year of writing) is shown on Fig. 2.4.

2.3 ATLAS

2.3.1 From proto-collaborations to Higgs discovery

In Evian meeting (see Table 2.1) four general-purpose experiment concepts were presented - too many for the budget. Two of them, toroid proto-experiments ASCOT and EAGLE (whose sketches are shown on Fig. 2.5) then merged to form the ATLAS⁵ (A Toroidal LHC ApparatuS) collaboration.

ATLAS then submitted a Letter of Intent [3] in 1992, where some key decisions about the detector were made and later refined for the ATLAS Technical Proposal (TP) [4]⁶. According to TP, detector optimization is guided by physics issues such as the sensitivity to the largest possible Higgs mass range, the searches for heavy W- and Z-like objects, the searches for supersymmetric particles, the searches for compositeness of the fundamental fermions, the investigation of CP violation in

⁵A vote decided the name, and funnily, the second-leading option in the vote was ALICE, but it has nothing to do with today’s ALICE (one of four big LHC experiments).

⁶In the LHCC open session, the TDR presentation consisted of four major talks. One of them is about the Calorimeter, notably for IJCLab, was given by Daniel Fournier, who received the Prix Lagarrigue in 2023 for his Calorimeter contributions.

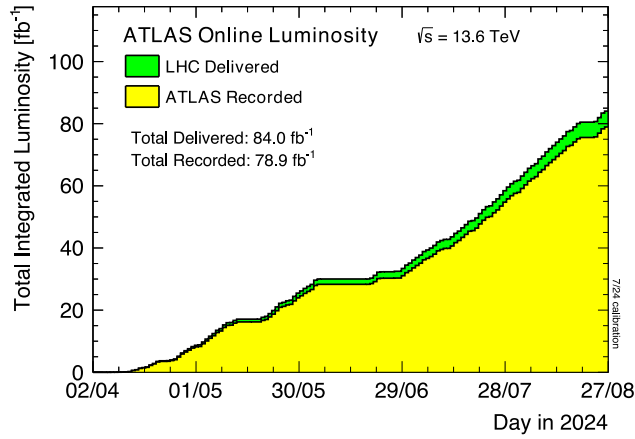


Figure 2.4: Cumulative luminosity versus time delivered to (green) and recorded by ATLAS (yellow) during stable beams for p-p collisions at 13.6 TeV center-of-mass energy in 2024. The delivered luminosity accounts for luminosity delivered from the start of stable beams until the LHC requests ATLAS to put the detector in a safe standby mode to allow for a beam dump or beam studies. The recorded luminosity reflects the DAQ inefficiency, as well as the inefficiency of the so-called “warm start“ [28].

B-decays, the detailed studies of the top quark - so a rich physics program was foreseen from the beginning. The Higgs search ⁷ was particularly important, and the detector had to cover the mass range $m_H > 80$ GeV (lower masses were already excluded by LEP experiments) by being sensitive to the following processes:

$80 < m_H < 100$ GeV : $H \rightarrow b\bar{b}$ from WH, ZH and $t\bar{t}H$ using a ℓ^\pm tag and b-tagging

$90 < m_H < 150$ GeV : $H \rightarrow \gamma\gamma$

$130 < m_H < 2m_Z$ GeV : $H \rightarrow ZZ^* \rightarrow 4\ell^\pm$

$2m_Z < m_H$: $H \rightarrow ZZ \rightarrow 4\ell^\pm, 2\ell^\pm 2\nu$

$m_H < 1000$ GeV : $H \rightarrow WW, ZZ \rightarrow \ell^\pm \nu jj, 2\ell^\pm jj$ from WW, ZZ using tagging of forward jets

Therefore, the detector should be able to provide as many signatures as possible using electrons, photons, muons, jets, missing transverse energy measurements, and b-quark tagging. Large pseudo-rapidity ($|\eta|$) acceptance is desired together with the capability of triggering on and measurements of particles at low transverse momentum (p_T) thresholds. Also, the cross-sections for most of these processes are small, and the detector should be able to cope with high instantaneous luminosities.

Taking into account the requirements from the physics program, the technologies available at the time and the budget constraints, the basic detector concepts were settled by the end of 1995 ⁸ and led to the following configuration

- A cylindrical, as hermetic as possible (for missing transverse momentum measurement)
- The usage of a toroidal magnet with eight superconducting coils in an air-core configuration

⁷According to “no-loose theorem“, there should either be a Higgs boson no heavier than approximately 1 TeV or otherwise, NP should occur near or below that energy scale.

⁸Some important decisions were made later; for example, TDAQ TDR was written only in 2003.

⁹Initially 12, but this was too expensive.

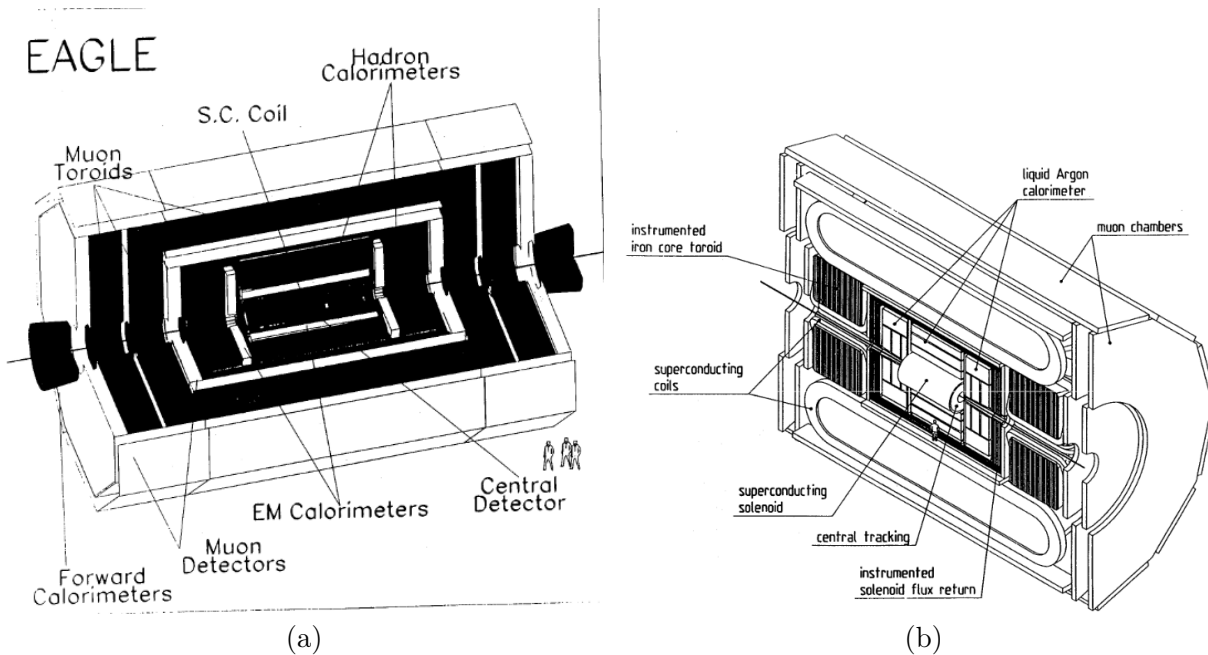


Figure 2.5: (a) EAGLE with warm iron barrel and end cap toroids [83] (b) ASCOT with a superconducting air-core barrel and warm iron end cap toroids [94].

- A configuration with a barrel (taken by innovative “accordion“ lead-LAr sampling EM calorimeter and pre-sampler) and two extended barrel cylinders (for iron-scintillator tile hadronic calorimeters)
- A muon spectrometer employing separate precision and trigger chambers
- An inner detector with pixel detectors for the innermost parts, followed by a Silicon strip detectors, followed by straw-tube tracker

Requirements for the sub-detectors are summarized in Table 2.2. After extensive R&D, sub-detectors reached the testbeam stage happening in 2002-2006, followed by two years of installation in the cavern. Once installed, cosmic ray tests were done in 2008-2009. The first stable colliding beams were recorded on December 5, 2009; the rest of the year was devoted to 900 GeV collisions. Run-1 happened in 2010-2012, collecting data for the Higgs discovery announced in 2012 [30]¹⁰ for which the Nobel Prize was awarded: a significant design goal was reached.

2.3.2 Run-3 detector configuration

ATLAS evolved from the TP to Run-3, and the schematic view of the current detector is shown on Fig. 2.6. It consists of an inner tracking detector (ID) surrounded by a thin superconducting solenoid, electromagnetic and hadronic calorimeters, and a muon spectrometer incorporating three large superconducting air-core toroidal magnets - most of this was foreseen in the TP. The dimensions of the detector are 25 m in height and 44 m in length, the overall weight of the detector is approximately 7000 T: it is the largest experiment at the LHC.

Among the detector sub-systems, the ID and forward sub-detectors will be shown in a bit more detail. The performance of the ID is strongly linked to and motivate the construction of the HGTD for the HL-LHC, which is discussed in Chapter 6, Chapter 7, Chapter 8. The timing information is complementary to the spatial information of the ID. The forward detectors are at the core of

¹⁰Also discovered by the CMS collaboration [32].

| Detector component | Minimally required resolution, characteristics | Measurement η coverage | Trigger η coverage |
|--|--|--|-----------------------------|
| | | Measurement | Trigger |
| EM calorimetry | $10\%/\sqrt{E} \oplus 0.7\%$ | ± 3 | ± 2.5 |
| Pre-shower detection | Enhanced $\gamma - \pi^0$ and γ -jet separation, direction measurements | ± 2.4 | |
| Jet and missing E_T Calorimetry barrel and end-cap forward | $50\%/\sqrt{E} \oplus 3\%$ $100\%/\sqrt{E} \oplus 10\%$ | ± 3 $3 < \eta < 5$ | ± 3 $3 < \eta < 5$ |
| Inner detector | 30% at $p_T = 500\text{GeV}$ Enhanced electron identification τ - and b-tagging Secondary vertex detection at initial luminosities | ± 2.5 ± 2.5 ± 2.5 ± 2.5 | |
| Muon detection | 10% at $p_T = 1\text{TeV}$ in stand-alone mode at highest luminosity | ± 3 | ± 2.2 |

Table 2.2: General detector performance goals [4].

the work on fJVT described in Chapter 4 and crucial to tag forward jets in the VBS analyses, combination of which is discussed in Chapter 3.

Inner detector

The ID schematic view is shown on Fig. 2.7. It is immersed in a 2 T magnetic field (which bends the particles track) generated by the central solenoid, which extends over a length of 5.3 m with a diameter of 2.5 m. The overall radial extension of ID is $0 < r < 1150$ mm, and length covers the region $0 < |z| < 3512$ mm. The ID covers $|\eta| \leq 2.5$ and is intended to reconstruct the trajectory, measure momentum, charge, and contribute to the PID of charged particles by detecting their interactions with the material at several points along the path. Another ID function is the location of the primary vertex of the events, which is done by extrapolating tracks to the beam axis.

The ID is composed of Pixel, SCT, and TRT sub-systems.

- The Pixel detector consists of the IBL (12 million channels), three barrel layers, and three disks on each side, and has approximately 80 million readout channels. IBL whose sensors have 50×250 ($r\phi, z$) μm pixels at an average radius of 33.4 mm. The pixel layers are segmented in $r\phi$ and z . Typically, a track crosses three pixel layers. For these three outer layers, all pixel sensors are identical, with a pixel size of 50×400 μm
- The SCT (having ≈ 6.3 million readout channels) has four strip layers (each is double-sided). In the barrel region, this detector uses small-angle (40 mrad) stereo strips to measure both $r\phi$ and z , with one set of strips in each layer parallel to the beam direction, measuring $r\phi$. They comprise two 6.4 cm long daisy-chained sensors with a strip pitch of $80\mu\text{m}$. In the endcap region, the detectors have a set of strips running radially and a set of stereo strips at an angle of 40 mrad. The mean pitch of the strips is also approximately 80 μm

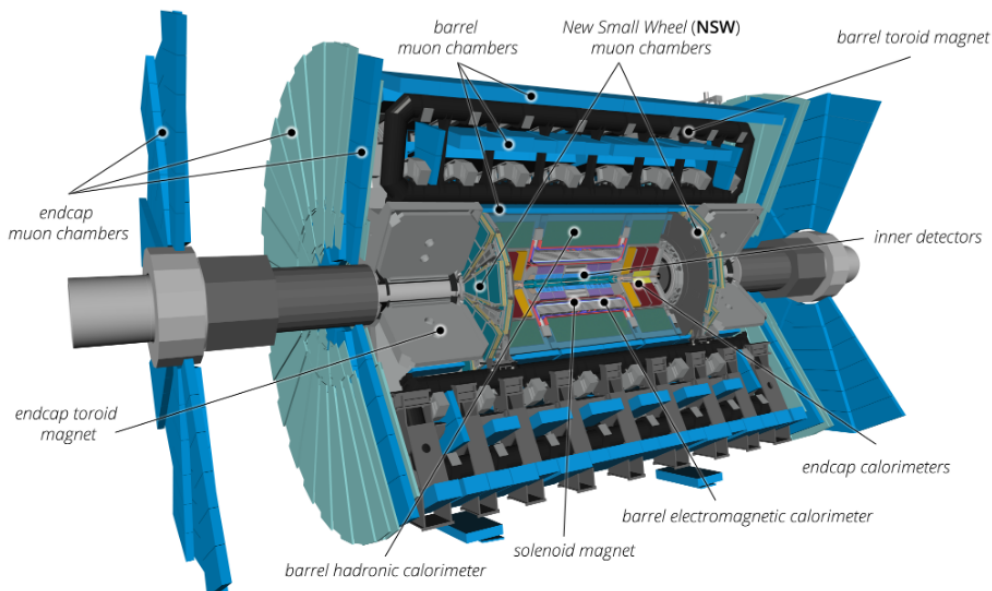


Figure 2.6: Cut-away view of the Run 3 configuration of the ATLAS detector indicating the locations of the larger detector sub-systems [51].

- The TRT is located furthest away and intended to provide continuous tracking and electron identification capability by detecting transition radiation X-ray photons. TRT is built from several layers of gas-filled straw tubes interleaved with transition radiation material. The 300000 thin-walled proportional-mode drift tubes provide on average 30 (r, ϕ) points with a $130 \mu\text{m}$ resolution for charged particle tracks with $|\eta| < 2$ and $p_T > 0.5 \text{ GeV}$.

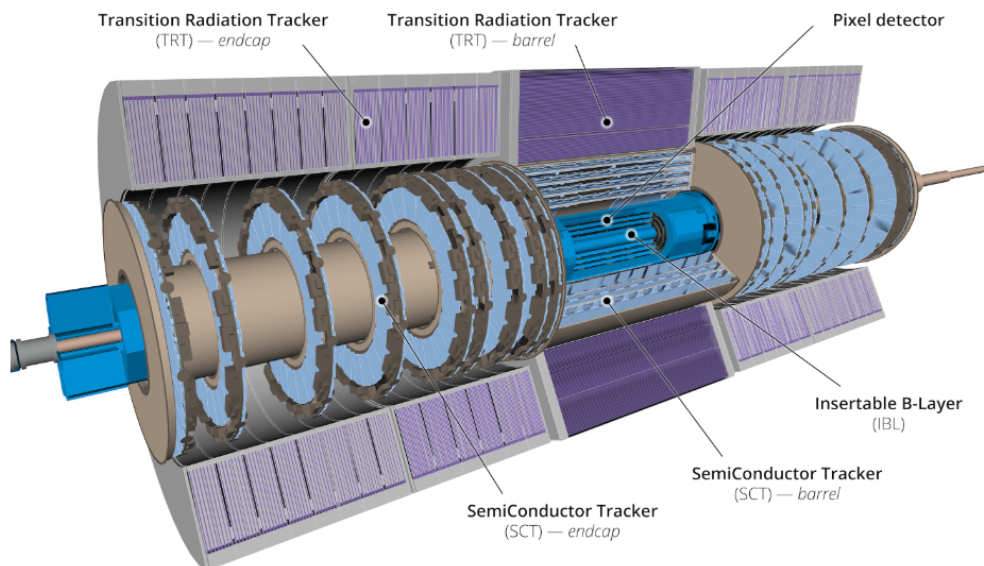


Figure 2.7: Cut-away view of the ATLAS ID [51]

The transverse momentum resolution is expressed as

$$\frac{\sigma_{p_T}}{p_T} = a \cdot p_T [\text{GeV}] \oplus b \quad (2.2)$$

with $a=0.05\%$ and $b=1.6\%$ for cosmic ray muons measurement.

Forward calorimeters

The purpose of the calorimeters is to measure the energies and positions of charged and neutral particles that interact electromagnetically or strongly by absorbing as much particle energy as possible. ATLAS used sampling calorimeters built from alternating layers of absorbing layers (intended to stop incoming particles, thickness depends on $|\eta|$) and active layers (intended to measure the deposits). A schematic view of all calorimeters is shown on Fig. 2.8; they are located outside of the ID.

The calorimeters in the forward $|\eta|$ region are LAr calorimeters and there are two systems covering different $|\eta|$ ranges: most-forward region $3.1 < |\eta| \leq 4.9$ is covered by FCal (has electromagnetic and hadronic part) and $1.5 < |\eta| \leq 3.2$ is covered by electromagnetic endcap (EMEC) and hadronic endcap (HEC)

- FCal has 3542 readout channels and comprises three layers: FCal1, FCal2, and FCal3, where the granularity is different in each, per $|\eta|$. For example FCal1 covers $3.15 < |\eta| \leq 4.83$ and $\Delta x \times \Delta y$ (cm) is 3.0×2.6 for $3.15 < |\eta| \leq 4.3$ but $\Delta x \times \Delta y$ is about four times finer for $3.10 < |\eta| \leq 3.15$ and $4.3 < |\eta| \leq 4.83$
- HEC has 5632 readout channels and four layers. The granularity in $\Delta\eta \times \Delta\phi$ is 0.1×0.1 for $1.5 < |\eta| \leq 2.5$ and 0.2×0.2 for $2.5 < |\eta| \leq 3.2$
- EMEC has 62208 readout channels and three layers. Organization of segmentation can be shown with 2nd layer, which has $\Delta\eta \times \Delta\phi$ is 0.025×0.025 for $1.425 < |\eta| \leq 2.5$ and larger for $1.375 < |\eta| \leq 1.425$ (0.05×0.025) and $2.5 < |\eta| \leq 3.2$ (0.1×0.1)

The energy resolution of the calorimeter is often expressed as

$$\frac{\sigma_E}{E} = \frac{a}{\sqrt{E}} \oplus \frac{b}{E} \oplus c \quad (2.3)$$

Noise term, $\frac{b}{E}$, is typically negligible. First term on the right-hand side is called “stochastic term“ and third term is called “constant term“. Overall for electromagnetic showers performance is better compared to hadronic. For EMEC (HEC) $a \approx 10\%$, $c \approx 1\%$ ($a \approx 50\%$, $c \approx 4\%$). For FCal $a \approx 100\%$, $c \approx 10\%$.

Other calorimeters, muon systems, TDAQ

Non-forward calorimeters include electromagnetic barrel (EMB, just outside of ID) and hadronic barrel Tile (concentric and outside of EMB), hadronic extended barrel Tile (located in the “corner“). EMB is an LAr calorimeter like the ones in the forward region. Tile(s) is the only ATLAS non-LAr calorimeter made of a plastic scintillator as an active material and a low-carbon steel absorber plate.

The Muon Spectrometer (MS) is a sub-system located at the largest radius (at $r=11$ m), behind the ID and the calorimeters for the reason that muons lose only a tiny fraction of their energy interacting with more inner-lying sub-detectors. A separate from ID magnetic field is used. As MS is large, one needs to use a detector technology “easily“ scalable in size but not in price - various kinds of gaseous detectors are used. MS covers $|\eta| < 2.7$ and can be used independently of other sub-detectors, however, combining its information with ID is beneficial.

The trigger and Data Acquisition (TDAQ) system is based on a two-level trigger system served by the Data Acquisition (DAQ) system. The trigger is responsible for the event selection. Given the rate of collisions, it’s impossible to both record and store all of them, so one needs to decide on what to keep. Two levels of triggers are implemented: a Level-1 Trigger (L1, based on custom-built electronics) and High-Level Trigger (HLT, based on software implemented on commodity

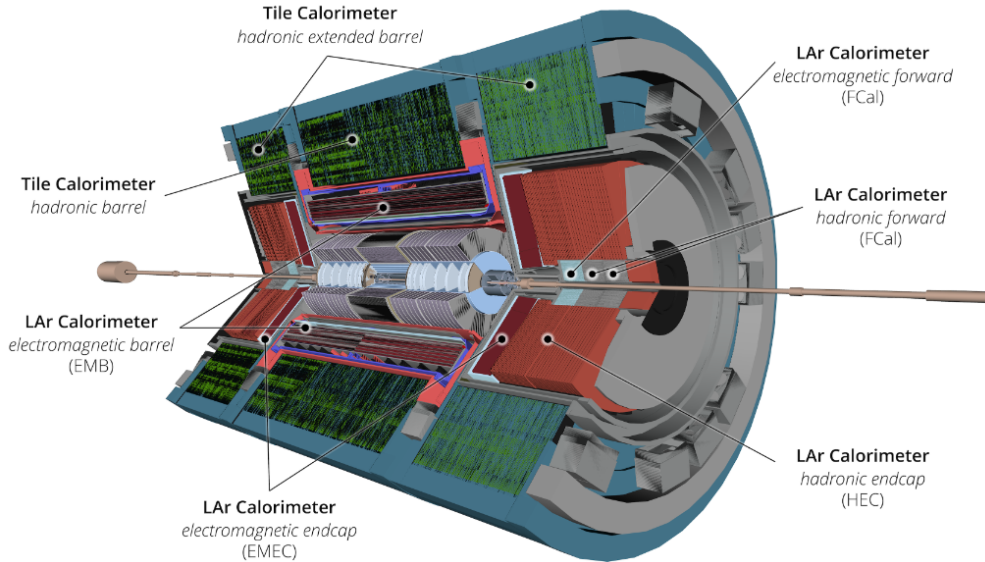


Figure 2.8: Cut-away view of the ATLAS calorimeters [51].

computers). After the trigger decision, DAQ transports data from custom sub-detector electronics to offline processing.

2.3.3 Object reconstruction

Most analyses rely on reconstructed jets and at least one another type of object: electron, photon, muon or MET. However, on object reconstruction, I only worked on jets (see Chapter 4) and therefore other types of objects would only be briefly mentioned, for completeness.

Jets

Isolated quarks or gluon cannot be observed due to color confinement, instead multiple of them hadronize together to form color singlets. As a result of chain of hadronizations occurring while particles are propagating from IP through detector, so-called “jet“ is formed. Illustration of such process is shown on Fig. 2.9. Experimental task, then, is to reconstruct the jet according to certain algorithm: cluster tracks (reconstructed from tracker hits, giving track jets), cluster calorimeter clusters (giving calorimeter jets) or combination of the two. In simulation, it’s possible to build so-called truth jets, which typically means inputs are particle-level (giving particle jets). Algorithm maps set of final state 4-momenta to jet 4-momenta. It’s desirable that algorithm has the following properties (called IRC safety requirements)

- Infrared safety: addition of soft particles among jet components does not affect the outcome of the clustering
- Collinear safety: splitting of one particle into two collinear ones does not affect the outcome of the clustering

Algorithm should work without taking too much computer resources.

The anti- k_t is a sequential pair-wise algorithm [25] chosen to be used at the LHC. The following strategy is employed: inputs are combined according to metric defined as

$$d_{ij} = \frac{1}{\max(p_{Ti}^2, p_{Tj}^2)} \frac{\Delta R_{ij}^2}{R^2} \quad (2.4)$$

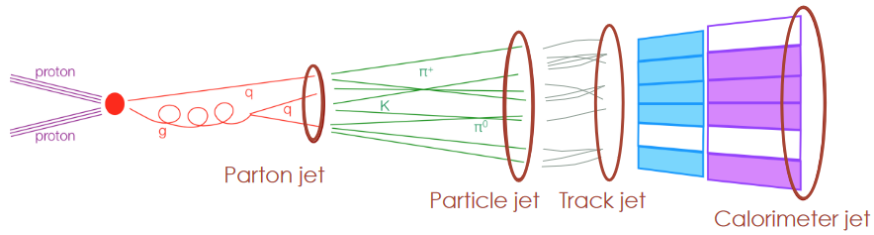


Figure 2.9: Illustration of jet formation [97].

$$d_{iB} = \frac{1}{p_{Ti}^2} \quad (2.5)$$

where p_{Ti}, p_{Tj} are transverse momenta of the input pair and $\Delta R_{ij} = \sqrt{(y_i - y_j)^2 + (\phi_i - \phi_j)^2}$ is a distance between them in $y - \phi$ space. Inputs should have $p_T > p_T^{min}$ where p_T^{min} a parameter user defines. R is another a free parameter that user defines. At each step, minimum between d_{ij} and d_{iB} is computed. If d_{iB} turns out to be smaller than d_{ij} i is declared to be a jet a removed from the list of inputs, otherwise if d_{ij} is smaller than d_{iB} i, j are combined into one single input by taking the sum of their 4-momenta. Most energetic inputs would be clustered first.

There are two main reasons why anti- k_t became the default jet algorithm (apart from IRC safety). One is that resulting jets have circular shape, as shown in Fig. 2.10a. Also resulting jet p_T is linear as function of transverse momentum of one of the inputs.

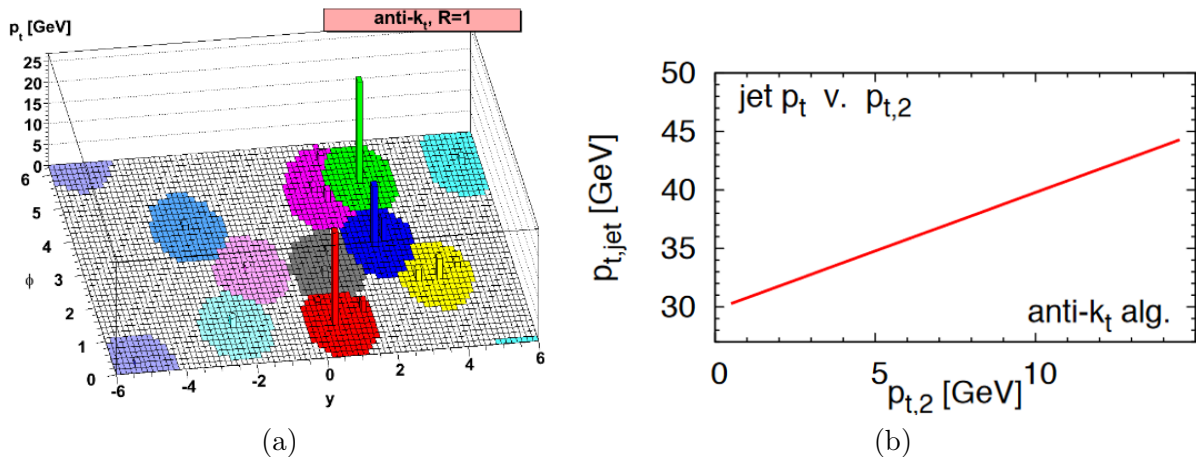


Figure 2.10: (a) A sample parton-level event together with many random soft “ghosts“, clustered with anti- k_t algorithm [25] (b) anti- k_t jets as function of transverse momentum of one of the inputs [99].

Typical values for R currently used in ATLAS range from 0.4 to 1. In what follows focus will be on $R=0.4$ jets, also called small- R jets, because that’s a most common type of jet used through the thesis - for forward Jet Vertex Tagging calibration (see Chapter 4) and in all analyses in VBS combination (see Chapter 3).

Currently, default ATLAS algorithm to prepare inputs to clustering algorithm is particle flow (PFlow) [7] and resulting jets are named “PFlow jets“. PFlow utilizes information from both the tracker and the calorimeter which are combined to form the signals. In chronologically previous approach jets were built from topological cluster of calorimeter cells (topo-clusters)[8] only and resulting jets are referred to as “EMtopo jets“. Motivations to use PFlow instead of EMtopo jets are that for low- p_T charged particles, tracker has (compared to calorimeter) significantly better momentum resolution,

lower p_T threshold (400 MeV) for reconstruction and better angular resolution. On the other hand, at high energies calorimeter's energy resolution is superior to that of tracker. Therefore, it is advantageous to combine the two types of information. Key steps of PFlow algorithm are summarized on Fig. 2.11 - major goal is to avoid double-counting of energy in the reconstruction. Either tracker or calorimeter measurement is used. If a particle's track measurement is to be used, the corresponding energy must be subtracted from the calorimeter measurement. Care is taken to accurately subtract all of a single particle's energy, without removing any energy deposited by any other particle. One example of benefits from utilization of PFlow is shown on Fig. 2.12a - p_T resolution is improved at low p_T up to 15%.

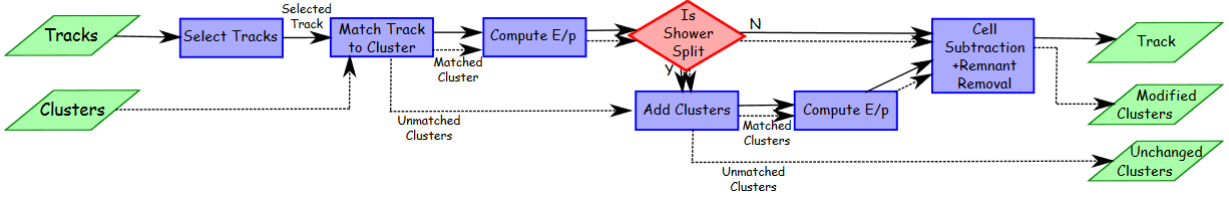


Figure 2.11: A flow chart of how the particle flow algorithm proceeds, starting with track selection and continuing until the energy associated with the selected tracks has been removed from the calorimeter. At the end, charged particles, topo-clusters which have not been modified by the algorithm, and remnants of topo-clusters which have had part of their energy removed remain [7].

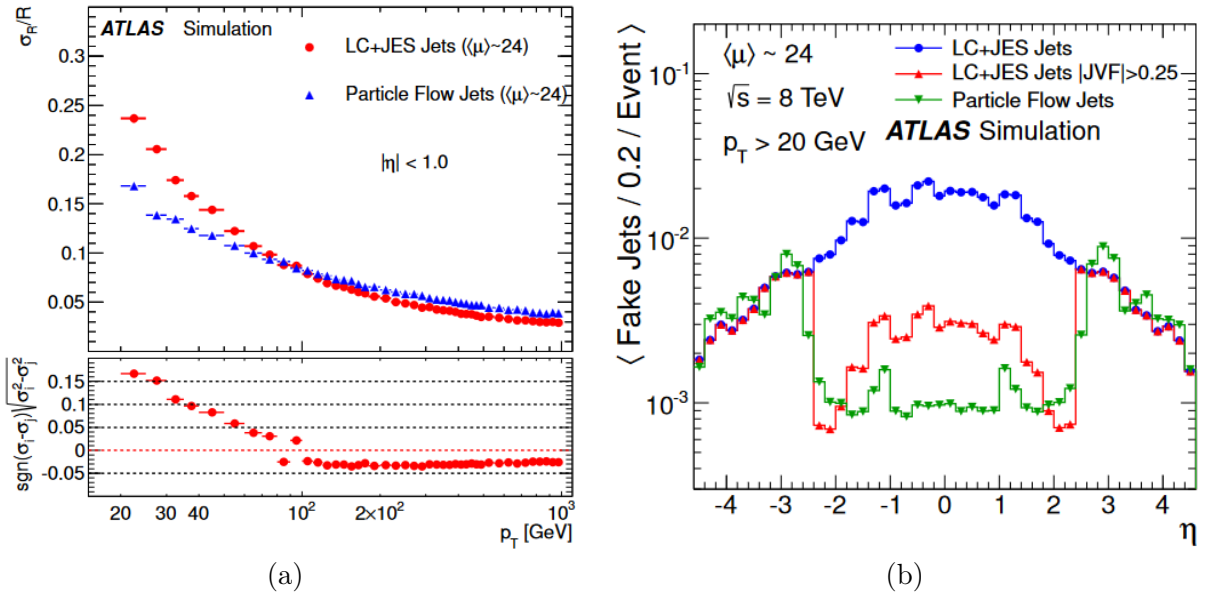


Figure 2.12: (a) The jet transverse momentum resolution as a function of p_T for jets with $|\eta| < 1.0$, determined in dijet MC events for calorimeter jets and particle flow jets. Simulated pile-up conditions are similar to the data-taking in 2012. To quantify the difference in resolution between particle flow and calorimeter jets, the lower figure shows the square root of the difference of the squares of the resolution for the two classes of jets. A local cluster (LC) weighting scheme is used to calibrate hadronic clusters to the correct scale [7]. (b) The number of pile-up “fake jets“ in dijet MC events. Simulated pile-up conditions are similar to the data-taking in 2012 [7].

In each bunch crossing, it's not just one proton colliding with another proton but multiple of them. During Run-3 in ATLAS typically around 50 collisions are happening simultaneously and therefore different objects would originate from different collisions. Different kinds of jets can be

distinguished. Typically, there is an interest in only interaction vertex called hard-scatter (HS) and jets coming from it HS jets. Jet is labelled as HS jet if truth HS jet with $p_T > 10$ GeV is found within $\Delta R < 0.3$ and if there are several matches, jet with highest p_T^{truth} among them is taken. All the other collisions are referred to as pile-up¹¹. Jets originating from pile-up interaction are called pile-up (PU) jets. Different types of jets are illustrated on Fig. 2.13 where one might see two types of PU jets:

1. QCD PU jets: the majority of constituents come from single vertex, but not the HS vertex of interest. At truth level historical ATLAS definition [34] of such jet is the one for which no truth-particle hard-scatter jet with $p_T > 4$ GeV is found within $\Delta R < 0.6$ but there is a pile-up truth jet within $\Delta R < 0.3$
2. Stochastic PU jets: typically not having contribution from single prevalent vertex but do often contain out-of-time pile-up. Not a jet in a sense of “energetic spray of hadronic showers“ but instead clustered accidentally. With truth stochastic PU jet is identified as the one for which no truth-particle hard-scatter jet with $p_T > 4$ GeV is found within $\Delta R < 0.6$ (this part of definition is same as for QCD PU) but there is no pile-up truth jet within $\Delta R < 0.6$

One might see truth PU definitions are not exhaustive in p_T and ΔR , rest cannot be unambiguously matched. Benefit of using PFlow for removal undesirable pile-up is shown on Fig. 2.12b in comparison to calorimeter jets. “Fake jets“ are stochastic jets, and they are almost absent in central region, but QCD PU still needs to be removed which is the purpose of NNJVT, considered below. There is no gain in forward region because there is no tracker there.

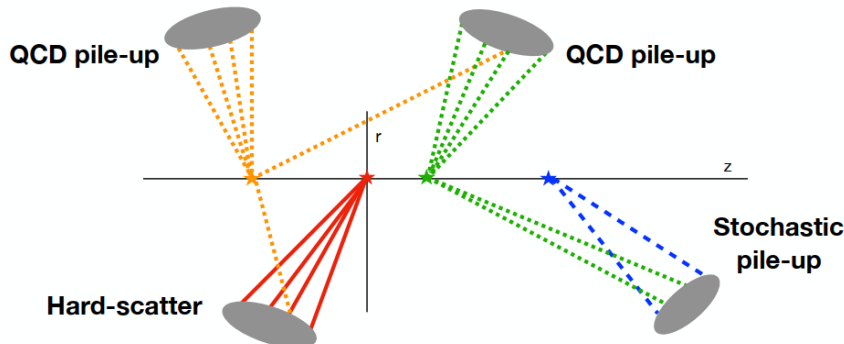


Figure 2.13: Schematic example of different jet types [87].

Jets needs to be calibrated, it’s described in [12],[15] done via steps summarized on Fig. 2.14. Goal of “Pile-up correction“ steps is to remove the dependence of p_T^{reco} on pile-up. Both in-time, out-of time types and correlation between them is addressed. It’s achieved by correcting measured jet transverse momentum as follows

$$p_T^{corr} = p_T^{reco} - \rho \times A - \alpha \times (N_{PV} - 1) - \beta \times \mu \quad (2.6)$$

where ρ is median pile-up momentum density (derived from central region) weighted to the jet area. α (β) are coefficients derived per $|\eta|$ bin sensitive to N_{PV} (μ) residual dependence.

Calibration proceeds with absolute MC-based calibration (jet energy scale and $|\eta|$), where the goal is to correct p_T^{reco} (both energy and direction) by taking into account for energy losses in passive material, out-of-cone effects and non-compensating calorimeter response, $|\eta|$ biases primarily caused

¹¹Actually in-time pile-up. There is also out-of-time pile-up formed from energy leftovers in calorimeter from previous or following bunch crossing.

by the transition between different calorimeter technologies and granularities. The next step is the Global Neural Network Calibration (GNNC) which is a recent addition superseding Global Sequential Calibration (GSC), corrects for differences between the calorimeter response to different types of jets, which improves the jet resolution without changing the jet energy response. GNNC is a DNN trained to predict p_T based on calorimeter, jet kinematics, tracking, muon segments, pile-up informations and taking into account correlations between variables. After all those steps, there still would be differences arising from MC mismodelling of detector material, detector response, EM and hadronic showers etc. - discrepancy between data and the MC simulation are accounted for.

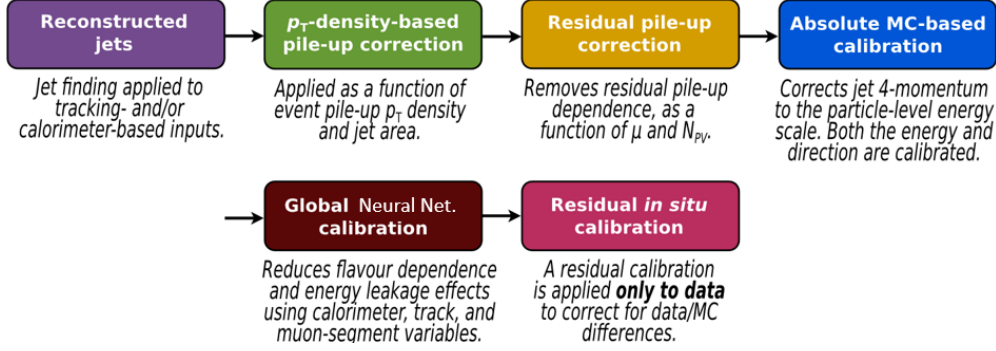


Figure 2.14: Stages of jet energy scale calibrations. Each one is applied to the four-momentum of the jet. Adapted from [12].

Subject of Chapter 4 is an algorithm designed to the rejection of PU jets in forward region. It's instructive to see how this is done in the central region, where Neural Network Jet Vertex Tagging (NNJVT) algorithm is utilized. NNJVT is a Neural Network continuation of JVT [6], providing fixed efficiency to select hard-scatter jet over $|\eta|$ in each p_T bin. JVT, in turn, is also a neural net: derived using simulated dijet events and based on a k-nearest neighbour (kNN) from $R_{pT,corrJVF}$ defined as

$$R_{pT} = \frac{\sum_k p_{T,k}^{\text{track}}(\text{PV}_0)}{p_T^{\text{jet}}} \quad (2.7)$$

$$\text{corrJVF} = \frac{\sum_m p_{T,m}^{\text{track}}(\text{PV}_0)}{\sum_l p_{T,l}^{\text{track}}(\text{PV}_0) + \frac{\sum_{n \geq 1} \sum_l p_{T,l}^{\text{track}}(\text{PV}_n)}{(k \cdot n_{\text{track}}^{\text{PU}})}} \quad (2.8)$$

Both variables are relying on track information. R_{pT} , shown on Fig. 2.15a, is the estimating fraction of jet p_T carried by tracks originating from the HS vertex. corrJVF is shown on Fig. 2.15b, and it's a measure of jet's tracks fraction associated to HS vertex, including correction for number for NPV.

Electrons and photons, Muons, MET

To reconstruct electrons and photons one mostly relies on EM calorimeters since those particles initiate EM showers. Also ID information is useful to distinguish between electron (charged particle, expected to leave track) and photon (doesn't have charge, should not be in ID hits). However, photon can be converted to electron-positron pair while propagating to calorimeter. In that case pair of tracks originating away from IP expected to be visible via tracker. Starting point for electron reconstruction is clustering of deposits in calorimeter result of which matched to tracks. If matching is not possible electron is tagged as converted photon. Correction for energy lost during interactions with material is done. Prompt electron is required to be identified as the originating from HS vertex. For the identification likelihood-based discriminant is used, relying on typical shape variables of EM

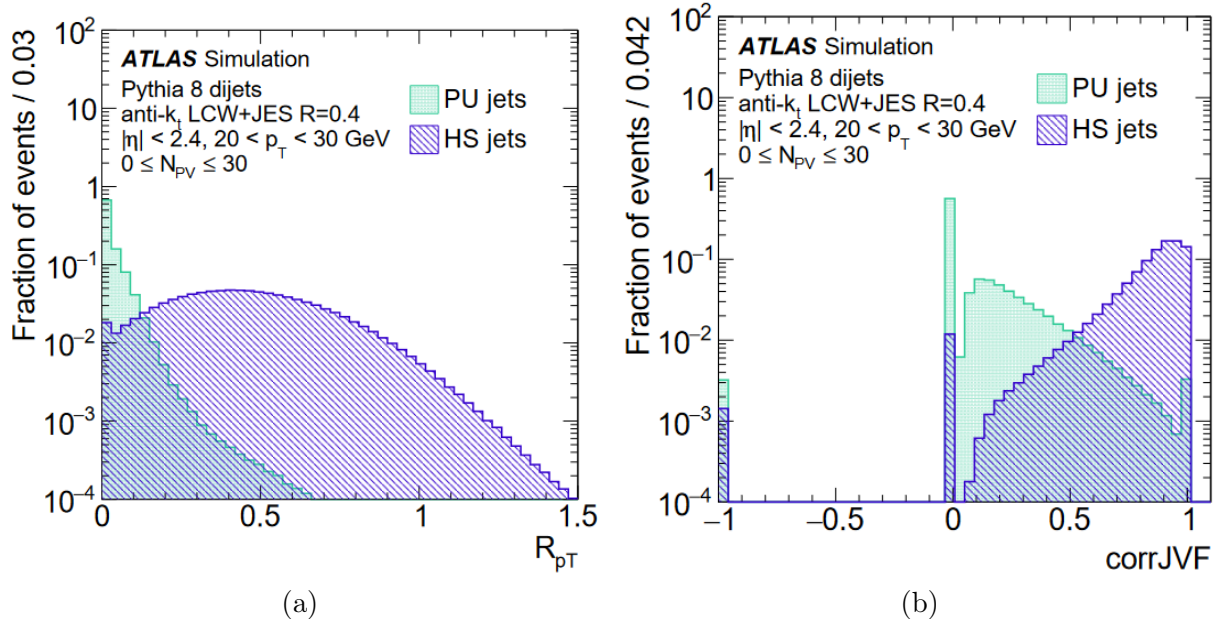
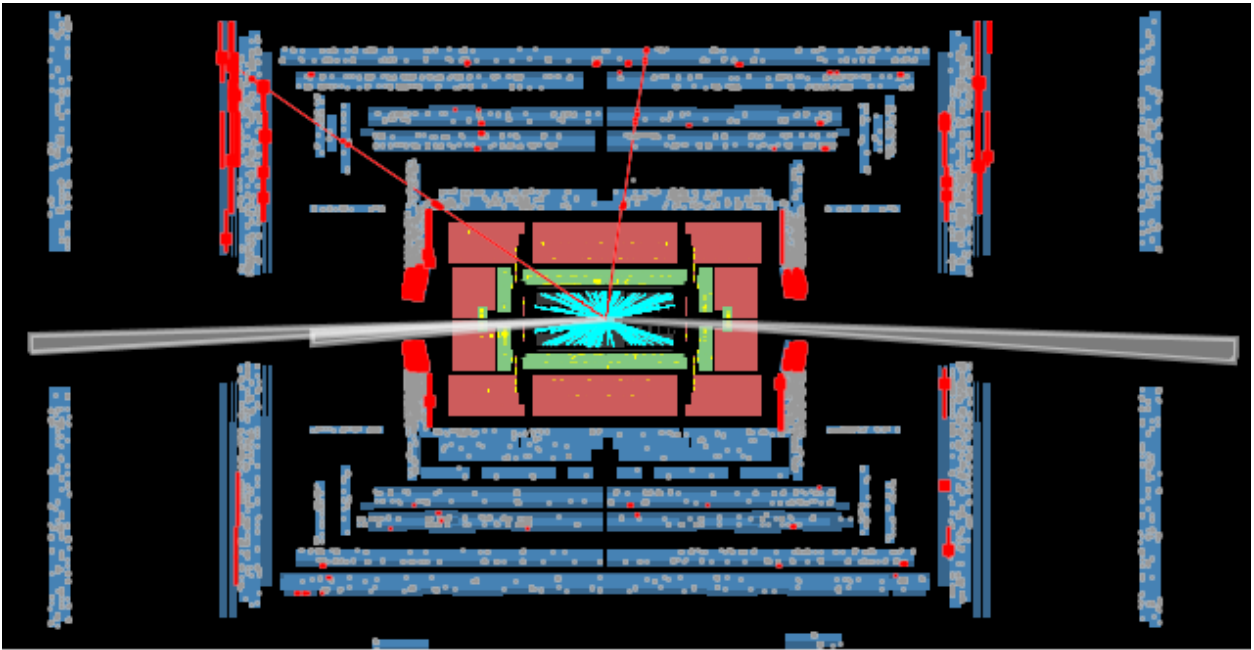


Figure 2.15: Distribution for pile-up (PU) and hard-scatter (HS) jets with $20 < p_T \leq 30 \text{ GeV}$ [6] of (a) R_{pT} (b) corrJVF

showers to reduce misidentification with other objects. Three working points: loose, medium, tight are utilized for electron and two for photon identification: loose, tight.

Muon, being a stable charged particle typically undergoing a little amount of interactions reaches furthest-away layers of detector. It thus may leave hits in both tracker and MS. MIP-compatible calorimeter hits also may be used for reconstruction. As MS from the beginning of ATLAS were designed to be able to work stand-alone if needed (it's only used as last resort) this regime can be utilized. For muon to be classified as prompt, various requirements are applied, such as compatibility between momentum ID and MS measurements, number of hits in each sub-detector, quality of χ^2 fit (hits from segments in different layers are fitted together). Three working points for $20 < p_T \leq 100$ muons are defined with selection efficiency ranging between 98.1% to 91.8%.

If there are neutrinos (or some other exotic non-interacting particle) in final state they will not be detected by any detector sub-system. Workaround can be utilized relying on detector hermeticity, detector design decision made in the very beginning. Because initial $\sum p_T$ in event is zero, if one measured everything else except neutrinos, resulting non-zero $\sum p_T$ would mean presence of neutrinos. One then defines Missing Transverse Energy (MET, confusingly not called Missing Transverse Momentum) as $\vec{E}_T^{\text{miss}} = -\sum_i \vec{p}_T^i$ where sum runs over both hard final state objects (reviewed above) and soft objects (un-associated to hard objects tracks), as everything should be included. Special care is taken to avoid double counting (e.g. same energy deposit should not be included in both jet and calorimeter), for which overlap removal procedure excludes hits from the list in particular order: electrons are prioritized, then photons, other leptons, jets and finally, tracks.



3 - aQGC EFT VBS Run-2 combination

3.1 Analyses involved

Many ATLAS Run-2 VBS analyses are already published or close to be published

- $Z\gamma$ with Z decaying leptonically [49] or into MET [48],
- ZZ decaying into four leptons [52] or into $ll\nu\nu$ [95] final states
- VBS semileptonic analysis [92]
- With at least one W: $W^\pm W^\pm$ [55], WZ [56], $W\gamma$ [31]

covering different di-boson pairs and final states involving various couplings. All of them are Standard Model analyses aiming at observing the process, measuring inclusive cross-sections, and various differential cross-sections. In addition, the results of these analyses are used to constraint anomalous Quartic Gauge Couplings (aQGC) even though they were not necessarily optimized for that purpose ¹. Analyses that did unfolding ² are: $Z(\rightarrow \bar{\ell}\ell)\gamma$, $ZZ \rightarrow 4\ell$, $W\gamma$. Rest are not unfolded.

3.2 Eboli operators

VBS process contains QGC, and therefore, one might study those couplings in the hunt for potential deviation from the SM. One needs dimension-8 EFT operators to act only on QGC without affecting triple gauge coupling. A complete set of those dimension-8 operators was derived in [105]; however, as it turned out later, it was not complete as it was missing two operators added in [62]. Twenty operators from [62] in the community are referred to as ‘‘Eboli operators’’ and constitute a basis for C-even and P-even aQGC operators ³ and include all possible modifications to VVVV, VVVH, and VVHH vertices compatible with conservation of C, P, electric charge. Eboli operators are grouped into three families: scalar, mixed, and tensor, depending on the content. Scalar (S) operators are built only from covariant derivatives of the Higgs field $D_\mu\Phi = \left(\partial_\mu + igW_\mu^j \frac{\sigma^j}{2} + ig'B_\mu \frac{1}{2}\right)\Phi$, where Φ is a Higgs doublet and $\sigma^j = \sigma^1, \sigma^2, \sigma^3$ are the Pauli matrices

$$\begin{aligned}
 \mathcal{O}_{S0} &= \left[(D_\mu\Phi)^\dagger D_\nu\Phi \right] \times \left[(D^\mu\Phi)^\dagger D^\nu\Phi \right] \\
 \mathcal{O}_{S1} &= \left[(D_\mu\Phi)^\dagger D^\mu\Phi \right] \times \left[(D_\nu\Phi)^\dagger D^\nu\Phi \right] \\
 \mathcal{O}_{S2} &= \left[(D_\mu\Phi)^\dagger D_\nu\Phi \right] \times \left[(D^\nu\Phi)^\dagger D^\mu\Phi \right]
 \end{aligned} \tag{3.1}$$

Mixed (M) operators, in addition to covariant derivatives of the Higgs field, contain field

¹This will be the program for some follow-up analyses.

²Process aiming to go from measured distribution to truth distribution.

³Currently under discussion is the CP-even basis, which, in addition to Eboli operators, includes two C-odd and P-odd operators, making them even under combined CP [70].

Table 3.1: Vertexes affected by aQGC operators

| Operators | SM | | | | Not SM | | | | |
|--------------------|------|------|-------------------|---------------|--------|--------------|-------------------|------------------------|----------------------------|
| | WWWW | WWZZ | WW $\gamma\gamma$ | WW γZ | ZZZZ | ZZZ γ | ZZ $\gamma\gamma$ | Z $\gamma\gamma\gamma$ | $\gamma\gamma\gamma\gamma$ |
| S0, S1 | ✓ | ✓ | | | ✓ | | | | |
| M0, M1, M7 | ✓ | ✓ | ✓ | ✓ | ✓ | ✓ | ✓ | | |
| M2, M3, M4, M5 | | ✓ | ✓ | ✓ | ✓ | ✓ | ✓ | | |
| T0, T1, T2 | ✓ | ✓ | ✓ | ✓ | ✓ | ✓ | ✓ | ✓ | ✓ |
| T3, T4, T5, T6, T7 | | ✓ | ✓ | ✓ | ✓ | ✓ | ✓ | ✓ | ✓ |
| T8, T9 | | | | | ✓ | ✓ | ✓ | ✓ | ✓ |

strengths $\widehat{W}_{\mu\nu} \equiv W_{\mu\nu}^j \frac{\sigma^j}{2}$ (for $SU(2)_L$) and $B_{\mu\nu}$ (for $U(1)_Y$):

$$\begin{aligned}
 \mathcal{O}_{M0} &= \text{Tr} \left[\widehat{W}_{\mu\nu} \widehat{W}^{\mu\nu} \right] \times \left[(D_\beta \Phi)^\dagger D^\beta \Phi \right] \\
 \mathcal{O}_{M1} &= \text{Tr} \left[\widehat{W}_{\mu\nu} \widehat{W}^{\nu\beta} \right] \times \left[(D_\beta \Phi)^\dagger D^\mu \Phi \right] \\
 \mathcal{O}_{M2} &= [B_{\mu\nu} B^{\mu\nu}] \times \left[(D_\beta \Phi)^\dagger D^\beta \Phi \right] \\
 \mathcal{O}_{M3} &= [B_{\mu\nu} B^{\nu\beta}] \times \left[(D_\beta \Phi)^\dagger D^\mu \Phi \right] \\
 \mathcal{O}_{M4} &= \left[(D_\mu \Phi)^\dagger \widehat{W}_{\beta\nu} D^\mu \Phi \right] \times B^{\beta\nu} \\
 \mathcal{O}_{M5} &= \left[(D_\mu \Phi)^\dagger \widehat{W}_{\beta\nu} D^\nu \Phi \right] \times B^{\beta\mu} + \text{h.c.} \\
 \mathcal{O}_{M7} &= \left[(D_\mu \Phi)^\dagger \widehat{W}_{\beta\nu} \widehat{W}^{\beta\mu} D^\nu \Phi \right]
 \end{aligned} \tag{3.2}$$

Finally, tensor (T) operators only contain field strengths

$$\begin{aligned}
 \mathcal{O}_{T0} &= \text{Tr} \left[\widehat{W}_{\mu\nu} \widehat{W}^{\mu\nu} \right] \times \text{Tr} \left[\widehat{W}_{\alpha\beta} \widehat{W}^{\alpha\beta} \right] \\
 \mathcal{O}_{T1} &= \text{Tr} \left[\widehat{W}_{\alpha\nu} \widehat{W}^{\mu\beta} \right] \times \text{Tr} \left[\widehat{W}_{\mu\beta} \widehat{W}^{\alpha\nu} \right] \\
 \mathcal{O}_{T2} &= \text{Tr} \left[\widehat{W}_{\alpha\mu} \widehat{W}^{\mu\beta} \right] \times \text{Tr} \left[\widehat{W}_{\beta\nu} \widehat{W}^{\nu\alpha} \right] \\
 \mathcal{O}_{T5} &= \text{Tr} \left[\widehat{W}_{\mu\nu} \widehat{W}^{\mu\nu} \right] \times B_{\alpha\beta} B^{\alpha\beta} \\
 \mathcal{O}_{T6} &= \text{Tr} \left[\widehat{W}_{\alpha\nu} \widehat{W}^{\mu\beta} \right] \times B_{\mu\beta} B^{\alpha\nu} \\
 \mathcal{O}_{T7} &= \text{Tr} \left[\widehat{W}_{\alpha\mu} \widehat{W}^{\mu\beta} \right] \times B_{\beta\nu} B^{\nu\alpha} \\
 \mathcal{O}_{T8} &= B_{\mu\nu} B^{\mu\nu} B_{\alpha\beta} B^{\alpha\beta} \\
 \mathcal{O}_{T9} &= B_{\alpha\mu} B^{\mu\beta} B_{\beta\nu} B^{\nu\alpha}
 \end{aligned} \tag{3.3}$$

The sum of a number of operators in Eq. 3.1, Eq. 3.2, Eq. 3.3, contrary to what was said above, is not 20. From Eq. 3.2 \mathcal{O}_{M6} was omitted as it is proportional to \mathcal{O}_{M1} . From Eq. 3.3 \mathcal{O}_{T3} , \mathcal{O}_{T4} were omitted as they vanish identically. Moreover, \mathcal{O}_{S0} , \mathcal{O}_{S2} from Eq. 3.1 are often merged in practice (only difference being $\mu \leftrightarrow \nu$ in second term of product). In the end, there are only 17 independent dimension-8 operators containing only SM fields.

Some of those operators modify existing SM couplings, and some add new ones, as summarized in Table 3.1.

3.3 Expectation from the combination

Analyses listed in Sec. 3.1 all individually derived limits on Wilson coefficients associated with operators shown in Eq. 3.1, Eq. 3.2, Eq. 3.3. From Table 3.1 not all the analyses are sensitive to all the operators - for example \mathcal{O}_{T8} , \mathcal{O}_{T9} are only appearing in electrically neutral vertices and can be probed by $Z(\rightarrow \bar{\nu}\nu)\gamma$, $Z(\rightarrow \bar{\ell}\ell)\gamma$, $ZZ \rightarrow \bar{\ell}\ell\nu\bar{\nu}$, $ZZ \rightarrow 4\ell$ and semileptonic VV(which contains all the pairs) but not $W^\pm Z$, $W^\pm W^\pm$. S family operators are unavailable in all analyses with photons: $W\gamma$, $Z(\rightarrow \bar{\ell}\ell)\gamma$, $Z(\rightarrow \bar{\nu}\nu)\gamma$, etc. By combining the analyses, one can put constraints on all the operators, opening the road for multi-dimensional constraints on the complete set.

When several analysis are sensitive to the same operator like \mathcal{O}_{M2} (just for concreteness) which can be probed by all the analyses; one might hope that the combined limit is more stringent than the best individual limits. It can be illustrated by results of previous aQGC ATLAS combination [14] done with Early-Run-2 data and including only early $W^\pm W^\pm$ and $W^\pm Z$ analyses. As seen on Fig. 3.1 combined \mathcal{O}_{T0} , \mathcal{O}_{T2} limits are more stringent than the best individual limit (which for those two cases turns out to be given by $W^\pm W^\pm$).

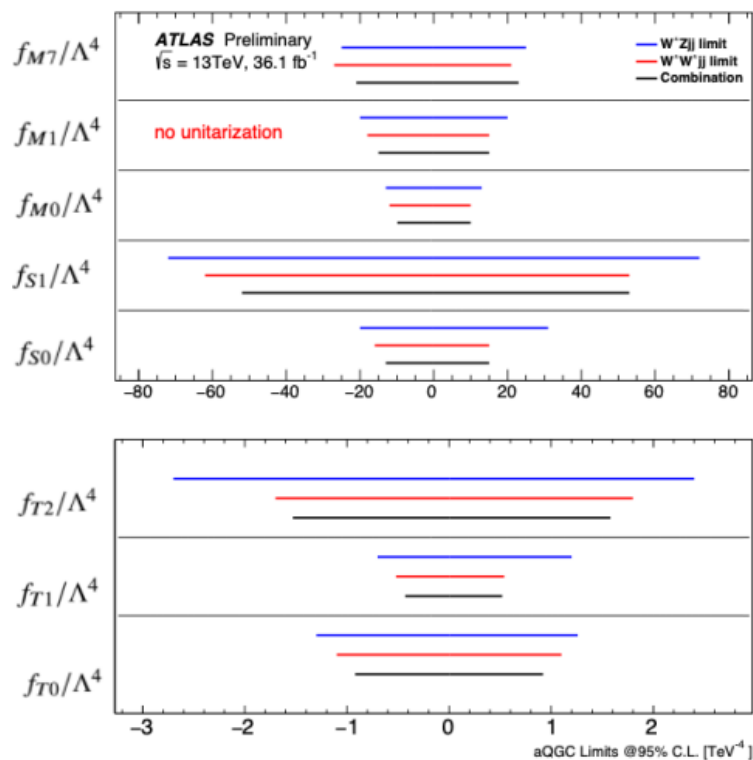


Figure 3.1: Observed lower and upper 95% confidence level limits on the parameters of the quartic operators M0, M1, M7, S0, S1, T0, T1 and T2 in $W^\pm Z$ jj and $W^\pm W^\pm$ jj individual channels and combination [14].

3.4 EFT samples generation

Inclusion of EFT into amplitude will give, compared to SM-only case

$$A_{SM} \rightarrow A_{SM} + \sum_{operator \neq o} c_o A_o \quad (3.4)$$

Where A_{SM} is SM amplitude, A_o is the contribution from each of EFT operators (like $\mathcal{O}_{T0}, \mathcal{O}_{T1}$ etc) with a corresponding Wilson coefficient c_o . Squaring this amplitude to obtain the cross-section

will give, focusing only on one operator with label i

$$\sigma_{SM+i} \propto |A_{SM} + A_i|^2 = |A_{SM}|^2 + c_i \cdot 2 \operatorname{Re} \left(A_{SM} A_i^\dagger \right) + c_i^2 |A_i|^2 \quad (3.5)$$

Among the three terms, the first one corresponds to SM-only contribution for cross-section, which one would observe in absence of New Physics(NP), the second term is the interference term between the SM and aQGC operator i, and the last term is a pure EFT contribution (also known as quadratic term).

Considering two operators i, j $A_{SM} + A_i + A_j$ and squaring to obtain the cross-section for this case gives now

$$\sigma_{SM+i+j} \propto |A_{SM}|^2 + \underbrace{c_i \cdot 2 \operatorname{Re} \left(A_{SM} A_i^\dagger \right)}_{\text{SM interference with EFT i}} + \underbrace{c_j \cdot 2 \operatorname{Re} \left(A_{SM} A_j^\dagger \right)}_{\text{SM interference EFT j}} + \underbrace{c_i^2 |A_i|^2 + c_j^2 |A_j|^2}_{\text{EFT quadratic terms}} + \underbrace{c_i c_j \cdot 2 \operatorname{Re} \left(A_i A_j^\dagger \right)}_{\text{EFT cross-term}} \quad (3.6)$$

where there is still the SM term but also two interference terms (one per operator) and two quadratic terms. A new addition is a cross-term between two aQGC operators, sometimes confusingly can be called an interference term, but this one has nothing to do with SM. $\sigma_{SM+i+j+k+\dots}$ with three or more operators will get decomposed into a corresponding number of interference, quadratic terms, and cross-terms from all the pairs of operators considered on top of the SM cross-section.

MC generation is done separately for SM, each interference, quadratic, and cross-term terms. Our end goal is to derive Confidence Limits (CL) driven by cross-sections/events obtained $\sigma_{operator(pair)}^{order}$, entering with a corresponding operator(s) coefficient(s) that we want to fit. For EFT generation, a Wilson coefficient equal to 1 is typically used. Whatever the value, it should be consistent between different samples. In this section and for analyses considered, EFT generation is done with MadGraph5 [20] and UFO model used is QA11_5_Aug21v2 ⁴, coming from FeynRules 2.3.47 [19] and integrated into ATLAS software ⁵. The current (published reasonably recently) version of the model allows us to obtain predictions for T3 T4 operators, however, they were not part of the original Eboli model MadGraph implementation and not used by most of the analyses (many started 5+ years ago) who used older implementation.

When deriving limits for one coefficient c_i at the time, all the others coefficients $c_{j \neq i}$ are set to zero and one is back at the configuration of Eq. 3.5, where there is no EFT cross-term. However, one should consider the cross-term(s) when fitting two or more coefficients simultaneously.

3.5 EFT cross-sections

Table 3.2 is showing a summary of the production cross-section of quadratic terms, all operators, for four di-boson pairs. Dashes correspond to cases where operators are not accessible by boson pair. The cross-section for the T operators family is typically larger than for S and M operators.

Table 3.3 is similar to Table 3.2 but for interference terms - showing (in comparison to the table above) characteristic feature of aQGC EFT: interference terms are mostly much smaller. Also, it can be seen that apart from quadratic terms, interference can be negative.

A representative example of the relationship between interference and quadratic terms depending on di-boson mass is shown on Fig. 3.2 (T6 operator of $W\gamma$ analysis) where both distributions are normalized to their corresponding cross-section. The interference term is negative, sharper, peaks at smaller $m_{W\gamma}$ and there is no slice of $m_{W\gamma}$ where quadratic terms would not dominate (apart from very low values). The cumulative distribution function of interference and quadratic terms sum

⁴<https://feynrules.irmp.ucl.ac.be/wiki/AnomalousGaugeCoupling>

⁵https://gitlab.cern.ch/atlas-generators-team/MadGraphModels/-/tree/main/EFT/QA11_5_Aug21v2?ref_type=heads

Table 3.2: Production cross-sections (in femtobarns) for quadratic EFT terms.

| | ZZ | Zy | WZ | Wy |
|-----|-------|--------|-------|-------|
| T0 | 75.33 | 42.08 | 35.26 | 9.65 |
| T1 | 47.58 | 26.45 | 79.54 | 22.27 |
| T2 | 11.42 | 6.41 | 9.43 | 2.63 |
| T5 | 12.19 | 39.32 | 5.80 | 19.35 |
| T6 | 5.01 | 8.50 | 6.34 | 21.61 |
| T7 | 1.08 | 2.83 | 1.05 | 3.58 |
| T8 | 18.03 | 122.80 | - | - |
| T9 | 3.92 | 26.79 | - | - |
| S02 | 0.08 | - | 0.11 | - |
| S1 | 0.03 | - | 0.01 | - |
| M0 | 2.85 | 0.04 | 0.49 | 0.06 |
| M1 | 0.22 | 0.01 | 0.20 | 0.02 |
| M2 | 1.44 | 0.29 | 0.15 | 0.52 |
| M3 | 0.12 | 0.10 | 0.06 | 0.21 |
| M4 | 0.20 | 0.08 | 0.61 | 0.15 |
| M5 | 0.10 | 0.13 | 0.34 | 0.21 |
| M7 | 0.06 | 0.01 | 0.12 | 0.01 |

shows no features of interference term basically follows quadratic term di-boson mass - interference term is small.

3.6 SM and EFT distributions

Effect of aQGC on various spectrums is shown on Fig. 3.3, Fig. 3.4, Fig. 3.5 together with SM distribution (for reference) for the distributions that differ the most. For aQGC T1 quadratic term is shown as a representative example, because all T operators turn out to have similar shapes and this is utilized later in Sec. 3.10 to replace missing operators.

As was seen in Table 3.2 quadratic terms dominate the cross-section, and from Fig. 3.2 example m_{VV} (proxy for Q^2 of the process) is peaking at around 2.5 TeV so quadratic effects are taking place at much larger Q^2 compared to the Standard Model. Then m_{4l} of $ZZ \rightarrow 4l$ analysis which is m_{VV} seen by detector also behaving in the similar way (Fig. 3.3). If m_{4l} , built from transverse momentums of four leptons, is different, one would expect to see some of the individual lepton distribution tails enhanced compared to the SM, and this is shown on Fig. 3.4. Tagging jets also may receive an enhancement, although not as dramatic, as shown on Fig. 3.5.

3.7 Unitarity bound

Within the Standard Model, VBS diagrams considered alone would diverge at high Q^2 and violate unitarity. The same applies to tri-linear gauge coupling diagrams and Higgs boson processes. However, considering all those three types together, unitarity is restored. aQGC considered in this chapter may violate unitarity, too, as EFT is not a complete model. When Wilson coefficients are small, unitarity can be violated at very high energies, but we know Higgs restores it there. In the case with more significant coefficients, unitarity may be violated even at lower energies, where we might hope to see signs of NP. Luckily, there is a benchmark provided by unitarity bounds

Table 3.3: Production cross-sections (in femtobarns) for SM-interference EFT terms.

| | ZZ | Z _y | WZ | W _y |
|-----|-------|----------------|-------|----------------|
| T0 | 3.97 | 2.25 | -1.43 | -0.28 |
| T1 | 0.96 | 0.52 | -5.59 | -1.52 |
| T2 | 1.41 | 0.78 | -3.04 | -0.79 |
| T5 | 1.13 | -2.16 | 0.57 | -0.30 |
| T6 | 0.23 | -0.32 | 1.11 | -0.97 |
| T7 | 0.37 | -0.67 | 0.68 | -0.55 |
| T8 | 0.01 | 0.08 | - | - |
| T9 | 0.01 | 0.05 | - | - |
| S02 | -0.03 | - | -0.10 | - |
| S1 | -0.00 | - | -0.03 | - |
| M0 | -0.21 | -0.04 | 0.16 | 0.02 |
| M1 | 0.09 | 0.01 | -0.06 | -0.02 |
| M2 | -0.03 | 0.07 | -0.02 | 0.01 |
| M3 | 0.01 | -0.02 | 0.02 | -0.06 |
| M4 | -0.01 | -0.01 | -0.02 | -0.04 |
| M5 | -0.02 | 0.03 | -0.01 | 0.01 |
| M7 | -0.04 | -0.01 | -0.01 | 0.01 |

depending on energy, derived in [62] that allows us to judge whether the derived Wilson coefficients are meaningful. Bounds for the case of 1 operator at the time are given in Table 3.4.

3.8 Clipping

Limits obtained in combination will be compared with unitarity bounds above, per energy. To check if results make sense, clipping technique [68] is used as it is simple and reproducible: clipping is a cut-off scale beyond which the Wilson coefficient is set to 0. In practice, fitted variable distribution is build for $m_{VV} \leq C$, where m_{VV} is taken from the truth information, particle before showering. An example of such distribution, obtained from $Z(\rightarrow \bar{\nu}\nu)\gamma$ events with corresponding analysis selections, is shown on Fig. 3.6 for $m_{Z\gamma}$ (Hard-Scatter level particles) and corresponding change of p_T^γ shape is shown on Fig. 3.7 for $C = 3000, 2000, 1500, 1000$ GeV together with reference distribution without clipping (aka clipping infinity point). Apart from shape change, cross-section is decreasing according to fraction of $m_{Z\gamma}$ selected. Taking $m_{Z\gamma} \leq C$ shifts p_T^γ shape toward lower values and cross-section decreases by a fraction contained in $m_{Z\gamma} > C$.

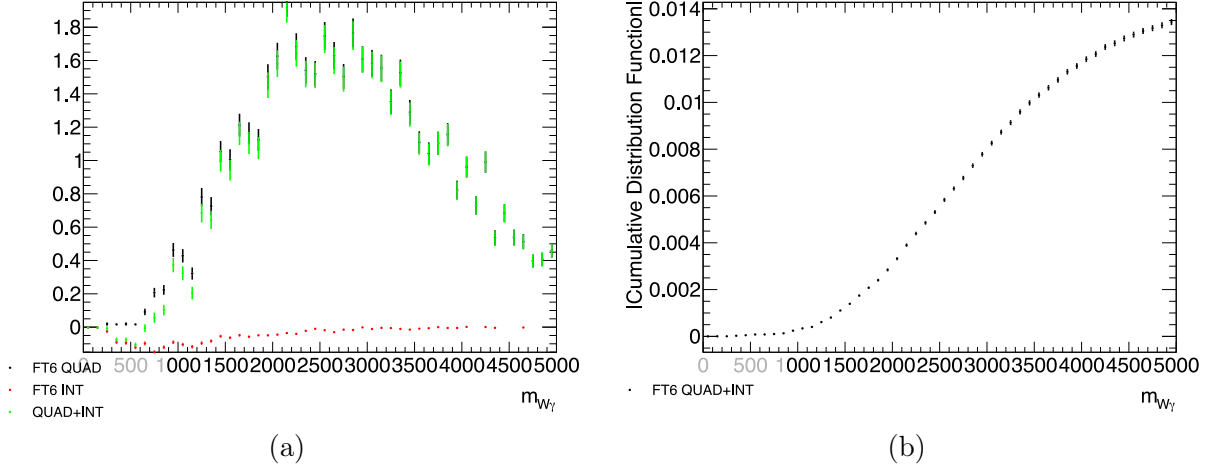


Figure 3.2: $W\gamma$ FT6 (a) m_{VV} interference, quadratic terms and their sum (b) Cumulative Distribution of absolute of interference+quadratic terms.

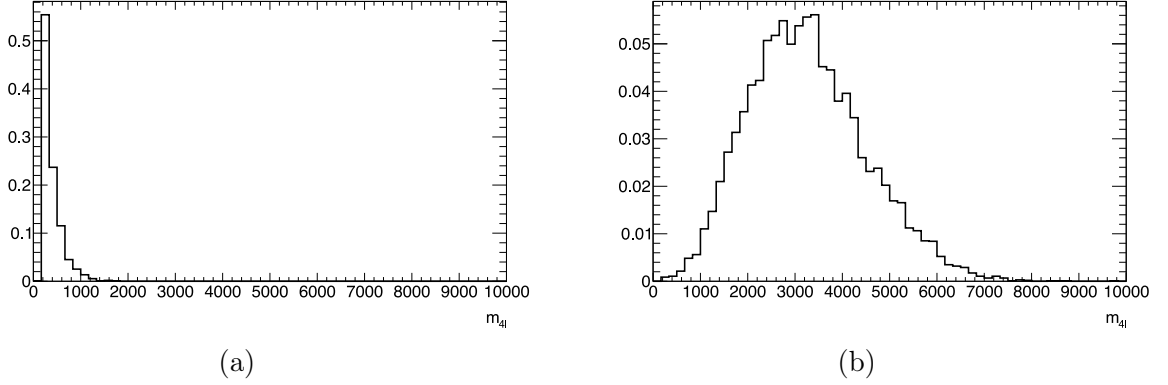


Figure 3.3: Particle-level $ZZ \rightarrow 4\ell$ events generated with **MadGraph** and with $ZZ \rightarrow 4\ell$ analysis selections applied: comparison of mass of four-lepton system (GeV) obtained in (a) SM (b) aQGC T1 quadratic term.

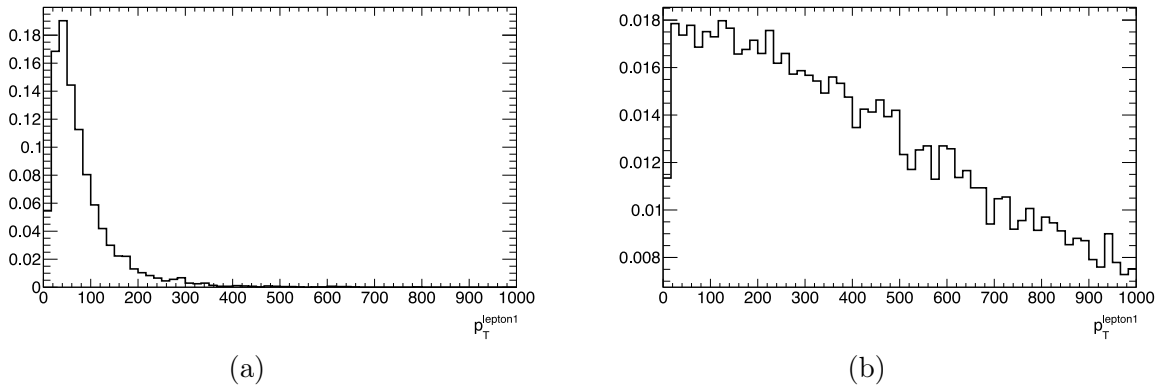


Figure 3.4: Particle-level $ZZ \rightarrow 4\ell$ events generated with **MadGraph** and with $ZZ \rightarrow 4\ell$ analysis selections applied: comparison of leading lepton p_T (GeV) obtained in (a) SM (b) aQGC T1 quadratic term.

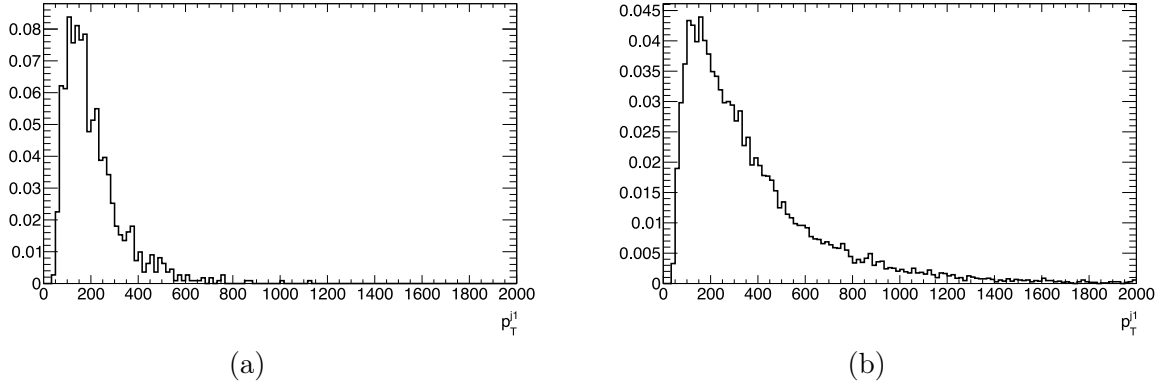


Figure 3.5: Particle-level $ZZ \rightarrow 4\ell$ events generated with `MadGraph` and with $ZZ \rightarrow 4\ell$ analysis selections applied: comparison of leading jet p_T (GeV) obtained in (a) SM (b) aQGC T1 quadratic term.

Table 3.4: 1D unitarity bounds for aQGC operators [62].

| Wilson coefficient | Bound |
|--|-------------------------------|
| $\left \frac{f_{T0}}{\Lambda^4} \right $ | $\frac{12/5\pi}{s^2}$ |
| $\left \frac{f_{T1}}{\Lambda^4} \right $ | $\frac{4/5\pi}{s^2}$ |
| $\left \frac{f_{T2}}{\Lambda^4} \right $ | $\frac{96/13\pi}{s^2}$ |
| $\left \frac{f_{T5}}{\Lambda^4} \right $ | $\frac{8/\sqrt{3}\pi}{s^2}$ |
| $\left \frac{f_{T6}}{\Lambda^4} \right $ | $\frac{48/7\pi}{s^2}$ |
| $\left \frac{f_{T7}}{\Lambda^4} \right $ | $\frac{32/\sqrt{3}\pi}{s^2}$ |
| $\left \frac{f_{T8}}{\Lambda^4} \right $ | $\frac{2/3\pi}{s^2}$ |
| $\left \frac{f_{T9}}{\Lambda^4} \right $ | $\frac{24/7\pi}{s^2}$ |
| $\left \frac{f_{M0}}{\Lambda^4} \right $ | $\frac{32/\sqrt{6}\pi}{s^2}$ |
| $\left \frac{f_{M1}}{\Lambda^4} \right $ | $\frac{127/\sqrt{6}\pi}{s^2}$ |
| $\left \frac{f_{M2}}{\Lambda^4} \right $ | $\frac{16/\sqrt{2}\pi}{s^2}$ |
| $\left \frac{f_{M3}}{\Lambda^4} \right $ | $\frac{64/\sqrt{2}\pi}{s^2}$ |
| $\left \frac{f_{M4}}{\Lambda^4} \right $ | $\frac{32\pi}{s^2}$ |
| $\left \frac{f_{M5}}{\Lambda^4} \right $ | $\frac{64\pi}{s^2}$ |
| $\left \frac{f_{M7}}{\Lambda^4} \right $ | $\frac{256/\sqrt{6}\pi}{s^2}$ |
| $\left \frac{f_{M7}}{\Lambda^4} \right $ | $\frac{256/\sqrt{6}\pi}{s^2}$ |
| $\left \frac{f_{S02}}{\Lambda^4} \right $ | $\frac{32\pi}{s^2}$ |
| $\left \frac{f_{S1}}{\Lambda^4} \right $ | $\frac{96/7\pi}{s^2}$ |

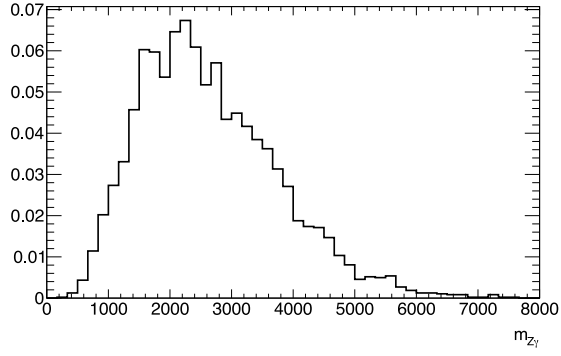
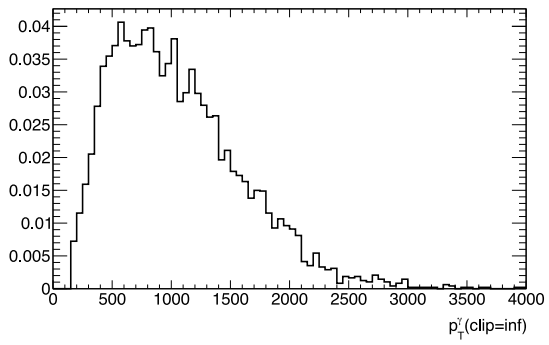
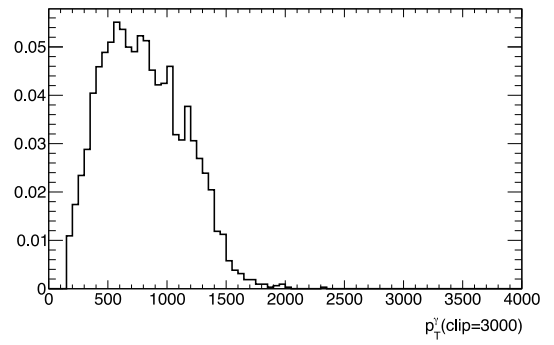


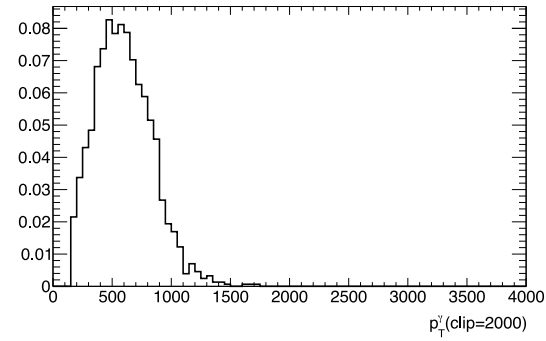
Figure 3.6: $Z(\rightarrow \bar{\nu}\nu)\gamma$ M3 quadratic term $m_{Z\gamma}$.



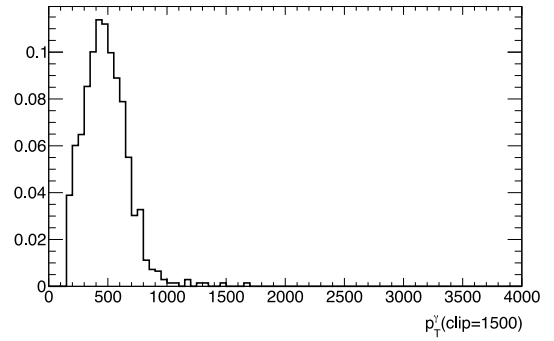
(a)



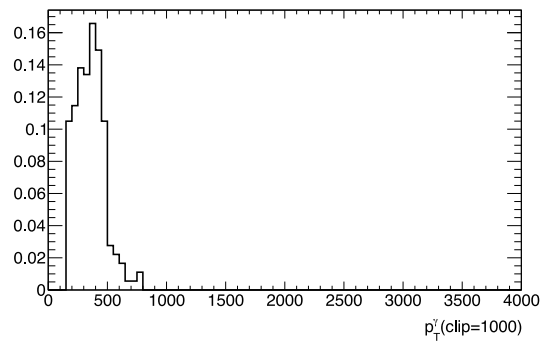
(b)



(c)



(d)



(e)

Figure 3.7: Change of p_T^γ shape with clipping, $Z(\rightarrow \bar{\nu}\nu)\gamma$ M3 QUAD.

3.9 Cross-term size

Most analyses didn't generate cross-terms (Eq. 3.6), but as we want to make 2D limits, the impact of their absence should be evaluated.

A custom metric was chosen to quantify the importance of cross-terms. Typically $\sigma_{INT} \ll \sigma_{QUAD}$ therefore one can compare σ_{CROSS} to $(\sigma_{QUAD1}, \sigma_{QUAD2})$: dealing with part of expression above where c_1, c_2 are unknown

$$c_1^2 |A_1|^2 + c_2^2 |A_2|^2 + c_1 c_2 \cdot 2 \operatorname{Re} \left(A_1 A_2^\dagger \right) \quad (3.7)$$

We want to build a metric that somewhat resembles the 2D limit curves we will obtain, and we know from some individual analyses who made 2D limits that curve very likely will be an ellipse. For this, we will choose the area excluded in the 2D plane, assuming we observed no events in Run-2. One can obtain the ellipse only considering the quadratic terms with area $S_{no-cross}$ and ellipse with cross-term taken into account with area S_{cross} . The metric chosen to quantify how important cross-term can be is ratio of two areas $S_{cross}/S_{no-cross}$ obtained from

$$\begin{aligned} S_{no-cross} &: 140 \cdot (c_1^2 \sigma_{Q1}^{gen} \epsilon_{Q1}^{evt.sel} + c_2^2 \sigma_{Q2}^{gen} \epsilon_{Q2}^{evt.sel}) \leq 3 \\ S_{cross} &: 140 \cdot (c_1^2 \sigma_{Q1}^{gen} \epsilon_{Q1}^{evt.sel} + c_2^2 \sigma_{Q2}^{gen} \epsilon_{Q2}^{evt.sel} + c_1 c_2 \sigma_{CROSS12}^{gen} \epsilon_{CROSS12}^{evt.sel}) \leq 3 \end{aligned} \quad (3.8)$$

where $\sigma_{Q1}^{gen}, \sigma_{Q2}^{gen}$ are cross-sections of quadratic terms for the pair of operators in question and $\sigma_{CROSS12}^{gen}$ is cross-section of pair cross-term. Each term is generated separately with **MadGraph** to obtain corresponding σ . $\epsilon_{Q1}^{evt.sel}, \epsilon_{Q2}^{evt.sel}, \epsilon_{CROSS12}^{evt.sel}$ are the selection efficiencies obtained from replicating analysis fiducial selections on the corresponding sample with Rivet. Number 140 (fb) is there to convert cross-section to counts. Number 3 is on the right-hand side as 3 is upper 95% CL on Poisson μ if nothing was observed and zero counts for BSM during Run-2 is a good approximation.

Fig. 3.8 shows possible relationships between ellipses with or without cross-terms. Each plot is taken from a different pair of operators with a corresponding set of $\sigma_{Q1}^{gen}, \sigma_{Q2}^{gen}, \sigma_{CROSS12}^{gen}$. Two things may happen: cross-term does modify the ellipse or not. If cross-term is relevant, the magnitude of area enlargement may be different. Depending on the sign of the cross-term (positive or negative cross-section), an ellipse is inclined in one way or another.

The importance of cross-terms is given by the ratio of areas of two ellipses $S_{cross}/S_{no-cross}$ - it is 1 when cross-term is negligible and above 1 when not. The higher the value, the more important it is. The ratio is taken between all pairs of operators available per analysis.

The resulting matrix for $Z(\rightarrow \bar{\nu}\nu)\gamma$ analysis is shown in Fig. 3.9. It can be seen that between families (T/M) ratio is always close to 1, and therefore, cross-term can be neglected. Within the same family (T/T, M/M), the ratio is often above one - it often happens within the pairs taken from sub-families (groups of operators that "look similarly") $(\mathcal{O}_{S0}, \mathcal{O}_{S1}, \mathcal{O}_{S2}), (\mathcal{O}_{M0}, \mathcal{O}_{M1}), (\mathcal{O}_{M2}, \mathcal{O}_{M3}), (\mathcal{O}_{M4}, \mathcal{O}_{M5}), (\mathcal{O}_{T0}, \mathcal{O}_{T1}, \mathcal{O}_{T2}), (\mathcal{O}_{T5}, \mathcal{O}_{T6}, \mathcal{O}_{T7}), (\mathcal{O}_{T8}, \mathcal{O}_{T9})$.

Similar matrices were produced for $W^\pm Z$ and $W\gamma$ analyses, shown on Fig. 3.10, Fig. 3.11, respectively, with the same conclusion as for $Z(\rightarrow \bar{\nu}\nu)\gamma$. Comparison between three analyses also shows that for the same pair of the operator when $S_{cross}/S_{no-cross} \neq 1$, the value can be different. Also, there are cases when for given pair $S_{cross}/S_{no-cross}$ is 1 for one analysis and above 1 for the other analysis - for example $(\mathcal{O}_{M1}, \mathcal{O}_{M5})$ in $Z(\rightarrow \bar{\nu}\nu)\gamma$ (Fig. 3.9) and $W^\pm Z$ (Fig. 3.10).

Given the above, cross-terms can be ignored between different families. This seems reasonable, given the varying structures within the families. Within a family (T/T), (M/M), (S/S), cross-terms can be significant, particularly within sub-families, and are expected to influence the limits. However, the extent of this impact depends on the specific case analysis. Therefore, they have to be studied individually for each analysis.

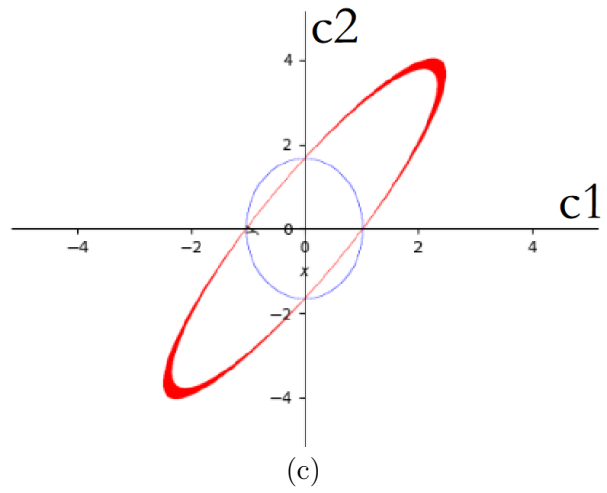
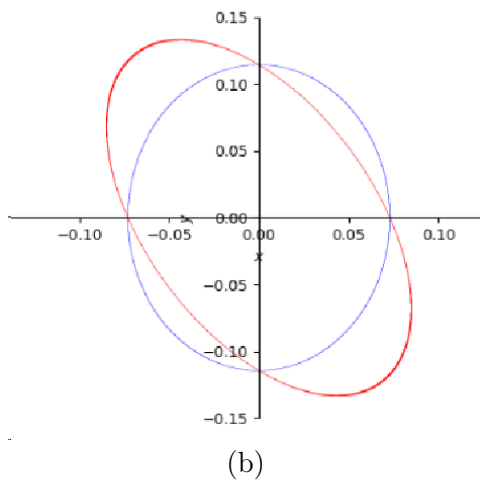
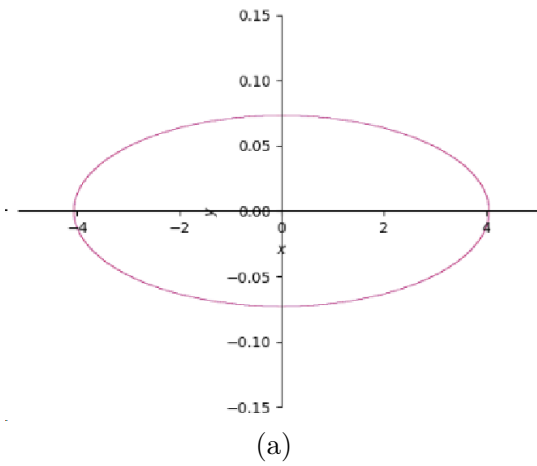


Figure 3.8: Possible cases for c_1, c_2 values based on templates cross-section when including (in red) or neglecting (in blue) cross-terms.

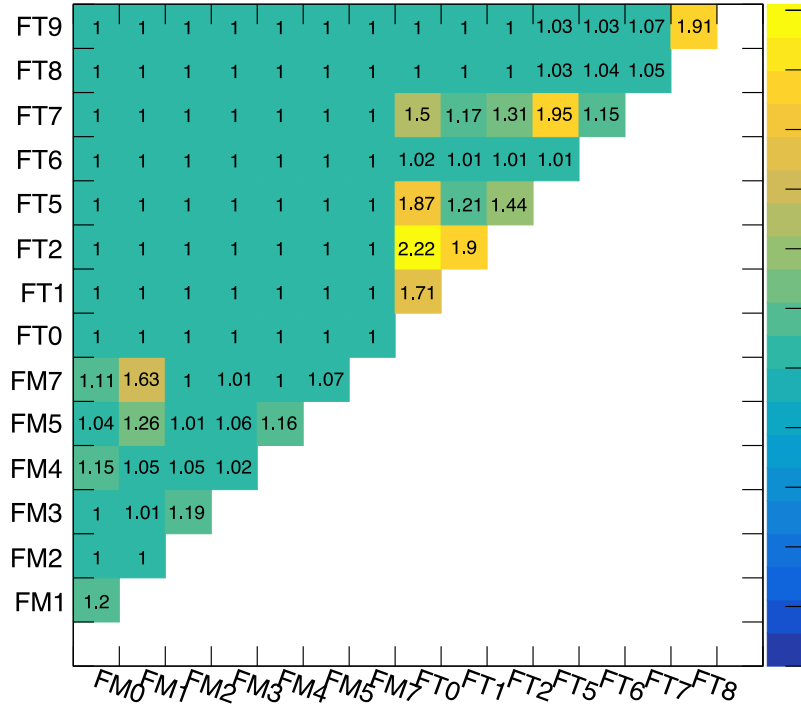


Figure 3.9: $Z(\rightarrow \bar{\nu}\nu)\gamma$ analysis $S_{cross}/S_{no-cross}$ matrix.

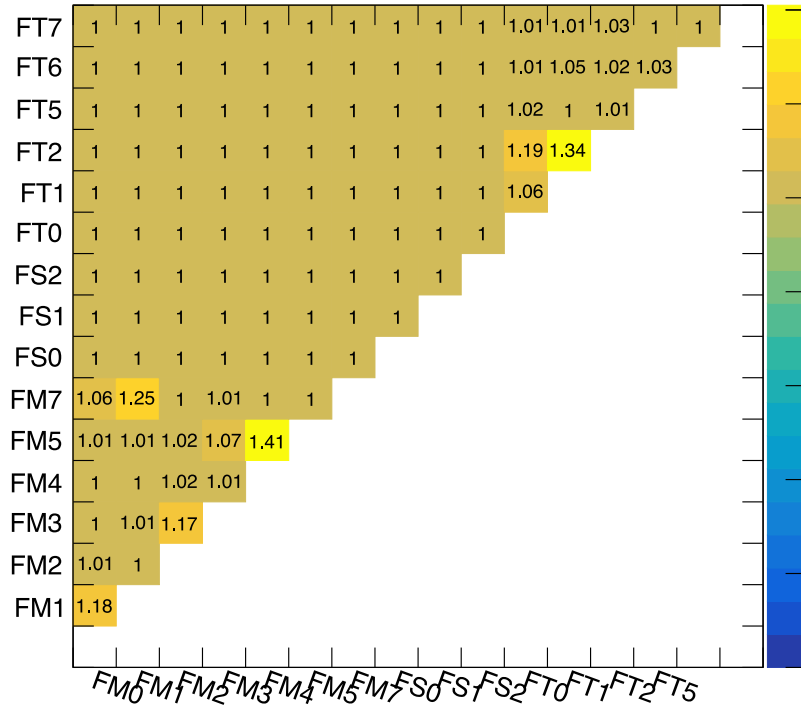


Figure 3.10: $W^\pm Z$ analysis $S_{cross}/S_{no-cross}$ matrix.

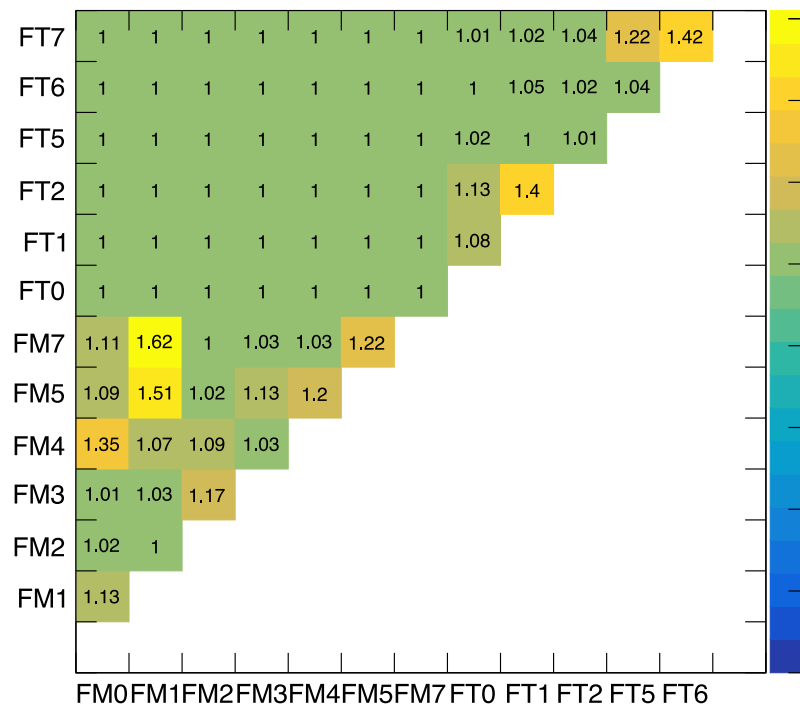


Figure 3.11: $W\gamma$ analysis $S_{cross}/S_{no-cross}$ matrix.

3.10 Operator replacement

For combination, it's beneficial that all analyses have all operators, including cross-terms, even if individual analysis does not provide a competitive limit for specific operators. All analyses are missing one piece or another, sometimes because of technical limitations at the time and sometimes because no combination was foreseen. The following subsections describe what is missing for each analysis.

Combination includes both reco-level and unfolded fits. Since getting all the missing samples with the full ATLAS simulation would be very time-consuming, an alternative method has been developed to achieve adequate results using only generator-level samples. This method, which modifies existing workspace has the additional benefit of being applicable even when the original analysis team does not exist any longer to make modifications to their workspaces. Its main goal is to insert missing operators and cross-terms by re-using existing workspace contents.

In each analysis, limits are obtained by fitting distributions where aQGC have some shape different from backgrounds and Standard Model VBS, e.g. p_T^γ in $Z(\rightarrow \bar{\nu}\nu)\gamma$. Generator-level comparisons show that many operators have similar shapes (normalized to unity, quantified by χ^2) in each signal region, and that also the change with clipping is similar. Therefore, one can use existing shapes in the workspaces, but they need to be re-scaled appropriately to match the cross-section of the original operator.

First, TRUTH EFT samples are generated with MadGraph. The typical size of the sample is 100000 events. They are passed through RIVET, where analysis selections are replicated, and distributions are built.

To insert the missing operator, one needs to add quadratic and interference terms of the missing operator to the workspace. Replacements are derived based on quadratic term shape agreement using clipping points ∞ , 3000, 2000 because they are the ones where statistics are high. Replacement chosen is an operator whose $\chi_\infty^2 + \chi_{3000}^2 + \chi_{2000}^2$ is the lowest. The decision is based only on quadratic terms, without looking at interference terms because they are often negligible (see Sec. 3.5). Instead, a decision based on quadratic terms is applied to interference terms. The same applies to other clippings points - the decision is based on three of them, then the same operator is applied on rest of clipping points (1500, 1000). In that way, one operator is substituted with another at all clipping points. With the shape match found, it needs to be re-scaled. For this, the ratio of normalization at the generator level is applied in the workspace.

The addition of the missing cross-terms is similar and based on existing quadratic terms.

Thus, this proxy solution, despite being based on TRUTH samples, also allows the modification of reco-level workspaces. The idea is that when replicating the analysis cuts at the generator level if you get the same shape, it's very likely that the shape will also be the same at the reco level. The reason is that the experimental acceptance $\varepsilon_{evt.sel.}$ is probably very similar if the shapes (and therefore the important kinematics) are the same.

When replacements are found, they need to be added to the original workspace. How this is done depends on what kind of workspace it is - all of the combination analysis provided `Roofit` workspaces but built with different software; there are two types: `EFTFun`⁶ (e.g. $Z(\rightarrow \bar{\nu}\nu)\gamma$, $W^\pm Z$) and `HistFactory` [84] (e.g. $W^\pm W^\pm$, semileptonic VV). We'll return to `HistFactory` in Sec. 3.10.3. Both $Z(\rightarrow \bar{\nu}\nu)\gamma$ and $W^\pm Z$ analyses, replacements for which are shown below, are `EFTFun` workspaces, where each bin contains the sum of EFT terms, and a string represents each EFT term depending on order

Interference term $[C_O] * N_{bin}^{INT} * unc^{INT}$

⁶<https://gitlab.cern.ch/eft-tools/eft-fun>

Quadratic term $[C_O] * N_{bin}^{QUAD} * unc^{QUAD}$

cross-term $[C_{O1}] * [C_{O2}] * N_{bin}^{CROSS} * unc^{CROSS}$

Where C_O is a coefficient being fitted and N_{bin}^{order} for reco-level analysis, N is a number of observed counts in a particular bin over Run-2. To add another missing EFT term, N_b^{order} are replaced by the ones obtained from re-scaling appropriate shape matches and systematic uncertainties (unc^{order}) of the base operator are copied.

To validate the method, ‘‘closure test’’ is done as follows. For any operator A in the workspace, one can use instead the shape of another operator also present in the workspace, A' , with a re-scaling coefficient obtained in the truth study. Then one obtains CL_A , $CL_{A'}$, hoping they are similar. To quantify the similarity ratio of CL width (most CLs are parabolas centered at 0) is taken given by

$$\frac{CL95_{A'}^{max} - CL95_{A'}^{min}}{CL95_A^{max} - CL95_A^{min}} \quad (3.9)$$

More details about each specific analysis are given below.

3.10.1 $Z(\rightarrow \bar{\nu}\nu)\gamma$ analysis

Operators already present in the workspace (interference and quadratic terms) are \mathcal{O}_{T0} , \mathcal{O}_{T5} , \mathcal{O}_{T8} , \mathcal{O}_{T9} , \mathcal{O}_{M0} , \mathcal{O}_{M1} , \mathcal{O}_{M2} - from each family there are representatives (scalar operators are not accessible by the topology). Then we want to include \mathcal{O}_{M3} , \mathcal{O}_{M4} , \mathcal{O}_{M5} , \mathcal{O}_{M7} and \mathcal{O}_{T1} , \mathcal{O}_{T2} , \mathcal{O}_{T6} , \mathcal{O}_{T7} based on available operators. Also, the analysis is missing the cross-terms.

Before injecting anything into the workspace, it’s good to check that the truth samples generated with **MadGraph** and processed with **RIVET** routine can reproduce the shapes already in the workspace. For this comparison, histograms from truth histograms are normalized to

$$\sigma_{gen} \times \epsilon_{ev.sel} \times L_{Run-2} \quad (3.10)$$

and workspace shapes are untouched. Overall, good agreement is seen in shape.

The starting point of looking for replacements is a matrix of χ^2 between all pairs of operators. One of them is partially shown for quadratic terms, clipping ∞ on Table 3.5. The table is symmetric across the diagonal, and both sides are kept for easier reading by column and row shape matching quality. For example, looking at the FM0 column, it can be seen that the lower value is 0.28 given by FM2 - meaning that the best replacement at clipping ∞ for FM0 is FM2, on which cross-section difference should be taken into account. As both \mathcal{O}_{M0} and \mathcal{O}_{M2} are available, this replacement is used during reshuffling for validation. Looking at one of the missing operators, for example, FM3, it can be seen that the best replacement for it is FM7 with $\chi^2 = 6.48$; however, \mathcal{O}_{M7} is also not in the workspace, and some other base for replacement should be used. Among available operators, \mathcal{O}_{M1} turns out to have the best (lowest) χ^2 .

The matrix shown above is used for each clipping point, and the decision is made based on the sum across the three highest clipping points. Results for missing operators are shown in Table 3.6 and Table 3.7 shows a similar table obtained for the closure of the method. It turns out, as it should be, that if X is a good replacement for Y, then the inverse is also true - e.g., FM0/FM2, showing the stability of the procedure for generated sample size of 100000 events. Reshuffling matched shapes will not be shown for brevity, but one example of shape comparison of replacement pair is shown in Fig. 3.12 - rest can be found in Appendix A.

Once a base for replacement is chosen, its cross-section is scaled with $RN^{clip} = \sigma_{missing}^{fid} / \sigma_{available}^{fid}$ where each σ^{fid} is obtained from the product of cross-section and analysis cuts selection efficiency. For missing operators, the table of RN^{clip} is shown in Table 3.8 for quadratic terms and in Table 3.9 for interference terms.

Table 3.5: $Z(\rightarrow \bar{\nu}\nu)\gamma$ χ^2 matrix, clipping ∞ , for part of QUAD operators.

| | FM0 | FM1 | FM2 | FM3 | FM4 | FM5 | FM7 | FT0 | FT1 | FT2 |
|-----|-------|-------|-------|-------|-------|-------|-------|-------|-------|-------|
| FM0 | | 74.1 | 0.3 | 107.9 | 1.3 | 77.7 | 109.9 | 856.7 | 771.5 | 786.5 |
| FM1 | 74.1 | | 73.9 | 8.6 | 82.1 | 2.4 | 6.7 | 435.0 | 379.2 | 385.8 |
| FM2 | 0.3 | 73.9 | | 107.0 | 1.5 | 76.2 | 107.6 | 846.2 | 761.9 | 776.9 |
| FM3 | 107.9 | 8.6 | 107.0 | | 119.1 | 7.7 | 6.3 | 313.0 | 267.5 | 273.8 |
| FM4 | 1.3 | 82.1 | 1.5 | 119.1 | | 85.0 | 117.5 | 871.8 | 787.7 | 802.1 |
| FM5 | 77.7 | 2.4 | 76.2 | 7.7 | 85.0 | | 3.1 | 390.8 | 339.7 | 346.6 |
| FM7 | 109.9 | 6.7 | 107.6 | 6.3 | 117.5 | 3.1 | | 345.5 | 296.4 | 302.7 |
| FT0 | 856.7 | 435.0 | 846.2 | 313.0 | 871.8 | 390.8 | 345.5 | | 4.1 | 2.0 |
| FT1 | 771.5 | 379.2 | 761.9 | 267.5 | 787.7 | 339.7 | 296.4 | 4.1 | | 1.0 |
| FT2 | 786.5 | 385.8 | 776.9 | 273.8 | 802.1 | 346.6 | 302.7 | 2.0 | 1.0 | |
| FT5 | 843.7 | 433.8 | 832.9 | 309.6 | 860.1 | 388.2 | 343.7 | 3.4 | 3.5 | 4.7 |
| FT6 | 259.3 | 56.8 | 256.1 | 27.7 | 272.4 | 48.6 | 30.7 | 199.9 | 159.6 | 164.5 |
| FT7 | 683.8 | 317.4 | 674.7 | 219.3 | 700.1 | 282.9 | 241.8 | 13.8 | 4.0 | 6.0 |
| FT8 | 630.4 | 297.3 | 621.7 | 208.8 | 644.4 | 264.1 | 226.2 | 10.2 | 4.3 | 5.6 |
| FT9 | 617.5 | 287.8 | 609.8 | 198.3 | 633.2 | 258.9 | 221.0 | 11.9 | 4.0 | 5.4 |

Table 3.6: χ^2 shape agreement results obtained for replacement of $Z(\rightarrow \bar{\nu}\nu)\gamma$ missing operators.

| missing | replacement | $\chi_\infty^2 + \chi_{3000}^2 + \chi_{2000}^2$ |
|---------|-------------|---|
| FM7 | FM1 | 24.5 |
| FM3 | FM1 | 17.2 |
| FM4 | FM2 | 22.4 |
| FM5 | FM1 | 22.9 |
| FT1 | FT5 | 8.6 |
| FT2 | FT0 | 4.6 |
| FT6 | FM1 | 90.0 |
| FT7 | FT9 | 6.1 |

Table 3.7: χ^2 shape agreement results obtained for replacement of in-workspace $Z(\rightarrow \bar{\nu}\nu)\gamma$ operators among themselves.

| available | reshuffling | $\chi_\infty^2 + \chi_{3000}^2 + \chi_{2000}^2$ |
|-----------|-------------|---|
| FM0 | FM2 | 2.7 |
| FM1 | FM0 | 131.4 |
| FM2 | FM0 | 2.7 |
| FT0 | FT5 | 7.3 |
| FT5 | FT0 | 7.3 |
| FT8 | FT9 | 6.6 |
| FT9 | FT8 | 6.6 |

Table 3.8: $Z(\rightarrow \bar{\nu}\nu)\gamma$ QUAD terms replacements renormalization applied on base sample to obtain cross-section matching the missing sample.

| missing | replacement | RN_∞ | RN_{3000} | RN_{2000} | RN_{1500} | RN_{1000} |
|---------|-------------|-------------|-------------|-------------|-------------|-------------|
| FM7 | FM1 | 0.38 | 0.39 | 0.40 | 0.41 | 0.46 |
| FM3 | FM1 | 6.67 | 6.4 | 6.34 | 5.97 | 5.87 |
| FM4 | FM2 | 0.31 | 0.32 | 0.33 | 0.34 | 0.41 |
| FM5 | FM1 | 9.59 | 9.7 | 9.92 | 10.2 | 10.88 |
| FT1 | FT5 | 0.66 | 0.65 | 0.64 | 0.6 | 0.59 |
| FT2 | FT0 | 0.14 | 0.15 | 0.15 | 0.16 | 0.16 |
| FT6 | FM1 | 819.5 | 687.13 | 590.09 | 527.18 | 538.61 |
| FT7 | FT9 | 0.14 | 0.14 | 0.14 | 0.15 | 0.14 |

Table 3.9: $Z(\rightarrow \bar{\nu}\nu)\gamma$ INT terms replacements renormalization applied on base sample to obtain cross-section matching the missing sample.

| missing | replacement | RN_∞ | RN_{3000} | RN_{2000} | RN_{1500} | RN_{1000} |
|---------|-------------|-------------|-------------|-------------|-------------|-------------|
| FM7 | FM1 | -0.41 | -0.41 | -0.40 | -0.40 | -0.43 |
| FM3 | FM1 | -2.00 | -1.99 | -1.97 | -1.99 | -2.08 |
| FM4 | FM2 | -0.12 | -0.13 | -0.13 | -0.13 | -0.12 |
| FM5 | FM1 | 3.55 | 3.3 | 3.31 | 2.87 | 2.12 |
| FT1 | FT5 | -0.14 | -0.14 | -0.15 | -0.15 | -0.16 |
| FT2 | FT0 | 0.31 | 0.31 | 0.31 | 0.31 | 0.29 |
| FT6 | FM1 | -46.0 | -45.13 | -41.83 | -34.23 | -23.82 |
| FT7 | FT9 | -32.99 | -31.51 | -30.54 | -29.77 | -29.84 |

Table 3.10: $Z(\rightarrow \bar{\nu}\nu)\gamma$ replacement closure with INT+QUAD.

| operator | c= ∞ | c=3000 | c=2000 | c=1500 | c=1000 |
|----------|-------------|--------|--------|--------|--------|
| T0r | 0.99 | 1.01 | 0.98 | 0.98 | 0.96 |
| T5r | 1.01 | 1.0 | 0.93 | 1.02 | 1.02 |
| T8r | 1.0 | 1.0 | 0.92 | 0.92 | 0.99 |
| T9r | 1.0 | 1.0 | 1.09 | 1.08 | 1.0 |
| M0r | 1.02 | 1.04 | 1.0 | 1.05 | 1.0 |
| M1r | 1.06 | 1.09 | 1.2 | 1.06 | 1.01 |
| M2r | 0.98 | 0.97 | 1.0 | 0.95 | 1.0 |

With the replacement for the missing operator and its renormalization found for each clipping, missing templates can be inserted into the workspace by first reading the base sample counts from the workspace, then scaling them by RN, and adding the resulting counts back to the workspace. No tool on the market can do that ⁷. Therefore, custom software was developed to edit the workspace, relying on `WSFactory` in `ROOT`.

One can then move to closure, the results of which are shown in Table 3.10 for observed Data. Overall, non-closure is below 10% and degrades when going to lower clipping values - this is expected because of larger statistical uncertainties in the signal templates.

Also Fig. 3.13 shows one example (\mathcal{O}_{M0} replacement validation) of NLL scan that gives the ratio in the table for clipping point 1500. According to Eq. 3.9 this case gives closure of $\frac{30.33 - (-29.89)}{28.91 - (-28.30)} = 1.05$ so non-closure is 5%. Other cases are shown in Appendix B.

Augmented workspaces were produced at all clipping points selected, containing in addition to the original operators, the ones previously missing, together with missing cross-terms.

3.10.2 $W^\pm Z$ analysis

Similarly to $Z(\rightarrow \bar{\nu}\nu)\gamma$, from M and T families, some operator shapes are available, and some are missing. Scalar $W^\pm Z$ operators are already in the workspace. Already present in the workspace (interference and quadratic terms) are \mathcal{O}_{M0} , \mathcal{O}_{M1} , \mathcal{O}_{M7} , \mathcal{O}_{T0} , \mathcal{O}_{T1} , \mathcal{O}_{T2} , \mathcal{O}_{S1} , \mathcal{O}_{S02} and we want to include, by relying on available ones, \mathcal{O}_{M2} , \mathcal{O}_{M3} , \mathcal{O}_{M4} , \mathcal{O}_{M5} from M family and \mathcal{O}_{T5} , \mathcal{O}_{T6} , \mathcal{O}_{T7} , \mathcal{O}_{T8} , \mathcal{O}_{T9} from tensor family. Also cross-terms are mostly absent.

Procedure for replacement was described for $Z(\rightarrow \bar{\nu}\nu)\gamma$ case, and here only $W^\pm Z$ specific details are highlighted.

The analysis uses a boosted decision tree that provides a score based on several kinematic variables. What is fitted to obtain the limit is detector-level one-dimension distribution of the two-dimensional combination of BDT score and M_T^{WZ} , example of which is shown on Fig. 3.14 At generator level with `MadGraph` and `RIVET` we can easily only check shapes similarity on M_T^{WZ} , but we expect other aQGC kinematics (entering the BDT) will be similar, too.

Replacements were derived based on M_T^{WZ} and re-normalizations are taken from appropriate pair of cross-sections. A closure test similar to what was done for $Z(\rightarrow \bar{\nu}\nu)\gamma$ was performed, and results are shown in Table 3.11. One finds that replacement based on M_T^{WZ} alone gives good closure for workspace using BDT. As the analysis team provided, for one of the clipping points, the workspace without BDT (where only M_T^{WZ} is used), validation was done twice: replacements were applied on workspace with and without the BDT and limit agreement was the same.

Missing operators and cross-terms were added, and now a complete workspace is available.

⁷Particularly `workspaceCombiner` doesn't allow independent manipulation of interference, quadratic, and cross-terms terms

Table 3.11: $W^\pm Z$ replacement closure with INT+QUAD.

| operator | c= ∞ | c=3000 | c=1500 | c=1000 |
|----------|-------------|--------|--------|--------|
| T0r | 1.12 | 0.99 | 0.89 | 0.78 |
| T1r | 1.03 | 1.03 | 1.0 | 0.98 |
| T2r | 0.97 | 0.97 | 1.0 | 1.02 |
| M0r | 0.92 | 0.94 | 1.0 | 1.25 |
| M1r | 1.1 | 0.99 | 1.0 | 1.03 |
| M7r | 0.91 | 1.02 | 1.0 | 0.95 |
| S02r | 1.02 | 1.01 | 1.03 | 1.01 |
| S1r | 1.1 | 1.06 | 1.0 | 0.8 |

3.10.3 Other analyses

- $W^\pm W^\pm$ analysis only lacks cross-terms and only at some clipping points. They can be added similarly to $Z(\rightarrow \bar{\nu}\nu)\gamma$, $W^\pm Z$ cases with two differences. One is that $W^\pm W^\pm$ workspace is not built with `EFTFun` but with `HistFactory` (HF). To modify HF workspace, it is exported to JSON, where each EFT term is one entry that contains an array of bin counts and separately minus sign for negative cross-section if needed, modified in this format, and then imported back to `HistFactory`. Another difference is that in the $W^\pm W^\pm$ analysis, EFT is not only in the Signal Region but also in the WZ Control Region. Therefore, there are more samples to track for replacements, and replacement should be done twice
- For VV semileptonic analysis, cross-terms were not generated, but interference+quadratic terms for all operators are available. The analysis is detector-level, so one can't just insert a truth sample into the workspace. The overall idea is the same as the one used in Sec. 3.10.1 and Sec. 3.10.2, but there are two difficulties. One is just the amount of samples to track, as this analysis is a combination in itself of ZZ, WW, and WZ topologies. Second is that the Recurrent Neural Network score is fitted, which cannot be obtained easily from simple kinematic distributions. However, the network is available, and one can feed information into it to get the RNN distributions. The χ^2 search can be applied to that distribution. VV semileptonic workspace was made with `HistFactory`, and technical implementation will rely on JSON similarly to $W^\pm W^\pm$ analysis case
- $W\gamma$ analysis (unfolded) originally was missing cross-terms. MC EFT samples were generated, based on which the analysis team produced an updated workspace, now containing cross-terms
- $ZZ \rightarrow 4\ell$ analysis (also unfolded) originally was missing cross-terms and only had quadratic and interference terms for T family operators. MC EFT samples were generated for cross-terms and M, S family operators, based on which the analysis team produced an updated workspace, now containing all operators and cross-terms

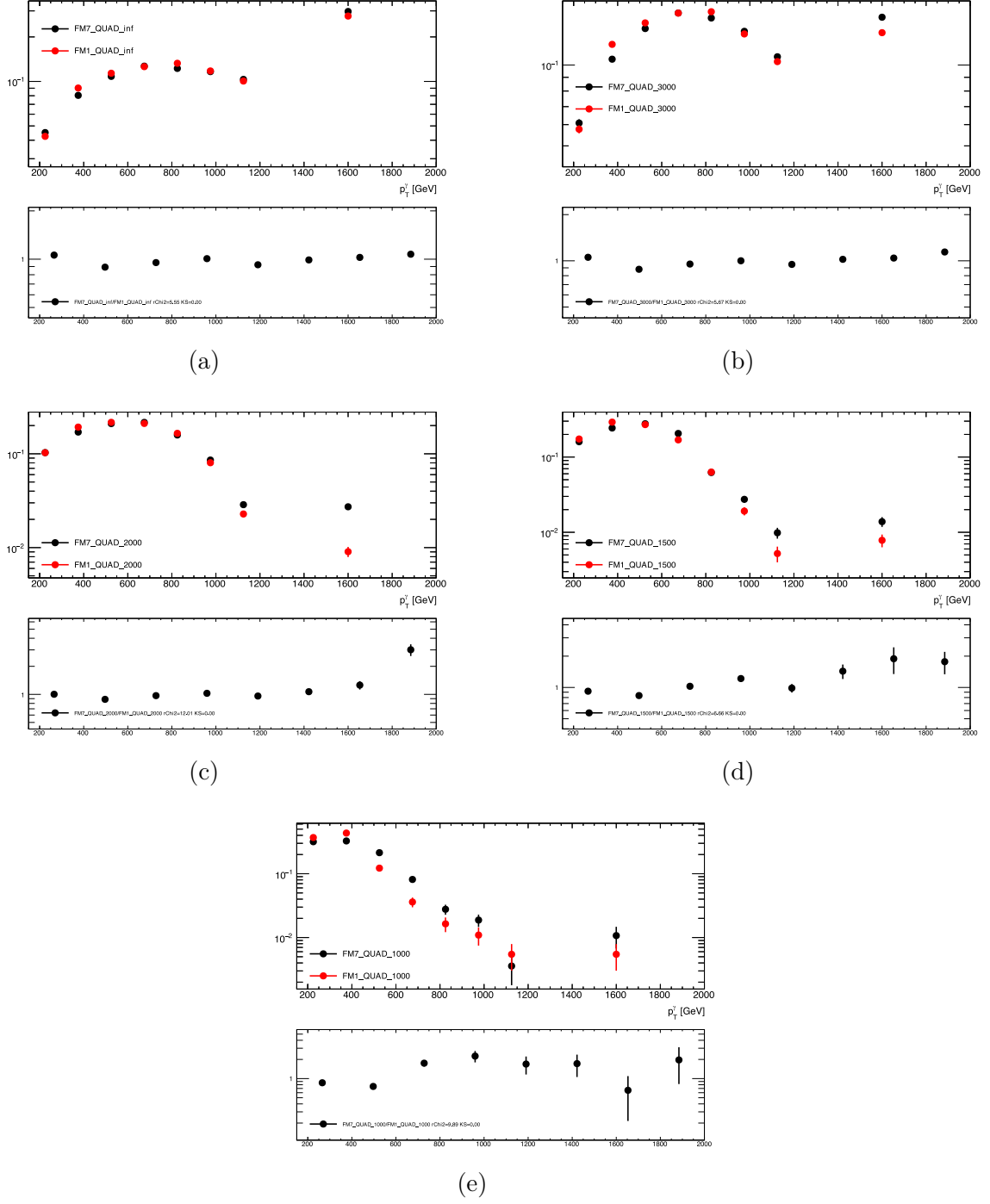


Figure 3.12: FM7vsFM1 shape comparison obtained in $Z(\rightarrow \bar{\nu}\nu)\gamma$ sample, replicating analysis selections. Bins match those used in the analysis. The bottom pad is the ratio between two operator shapes (a) without clipping (b) clipping=3000 (c) clipping=2000 (d) clipping=1500 (e) clipping=1000.

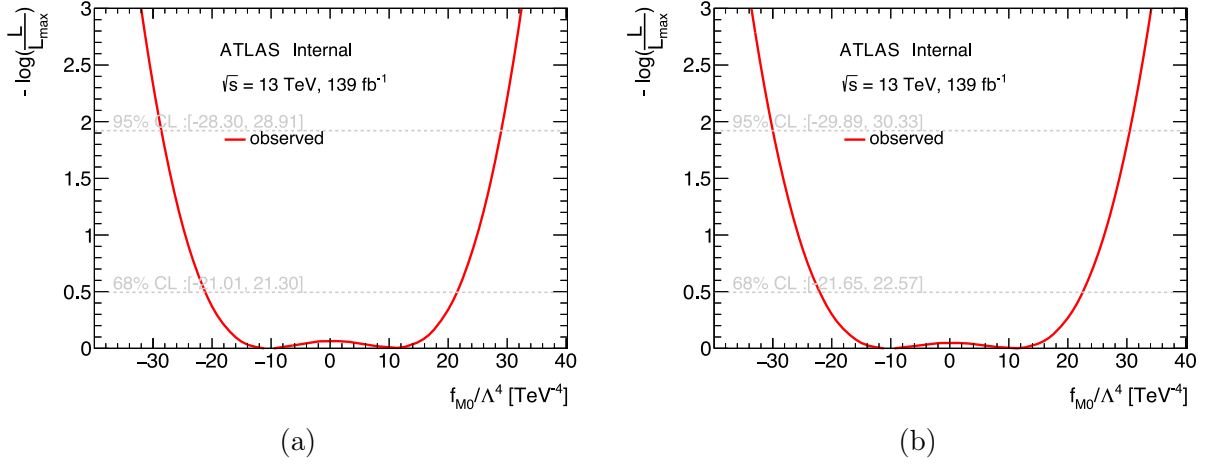


Figure 3.13: $Z(\rightarrow \bar{\nu}\nu)\gamma$ analysis replacement validation: comparison between M0 (a) original limit (b) replaced limit.

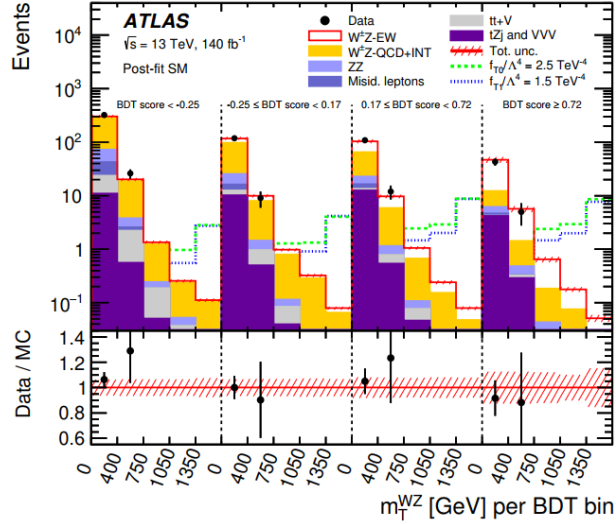


Figure 3.14: Detector-level one-dimension distribution of the two-dimensional combination of BDT score and M_T^{WZ} T observables used to obtain limits on EFT coefficients [56].

3.11 Preliminary results

The combination means that we want to do a simultaneous fit to all the workspaces to derive limits on Wilson coefficients for all the operators. We do so [89] by combining workspaces into one “combined“ using `workspaceCombiner`⁸ and working with several combined workspaces, one per clipping point. In combination, we want to correlate the systematic uncertainties as much as possible between the various analyses to have a consistent treatment - a summary of correlations (100% correlation) is shown in Table 3.12.

At the moment of writing, not all the building blocks are available to do the full combination

- Missing cross-terms in VV semileptonic, $W^\pm W^\pm$ analyses
- Missing clipping points 1000, 700 in VV semileptonic analysis
- We don’t want certain data events to be selected by multiple analyses to avoid the time-consuming task of evaluating and correcting for potentially arising statistical correlations. Unfortunately, it happens because individual analyses’ selections are not orthogonal to each other. Most overlapping events in our case, are expected to be between the Control Region in one analysis and Signal Region in another analysis, so no large impact on the final results is expected, but still requires careful treatment. Orthogonality studies are ongoing

Cross-terms are not involved for 1D limits; therefore, one can obtain them for the time being, ignoring the overlap. As shown in Table 3.13, without clipping, $Z(\rightarrow \bar{\nu}\nu)\gamma$ analysis leads the combination. For M, S typically, VV semileptonic analysis is leading.

3.11.1 1-D limits

Expanding the combination machinery to cover all the clippings points and considering for the time being only four analysis: $Z(\rightarrow \bar{\nu}\nu)\gamma$, $W^\pm Z$, $W\gamma$, $ZZ \rightarrow 4\ell$ one can already obtain limits that should be close to the final ones for T operators. Results are shown Fig. 3.15 for clipping points up to 1000. It can be seen that $Z(\rightarrow \bar{\nu}\nu)\gamma$ is leading the combination at higher clippings as expected, however, at lower clippings for some operators, it becomes comparable with other analyses - likely because here SM background is coming into play. As was shown in Fig. 3.7, without clipping, distribution is peaking at high values which are greatly separated from the Standard Model background. At lower clipping, this is not the case anymore, and one may have a Standard Model “pedestal“ underneath the aQGC signal - degrading the limit. Also, gain from the combination is visible when there are several comparable analyses, for example at clipping=1000 \mathcal{O}_{T2} individual $Z(\rightarrow \bar{\nu}\nu)\gamma$ and $W^\pm Z$ limits are the same and worse than the combined limit.

On Fig. 3.16, the combined limits are compared with unitarity bounds (see Sec. 3.7). At clipping 3000, unitarity is often violated (when limits are larger than the unitarity bound) as expected, but at clipping 2000, all the operators except T8 are better than the unitarity bound.

3.11.2 2-D limits

The main interest in 2D limits is the correlation between limits (as magnitude will follow 1D results). An example of several analyses for one pair is shown on Fig. 3.17 - there is a gain from the combination, but mostly, the combined limit follows the $Z(\rightarrow \bar{\nu}\nu)\gamma$ one. This is a typical situation for all T-T 2D limits obtained. A summary of limit correlations is shown on Fig. 3.18 - each cell is a correlation of two-dimensional limits obtained in combination. Cross-terms drive those correlations - just like ellipses considered in Sec. 3.9.

⁸https://gitlab.cern.ch/atlas_higgs_combination/software/workspaceCombiner/

Table 3.12: Correlations of systematic uncertainties in combination. Adapted from [90].

| | VV Semileptonic | $W^\pm W^\pm$ | $W^\pm Z$ | $W\gamma$ | $Z(-\rightarrow \bar{\nu}\nu)\gamma$ | $ZZ \rightarrow 4\ell$ | Correlated |
|--------------------------------|-----------------|---------------|-----------|-----------|--------------------------------------|------------------------|------------|
| Luminosity | x | x | x | x | x | x | x |
| Pile-up reweighting | x | x | x | x | x | x | x |
| EMPF low jets | x | x | x | x | | x | x |
| E_T^{miss} | x | x | x | x | x | | x |
| Electrons | x | x | x | x | x | x | x |
| Muons | x | x | x | x | x | x | x |
| Photons | | | | x | x | | x |
| b -tagging extrapolation | x | x | x | x | | | x |
| Other b -tagging systematics | x | x | x | x | | | |
| Background modelling | x | x | x | x | x | x | |
| Parton shower | x | x | x | | x | | x |
| QCD scale on VBS signal | x | x | x | x | x | x | |
| PDF/ α_s on VBS signal | x | x | x | x | x | x | x |
| QCD scale on aQGC signal | x | x | x | | | | x |
| PDF/ α_s on aQGC signal | x | x | x | | | | x |

Table 3.13: Individual and combined observed limits without clipping [91]

| Operator | VV Semileptonic | $W^\pm W^\pm$ | $W^\pm Z$ | $W\gamma$ | $Z(\rightarrow \bar{\nu}\nu)\gamma$ | $ZZ \rightarrow 4\ell$ | Combined |
|-------------------|-----------------|---------------|---------------|---------------|-------------------------------------|------------------------|-----------------|
| FS02/ Λ^4 | [-3.72, 3.73] | [-5.88, 5.93] | [-10.0, 10.0] | Absent | Absent | [-26.6, 26.8] | [-3.41, 3.40] |
| FS1/ Λ^4 | [-7.62, 7.63] | [-23.5, 23.6] | [-30.0, 29.6] | Absent | Absent | [-41.8, 42.0] | [-7.17, 7.14] |
| FM0/ Λ^4 | [-1.20, 1.19] | [-4.11, 4.13] | [-5.56, 5.55] | [-24.0, 23.8] | [-4.57, 4.65] | [-4.85, 4.88] | [-1.10, 1.07] |
| FM1/ Λ^4 | [-3.77, 3.77] | [-6.73, 6.98] | [-8.49, 8.41] | [-36.7, 37.8] | [-7.66, 7.65] | [-17.9, 17.8] | [-3.18, 3.18] |
| FM2/ Λ^4 | [-1.76, 1.76] | Absent | [-10.5, 10.6] | [-8.60, 8.57] | [-1.89, 1.89] | [-7.38, 7.41] | [-1.35, 1.35] |
| FM3/ Λ^4 | [-5.43, 5.44] | Absent | [-15.9, 16.0] | [-13.4, 13.7] | [-2.96, 2.97] | [-25.9, 25.9] | [-2.71, 2.72] |
| FM4/ Λ^4 | [-2.82, 2.83] | Absent | [-4.43, 4.44] | [-15.4, 15.5] | [-3.31, 3.33] | [-19.4, 19.4] | [-2.10, 2.11] |
| FM5/ Λ^4 | [-4.20, 4.21] | Absent | [-6.27, 6.29] | [-14.0, 12.3] | [-2.35, 2.35] | [-27.5, 27.6] | [-2.18, 2.19] |
| FM7/ Λ^4 | [-6.32, 6.15] | [-9.70, 9.47] | [-11.3, 11.4] | [-66.0, 65.2] | [-12.2, 12.3] | [-33.9, 34.2] | [-5.20, 5.22] |
| FT0/ Λ^4 | [-0.24, 0.21] | [-0.36, 0.36] | [-0.56, 0.55] | [-2.11, 2.22] | [-0.093, 0.084] | [-0.97, 0.92] | [-0.095, 0.083] |
| FT1/ Λ^4 | [-0.23, 0.23] | [-0.17, 0.19] | [-0.40, 0.35] | [-1.32, 1.44] | [-0.12, 0.11] | [-1.22, 1.21] | [-0.10, 0.10] |
| FT2/ Λ^4 | [-0.53, 0.53] | [-0.63, 0.74] | [-1.20, 1.00] | [-3.44, 3.90] | [-0.24, 0.22] | [-2.50, 2.41] | [-0.24, 0.22] |
| FT5/ Λ^4 | [-0.61, 0.55] | Absent | [-1.43, 1.45] | [-1.52, 1.55] | [-0.088, 0.099] | [-2.50, 2.41] | [-0.088, 0.097] |
| FT6/ Λ^4 | [-0.71, 0.68] | Absent | [-1.33, 1.41] | [-1.19, 1.23] | [-0.26, 0.26] | [-3.88, 3.84] | [-0.25, 0.25] |
| FT7/ Λ^4 | [-1.86, 1.61] | Absent | [-3.87, 3.87] | [-3.03, 3.16] | [-0.27, 0.31] | [-8.44, 8.12] | [-0.32, 0.35] |
| FT8/ Λ^4 | [-0.47, 0.47] | Absent | Absent | Absent | [-0.060, 0.060] | [-2.11, 2.11] | [-0.059, 0.059] |
| FT9/ Λ^4 | [-1.01, 1.01] | Absent | Absent | Absent | [-0.13, 0.13] | [-4.52, 4.52] | [-0.13, 0.13] |

Table 3.14: $ZZ \rightarrow \ell\bar{\ell}\nu\bar{\nu}$ expected limits without clipping and at clipping=1000 GeV.

| operator | no clip | clip=1000 |
|----------|---------------|-----------------|
| T0 | [-0.66, 0.63] | [-5.63, 5.57] |
| T1 | [-0.72, 0.71] | [-5.17, 5.12] |
| T2 | [-1.50, 1.46] | [-10.88, 10.84] |
| T5 | [-1.16, 1.11] | [-9.01, 8.96] |
| T6 | [-1.72, 1.71] | [-9.52, 9.54] |
| T7 | [-5.23, 4.88] | [-27.78, 27.34] |
| T8 | [-0.91, 0.91] | [-8.9, 8.92] |
| T9 | [-1.98, 1.98] | [-18.93, 18.90] |

3.12 Outlook

3.12.1 Inputs

There is a hope to add more analyses, for example, $ZZ \rightarrow \ell\bar{\ell}\nu\bar{\nu}$ and $Z(\rightarrow \bar{\ell}\ell)\gamma$.

$ZZ \rightarrow \ell\bar{\ell}\nu\bar{\nu}$ analysis is blinded at the moment of writing; however, with Asimov, EFT limits are finalized. Currently, only T limits are considered. Results are shown on Table 3.14 - it will not be a leading analysis, but valuable input to cover all the VBS processes.

$Z(\rightarrow \bar{\ell}\ell)\gamma$ analysis was published but lacks the EFT part - it will be added. Naively one may expect limits to be the ones of $Z(\rightarrow \bar{\nu}\nu)\gamma$ but worse by branching fraction.

3.12.2 1-D limits

Limits on T family Wilson coefficients were shown with four analyses combined in the clipping region where one is competitive with unitarity bound, there are several comparable analyses, despite the expectation that $Z(\rightarrow \bar{\nu}\nu)\gamma$ analysis would dominate because this is the case without clipping. It's interesting to see if VV semileptonic, $W^\pm W^\pm$ and potentially $ZZ \rightarrow \ell\bar{\ell}\nu\bar{\nu}$, $Z(\rightarrow \bar{\ell}\ell)\gamma$ would also contribute.

For scalar and mixed operator families, the expectation is that VV semileptonic would lead, but given experience with T, it may not be the case. The goal is to check that by combining all the analyses at all clipping points (at the moment, this is not possible because of missing VV semileptonic workspaces).

With that, one wants to obtain unitarized limits: at energy where unitarity bound and measured limits cross. Need to compare continuous (in m_{VV}) unitarized bound with limits obtained at discrete m_{VV} points (1000, 1500, 2000, 3000, inf were shown). Some well-motivated interpolation clippings points should be chosen.

Also, non-orthogonality removal will be done; potentially, some studies on systematics correlation are missing.

3.12.3 n-D limits

Once missing crosses are added to VV Semileptonic and $W^\pm W^\pm$ analyses, one can obtain a two-operator limit correlation. As was shown, at lower clippings, 1D limits become comparable between two analyses - then one can expect for this case and also when correlations are in opposite directions, like for Fig. 3.19 case, that resulting combined shape will be the one more complicated than just ellipse.

Going further to n-D limits, one can look at collective deviations of operator limits.

Limits obtained by simultaneous fit to two operators, some of which were shown on Fig. 3.17 and Fig. 3.19 are described by an ellipse. While fitting three operators at the time, the resulting shape

will likely be an ellipsoid. Continuing along the same lines, one might obtain an 18-dimensional ellipsoid (for all the operators) showing how all the Wilson coefficients are related to each other. The shape obtained and projected into the original Eboli coordinates should give something resembling one-dimensional limits. But projection also can be made into some other, non-rectangular coordinates and with this mapping, one might indirectly test concrete models of anomalous gauge couplings.

3.13 Conclusion

I've worked on both inputs to combination (without complete inputs, there is nothing to combine) and the combination itself.

The operator content of published analyses is non-homogeneous, which doesn't allow us to really probe the full Eboli model. At the moment of writing, I contributed in one way or another to four out of six ($W^\pm Z$, $W^\pm W^\pm$, $W\gamma$, $Z(\rightarrow \bar{\nu}\nu)\gamma$, $ZZ \rightarrow 4\ell$, VV semileptonic) analyses that are available for combination. The method was developed to add missing operators to an analysis. The method was implemented on $Z(\rightarrow \bar{\nu}\nu)\gamma$ and $W^\pm Z$ analyses, and non-closure of replacement was evaluated, typically giving CL agreement within 10%. The method will be applied on $W^\pm W^\pm$ and VV Semileptonic analyses but with different technical implementations. Two analyses, $ZZ \rightarrow 4\ell$ and $W\gamma$, now also have full operator content by relying on Monte Carlo samples I generated. Additionally, I participated in the derivation of $ZZ \rightarrow \ell\bar{\ell}\nu\bar{\nu}$ analysis expected limits, currently finished.

In combination itself, studies were done on reduced set (T family) of one-dimensional operator limits, already showing at times the power of combination at lower clipping values, despite the opposite expectation because of one clearly leading unclipped analysis. EFT cross-terms added to analyses are essential to multi-dimensional limits - two-dimensional limits were evaluated and correlation of limits was studied between T family operators individually and in combination.

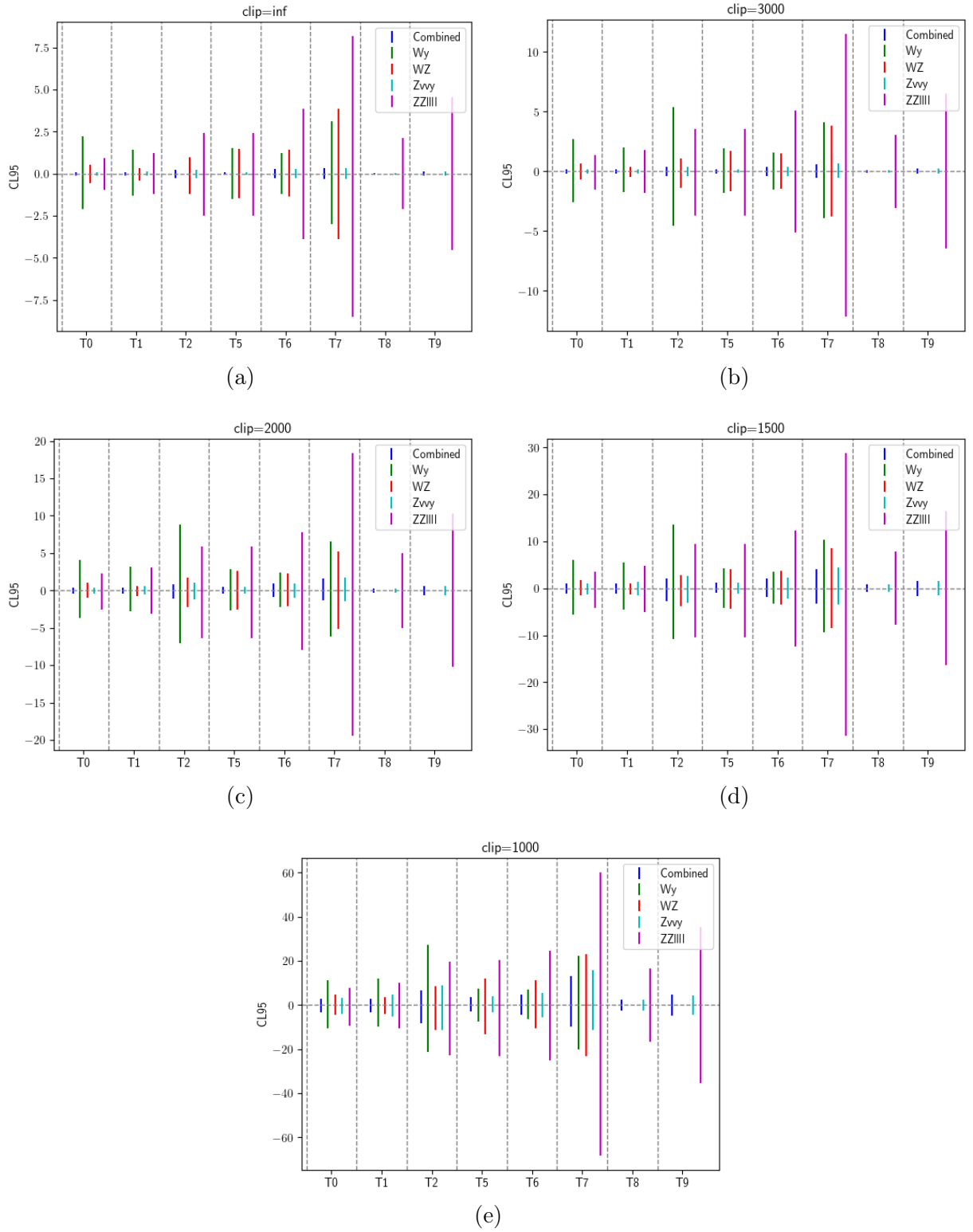


Figure 3.15: Individual $Z(\rightarrow \bar{\nu}\nu)\gamma$, $W^\pm Z$, $W\gamma$, $ZZ \rightarrow 4\ell$ and combined one-dimensional T family limits for (a) without clipping (b) clipping=3000 (c) clipping=2000 (d) clipping=1500 (e) clipping=1000.

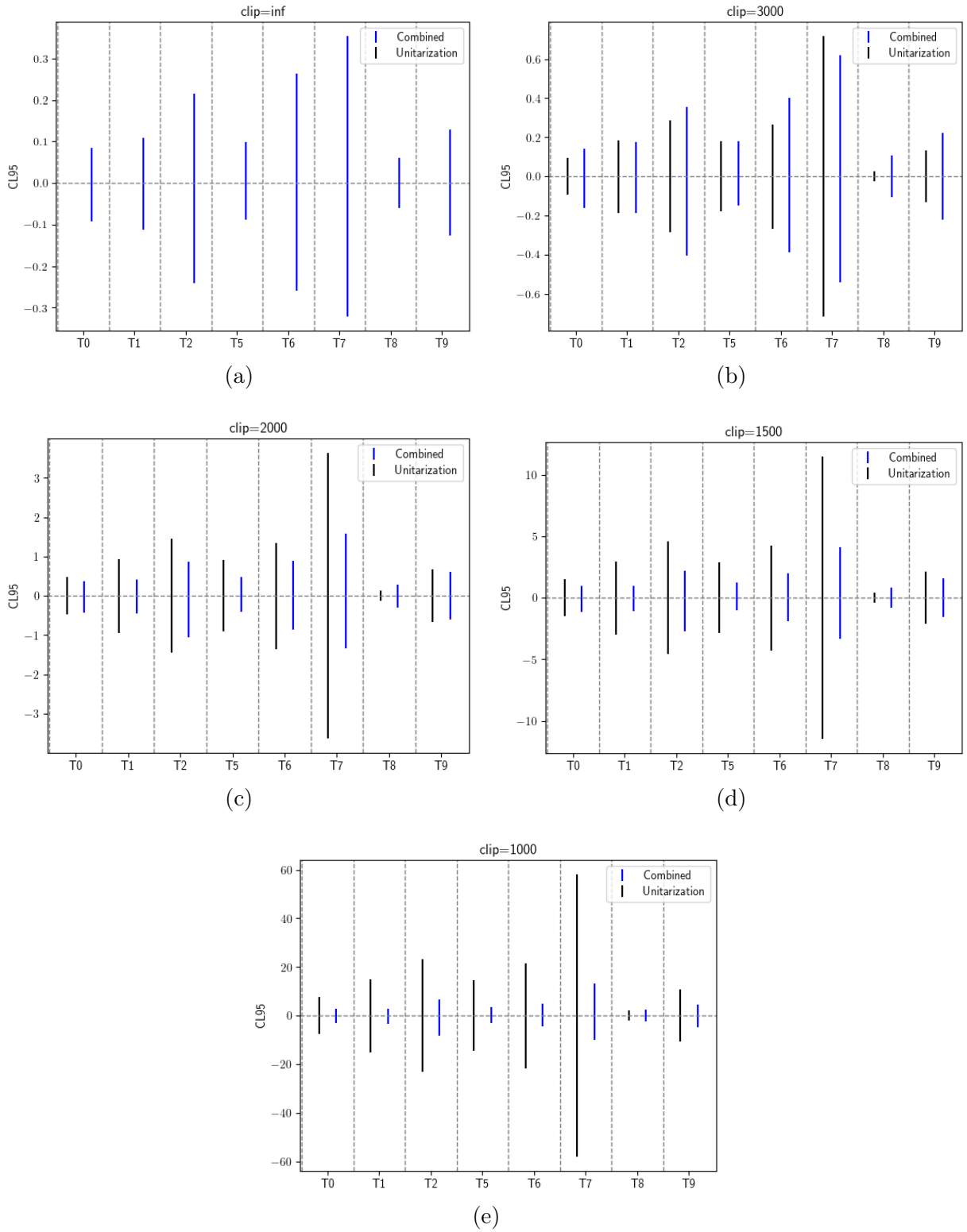
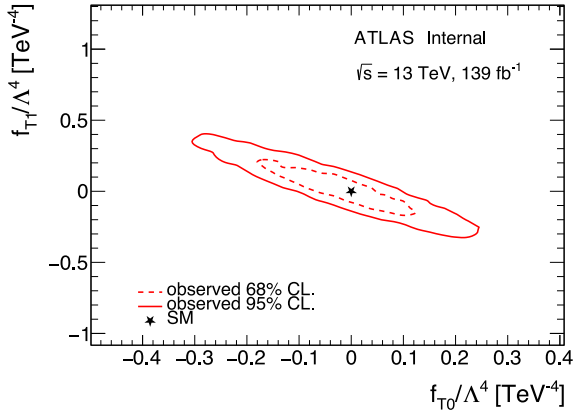
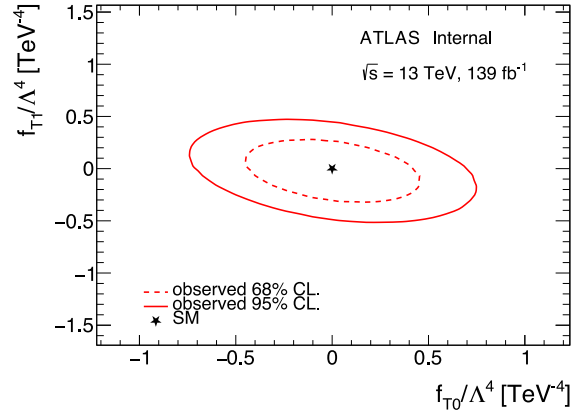


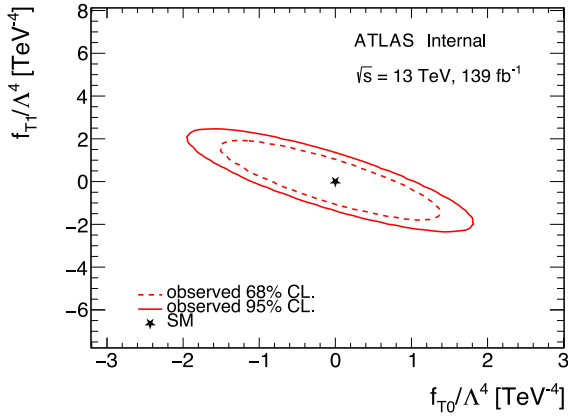
Figure 3.16: Combined $Z(\rightarrow \bar{\nu}\nu)\gamma$, $W^\pm Z$, $W\gamma$, $ZZ \rightarrow 4\ell$ one-dimensional T family limits and unitarity bounds (a) without clipping (b) clipping=3000 (c) clipping=2000 (d) clipping=1500 (e) clipping=1000.



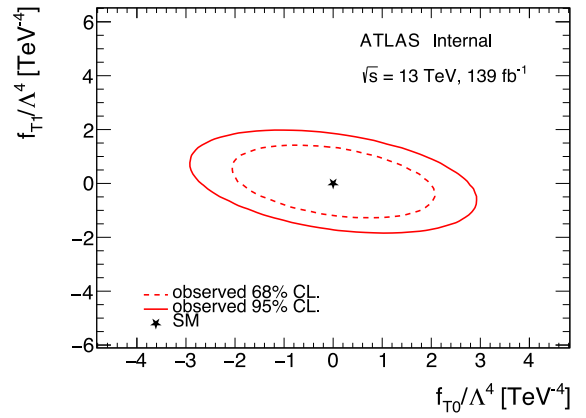
(a)



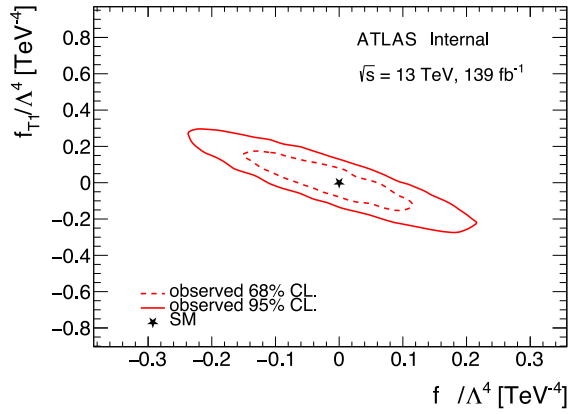
(b)



(c)



(d)



(e)

Figure 3.17: T0vsT1 two-dimensional limit for (a) $Z(\rightarrow \bar{\nu}\nu)\gamma$ (b) $W^\pm Z$ (c) $ZZ \rightarrow 4\ell$ (d) $W\gamma$ (e) combined.

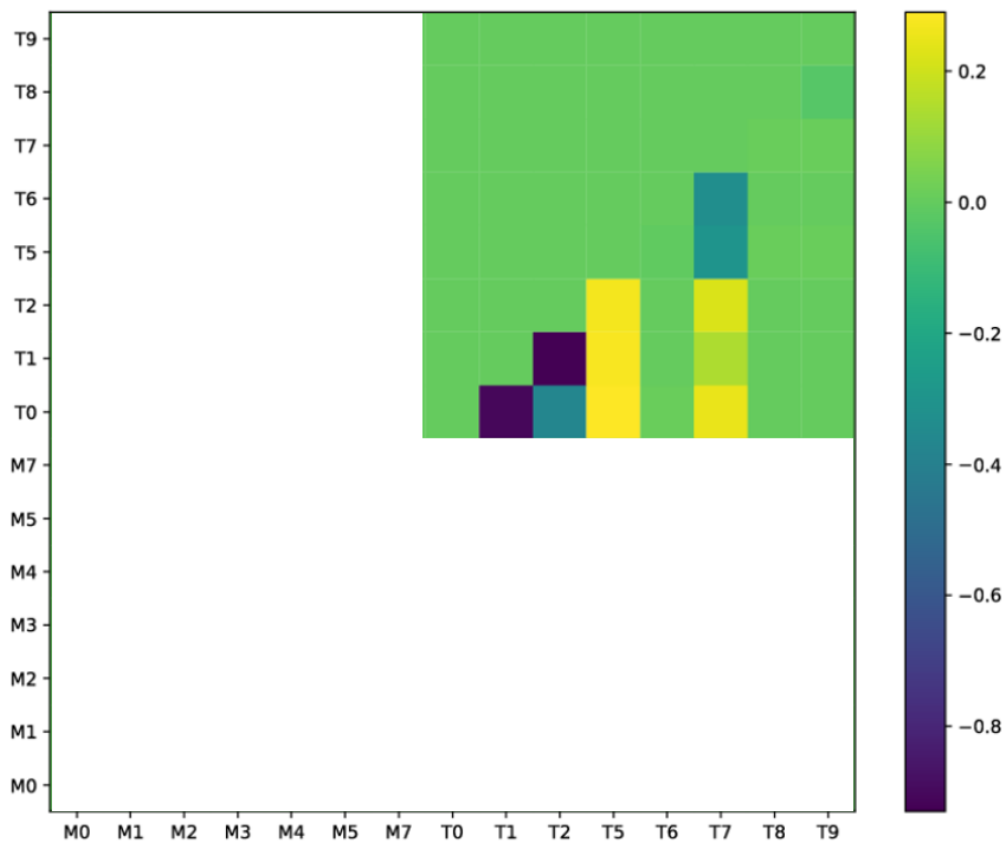
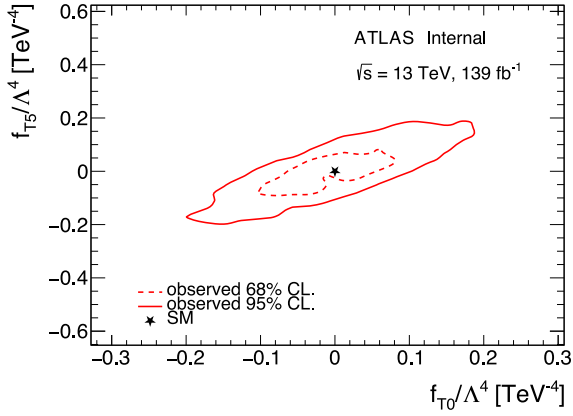
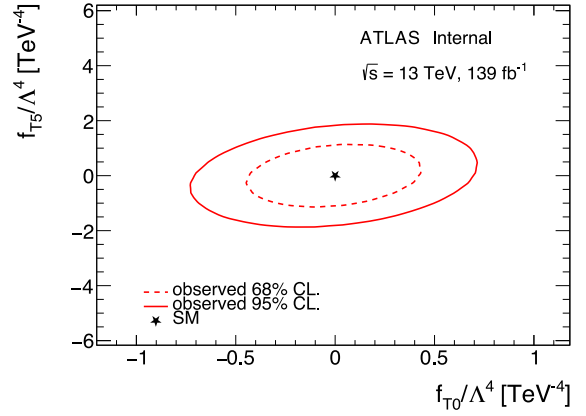


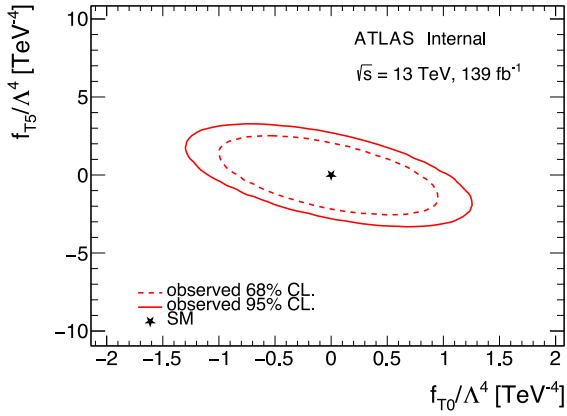
Figure 3.18: Summary of 2D T pairs limit correlations (combined).



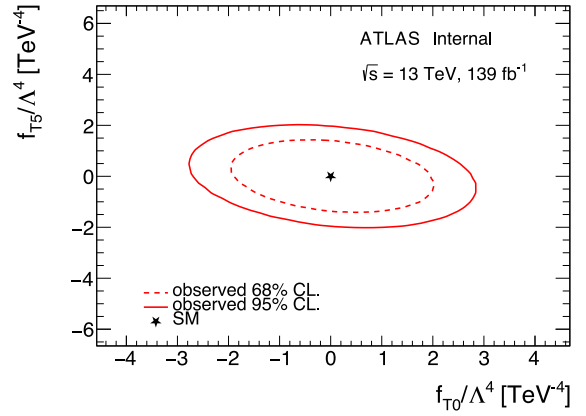
(a)



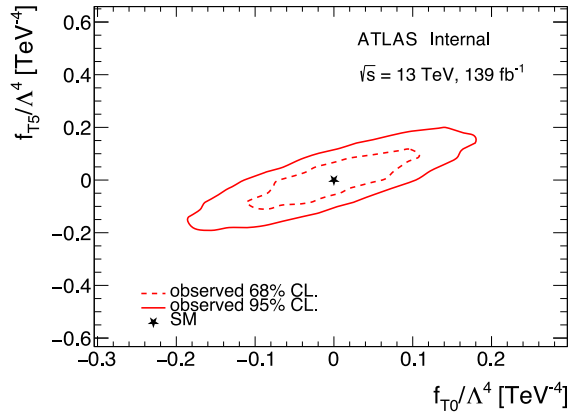
(b)



(c)



(d)



(e)

Figure 3.19: T0vsT5 two-dimensional limit for (a) $Z(\rightarrow \bar{\nu}\nu)\gamma$ (b) $W^\pm Z$ (c) $ZZ \rightarrow 4\ell$ (d) $W\gamma$ (e) combined.



4 - Forward Jet Vertex Tagger

ATLAS detector doesn't have a tracker for $|\eta| \geq 2.5$ and in this region, a separate pile-up tagging (for introduction of pile-up jets see Sec. 2.3.3) method is used (as opposed to barrel region with Jet Vertex Tagger), called forward Jet Vertex Tagger¹ (fJVT). fJVT algorithm was introduced in EMTopo times[34], then ported to PFlow jets [44, 87] and calibrated [96] in Release 21 (R21) ATLAS software for Run-2. Release 22 (R22) is a major update to ATLAS software intended for Run-3 and above.

The need for pile-up rejection for $|\eta| \geq 2.5$ is shown on Fig. 4.1, where the fraction (out of a total number of forward jets) of HS, QCD PU, and stochastic PU jets is shown depending on the number of p-p interactions in the event. Dependencies are obtained from MC Sherpa $Z \rightarrow \ell\bar{\ell} + jets$ sample. It can be seen that especially at μ values close to Run-3 conditions, HS jets constitute about 10% of all forward jets - the rest is pile-up, roughly equally divided between QCD and stochastic pile-up.

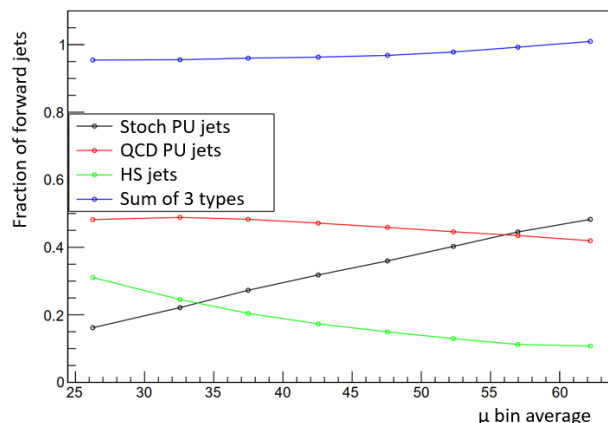


Figure 4.1: Fraction of HS, QCD PU, stochastic PU forward jets depending on number of p-p interactions

4.1 Principle of operation

Key steps of the algorithm are summarized in Fig. 4.2. The goal of the method is to find the vertex v (out of ≈ 40 in Run-2) whose \overrightarrow{MET}_v balances forward jet j with a transverse momentum $\overrightarrow{p}_T^{vj}$ under consideration where the first index corresponds to the vertex with respect to which momentum is calculated and the second index is for the jet. For this, all the objects in the event, including jets, are re-built with respect to each vertex except for the Hard Scatter (HS) vertex. \overrightarrow{MET}_v is computed excluding objects associated to HS vertex, as identified with JVT (R21)/NNJVT (R22) and R_{p_T} . Metric for \overrightarrow{MET}_v and $\overrightarrow{p}_T^{vj}$ balance is the normalized scalar product of them - as illustrated on Fig. 4.3. Then, fJVT for jet j is defined as

$$fJVT^{vj} = \max_v \left(\frac{\overrightarrow{MET}_v \cdot \overrightarrow{p}_T^{vj}}{|\overrightarrow{p}_T^{vj}|^2} \right) \quad (4.1)$$

$$fJVT_j = \max_v (fJVT^{vj}) \quad (4.2)$$

¹Name can be misleading as algorithm working principle has nothing to do with JVT.

The resulting example fJVT distribution is shown in Fig. 4.4 for Hard-Scatter (HS) jets and Pile-up (PU) jets (inclusive, no difference between QCD and Stochastic PU made) jets (labeled with truth² MC information) - degree of separation visible. HS jets tend to be closer to 0, as they do not balance PU vertices' momentum. Also, the long tail of high fJVT values is visible - from looking at Eq. 4.2, it can be expected to be coming from events where the MET of the selected vertex was large. Dependence is shown on Fig. 4.5 and supports the intuition. For this distribution custom derivation³ format was developed⁴ because information on fJVT MET of vertex typically gets rejected.

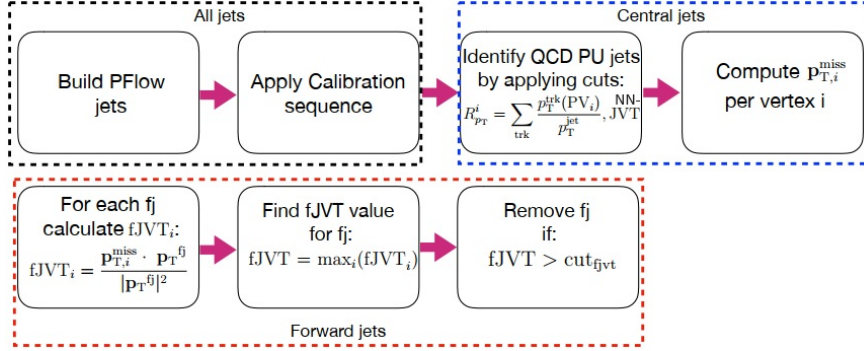


Figure 4.2: fJVT algorithm. Adapted from [87].

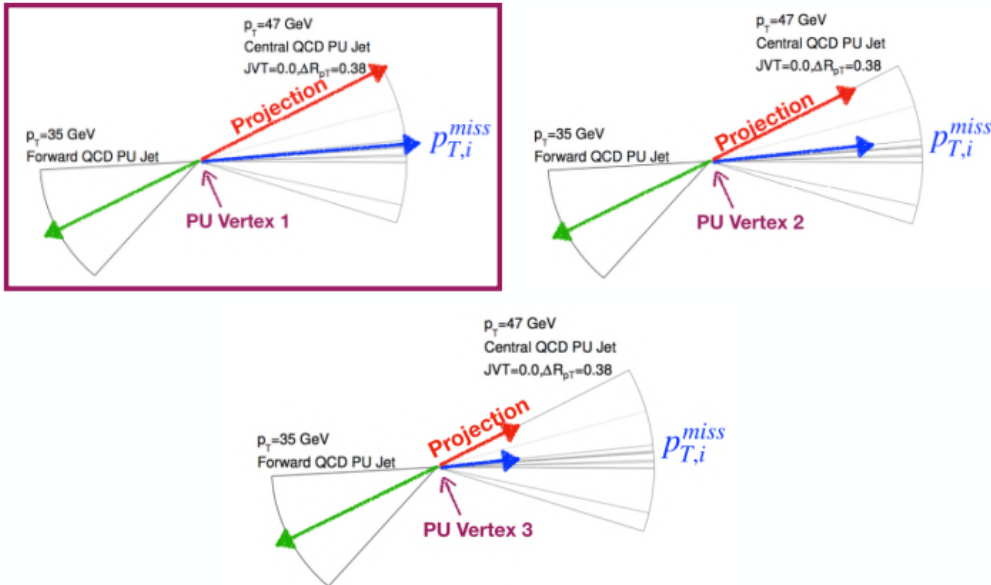


Figure 4.3: fJVT algorithm illustration [87].

The performance of the algorithm is quantified with a receiver operating characteristic (ROC)

²For the typical philosopher of science, particularly for Age Of Enlightenment (particularly French) authors, the term is nonsense, as in physics, being an experimental science, truth is given by the measurement and not by whatever thought or computer simulation one might do.

³One of the data processing stages in ATLAS.

⁴Instead of DAOD_PHYS used elsewhere.

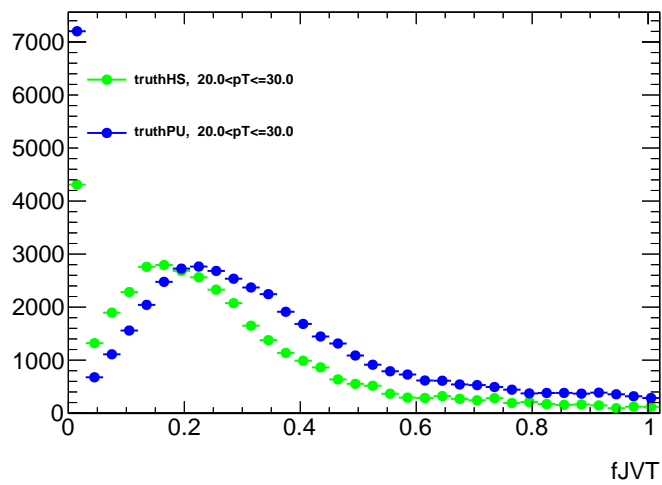


Figure 4.4: Distribution of fJVT for truth HS and inclusive PU jets, $20 < p_T \leq 30$ GeV, $35 < \bar{\mu} \leq 45$, fJVT calibration selections (see Sec. 4.3.1.)

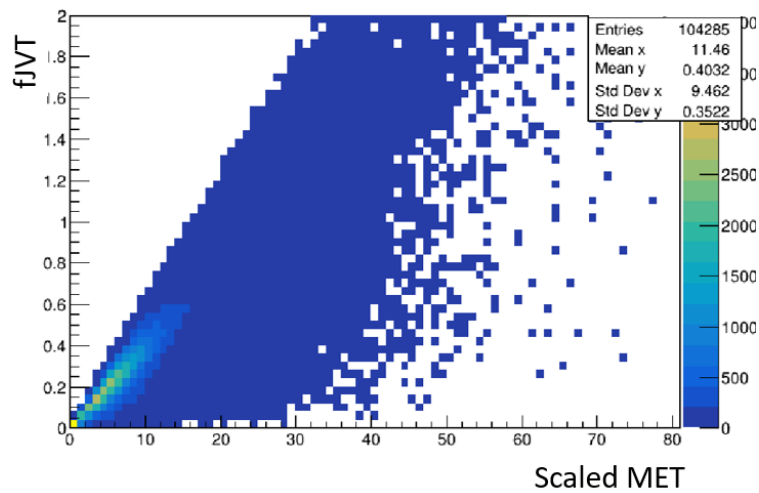


Figure 4.5: Distribution of fJVT depending on MET of vertex where it's taken from.

curve, which in MC (with truth selection) is built from ε_{HS} , ε_{PU} , defined according to Eq. 4.3.

$$\begin{cases} \varepsilon_{HS} = \frac{\int_0^{cut(WP)} f_{JVTHS}}{\int_0^\infty f_{JVTHS}} \\ \varepsilon_{PU} = \frac{\int_0^{cut(WP)} f_{JVTPU}}{\int_0^\infty f_{JVTPU}} \end{cases} \quad (4.3)$$

Scanning over fJVT cuts values, each cut gives $(\varepsilon_{HS}, \varepsilon_{PU})$ point. Resulting curves for four p_T bins in $0 < \bar{\mu} \leq 35$ are shown on Fig. 4.6a and for $45 < \bar{\mu} \leq 55$ on Fig. 4.6b. In both cases $cut_{fJVT} \in [0.05, 0.1, 0.15 \dots 1.5]$, where perfect performance is in the right-bottom corner, as one wants to obtain ε_{HS} as high as possible and ε_{PU} as low as possible. Degradation of performance (shift of ε_{PU} towards higher values) is visible with increasing average number of proton-proton interactions per collision (denoted as $\bar{\mu}$). This is intuitively expected for algorithm relying on balance that it gets more challenging in a busier environment.

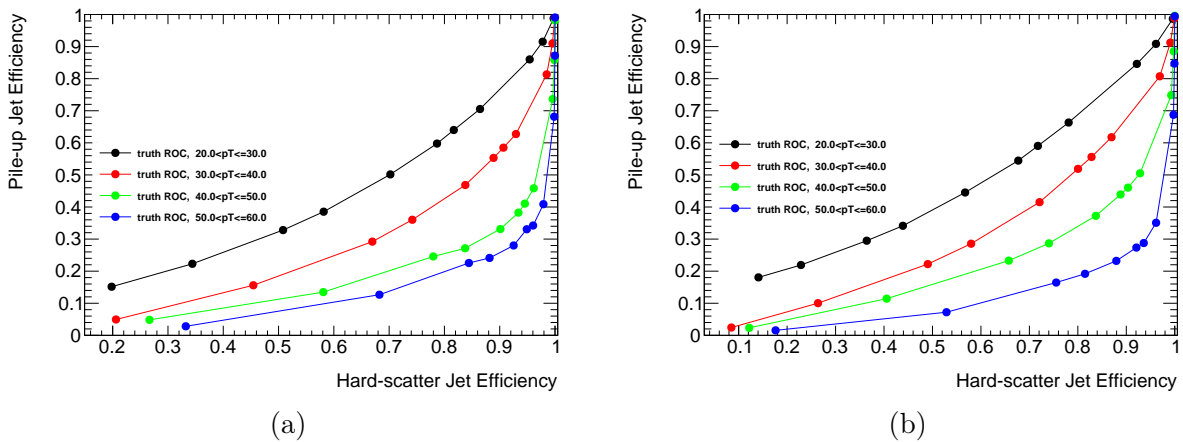


Figure 4.6: (a) fJVT truth ROC curve for $0 < \bar{\mu} \leq 35$ (b) fJVT truth ROC curve for $45 < \bar{\mu} \leq 55$.

4.2 Release 22 update

Both HS and PU distributions in Fig. 4.4 display peak in the first bin, which dominantly consists of cases where fJVT value is exactly zero. Zero is a fJVT default value that gets overwritten once the calculation is done, but the calculation is done only for forward jets⁵ with transverse momentum is above the user-defined threshold T ($p_T \geq T$). The p_T value attached to the jet depends on the calibration used and in a processing chain p_T value changes several times for the same jet - sometimes resulting in a situation where jet seen by fJVT had $p_T < T$ and moment was not calculated, but at the end of full processing, the user sees a jet with different $p_T \geq T$ and fJVT=0. The amplitude of the peak at fJVT=0 is bigger if the larger value for T is used⁶. In R22, a value of 18 GeV is chosen as a compromise between suppression of peak and CPU cost (because of steeply falling jet p_T spectrum). Despite being ugly, there is no problem as the effect has minimal effect on the algorithm performance (seen by comparison of obtained ε_{HS} to R21).

The crucial step of the algorithm is excluding HS objects (the ones geometrically close to JVT-identified HS jet in the event, if any) from each PU vertex's MET calculation. Because of misconfiguration, this was not done in R22 initially, and the resulting ROC curves are shown in Fig. 4.7 (no $\bar{\mu}$ selection is applied but as this is Run-2 data the peak of the distribution can be assumed to

⁵For central jets with $|\eta| \leq 2.5$ fJVT is always 0 as the algorithm is not executed on them.

⁶In R21 peak was absent and the threshold was set at 20 GeV.

be ≈ 30 [27]). They are to be compared with Fig. 4.6a - while excluding HS vertex objects ⁷ much better performance and different behavior are seen.

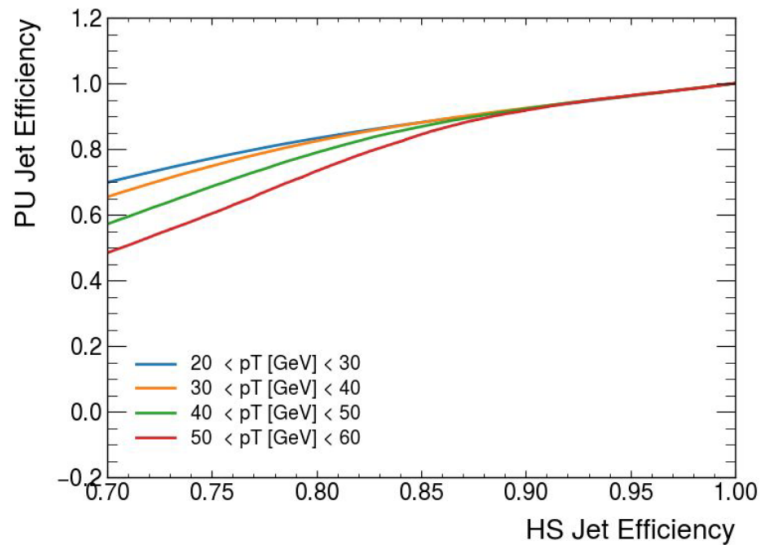


Figure 4.7: fJVT ROC curves if HS objects are not rejected in MET calculation [80]

Another update to the algorithm is migration to NNJVT instead of JVT for the identification of HS objects to be rejected. For NNJVT “FixedEffPt“ working point ⁸ is used corresponding to fixed efficiency across $|\eta|$ in each p_T bin (88% to 99% HS jet efficiency for jets with p_T between 20 GeV and 60 GeV). A slight change of logic is done for this: JVT recommendation was a flat cut value, and therefore, if a specific jet had a value above the recommended one, it was rejected - with NNJVT, there are many values depending on the bin in question to be compared with, and therefore, only the NNJVT pass/not flag is used.

⁷Regulated by `m_includePV` parameter of fJVT algorithm [86] - it is now set to `False` [88].

⁸<https://twiki.cern.ch/twiki/bin/viewauth/AtlasProtected/PileupJetRecommendations>

4.3 fJVT calibration

For the algorithm to be used in actual analysis with real data, it should be calibrated, as MC doesn't reproduce real life perfectly. This time, truth information is unavailable, and the procedure described above cannot be used to characterize performance. This section describes Run-2 and Run-3 fJVT data/MC calibration - using R22+ software (see Sec. 4.2).

4.3.1 Methodology

Method from [96] with modifications is used to quantify data/MC disagreement. Instead of selecting HS or PU jet using truth MC variable, one relies on $\Delta\phi(Z, jet)$ selection in $Z \rightarrow \ell\bar{\ell} + jets$ events to measure ε_{HS} . For this HS-enriched Signal Region (SR) is defined together with Control Region (CR) used to estimate PU contamination in SR.

One looks at $Z \rightarrow \ell\bar{\ell} + jets$ events and uses a variation of the ‘‘tag-and-probe’’ method. Both $Z \rightarrow e\bar{e}$ and $Z \rightarrow \mu\bar{\mu}$ are included. Jets from HS are expected to be balanced by Z (reconstructed from two leptons). The measure of balance is how back-to-back it is in $\Delta\phi(Z, jet)$. Events with only one jet, which is the forward jet, are selected. The number of central HS jets is required to be zero. One then defines CR enriched in pile-up and SR enriched in HS by looking at Fig. 4.8a. The method is inspired by Monte-Carlo, but truth information is not used for calibration. Pileup is flat as a function of $\Delta\phi(Z, jet)$, and Hard-scatter is peaking around $\Delta\phi(Z, jet) = \pi$. Pileup, being flat, gives a pedestal for HS jets. Then, in the case of real data, one defines pileup CR to be $\Delta\phi(Z, jet) < 1.2$ (based on this plot, anything until ≈ 1.8 will also do the job). SR is defined to be $\Delta\phi(Z, jet) > 2.8$ to contain the HS peak. In SR to obtain actual HS contribution, CR contribution takes into account the difference in width of SR and CR given by

$$c_w = \frac{\pi - 2.8}{1.2} \quad (4.4)$$

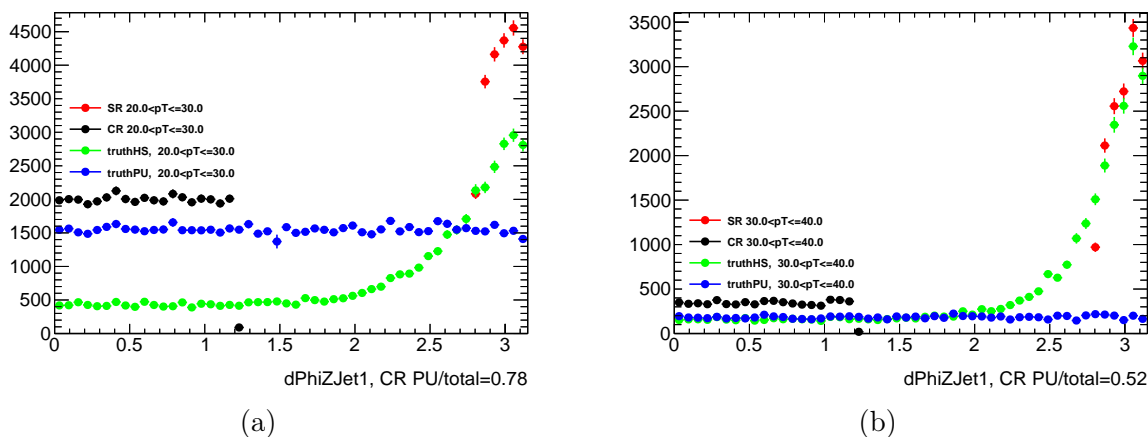


Figure 4.8: (a) $\Delta\phi(Z, jet)$ used to select SR and CR for fJVT calibration, $20 < p_T \leq 30$ (b) $\Delta\phi(Z, jet)$ used to select SR and CR for fJVT calibration, $30 < p_T \leq 40$.

CR and SR events are used together to get ε_{HS} from fJVT distribution

$$\varepsilon_{HS}^{WP} = \frac{N_{SR}^{WP} - c_w N_{CR}^{WP}}{N_{SR}^{total} - c_w N_{CR}^{total}} = \frac{\int_0^{cut(WP)} f_{JVT}^{SR} - c_w \int_0^{cut(WP)} f_{JVT}^{CR}}{\int_0^{\infty} f_{JVT}^{SR} - c_w \int_0^{\infty} f_{JVT}^{CR}} \quad (4.5)$$

ε_{HS} is derived in this way twice: for MC and real data, and the goal of the calibration is to derive Scale Factors (SF) that give corrections to MC necessary to reproduce algorithm behavior in data:

$$SF = \frac{\varepsilon_{HS}^{data,WP}}{\varepsilon_{HS}^{MC,WP}} \quad (4.6)$$

4.3.2 $Z \rightarrow \ell\bar{\ell} + jets$ samples and validation

Both dimuon and dielectron samples are used. Medium muons [47] and tight electrons [53] are selected. Both single-lepton and multi-lepton triggers are in use, and most of the statistics come from the former. Z window mass cut is 15 GeV. The starting point for calibration is common ntuples⁹ of MET/PU sub-group (of ATLAS Jet/Etmiss) - they are produced with METPerformance package [2]. Calibration is done within METPerfHistogramming[1] package, for which fJVT “module“ was developed. The purpose of METPerfHistogramming is to produce a correctly normalized set of histograms with certain selections. The selections needed were described above. Cell timing cut[54] is applied in all samples.

Run-2 is divided into three campaigns: 2015+2016, 2017, 2018. For each, $Z \rightarrow e\bar{e}$ and $Z \rightarrow \mu\bar{\mu}$ samples are used. Electron and muon trigger scale factors have been available and applied for all years. The generators are Powheg, Sherpa, and MadGraph.

Run-3 data used for calibration is coming from 2022 and 2023 campaigns. For each, $Z \rightarrow e\bar{e}$ and $Z \rightarrow \mu\bar{\mu}$ samples are used. Among generators, Powheg and Sherpa were considered, but not MadGraph because the statistics generated don’t allow for the necessary statistics for calibration on all bins required. The muon and electron trigger scale factors were not available for 2023 data, however no effect on main distributions (fJVT, $\Delta\phi$) is seen and therefore no ad-hoc correction applied.

Before starting fJVT calibration, it’s good to see the absence of strange features in those samples - in both data and MC. As Run-2 largely has the same detector configuration and the same processing is used, one doesn’t expect a significant difference compared with Run-3. In Run-2 2018, some muon sample plots will be shown as having the most data. In Run-3, for brevity among four possibilities, only 2022 muon distributions will be shown. Not electrons as muons have larger statistics. Not 2023 because trigger SF is available for 2022 data.

Here, only variables actually used for calibration, $\Delta\phi$ and fJVT are shown on Fig. 4.9, Fig. 4.10 for brevity. All data and MC distributions are normalized to the same area to compare the shape. Data integral (all the weights are applied) is written in legend near DataX (where X is a year), and MC integrals are written near relative to data normalization. Relatively good agreement is seen. Other distributions, including $\bar{\mu}$ (before and after PRW), jet and lepton p_T , jet and lepton η , and some others are in Appendix C, all showing acceptable agreement.

4.3.3 Binning and working points

SF is derived in $p_T \times \bar{\mu}$ bins (for different working points) because, as we saw above with truth, performance changes as a function of them. p_T bins considered are within range $20 < p_T \leq 60$. The contribution above 60 GeV pile-up is small, and there is likely no need for the algorithm, as can already be seen on truth curves. In addition because $20 < p_T \leq 60$ is the range for which NNJVT is calibrated, and it’s used inside of fJVT. Therefore, it is better for NNJVT and fJVT to have consistent p_T binning.

The working points defined are $fJVT \leq 0.2$ (named Tighter), $fJVT \leq 0.4$ (named Tight), and $fJVT \leq 0.5$ (named Loose).

4.3.4 Uncertainties

⁹v0.6 ntuples stored in /eos/atlas/atlascerngroupdisk/perf-jets/Etmiss/METPerformance/METPerformance_v0.6/.

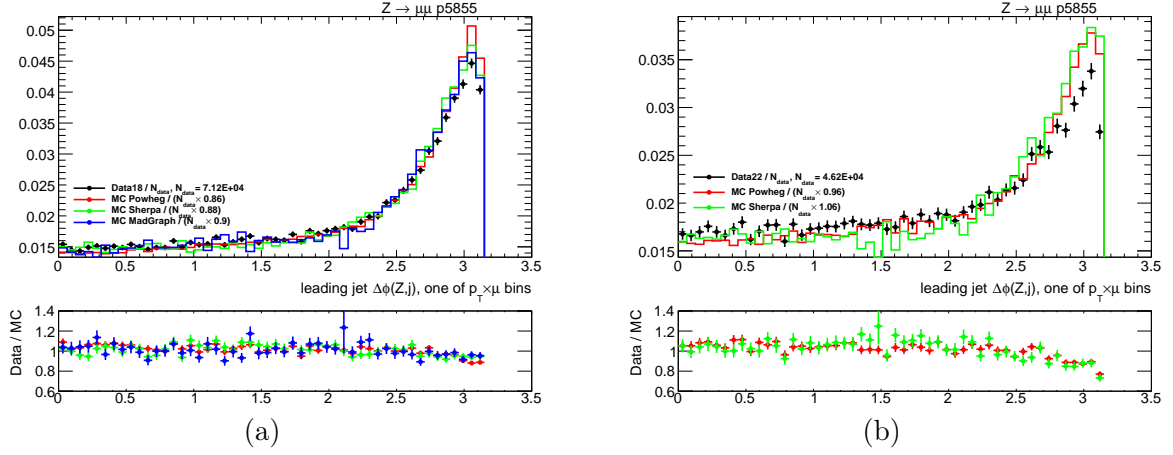


Figure 4.9: Data/MC comparison of $\Delta\phi(jet_1, Z)$, fJVT calibration selections (a) Run-2: 2018 $Z \rightarrow \mu\bar{\mu}$ (b) Run-3: 2022 $Z \rightarrow \mu\bar{\mu}$.

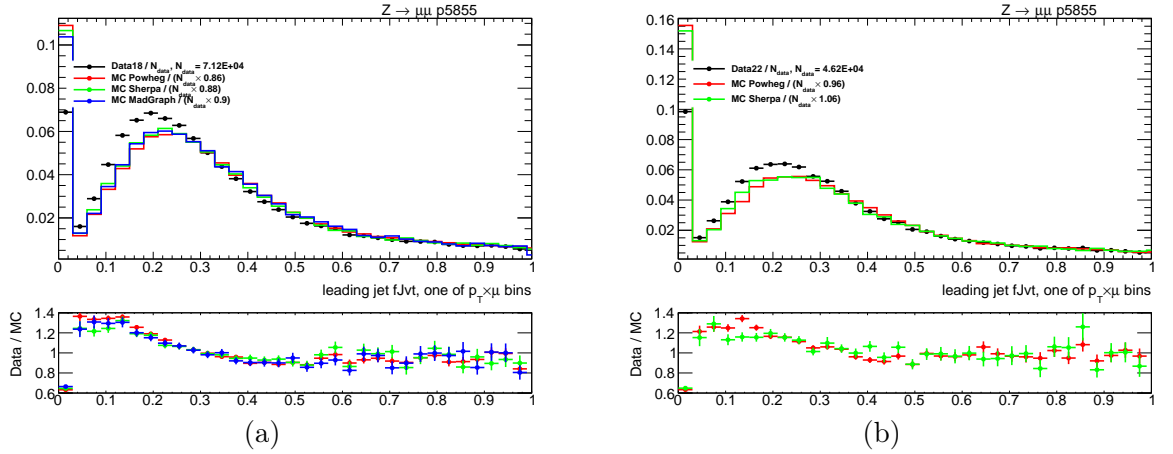


Figure 4.10: Data/MC comparison of $fJVT_{jet_1}$, fJVT calibration selections (a) Run-2: 2018 $Z \rightarrow \mu\bar{\mu}$ (b) Run-3: 2022 $Z \rightarrow \mu\bar{\mu}$.

The uncertainties are from statistical and systematic sources. The latter ones originate from five different sources: MC generator dependence, data-taking campaign dependence, calibration final state, CR PU misestimation, forward sub-detector.

Statistical uncertainty on efficiency is computed as

$$\sigma_{\varepsilon_{HS}} = \sqrt{\frac{\varepsilon_{HS}(1 - \varepsilon_{HS})}{N_{SR}^{total} - c_w N_{CR}^{total}}} \quad (4.7)$$

where ε_{HS} is taken from Eq. 4.5 and denominator under square root gives PU-subtracted SR content before application of certain fJVT cut - see Eq. 4.5 denominator. $\sigma_{\varepsilon_{HS}^{data}}, \sigma_{\varepsilon_{HS}^{MC}}$ are then propagated to obtain $\sigma_{SF_{stat}}$.

Systematic uncertainties are obtained as “envelopes”: SFs are obtained for several cases (minimum 2 cases are needed), let’s say A, B, N (for nominal) giving $SF_{Nominal}, SF_A, SF_B$ then Nominal results are compared to other cases (here A, B) by taking differences and considering their absolute values

$$\Delta_A^{SF} = |SF_{Nominal} - SF_A| \quad (4.8)$$

$$\Delta_B^{SF} = |SF_{Nominal} - SF_B| \quad (4.9)$$

then envelope gives the symmetric error

$$envelope = \max(\Delta_A^{SF}, \Delta_B^{SF}) \quad (4.10)$$

MC modeling dependence (part) is taken into account through the generator envelope - depending on the list of generators considered, which is different for Run-2 and Run-3. The nominal generator in both cases is Sherpa.

Correction for possible differences between jets reconstructed in different forward sub-detectors (see Sec. 2.3.2) is done. Nominal case is inclusive $2.5 \leq |\eta| \leq 4.9$ In addition scale factors are derived for $2.5 \leq |\eta| \leq 3.2$ and $3.2 \leq |\eta| \leq 4.9$. Envelope over three cases is then taken.

The potential difference between different years of data-taking - this includes, for example different $\bar{\mu}$ shape or detector configuration, is removed by considering the envelope over the years within each $\bar{\mu}$ bin. For example, in Run-3, ε_{HS} and SFs are calculated separately for nominal, 2022, and 2023, and an envelope is taken separately in each $\bar{\mu}$ bin. The total per Run-2 or Run-3 is a nominal case; other contributions are each campaign year separately. In some $\bar{\mu}$ bins (like in Run-3) this is not possible, for example in $\bar{\mu} > 55$ there is only data taken in 2023 and in 2022 $\bar{\mu}$ has lower values. For those cases, when one doesn't have at least two years, the year envelope is 0.

As both $Z \rightarrow e\bar{e}$ and $Z \rightarrow \mu\bar{\mu}$ events are used, the difference in results between them is checked. Nominal case is $Z \rightarrow e\bar{e} + Z \rightarrow \mu\bar{\mu}$ combined. $Z \rightarrow \mu\bar{\mu}$ SF and $Z \rightarrow e\bar{e}$ SFs are derived separately, and 3 cases are put into an envelope. Contribution is denoted later as σ_{FS} , where FS stands for final state.

The last uncertainty is coming from possible PU misestimation. As already seen on Fig. 4.8a for $20 < p_T \leq 30$ pile-up constitutes most of CR but not all of it (78%). This can be compared to Fig. 4.8b for $30 < p_T \leq 40$ where CR PU purity is lower (52%) However, CR itself shrinks compared to SR. To take into account CR PU non-purity, SFs are derived in the nominal case and also in up, down PU variation cases where the amount of non-purity gives variation magnitude. Rewriting more compactly Eq. 4.5 together with variation factor V gives

$$\varepsilon_{HS}^{WP} = \frac{N_{SR}^{WP} - c_w N_{CR}^{WP} \times V}{N_{SR}^{total} - c_w N_{CR}^{total} \times V} \quad (4.11)$$

Nominal case gives $V=1$, for particular case shown on Fig. 4.8b for up and down variations $V=0.52$ and $V=1/0.52$. This is repeated in each $p_T \times \bar{\mu}$ bin. The envelope is taken over 3 cases. PU uncertainty is not increasing with p_T because CR becomes negligible.

To summarize, uncertainty on the SF factor in the given bin (where components are added in quadrature) is given by

$$\sigma_{SF} = \sigma_{stat} \oplus \sigma_{gen} \oplus \sigma_{\eta} \oplus \sigma_{year} \oplus \sigma_{FS} \oplus \sigma_{PU.est.} \quad (4.12)$$

4.3.5 Run-2 R22 calibration

Run-2 $\bar{\mu}$ is shown on Fig. 4.11a and $\bar{\mu}$ binning chosen for calibration is $0 < \bar{\mu} \leq 25$, $25 < \bar{\mu} \leq 35$, $35 < \bar{\mu} \leq 45$, $45 < \bar{\mu} \leq \infty$ - to have enough statistics in each bin. Finer binning is possible but not very useful as ε_{HS} vs $\bar{\mu}$ dependence is not that strong. $20 < p_T \leq 30$, $30 < p_T \leq 40$, $40 < p_T \leq 50$, $50 < p_T \leq 60$.

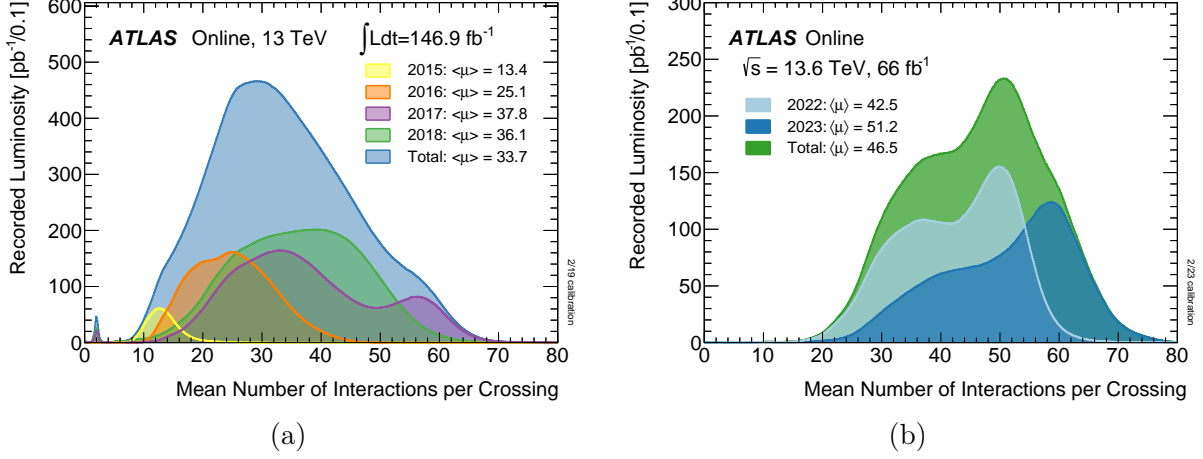


Figure 4.11: $\bar{\mu}$ distributions, total and per year, for campaigns: (a) Run-2 [27] (b) Run-3 [28]

Most of the data is in $35 < \bar{\mu} \leq 45$ bin, and the results of calibration for it, applying the method described above, are shown on Fig. 4.12 for Tight working point (the “medium“ one among the three considered) - other two WPs are shown in Appendix D, Appendix E (Fig. D.1, Fig. E.1).

Summary of results, including this time other $\bar{\mu}$ bins, is shown on Fig. 4.13, Fig. 4.14, Fig. 4.15 - this constitutes a recommendation for collaboration. Improvement of efficiency with increasing p_T is again visible together with a decrease with growing $\bar{\mu}$. Scale factors are close to 1 overall, getting closer to 1 for higher p_T . Typically, disagreement with MC is below 5%. A comparison with the previous calibration in a comparable $\bar{\mu}$ bin gave similar results.

4.3.6 Run-3 R22 calibration

Run-3 $\bar{\mu}$ is shown in Fig. 4.11b (at the time of writing, 2024 data-taking is still ongoing and 2024 data is not considered) and binning chosen for calibration is different from Run-2; it is: $0 < \bar{\mu} \leq 35$, $35 < \bar{\mu} \leq 45$, $45 < \bar{\mu} \leq 55$, $55 < \bar{\mu} \leq \infty$ - smaller statistics compared to Run-2 but still capture ε_{HS} vs $\bar{\mu}$ dependence.

Similar to the Run-2 section, the biggest $\bar{\mu}$ bin (now it's $45 < \bar{\mu} \leq 55$) calibration results are shown in Fig. D.2, Fig. 4.16 for Tight working point - other two WPs are shown in Appendix D, Appendix E (Fig. D.2, Fig. E.2).

Summary of results, including this time other $\bar{\mu}$ bins, is shown on Fig. 4.17, Fig. 4.18, Fig. 4.19 - this again constitutes a recommendation for collaboration. Behavior is similar to Run-2 calibration.

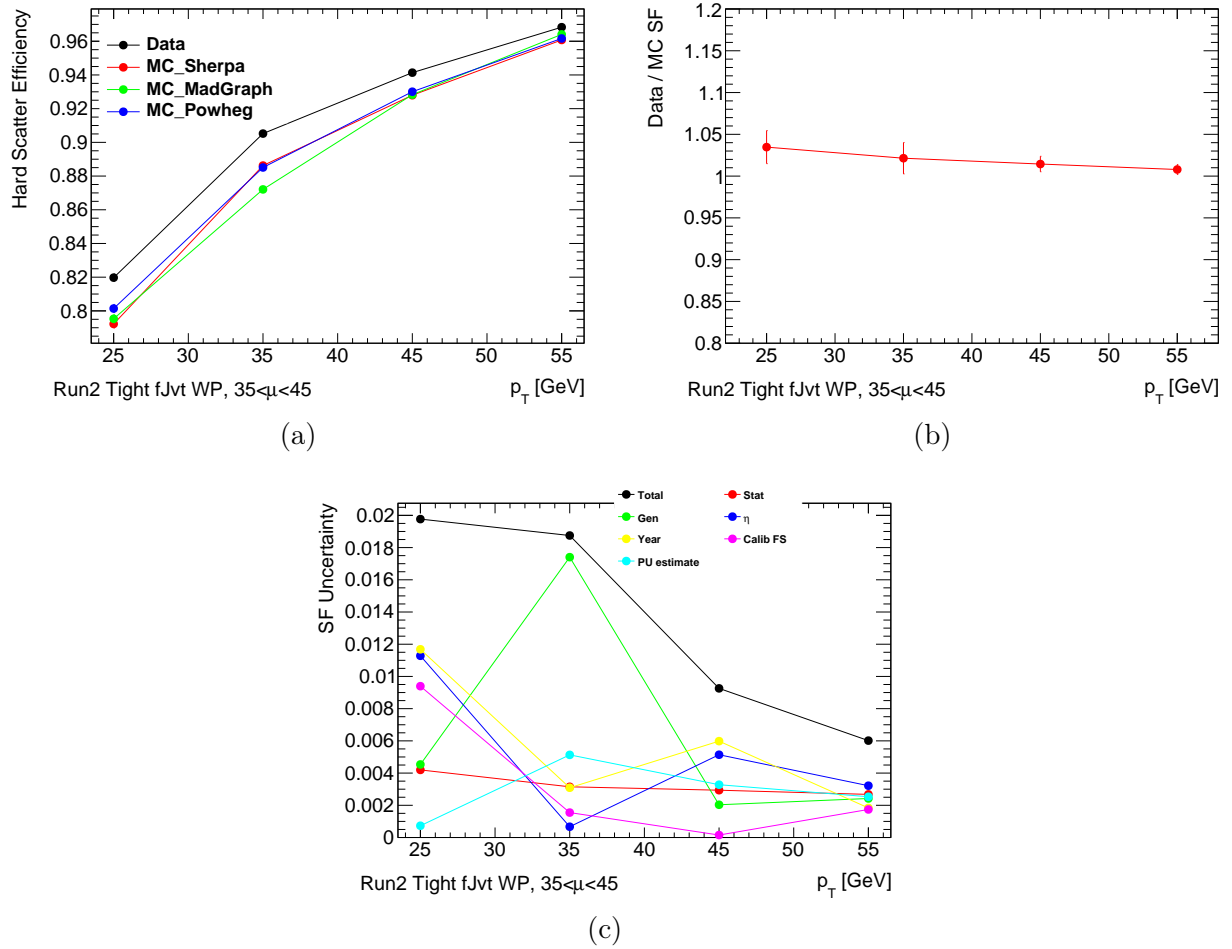


Figure 4.12: Run2 calibration results in $35 < \bar{\mu} \le 45$, Tight working point (a) Hard-Scatter efficiency (b) Scale Factor (c) Scale Factor uncertainty breakdown.

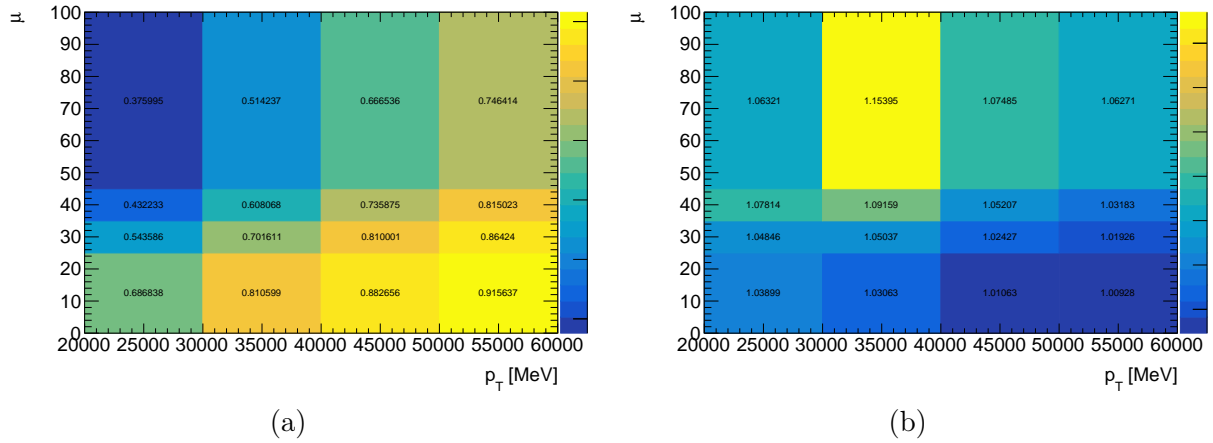


Figure 4.13: Run2 calibration results for Tighter working point (a) MC Hard-Scatter efficiency (b) Scale Factor.

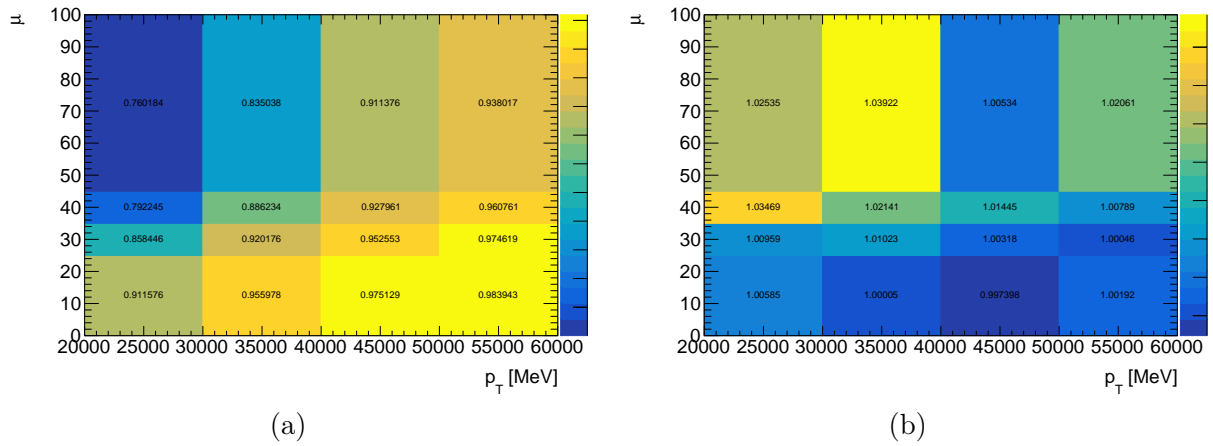


Figure 4.14: Run2 calibration results for Tight working point (a) MC Hard-Scatter efficiency (b) Scale Factor.

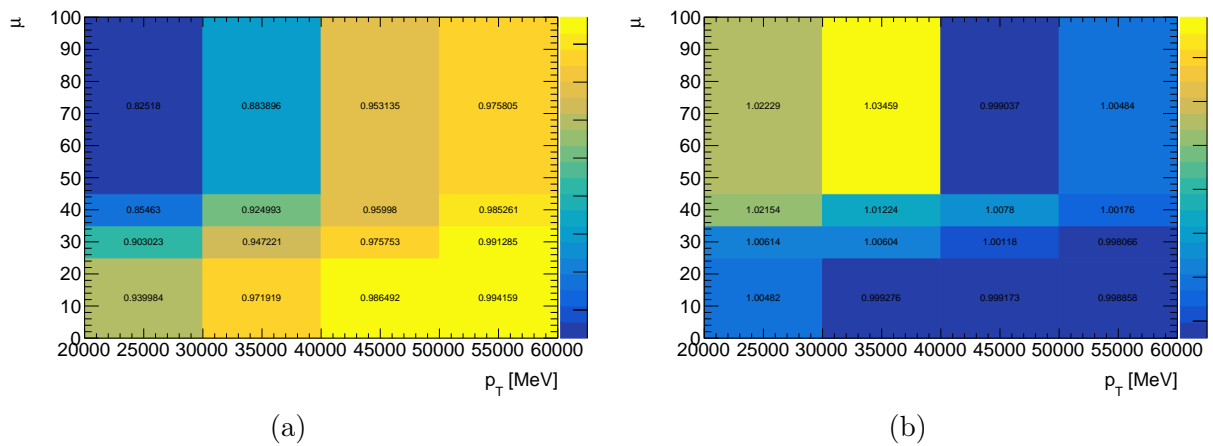
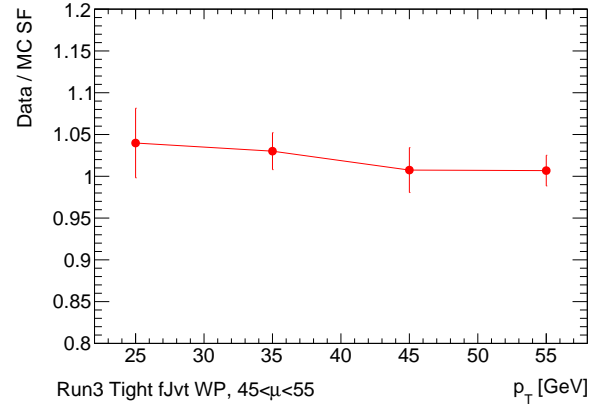
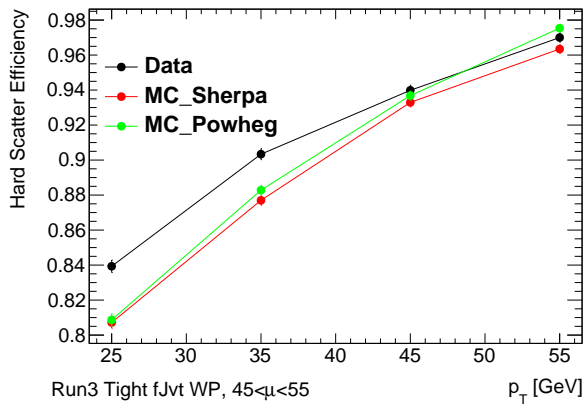
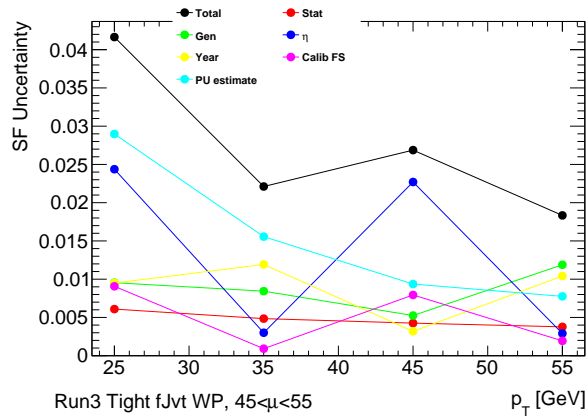


Figure 4.15: Run2 calibration results for Loose working point (a) MC Hard-Scatter efficiency (b) Scale Factor.



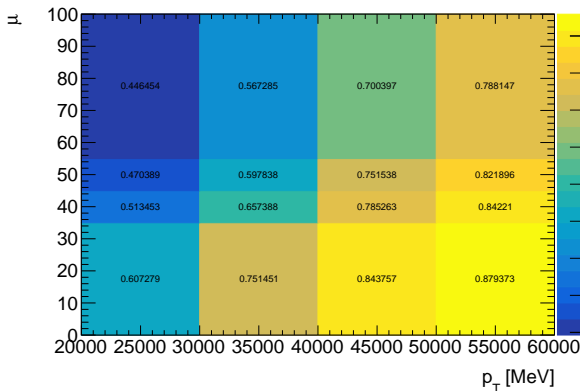
(a)

(b)

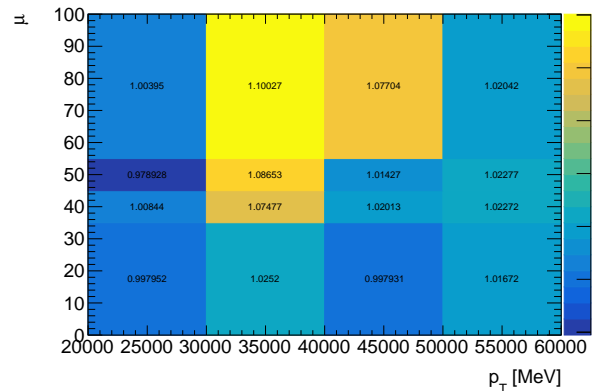


(c)

Figure 4.16: Run3 calibration results in $45 < \bar{\mu} \leq 55$, Tight working point (a) Hard-Scatter efficiency (b) Scale Factor (c) Scale Factor uncertainty breakdown.



(a)



(b)

Figure 4.17: Run3 calibration results for Tighter working point (a) MC Hard-Scatter efficiency (b) Scale Factor.

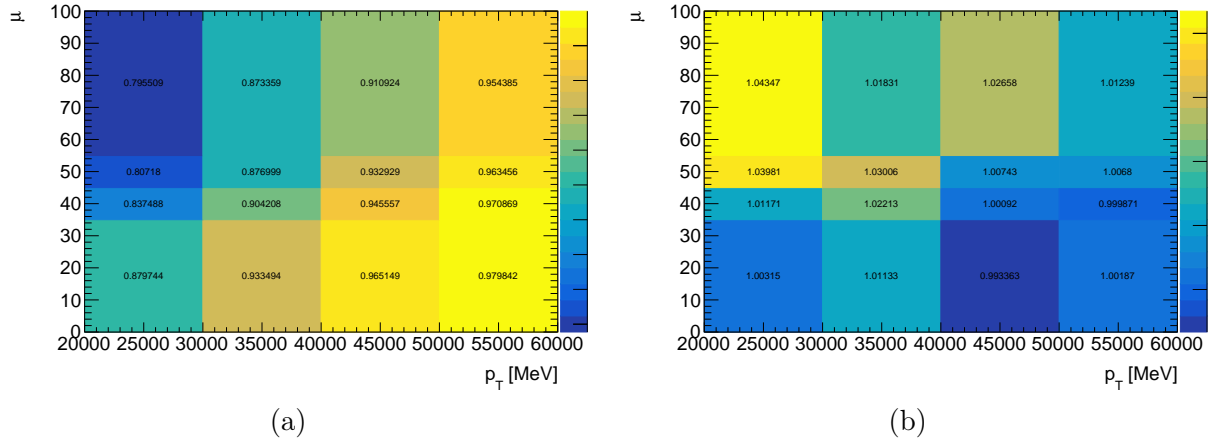


Figure 4.18: Run3 calibration results for Tight working point (a) MC Hard-Scatter efficiency (b) Scale Factor.

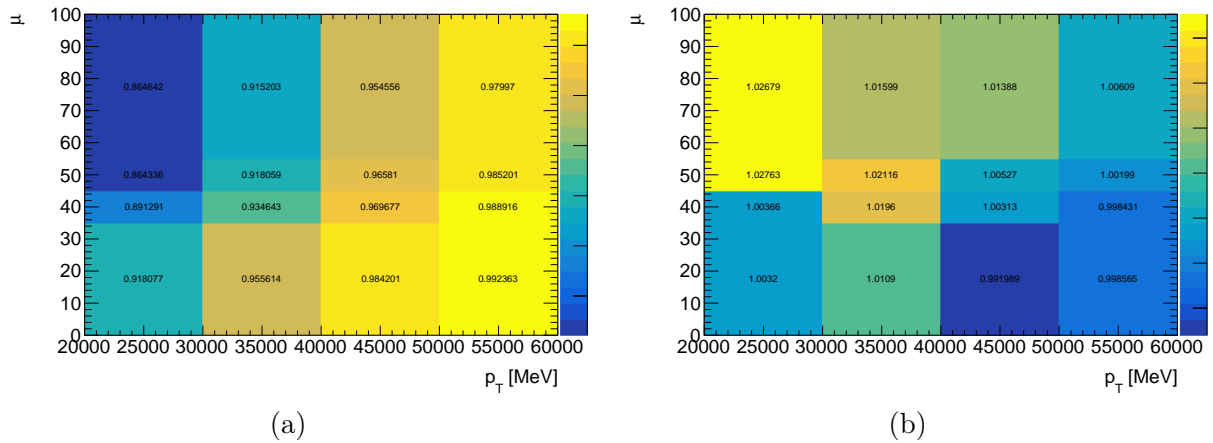


Figure 4.19: Run3 calibration results for Loose working point (a) MC Hard-Scatter efficiency (b) Scale Factor.

4.4 Potential improvement

4.4.1 Shape information

fJVT is not the only possible discriminant against PU; shape information can also be used. As a simple demonstration, one can look at the width calculated according to:

$$w = \frac{\sum_k \Delta R(\text{jet}, k) p_T^k}{\sum_k p_T^k} \quad (4.13)$$

ATLAS software already has a tool¹⁰ providing the variable. Distribution of width (scaled to get nicer numbers) is shown on Fig. 4.20 for $20 < p_T \leq 35$ forward jets. It can be calculated more finely with topo-towers re-introduced relatively recently. PU jets are seen to peak at higher width values. ROC curve obtained by using discrimination by width only is also shown and can be compared with “throw a coin“ scenario indicated by a dashed line.

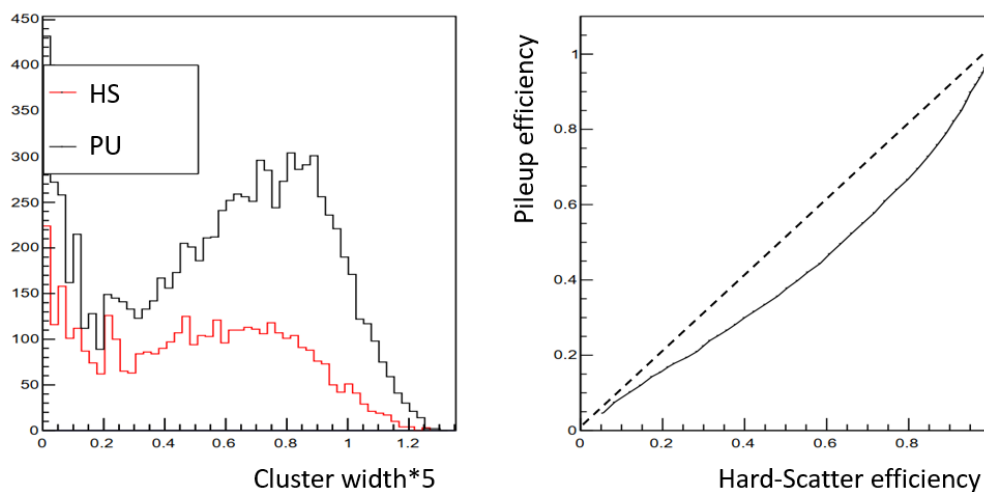


Figure 4.20: For $20 < p_T \leq 35$ forward jets in $Z \rightarrow \mu\bar{\mu}$ sample (left) width distributions (no use of topo-clusters) of HS and PU jets (right) ROC curve of ε_{HS} vs. ε_{PU} using the width

Similarly to fJVT, HS/PU separation by width variable is not dramatic; however, combined with fJVT in some kind of BDT has potential. One attempt was done already in 2018[96] however did not make into recommendation because of quark-gluon dependence. However, since then, decorrelation methods arrived, which gives the potential to revise the approach. Moreover, as both quark-gluon and HS-PU discriminations are sensitive to overlapping sets of variables, it makes sense to develop a combined quark/gluon/HS/PU tagger.

4.4.2 Targeting specific type of pile-up

Hard-scatter and Pile-up discrimination ROC curves were shown on Fig. 4.6a, where there is no distinction between QCD and Stochastic Pile-up. It’s interesting then to see how fJVT performs in distinguishing between specifically (HS, QCD PU) and between (HS, stochastic PU) separately - rather surprisingly, there is no difference, as seen from comparison of two ROC curves shown on Fig. 4.21, both made for $20 < p_T \leq 30$.

However, specialized methods exist for stochastic pile-up tagging. One of them is γ -discriminant [34]. It relies on the fact that the hard-scatter jet distribution in $\eta \times \phi$ plane displays a sharply peaked distribution, while the stochastic pile-up jet distribution is flat with various off-center features,

¹⁰JetWidthTool

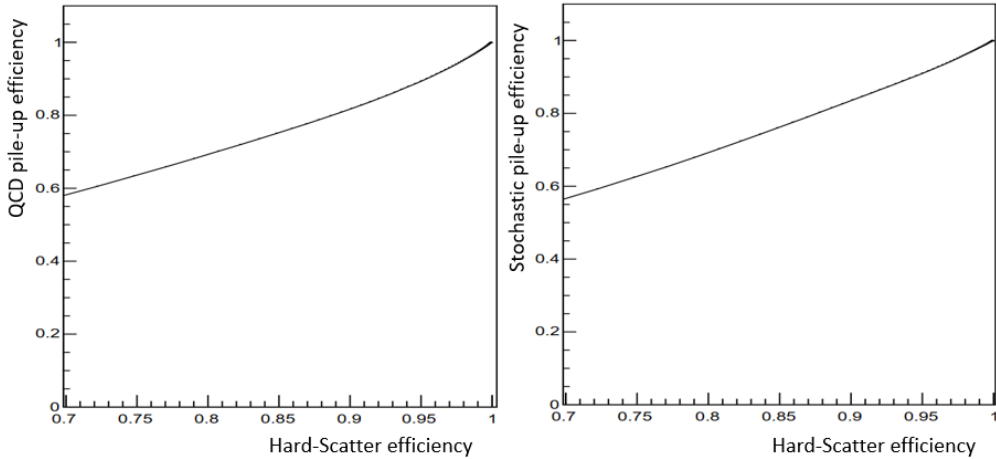


Figure 4.21: For $20 < p_T \leq 30$ forward jets in $Z \rightarrow \mu\bar{\mu}$ sample (left) ROC curve of separating HS jets from QCD PU jets (right) ROC curve of separating HS jets from Stochastic PU jets

reflecting the randomness of the underlying processes. 2D $\eta \times \phi$ distribution is fitted with

$$f = \alpha + \beta\Delta\eta + \gamma e^{-\frac{1}{2}\left(\frac{\Delta\eta}{0.1}\right)^2 - \frac{1}{2}\left(\frac{\Delta\phi}{0.1}\right)^2} \quad (4.14)$$

where α and β are the constant and linear terms to capture the average stochastic pile-up contribution to the jet p_T distribution. One of the parameters involved, γ , has different values for stochastic and HS jets. The ROC curve obtained is shown on Fig. 4.22, showing up to 40% better performance compared to how fJVT can distinguish between the two.

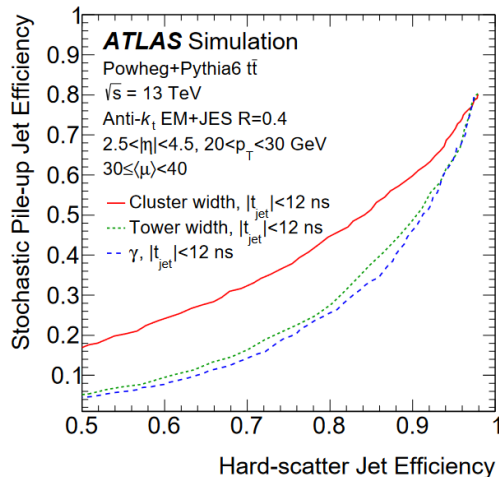


Figure 4.22: Efficiency for stochastic pile-up jets as a function of the efficiency for hard-scatter jets using different shape-based discriminants: $30 < \bar{\mu} \leq 40$ in simulated $t\bar{t}$ events [34]

Therefore, it makes sense not just to have one tagger but several ones depending on the type of pile-up (e.g. use fJVT for to reject QCD PU and γ to reject stochastic pile-up) and then mix them in some way. Given Sec. 4.4.1, it can also make sense to develop a combined quark/gluon/HS/QCD/stochastic tagger.

4.4.3 Detector upgrades

The algorithms shown above rely on variables built from spatial information, such as the position of the sensor hit. In central region, new HL-LHC tracker (ITk) $|\eta|$ coverage will be extended. In

addition, knowledge of the time when the sensor was hit is beneficial. A new forward sub-detector called HGTD will be installed for timing measurements, which will be the subject of subsequent chapters.

4.5 Conclusion

The fJVT algorithm, responsible in ATLAS for forward pile-up rejection, was integrated into updated ATLAS software. Its performance is validated in MC. Performance is also validated in real data and disagreement with MC is quantified through scale factors derived in $p_T \times \bar{\mu}$ bins, for three working points. Overall, a good agreement between data and MC is seen. Calibration is now released, covering both Run-2 and early Run-3, and available for the whole ATLAS collaboration [81, 23]. Potential ways for fJVT improvement are briefly discussed.



5 - HL-LHC

5.1 Project overview

Rising interest in search for rare processes, precision measurements in Higgs, Top and Electroweak sectors leads to a need to increase the data rate LHC is providing and ATLAS is recording: higher luminosity is required, pileup and radiation also will increase. Moreover, the lifetime of some components in terms of radiation in both the accelerator and detector is ending. Both accelerator and detectors will be upgraded: it was decided to move on to the High Luminosity Large Hadron Collider (HL-LHC) stage, where the design goal is a significant increase of integrated luminosity through a five-fold increase in instantaneous number of proton-proton collisions. The adapted timeline is shown on Fig. 5.1. At the moment of writing, we are at the end of Run-3, the third year of data-taking (out of four). At HL-LHC, the center-of-mass will be the same or will increase slightly, and bunch spacing of 25 ns will stay the same. The design goal during operation, planned until 2040, is to accumulate a dataset of 3000 fb^{-1} , which is roughly a factor ten higher than combined Run-2 + Run-3 integrated luminosity. HL-LHC will likely be the end of LHC ¹. Already in 2006, the CERN Council adopted the European Strategy for Particle Physics, and it was agreed that “The LHC will be the energy frontier machine for the foreseeable future, maintaining European leadership in the field; the highest priority is to fully exploit the physics potential of the LHC ... A subsequent major luminosity upgrade (SLHC), motivated by physics results and operation experience will be enabled by focussed R&D; to this end, R&D for machine and detectors has to be vigorously pursued now and centrally organized towards a luminosity upgrade ...”[75]. Strategy only works if the budget is allocated, and this was done, particularly in the session of June 2016, the CERN Council approved the whole HL-LHC project - where 950 MCHF is until 2026 ². It is planned, as shown in Fig. 5.1, to make a break after Run-3 and install main components over three years of Long Shutdown 3 (starting 2026) and commission them for one year afterward.

5.2 Accelerator upgrades

Constraints from the detector on manageable level of pile up and from the accelerator on energy deposition lead to the constraint on peak luminosity. Then, one must operate the machine at a lower than maximum possible luminosity, shown in the red curve at time=0 on Fig. 5.2. In order to still reach target of 3000 fb^{-1} , lower-than-maximum luminosity will be held roughly constant for a long periods of time - as shown in a blue curve on Fig. 5.2. This is called luminosity levelling and will be done for HL-LHC ³. Nominal HL-LHC luminosity is $5 \times 10^{34} \text{ cm}^{-2}\text{s}^{-1}$.

Luminosity will be increased via reduction of β^* to 15 cm (can be compared to 55 cm in the LHC design report), which in turn implies two aspects. One is that IT quadrupole magnets need to double the aperture, giving peak field up to 12 T - twice larger than present LHC (uses Nb-Ti technology), and this calls for the usage of new Nb_3Sn superconducting technology. Second aspect is larger crossing angle and corresponding reduction of geometrical luminosity factor ($\equiv R$), as shown on Fig. 5.3. The adapted solution is the usage, for the first time at a hadron collider, of novel crab

¹it’s not completely clear what will happen next - one of the scenarios discussed is going to even higher collision energy, 100 TeV, via Future Circular Collider (FCC). The FCC feasibility study is expected to be completed in 2025. If built, existing CERN infrastructure will be re-used, similarly to LHC is being partially built in the LEP tunnel.

²full cost of HL-LHC project is expected to be 1139.4 MCHF

³in fact, was already used in Run-3

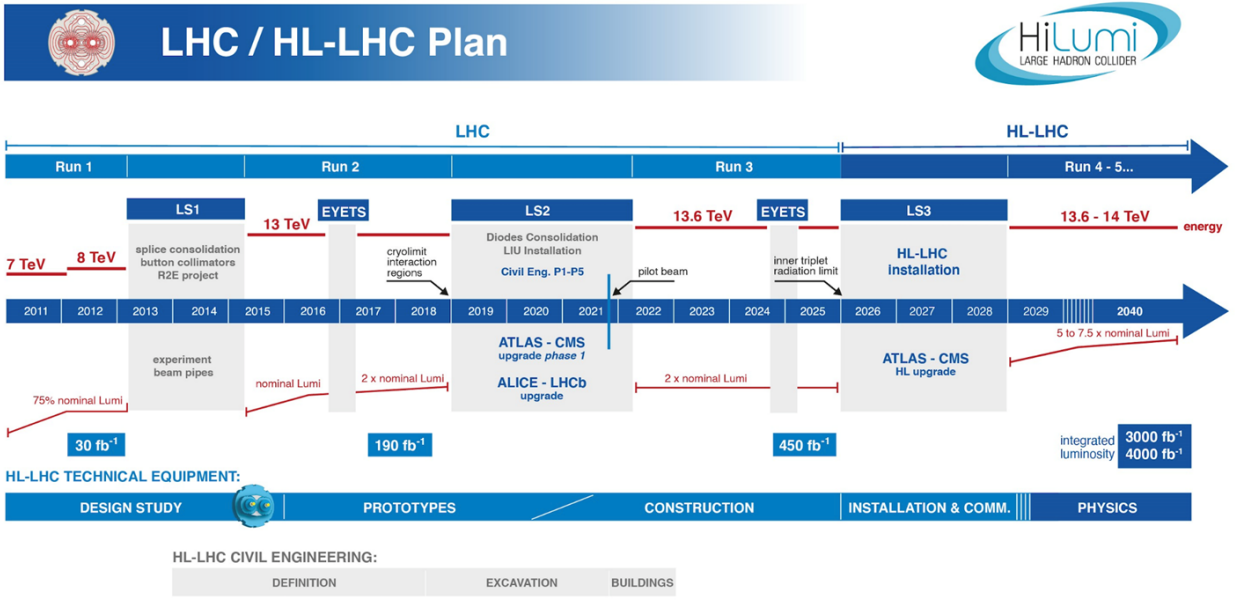


Figure 5.1: LHC baseline plan for the next decade and beyond showing the collision energy (upper line) and luminosity (lower line). LS2 sees LHC consolidation and the HL-LHC underground excavation, as well as the upgrade the LHC injectors and Phase 1 upgrade of the LHC detectors. After LS3, the machine will be in the high-luminosity configuration. Covid-19 restrictions have led to the shift of the start of Run-3 to February 2022 while the start of LS3 is maintained at end of 2024 [72]

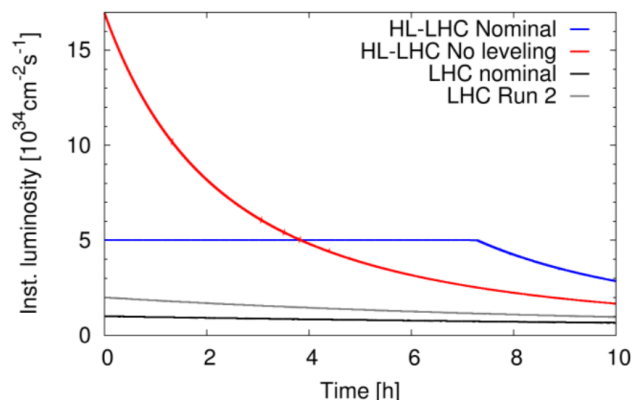


Figure 5.2: Luminosity profile with and without levelling, for a single long run [72]

cavities (CC). CC generates a voltage kick to rotate each bunch just before the collision. Such two trains overlap more - it's illustrated on Fig. 5.4. After the collision, beams are rotated back. CC also can be used as levelling tool.

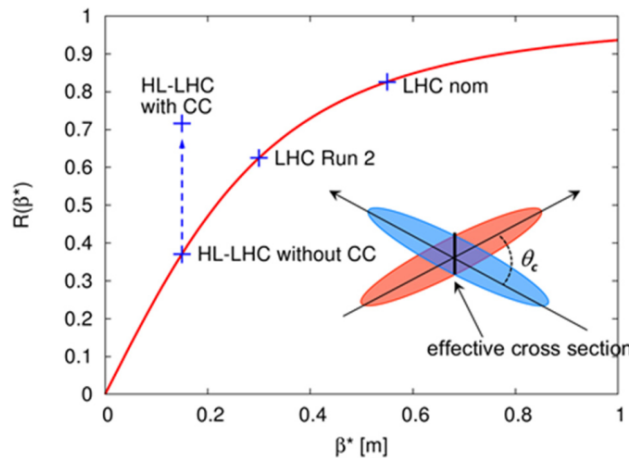


Figure 5.3: Behavior of geometrical reduction factor of luminosity vs. β^* for constant normalized beam separation with indicated various operating points [72].

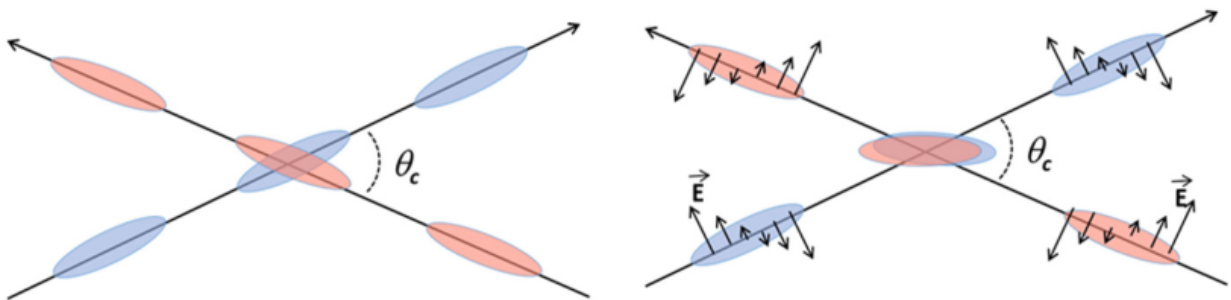


Figure 5.4: Effect of the crab cavity on the beam: left, bunch collision geometry without CC; right: with CC, small arrows indicate the transverse varying RF Electric field \vec{E} when crossing the CC [64].

5.3 ATLAS Phase-II upgrades

A detector upgrade is required to cope with up to 200 collisions per bunch crossing (the ATLAS environment is illustrated at Fig. 5.6) foreseen (in Run-3, peak is at around 50). Mean value, as shown in [5], given by

$$\bar{\mu} = \frac{\sigma_{inel} L}{n_b f_r} \quad (5.1)$$

where f_r (revolution frequency) is 11245 Hz, n_b (number of colliding bunches, design value) is 2808. σ_{inel} is inelastic cross-section, summary of which are shown on Fig. 5.7 as a function of center-of-mass energy. Flagship measurement of σ_{inel} done by TOTEM - resulting in $\sigma_{inel} = 74.7 \pm 1.7$ mb. Substituting numbers gives $\mu_{mean} \approx 140$ (still around factor three busier than Run-3). Increased occupancies in sub-detectors and higher radiation levels are challenging. All sub-detectors will be upgraded in one way or another together with TDAQ. Preparation is documented in six Technical Design Reports ⁴ : tracker[37], Liquid Argon[33] and Tile[40] calorimeters, muon[38], HGTD [46]

⁴most of them published in 2017

and TDAQ[39]. Moreover, a corresponding computing upgrade is required, described in [45]. A very short summary is given below.

5.3.1 Trigger and Data Acquisition

Let's look first at the system orchestrating other sub-detectors - Trigger and Data Acquisition (TDAQ), which, as before, will function in stages. The first stage is a Level-0 hardware trigger operating with a read-out rate of 1 MHz and a latency of 10 μ s. It relies on information from calorimeter and muon systems. It's possible that tracker information also will be used. Existing Calorimeter Feature Extractors (FEX) will be kept, but more will be installed (to process forward calorimeter data), and firmware will be updated. On the other side, the muon trigger processor would be replaced with upgraded modules to process information from Resistive Plate Chambers (RPC), Thin Gas Chambers (TGC), small-strip Thin Cap Chambers (sTGC), and MicroMegas (MM). The capabilities of the new Global Trigger to execute offline-like algorithms are superior to current Topological Processor. On the Level-0 trigger decision, detector data is transmitted to the second trigger stage, Event Filter (EF), though Front-End Link eXchange (FELIX, used by all sub-detectors). EF makes the final decision, and the events selected are transferred to permanent storage at 10 kHz. There are two options for base EF technology choice: custom electronics (Hardware Tracking for the Trigger) or the employment of commodity CPUs.

5.3.2 Inner Tracker

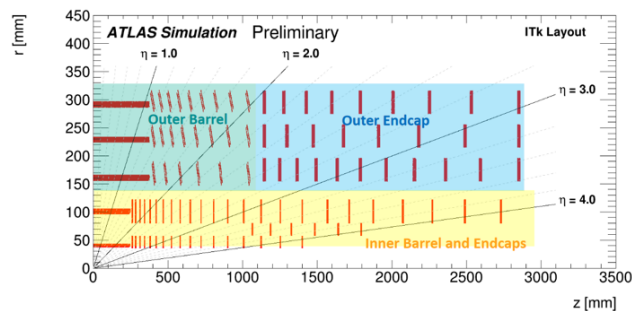


Figure 5.5: ITk layout

Tracker performance is crucial for the reconstruction and identification of charged particles, converted photons, and flavor tagging. The current design was made for factor four smaller track density (compared to HL-LHC). The SCT radiation tolerance is 700 fb^{-1} equivalent and 850 fb^{-1} for IBL. Instead, for HL-LHC, a new tracker system called ITk (Inner Tracker) will be installed. Layout is shown on Fig. 5.5. It will be an all-silicon detector - pixel sensors ⁵ closer to the beam, and strip sensors further away. One change compared to the current design is Pixel Detector $|\eta|$ coverage up to 4 - for better reconstruction of forward objects (e.g., tagging VBS jets). The Strip Detector covers $|\eta| < 2.7$. Different sensors would be used in different parts: 3D sensors and thin 100 μ m planar sensors in the inner sections and 150 μ m planar sensors elsewhere. The front-end electronics will be replaced. The connection between ASIC and sensors is done with bump-bonding. Assumed pixel cell size is $50 \times 50 \mu\text{m}^2$ everywhere except for the first layer of barrel where it would be $25 \times 100 \mu\text{m}^2$. In the innermost layers, shorter strips of 24.1 mm length will be used and further away from the beam strip length will be increased to 48.2 mm (because of lower occupancy). The granularity is increased, resulting in an average occupancy of 0.16% in the Pixel and 1.2% in the Strip detectors. The same 2T magnetic field will be used. The design target is providing 13 (9)

⁵there will be five layers and two most inner ones would be replaced due to unsustainable level of irradiation received

hits per track in the barrel (forward) region for transverse momentum above 1 GeV. The goal is to reduce to 50% the material budget before the calorimeter - to minimize losses from bremsstrahlung and hadronic interactions. Less material also helpful to suppress the photon conversion.

5.3.3 Calorimeters

Energy-absorbing layers of calorimeters, doesn't suffer from irradiation (e.g. Liquid Argon response is rather stable with respect to irradiation levels), and this part doesn't need to be changed - which is not true for electronics: front-end, back-end, and calibration. Moreover, some of the commercial components originally used are not available anymore. Also, the existing calorimeter readout structure is incompatible with the HL-LHC trigger (readout rate and latency). Therefore, all electronics will be replaced. New 1524 LAr Front-End Boards would process 128 signals from calorimeter cells: amplified signal is split into two overlapping linear gain scales, on which shaping is done. LAr front-end data is sent to 372 LAr Signal Processor modules via 31900 fibers, then to TDAQ. The new calibration system would inject (as now) directly into calorimeter cells and have better than 0.1% precision over a 16-bit dynamic range. Tile calorimeter would undergo mechanical structure re-organization - each module will be serviced by four "mini-drawers" for easier installation and maintenance of 12 PMTs and their (new) electronics.

5.3.4 Muon

For muon detectors, installation of a New Small Wheel (NSW) in the endcap was done already before Run-3. Its primary goal is the suppression of fake muon triggers in the forward region - as material in endcap toroids become activated, the big wheels of the Muon Spectrometer receive flux of neutrons, creating tracks that look like the tracks from the interaction region. Those "tracks" cannot be vetoed easily without NSW. Previous design doesn't have the necessary resolution in radial bending direction to match SW (Small Wheel) track to BW (Big Wheel) hit in TGC. NSW is based on precision sTGC (used for triggering) and MM (used for tracking, new technology for ATLAS that was not produced at this scale before). Just before Phase-II RPC, TGC and electronics will be upgraded. A new RPC will be installed in the inner barrel layer and will have an increased rate capability to provide better robustness and acceptance of the barrel muon trigger. Part of RPC chambers in $|\eta| < 0.8$ region of middle and outer barrel layers would be refurbished - goal being operation at reduced high voltage (but without efficiency loss). In the barrel-endcap transition region, TGC triplets would replace TGC doublets to provide finer readout granularity that, in turn, allows the implementation of more robust majority logic. Just like in the case of calorimeters, a significant fraction of on - and off-detector electronics will be upgraded to be compatible with HL-LHC trigger requirements.

5.3.5 High Granularity Timing Detector

One new forward sub-detector aiming at making precise timing measurements, HGTD, will be installed and will be considered separately in Sec. 5.5.

5.3.6 Computing

Finally, as no detector is functional without software operating it and processing data from it, challenges in that area must be overtaken. Challenges arise from both the amount of data (3000 - 4000 fb^{-1}) and its recording rate (10 kHz) - it has to be collected, stored, reconstructed, and analyzed. Moreover, Monte Carlo needs to be generated in similar numbers. ATLAS currently spends about 40% of CPU on detector simulation where there are two types: "full" (GEANT4) and "fast" (GEANT4 except for the calorimeter where the parametrized response model is used). Full simulation is about factor five CPU-expensive compared to fast. Studies are ongoing to extend to all parts of the detector, not only the calorimeter. Another big consumer of CPU could be ITk - ATLAS

initiated the ACTS [103] open-source project to develop the next generation tracking software in a common cross-experiment project, with the aim of using ACTS to achieve both CPU reduction and excellent physics performance. Athena, the main ATLAS framework, will rely more on multi-threading - ACTS is one of the examples. Derivations⁶ consume a lot of space, and there is a lot of overlap between different derivation formats - to avoid this and as preparation to HL-LHC, already in Run-3 ATLAS started to move to DAOD_PHYS (50KB/event) and DAOD_PHYSLITE (10KB/event) formats - the first one contains all of the variables needed to apply calibrations to reconstructed objects, and the second contains pre-calibrated reconstructed quantities, and in consequence, the variables needed to apply the calibrations do not need to be stored. A two-fold decrease in disk space is expected. In Run-4, mostly DAOD_PHYSLITE is expected to be used. Storage needs will grow together with the data accumulated - one of the ideas explored is staging AOD data from tape to disk only when it's required instead of permanent storage: it can halve the total AOD permanent volume but also would mean that processing would be less frequent. The backbones of ATLAS distributed data processing and management - Panda and Rucio will need to be scaled up to HL-LHC workloads and volumes.

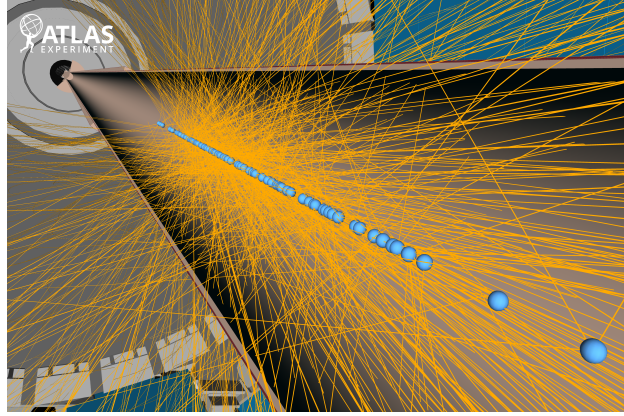


Figure 5.6: Simulated top-antitop pair production in ATLAS at 14 TeV and $\mu=200$. Blue balls are marking reconstructed primary vertices, and tracks from them are shown as orange lines [21]

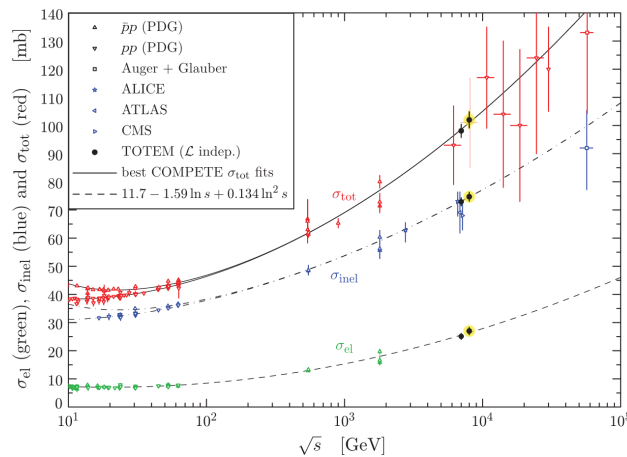


Figure 5.7: Compilation of the total (σ_{tot}), inelastic (σ_{inel}) and elastic (σ_{el}) cross-section measurements from various experiments [59]

⁶One of the data processing stages in ATLAS

5.4 Physics case - VBS

A rich physics program is foreseen at HL-LHC, but only VBS prospects would be mentioned for brevity. Statistical uncertainties in Run-2 VBS analyses are non-negligible. Measured fiducial cross-sections for electroweak production in $W^\pm W^\pm$ analysis [55] has 0.22 fb statistical and 0.19 fb systematic uncertainty. For the $W^\pm Z$ analysis [56] (ZZ [50], 4-lepton channel) they are 0.037 (0.12) fb and 0.059 (0.076) fb respectively. Therefore, VBS analyses will benefit from a larger dataset collected at HL-LHC. Also, forward upgrades like HGTD and extended $|\eta|$ tracker coverage should be beneficial, as the signature of VBS is two forward jets - in Run-2, all analyses relied on this.

Both ATLAS and CMS projected analysis sensitivities for measuring cross-sections of electroweak VBS in $W^\pm W^\pm$ [43], $W^\pm Z$ [42] and ZZ [41] processes. Early Run-2 data analysis strategy is used but with more data and different uncertainty scenarios are considered. If possible, ATLAS results will be considered for comparison with Run-2 section. Projections shown (and their CMS counterparts) became part of CERN Yellow Report [65] and Snowmass White Paper (American counterpart of ESPP) [22].

Leptonic decays are considered everywhere. Luminosities range roughly from Run-2 dataset size to 3000 fb^{-1} (nominal HL-LHC) to 8000 fb^{-1} (optimistic ATLAS and CMS combined). Semileptonic analysis projection was also done. However, analysis changed significantly since therefore and will not be considered here.

Apart from EW cross-section, it is interesting in VBS to measure the case where both bosons are longitudinally polarized. In the SM, this process is unitarized thanks to the presence of Higgs boson contributions and deviations from this would indicate the presence of BSM physics. Due to the cross-section being even smaller, this is a challenging but essential part of the HL-LHC physics program.

5.4.1 $W^\pm W^\pm$ analysis

Statistical uncertainty

For the EFT combination, dilepton mass distribution was fitted - projected distribution at 3000 fb^{-1} is shown on Fig. 5.8a. Statistical uncertainty on the cross-section as a function of luminosity is shown at the black curve of Fig. 5.8b; it starts from the value of Run-2 luminosity. With a nominal luminosity of 3000 fb^{-1} , it's expected to decrease by more than factor three and reach plateau.

$W_L^\pm W_L^\pm$ prospects

Two variables are seen to be sensitive to polarization - dijet azimuthal separation $\Delta\phi(j, j)$ where Longitudinal-Longitudinal (LL) distribution is seen to be shaper around larger value and leading p_T lepton p_T^{lep1} (LL distribution is larger around bigger value) - this is shown on Fig. 5.9. Expected significance of the observation of the $W_L^\pm W_L^\pm jj$ is shown on Fig. 5.10, where for baseline estimation rate uncertainties on the backgrounds are halved and in "optimistic" set of uncertainties where the uncertainties on the non-data-driven backgrounds are aggressively reduced. It can be seen that using any of the two sets of uncertainties with all sources uncertainties, after ten years of data-taking and combination with CMS ATLAS will only reach 1.8σ - therefore, just having more data will not solve the problem and various optimizations would be required.

5.4.2 ZZ analysis

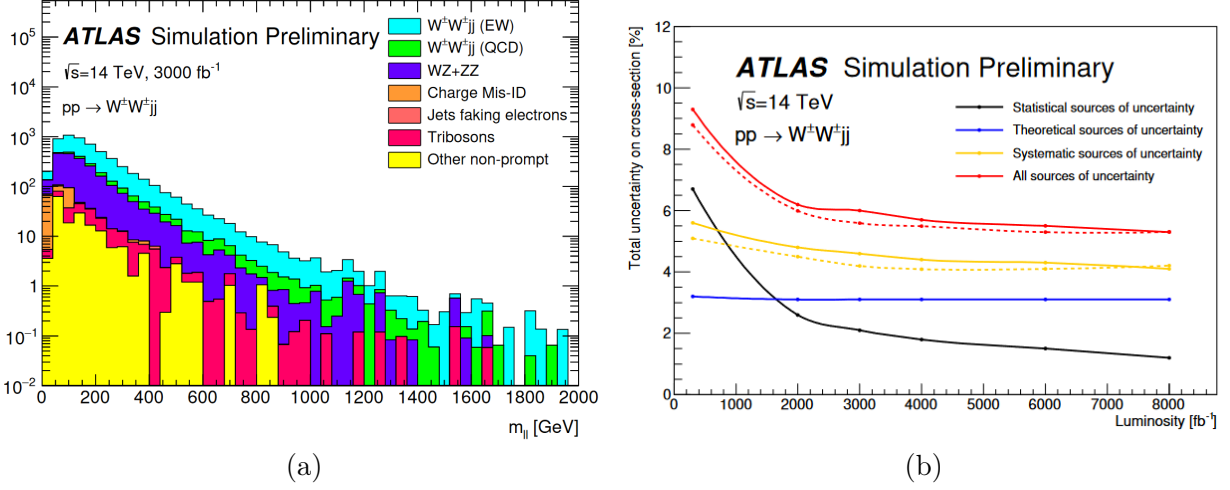


Figure 5.8: (a) Dilepton invariant mass distribution for events passing all selection criteria of the signal region, with event selection applied [43] (b) Projection of the statistical (black), theoretical (blue), systematic (yellow), and total (red) uncertainties on the cross-section as a function of integrated luminosity for the optimized event selection using the baseline scenario (solid lines).

The dashed lines show the systematic and total uncertainties on the cross-section for the optimistic scenario. The theoretical uncertainty refers only to the signal [43]

Statistical uncertainty

Extended tracker coverage helps with improving four-leptons detection efficiency. Main systematics for 4ℓ channel is theoretical modeling of the QCD-ZZjj background - for projection, three scenarios are considered: conservative 30% (relying on PDF4LHC recommendation), optimistic 5% (assuming enough data events from QCD enriched control region at the HL-LHC could be used to provide constraints on the theoretical modeling of QCD-ZZjj processes) and intermediate 10%. Distributions of two variables that were previously used for aQGC fit, m_{jj} and $m_{4\ell} \equiv m_{ZZ}$ are shown on Fig. 5.11 but now, with the HL-LHC expected dataset. Distributions obtained as

$$\sigma = \frac{N_{pseudo-data} - N_{QDC-ZZjj}}{L \times C_{EW-ZZjj}}, C_{EW-ZZjj} = \frac{N_{EW}^{detector}}{N_{EW}^{particle}} \quad (5.2)$$

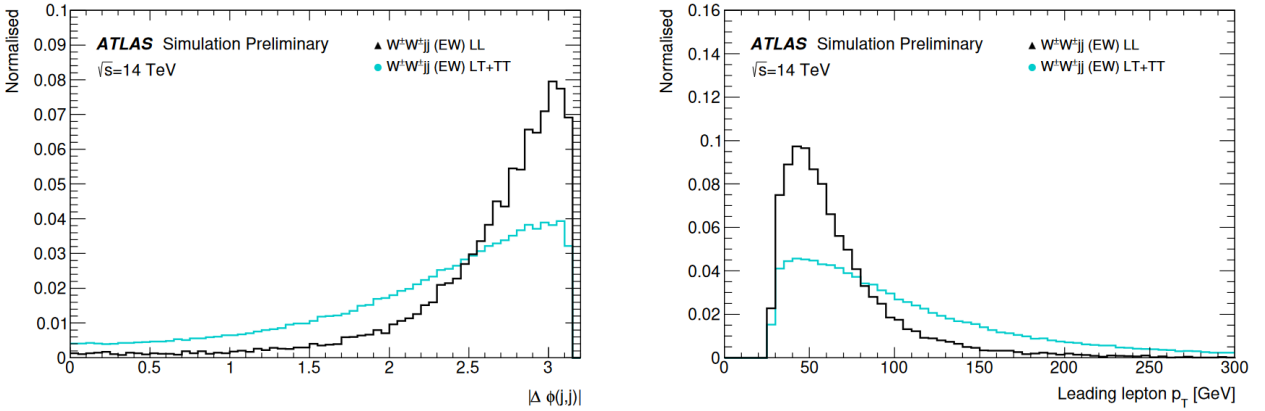


Figure 5.9: Shape comparisons for the dijet azimuthal separation $\Delta\phi(j, j)$ (left) and leading lepton p_T (right) distributions for the purely longitudinal (LL) and combined mixed and transverse (LT+TT) $W^\pm W^\pm jj$ events [43]

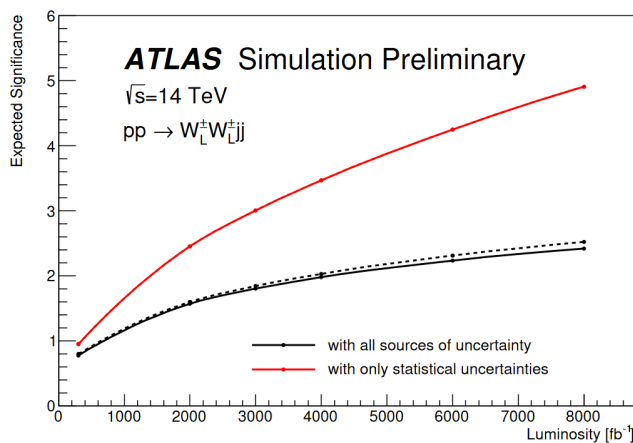


Figure 5.10: Projection of the expected significance of the observation of the $W_L^\pm W_L^\pm jj$ process as a function of integrated luminosity, for the optimized event selection using the baseline scenario, considering all the sources of uncertainty (black) or only the statistical uncertainty (red). The dashed lines show the expected significance for the optimistic uncertainty scenario in which modelling uncertainties are reduced by factor 2-3. [43]

where $N_{pseudo-data}$ is the expected number of data events with 3000 fb^{-1} luminosity, $N_{QCD-ZZjj}$ and $N_{EW-ZZjj}$ are the number of predicted events from QCD-ZZjj and EW-ZZjj processes, respectively. The $C_{EW-ZZjj}$ factor refers to the detector efficiency for EW-ZZjj processes, calculated as the number of selected signal events at the detector level ($N_{EW}^{detector}$), divided by a number of selected events at the particle level in the fiducial phase space ($N_{EW}^{particle}$). Uncertainty may significantly change (Fig. 5.11) in case conservative 30% theoretical uncertainty scenario is realized.

$Z_L Z_L$ prospects

ATLAS did not perform VBS $Z_L Z_L \rightarrow 4\ell$ sensitivity study, but it was done by CMS. The most sensitive variable is $\cos\theta^*$ where θ^* is the angle between the lepton direction in the Z decay rest frame and Z momentum in the laboratory frame. This variable, together with other polarization-sensitive variables and variables used for discrimination from QCD background, are combined into BDT used to separate $Z_L Z_L$ from $Z_T Z_T, Z_L Z_T$. It's assumed that ratio will be measured instead of absolute $Z_L Z_L$ cross-section - to cancel systematics. The result is shown on Fig. 5.12: just increasing the dataset is not enough for observation.

5.4.3 $W^\pm Z$ analysis

CMS projection will be shown as the study of uncertainty reduction with luminosity was done, unlike for ATLAS. Typical selections are made. MC samples with full detector simulation at 13 TeV are used, and for projection, they are scaled from to 14 TeV using SM predictions. Data-driven background estimates are used and scaled using an appropriate mixture of simulated events. The additional scaling factor is applied to increase pseudo-rapidity coverage at HL-LHC. With this at 3000 fb^{-1} , 2757 EW-WZjj events are expected, and 3486 of QCD-WZjj. Important backgrounds are tV/VVV (1374), non-prompt (1192), and $VV, Z\gamma$. To extract the EW signal, CMS used distribution projection of which is shown on Fig. 5.13a - it's a m_{jj} discriminant unrolled in bins of $\Delta R(j, j)$. Relative uncertainty on EW cross-section is shown on Fig. 5.13b for different integrated luminosity values - close to two-fold reduction is seen at 3000 fb^{-1} , where the plateau is also reached.

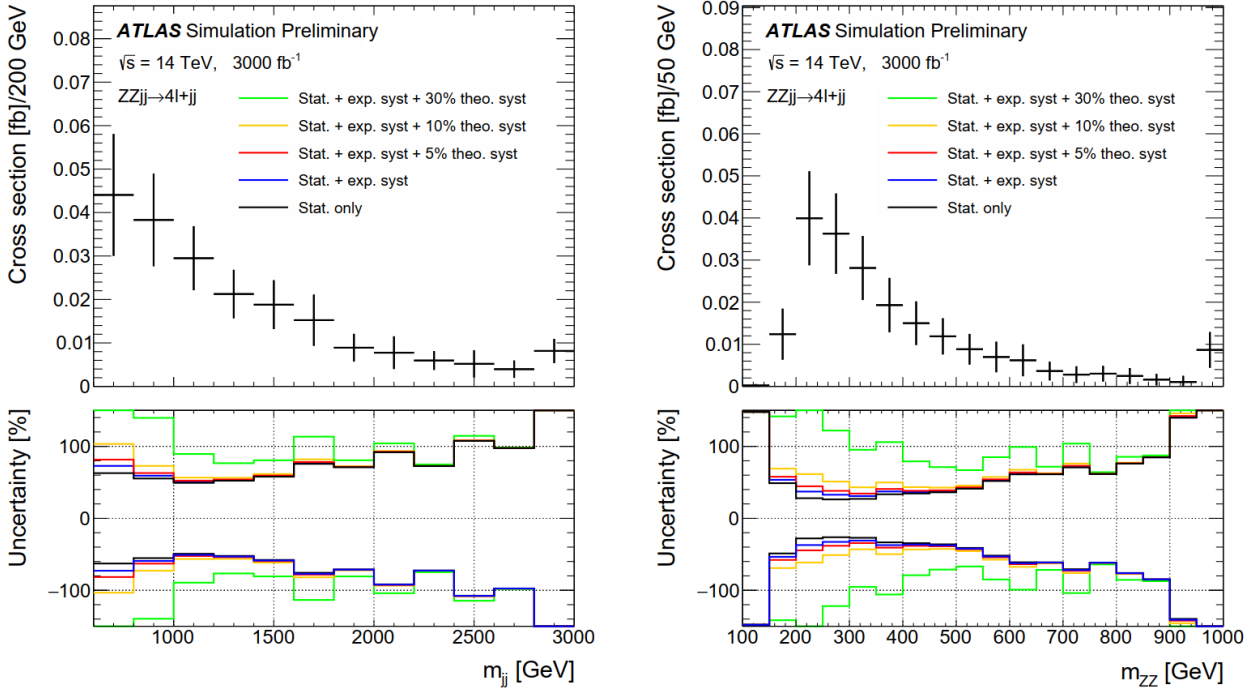


Figure 5.11: Expected differential cross sections at 14 TeV for the EW-ZZjj processes as a function of m_{jj} (left) and m_{ZZ} (right). Results are shown with different sizes of systematic uncertainties [41].

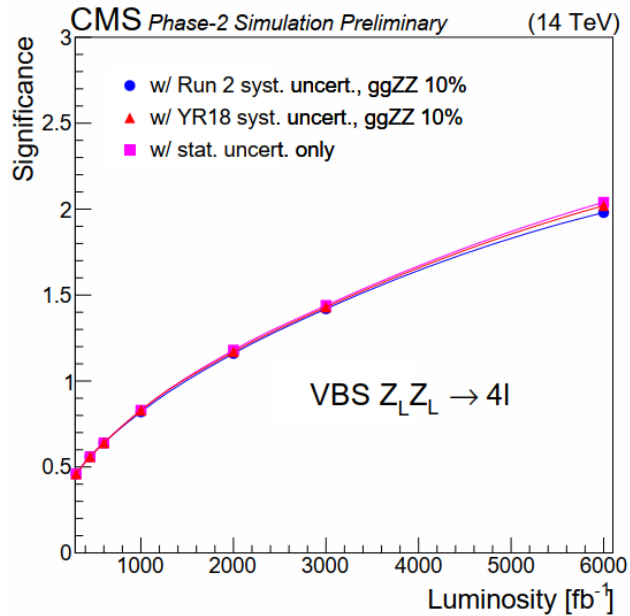


Figure 5.12: Expected significance for the VBS $Z_L Z_L$ fraction as a function of the integrated luminosity and for different systematic uncertainties scenario, as well as with only the statistical uncertainties [58].

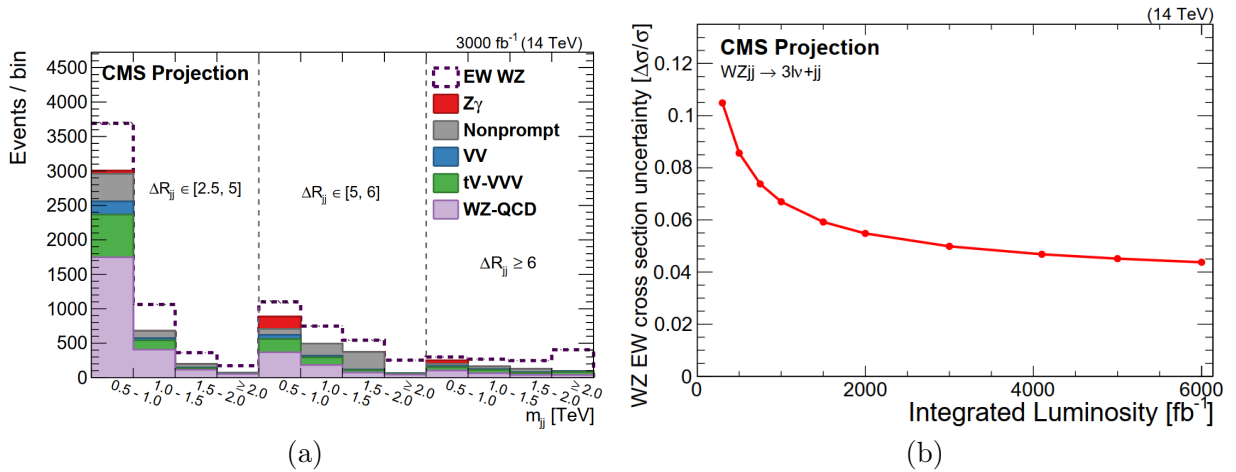


Figure 5.13: (a) The m_{jj} distributions in bins of $\Delta R(j, j)$ for 3000 fb^{-1} [57] (b) Expected relative uncertainty on cross-section as a function of integrated luminosity [57]

$W_L^\pm Z_L$ prospects

CMS (again) studied the double longitudinal process. The same distribution is fitted, shown in Fig. 5.14a - LL configuration in some bins differs from non-LL by up to 7%. The significance of EW-WZjj LL as a function of luminosity is shown on Fig. 5.14b - not reaching discovery value again, and we can see that systematic uncertainties are sizeable.

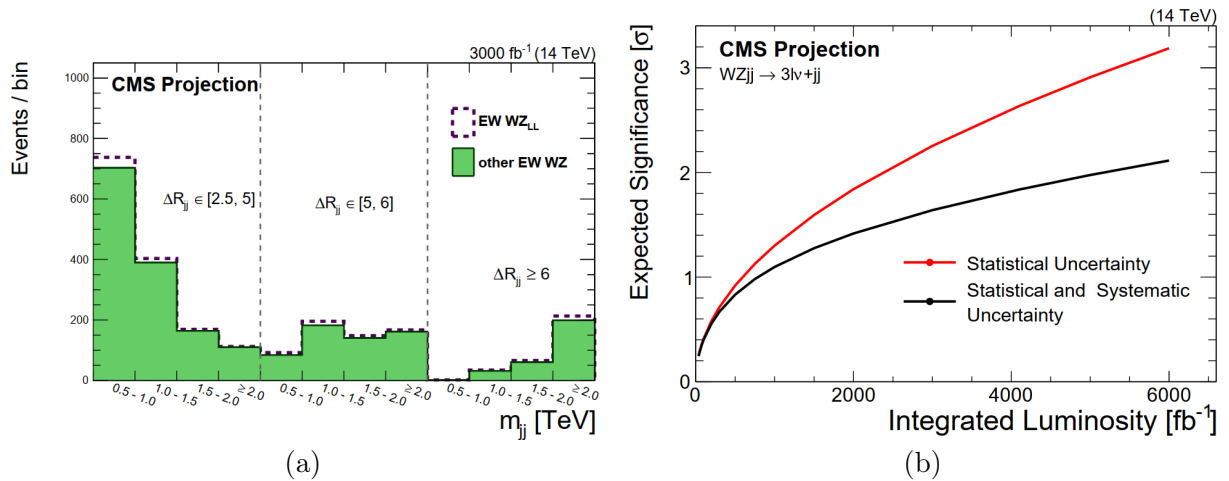


Figure 5.14: (a) The m_{jj} distributions in bins of $\Delta R(j, j)$ for 3000 fb^{-1} , for two cases: EW WZ doubly longitudinal and other polarization configurations [57] (b) Significance of the $W_L^\pm Z_L$ observation with and without systematic error [57]

5.5 HGTD

Increased pileup density (as what matters is not the number of p-p interactions but how far they are separated) poses a significant challenge for object reconstruction (and analysis using them) at HL-LHC. The luminous region will have an estimated Gaussian spread of 30–60 mm along the beam direction. Distributions comparing Run-2 conditions ($\bar{\mu} = 30$) and HL-LHC is shown

on Fig. 5.15a - a seven-fold increase of mean value is foreseen; the same applies for maximum value. How busy events can be is demonstrated on Fig. 5.15b in time and space planes using one top pair event - the prerequisite for the experiment to reconstruct physics objects is to distinguish HS vertex (marked with a red star) from all the others. Using spatial information from ITk (with a resolution of about 4,5 mm), one would select the x-axis slice, but there are still many vertices there. In addition, knowing the interaction time, displayed in the y-axis, would allow one to do another slice - significantly reducing the number of candidate events. Time should be measured more precisely than what is currently possible (for example, in LAr with resolution ≈ 1 ns). Therefore, a new sub-detector called High Granularity Timing Detector (HGTD) will be installed for this.

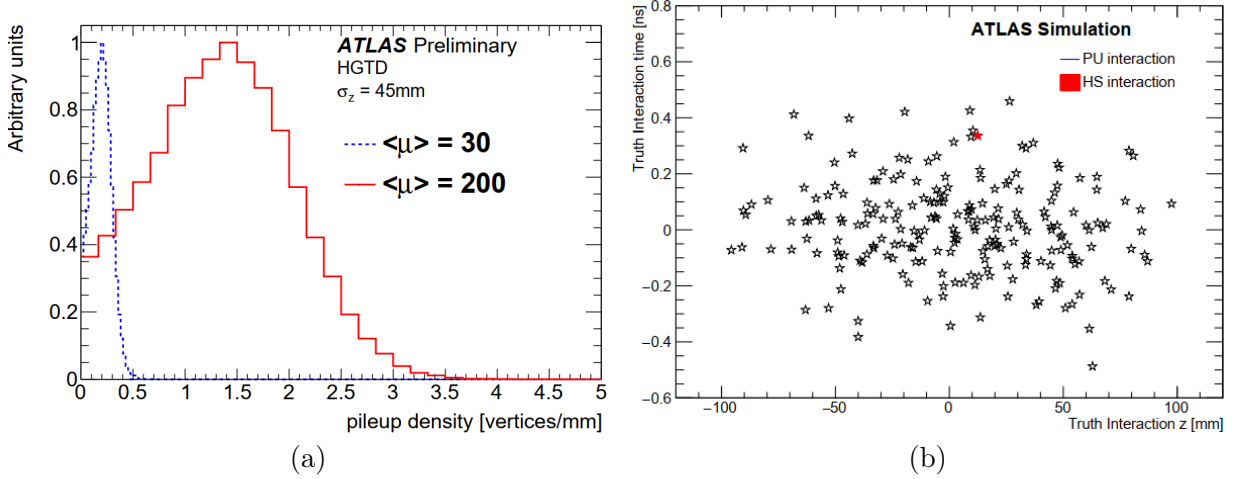


Figure 5.15: (a) Local pileup vertex densities at generator level for two values of $\bar{\mu}$: $\bar{\mu} = 30$ and $\bar{\mu} = 200$ [46] (b) Visualisation of the truth interactions in a single bunch crossing in the z-t plane, showing the simulated Hard Scatter (HS) tt event interaction (red) with pileup interactions superimposed (black) for $\bar{\mu} = 200$ [46]

5.5.1 Detector overview

HGTD will be installed in the forward region, outside of the ITk volume, and in front of the end-cap and forward calorimeters, illustrated in Fig. 5.16. HGTD will provide timestamp⁷ for tracks with $2.4 < |\eta| < 4$. Fig. 5.17 illustrates why having timing information only in this $|\eta|$ region is enough: for low momentum and high $|\eta|$ resolution of the determination of the track longitudinal impact parameter by the ITk grows significantly. Still, one wants it to be much smaller than the average inverse pileup density (will be $700 \mu\text{m}$ for the HL-LHC) for good identification of the primary vertex. For low $|\eta|$, spatial information from ITk alone is enough to separate vertices. Fig. 5.18 shows the benefit of using HGTD for pileup jet rejection in comparison with ITk-only reconstruction. The pileup jets rejection for $30 < p_T < 50$ GeV and $2.4 < |\eta| < 4.0$ is shown as a function of the efficiency for selecting hard-scatter jets. For example, for 85% efficiency, it can be seen that if we use the HGTD, the rejection is better by approximately a factor of 1.5.

The radial extend of the HGTD is from 110 mm to 1000 mm. It is divided into three active regions: $120 \text{ mm} < r < 230 \text{ mm}$, $230 \text{ mm} < r < 470 \text{ mm}$, and $470 \text{ mm} < r < 640 \text{ mm}$, which are visible on Fig. 5.16. Peripheral electronics occupy the fourth inactive region with $640 \text{ mm} < r < 1000 \text{ mm}$. Fig. 5.19a shows HGTD components: it consists of one hermetic vessel, two

⁷HGTD also will be used for bunch-by-bunch luminosity measurement. It will be a relative measurement to be used together with absolute measurement given by Van der Meer scan and combined with other relative measurements

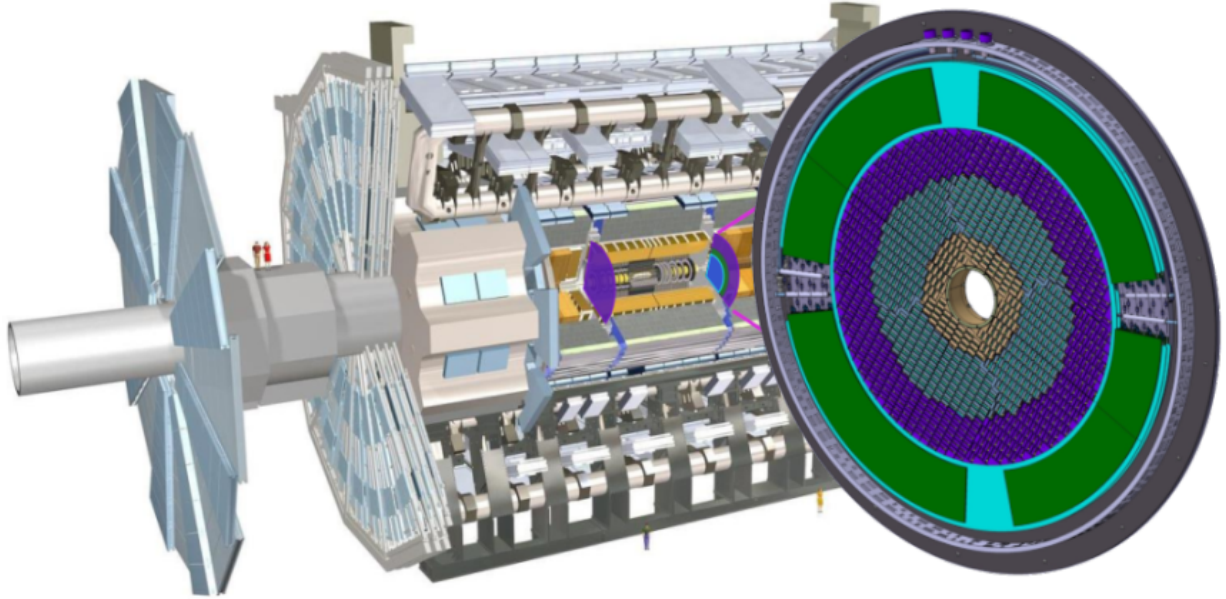


Figure 5.16: Position of the HGTD within the ATLAS Detector. The HGTD acceptance is defined as the surface covered by the HGTD between a radius of 120 mm and 640 mm at a position of $z = \pm 3.5$ m along the beamline, on both sides of the detector [46]

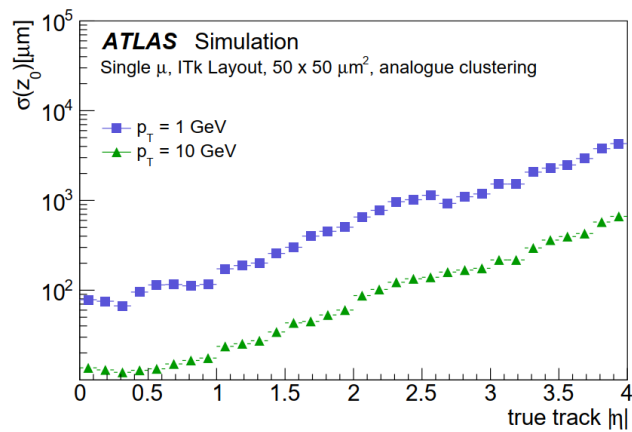


Figure 5.17: Resolution of the longitudinal track impact parameter, z_0 , as a function of true track $|\eta|$ for muons of $p_T = 1$ GeV and $p_T = 10$ GeV using ITk alone [46]

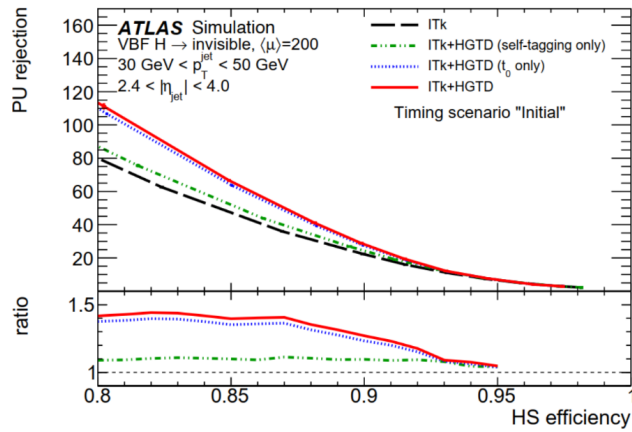


Figure 5.18: Pileup jet rejection (for jet with $30 < p_T < 50$ GeV) as a function of hard-scatter jet efficiency in the $2.4 < |\eta| < 4.0$ region at the beginning of the lifetime of the detector, VBF H to invisible sample, for the ITk-only and combined ITk + HGTD reconstruction. “ t_0 only” assumes knowledge of vertex time and comparison is done to it, while “self-tagging only” relies on consistency of hit times only [46]

instrumented double-sided layers (mounted on two cooling/support disks), and two moderator pieces placed inside and outside the hermetic vessel. Each cooling/support disk is physically separated into two half circles. Furthermore, the layers are rotated in opposite directions with respect to one another by 15° to 20° to maximize the hit efficiency and provide space for cooling pipes. Three different active regions have different overlaps between two sides of instrumented layers, which is illustrated in Fig. 5.19b. Regions closer to the beam have higher overlap to compensate for faster degradation (compared to outer regions) of resolution per hit and obtain less steep drop in resolution per track. The average number of hits per track is 2.6 (inner radial region), 2.4 (middle region), and 2.0 (outer region). The overall spacing and the overlap between modules are optimized to maintain a constant time resolution per track as a function of $|\eta|$.

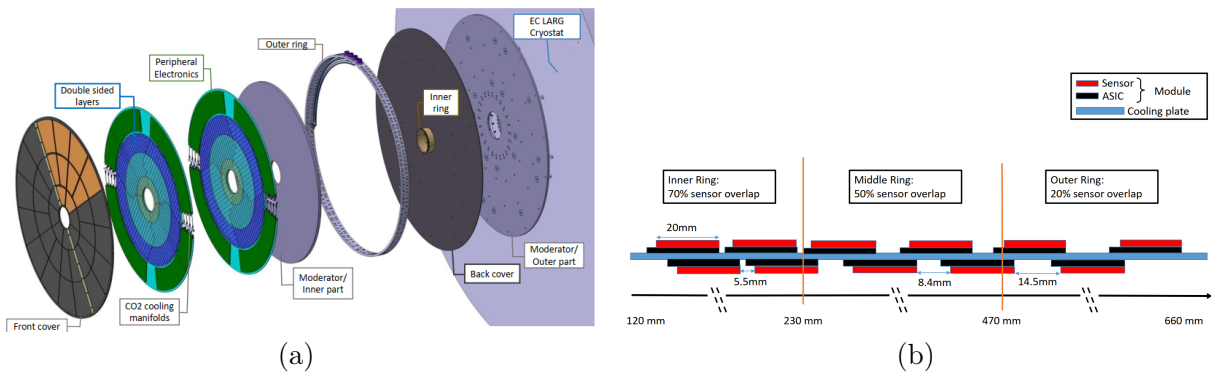


Figure 5.19: (a) Global view of the HGTD to be installed on each of two end-cap calorimeters. The various components are shown: hermetic vessel (front and rear covers, inner and outer rings), two instrumented double-sided layers (mounted in two cooling disks), two moderator pieces placed inside and outside the hermetic vessel [46] (b) The schematic drawing shows the overlap between the modules on the front and back of the cooling disk. There is a sensor overlap of 20% for $r > 470$ mm, 54% for $230 < r \leq 470$ mm and 70% for $r < 230$ mm [46]

HGTD should be able to maintain its outstanding performance in the extremely harsh irradiation conditions of the forward region for the entirety of the HL-LHC lifetime: it must survive a nominal neutron-equivalent fluence of 8.3×10^{15} neq/cm² (at the lowest radius of HGTD) and a total ionizing

dose of 7.5 MGy, that will be reached at the end of the HL-LHC. Low-Gain Avalanche Detector (LGAD, Si sensor chosen for HGTD that will be briefly described below) sensors cannot provide the required charge given this radiation damage. Therefore, the region closest to the beam radially, where the radiation damage is the highest, will be replaced three times. The middle layer will be replaced once. The outer layer will not be replaced.

The HGTD active area comprises $4 \times 2 \text{ cm}^2$ modules. Module consists of a two LGAD sensors each with size $1.3 \text{ mm} \times 1.3 \text{ mm}$, two read-out Application-Specific Integrated Circuits (ASIC), and a flex board that provides connection with flex cable. The flex cable is used to connect the module and the peripheral electronics.

Expected occupancy is shown on Fig. 5.20: rises for regions closer to the beam compared to the innermost layer, primarily caused by the increased probability of initiating showers due to hadronic interactions as more material is traversed. Dependency was obtained in minimum bias events with the highest expected pileup.

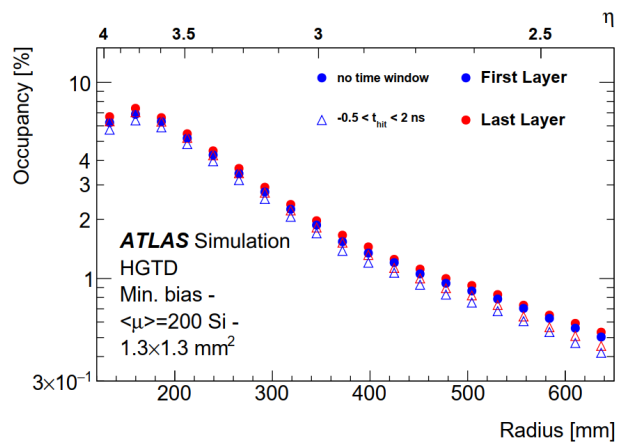


Figure 5.20: The occupancy per module as a function of the radius and $|\eta|$ for a pad size $1.3 \text{ mm} \times 1.3 \text{ mm}$ at a pileup of $\bar{\mu} = 200$. [46]

5.5.2 Sensor

Average time resolution per hit is required to be $\approx 35 \text{ ps}$ at the start of an operational lifetime and $\approx 70 \text{ ps}$ in the end. Components of time resolution will be considered later; for the time being, it's enough to say that to achieve such a resolution, the sensor cannot have a time resolution larger than per hit resolution. LGAD sensors are chosen to provide the needed radiation tolerance and excellent timing performance. The design is based on a traditional n-in-p silicon detector. The p-n junction is inversely polarized by an externally applied bias voltage, thus creating a large depletion region. When a charged particle crosses the sensor, it creates electron-hole pairs that, due to the applied electric field, drift in opposite directions toward the cathode and the anode, respectively. Unlike traditional sensors, LGAD has a highly doped p+ layer below the cathode. This modification causes a large increase of the electric field over a thin avalanche region, as shown in Fig. 5.21. In this region, the number of charge carriers will be multiplied. The total generated current is a sum of the currents induced by the movement of both primary and avalanche holes and electrons. It can be shown that the optimum gain for LGAD is 20. Fig. 5.23 shows the LGAD signal in comparison with the signal from a traditional sensor, where it can be seen that the LGAD signal has a bigger amplitude and longer pulse duration. As shown on Fig. 5.22, a time resolution smaller than 70 ps per hit (which is close to the required resolution) is achievable if the charge is above 4 fC . With increasing radiation damage, the charge will go below, which is why one needs to replace sensors during the HL-LHC phase.

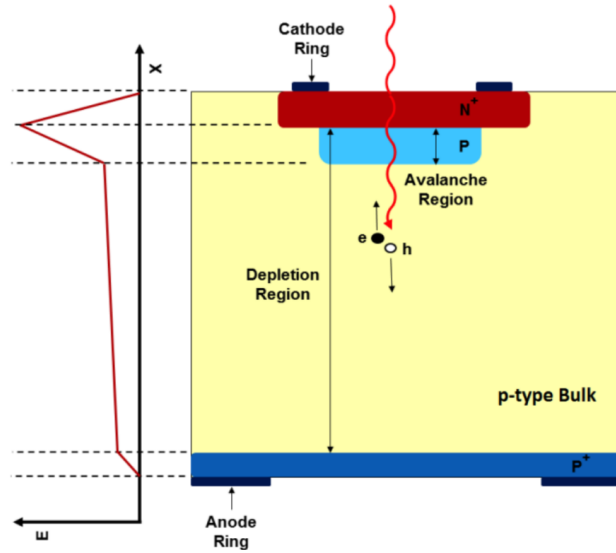


Figure 5.21: Schematic of LGAD electric field and layers [46]

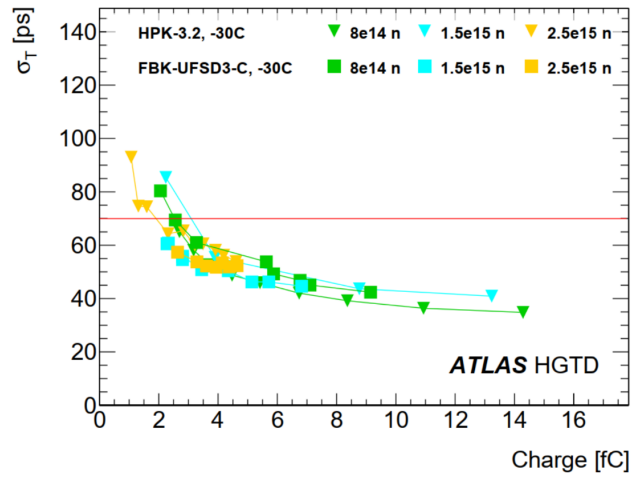


Figure 5.22: Time resolution as a function of the collected charge for neutron-irradiated LGADs from different manufacturers with a $50 \mu\text{m}$ active thickness [46]

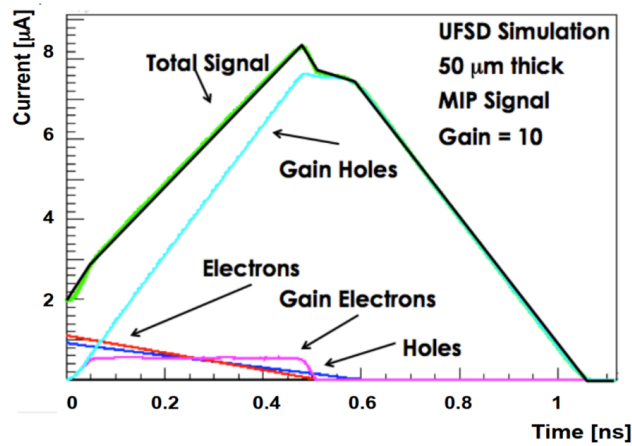


Figure 5.23: LGAD current signal and traditional sensor signal [46]

LGAD development reached a stage where irradiated sensors (alone, without ASIC) were tested with particles - results for key quantities are shown in Fig. 5.24 - all key requirements are reached, Those are carbon-enriched sensors, as it was seen to improve radiation hardness. The next step is to test those sensors together with ASIC .

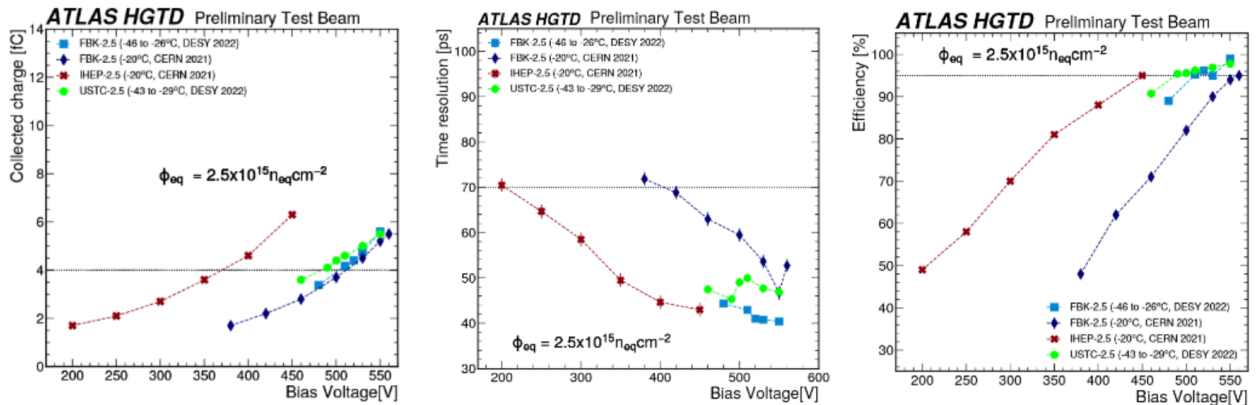


Figure 5.24: Performance of carbon-enriched irradiated LGAD in testbeam (left) collected charge depending on bias voltage (middle) time resolution depending on bias voltage (right) hit efficiency vs bias voltage [98]

5.5.3 Time resolution components

Average time resolution of 35 ps per hit (in the beginning of operation) is composed of contributions coming from sensor, read-out electronics, and clock

$$\sigma_{total}^2 = \sigma_L^2 + \sigma_{elec}^2 + \sigma_{clock}^2 \quad (5.3)$$

σ_L^2 arises because of the non-uniformity of the energy deposition process by an impinging charged particle in silicon. The local density of electron-hole pairs created along the trajectory is not the same in each event - this produces irregularities in the current signal (Landau noise). Also, the total number of electron holes will vary. With a chosen 50 μm thick LGAD sensor, the Landau term is approximately 25 ps. σ_{clock}^2 is the contribution from the reference clock: one measures the time of a hit with respect to the LHC clock, which should be precisely distributed to each of the channels. Imperfections of the clock distribution are estimated to give a contribution of 15 ps. σ_{elec}^2 in fact consists of three terms:

$$\sigma_{elec}^2 = \sigma_{TimeWalk}^2 + \sigma_{Jitter}^2 + \sigma_{TDC}^2 \quad (5.4)$$

σ_{TDC}^2 arises because one is doing a digitization of the time measurement with Time-to-Digital Converters (TDC) that have some finite non-zero binning. If bins are of equal size ΔT , the contribution is $\Delta T/\sqrt{12}$. In HGTD, the read-out ASIC will minimize this term by using a fine $\approx 20ps$ binning. $\sigma_{TimeWalk}^2$ arises because of the unavoidable effect that more significant signals cross a given threshold earlier than smaller ones. This is illustrated on Fig. 5.25. Results of time measurements have a dependence on the amplitude of the signal. Assuming a linear signal, it can be shown that

$$\sigma_{TimeWalk} \propto \left(\frac{V_{threshold}}{S/t_{rise}} \right)_{RMS} \quad (5.5)$$

Where $V_{threshold}$ is the threshold value, S is signal amplitude, and t_{rise} is the signal rise time. Therefore, the time-walk is minimized by systems with a high slew rate. Also, time-walk can be corrected using Time over Threshold (TOT) information - the HGTD front-end ASIC is designed to make the TOT information available.

σ_{Jitter}^2 represents the uncertainty in the time measurement due to the presence of noise in the signal, which is illustrated on Fig. 5.25. The discriminator will be fired later or earlier because of this noise. Again, assuming constant slope and denoting system noise as N , one can write

$$\sigma_{Jitter} = \frac{N}{dV/dT} \sim \frac{t_{rise}}{S/N} \quad (5.6)$$

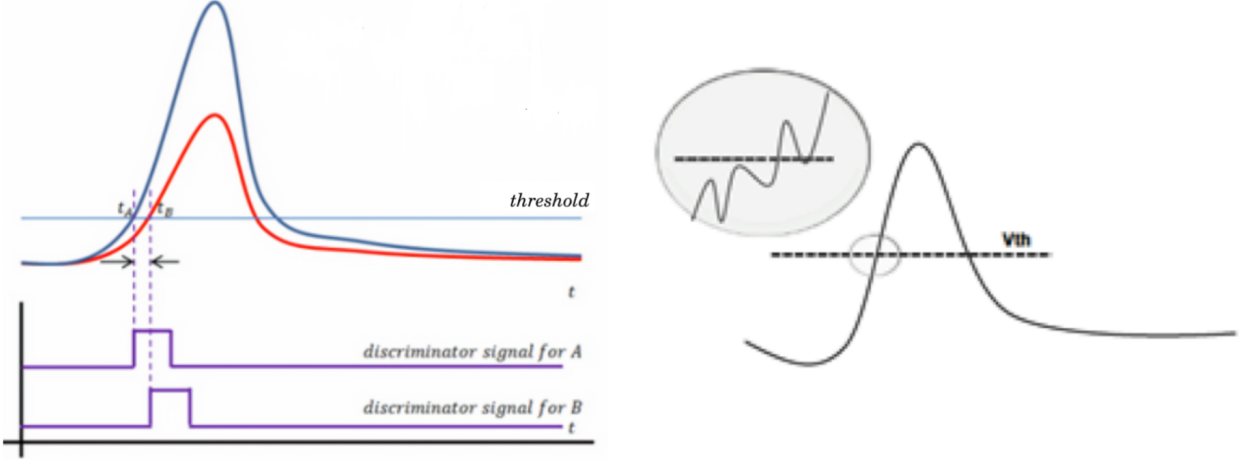


Figure 5.25: (left) Time-walk: signals of different amplitude cross a fixed threshold at different times (right) Jitter: noise crossing the threshold value

5.5.4 Front-end electronics

ATLAS LGAD Timing Read-Out Chip (ALTIROC) is a front-end ASIC for the HGTD. The read-out electronics timing performance must be comparable to benefit fully from the LGAD timing performance. Requirements for ALTIROC are summarized below.

Be able to process the 4 fC charge and therefore, the minimum threshold should be 2 fC . The cross-talk between channels should be kept below 5% for such a low threshold. The dynamic range should be 4 - 50 fC . Jitter should be < 25 ps at 10 fC and < 70 ps at 4 fC. σ_{TDC} is below 10 ps. $\sigma_{TimeWalk}$ should be also below 10 ps. Single-pad noise should be below 0.5 fC . The clock phase adjustment precision should be below 100 ps to properly center the 2.5 ns measuring window at the bunch-crossing. The chip should survive the HGTD radiation levels within the replacement plan foreseen. Conversion time should be below 25 ns to finish before the next proton-proton collision begins. Capability of handling up to $5\mu A$ leakage current from the sensor without degrading the ASIC performance. Average power dissipation should be below 1.2 W per ASIC because one doesn't have a lot of space for cooling. Have the necessary memory to save data during L0/L1 trigger latency.

The chip will have a size of 20 mm \times 22 mm with 225 channels organized in a 15 \times 15 matrix. Fig. 5.26 shows the general architecture of a chip with a channel matrix organized along columns for the read-out and with the common digital electronics at the bottom. The schematic of one electronics channel is displayed on top of the channels matrix.

Single-channel electronics is the same in all 225 channels: digital and analog block. The digital front-end block is responsible for identifying and storing the hits (including the separate block for processing the luminosity information). Analog block, shown on Fig. 5.28 : preamplifier, discriminator, and two TDCs. The sensor signal is amplified using a preamplifier. Two types of preamp were initially studied: Voltage Preamplifier (VPA) and Trans Impedance (TZ). The preamplifier is followed by a fast discriminator, which produces an output signal when the input signal goes above a certain threshold. Time of start of the signal, Time of Arrival (TOA, illustrated on Fig. 5.27), is

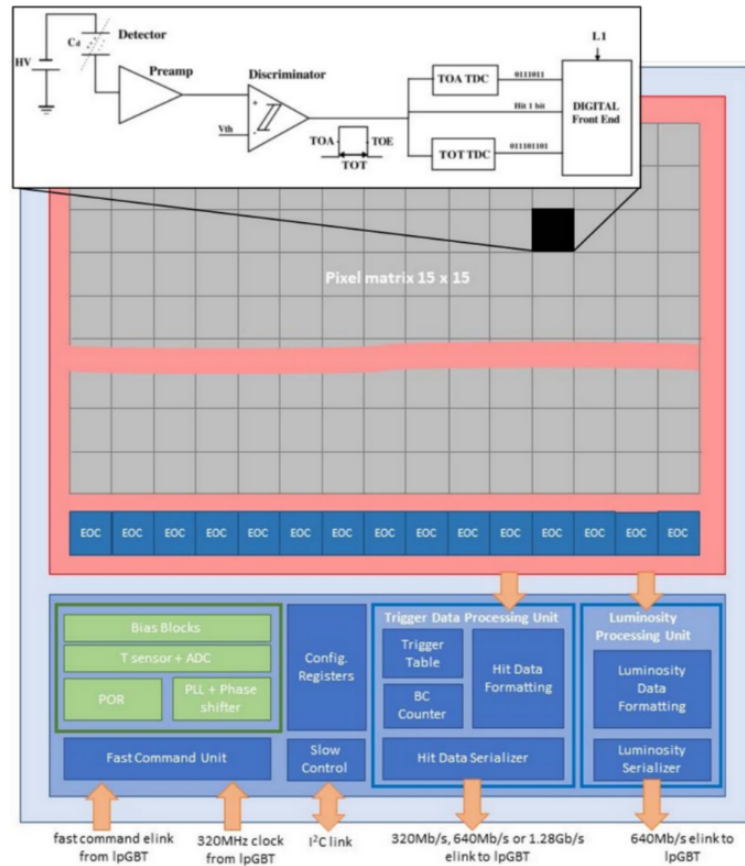


Figure 5.26: Global architecture of the ALTIROC ASIC. The schematic of one Front End electronics channel is displayed on top of the channels matrix, with the preamplifier followed by a discriminator, two TDCs, and a digital front-end block [46]

digitized with a dedicated 7-bit TDC . The TOA measurement is done in a 2.5 ns window centered on the bunch crossing. Since the expected time dispersion of the hits is around 300 ps, this window allows for the full collection of hits. The TOA time-walk problem is solved by using Time-over-Threshold (TOT, illustrated on Fig. 5.27) information since TOT is a proxy for signal amplitude. TOT uses the second 9-bit TDC.

There are leading and falling-edge discriminators (only used for Time of End measurement in TOT). A leading-edge discriminator is connected to the preamplifier's output and compares the preamp signal to a threshold voltage. `en_hyst` (see Fig. 5.28) is a part of the hysteresis system integrated to avoid re-triggering on the noise of the falling edge of discriminator - the principle is illustrated in Fig. 5.29: As soon as there is a discriminator pulse, the threshold voltage of the discriminator is automatically slightly decreased. This is done by adding a small current ($\approx 1\mu A$) in one of the branches of the discriminator input differential pair. When the discriminator output goes back to 0, the threshold returns to its initial value.

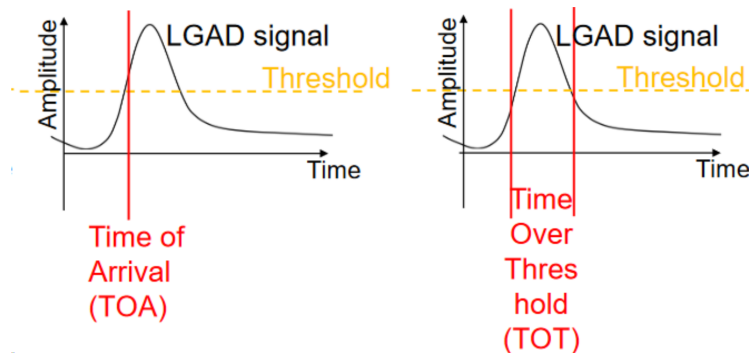


Figure 5.27: Illustration of (left) TOA and (right) TOT

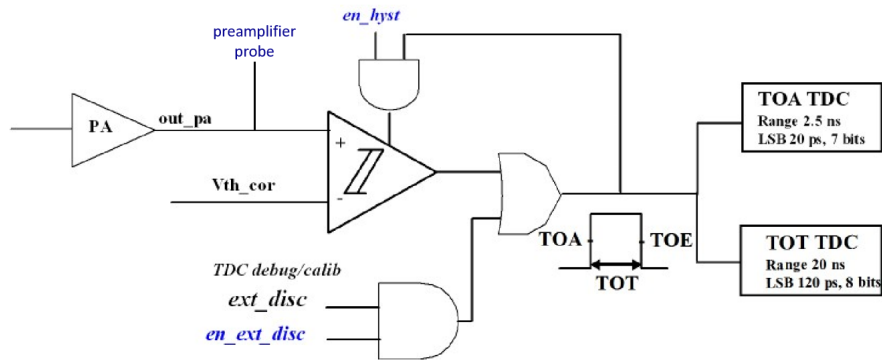


Figure 5.28: ALTIROC single pixel analog part. Adapted from [73]

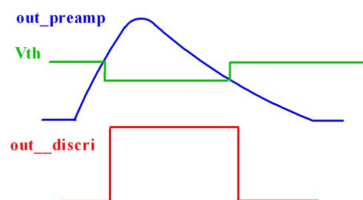


Figure 5.29: Hysteresis principle [73]

In practice, VPA and TZ preamplifiers are different by fall time of signal - it's about factor 5 longer for VPA . A comparison of waveforms is shown on Fig. 5.30. Therefore, one might think that

having a longer signal is better for accurate amplitude proxy measurement (TOT) and timewalk correction. As will be shown, the VPA signal is too long because it picks up unwanted coupling that breaks the proportionality between amplitude and TOT value - unlike TZ .

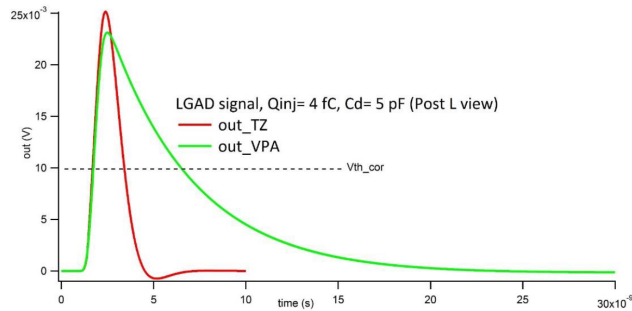


Figure 5.30: VPA and TZ output waveforms [73]

End-of-column logic reads the data along each of the 15 columns and transfers data to the digital part. The digital part is common to all channels. It prepares the received data for transmission to the peripheral electronics and transmits data. It also contains a phase-locked loop, a phase shifter, and a command decoder. The event timing data from the ASIC will be sent to the peripheral electronics for further processing when the trigger signal arrives at the ASIC. The luminosity information is the number of hits per ASIC and is sent at every bunch - for a fraction of ASICs (to save bandwidth). ALTIROC will measure the sum of hits within two different time windows - where smaller window (of size 3.125 ns) is inside of the larger window (of adjustable size $N \times 3.125$ ns). Larger window allows to get information about the background.

5.5.5 ASIC characterization aspects

The work on ALTIROC R&D started in 2016. Since there, multiple prototype versions been produced, latest being ALTIROC-A (2024) - summary is given below.

Prototype versions

| Version | Production Year | Description |
|-------------|-----------------|--|
| ALTIROC0 | 2017 | 2x2 pixel array only preamplifier and discriminator stages of the analog part |
| ALTIROC1v1 | 2018 | 5x5 pixel array TDC and channel memory blocks included |
| ALTIROC1v2 | 2019 | Improved TDC - both VPA and TZ included |
| ALTIROC1v3 | 2020 | VPA only TDC |
| ALTIROC1v3b | 2021 | TZ TDC brought back |
| ALTIROC2 | 2021 | First prototype with 225 channels; VPA and TZ TDCs |
| ALTIROC3 | 2023 | Radiation hard full-scale prototype; TZ-only |
| ALTIROC-A | 2024 | Pre-production chip |

Table 5.1: Brief recap of ALTIROC prototypes

TDC discretization step

TOA and TOT are measured in separate TDCs. Each of them has their own discretization step, also called Least Significant Bit (LSB). LSB is a conversion factor with units of time; in our case, picoseconds typically are convenient:

$$\begin{cases} TOA[ps] = LSB_{TOA}[ps] \times TOA[binary] \\ TOT[ps] = LSB_{TOT}[ps] \times TOT[binary] \end{cases} \quad (5.7)$$

Architecture of the TOA TDC relies on the Vernier delay line (as the target LSB is smaller than the gate-propagation delay in the 130 nm technology) and illustrated on Fig. 5.31. The START pulse corresponds to the rising edge of the discriminator. It comes first and initializes the TDC operation. The STOP pulse corresponds to the first rising edge of the 40 MHz TDC clock (The clock can be shifted from the rising edge of the external discriminator signal, and this is used routinely for calibration) that follows the START signal (notice TOA is measured concerning the falling edge of the current cycle), with a delay that represents the time interval to be digitalized. At each tap of the Delay Line, the STOP signal catches up to the START signal by the difference of the propagation delays of cells in Slow and Fast branches of the delay line: i.e., $140ps - 120ps = 20ps$, and this is what gives the TOA TDC LSB. The number of cells necessary for the STOP signal to surpass the START signal represents the result of TDC conversion. TDC range is equal to $128 \times TOALSB \approx 128 \times 20 ps = 2.56 ns$.

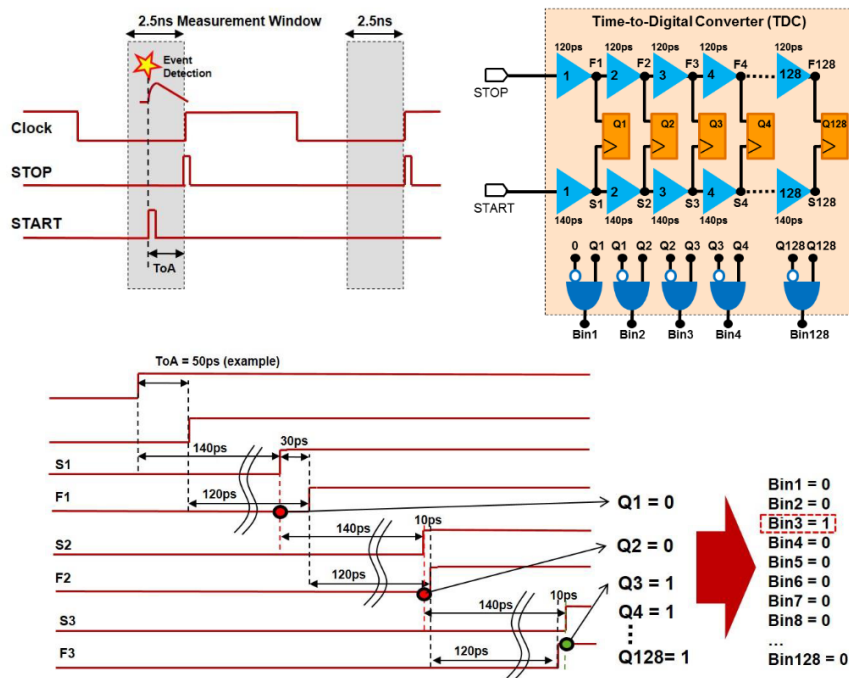


Figure 5.31: TDC for TOA measurement: principle and delay Vernier line [73]

ALTIROC1 and ALTIROC3, ALTIROC-A TOT TDC have two LSBs: coarse and fine because digitization is done in two steps. In step 1, coarse delay line with $\approx 160 ps$ LSB. After that, the signal goes to Vernier line similar to TOA TDC but now with LSB of $\approx 40ps$.

TDC Differential and Integral Non-linearity

Differential Non-linearity (DNL) is a measure of the variation in the step size of the converter. It quantifies the deviation of the actual step size between adjacent digital codes from the ideal step

size. DNL is expressed in terms of LSB. Ideally, each step in the TDC should correspond to one LSB (in case of TOA - 20ps), but DNL measures the deviation from this ideal (in practice, the average is taken), for code i (0-127 for TOA) according to

$$DNL_i = \frac{LSB(ps)_i - LSB(ps)_{average}}{LSB(ps)_{average}} \quad (5.8)$$

Integral Non-linearity (INL) is used to characterize the deviation of the actual transfer function of the TDC from the ideal transfer function. Ideally, for a TDC, each step in the digital output code should correspond precisely to a consistent time interval. However, due to imperfections in the circuitry (true for Vernier architecture) and manufacturing variations, the actual transfer function may deviate from the ideal. Integral Non-linearity is quantified by measuring the cumulative deviation of the actual transfer function from the ideal one over the entire range of input time intervals. INL is often expressed in terms of LSB:

$$INL_i = \frac{\sum_0^i LSB_i(ps)_i - center(ps)_i}{LSB(ps)_{average}} \quad (5.9)$$

Calibration systems

Coming back to Fig. 5.28, `ext_disc` block is visible - responsible for external discriminator signal delivered by the command pulse generator module located in the digital periphery or from the I/O PAD. External discriminator signals can be injected into TDC to simulate a discriminator pulse instead of using the discriminator output of the pixel. In that case, the discriminator must be bypassed/ switched off. Alternatively, the threshold value can be set to a high value to prevent the discriminator from being triggered. The width of the external discriminator signal is tunable.

Another way of calibration is using an internal pulser, which is common to all channels. The amplitude of the resulting voltage step is equal to $V_{step} = -R \times I_{DAC}$, where I_{DAC} is selected by the user, and it flows into $R=50K$ Ohm resistor. Amplitude is sent to the selected internal C_{test} capacitor (200 fF in ALTIROC1) of each channel, simulating an input charge $Q_{inj} = C_{test} \times V_{step}$. In that way, whole analog chain is involved, not just the TDC, as in the case of an external trigger.

Preamplifier probe

Checking preamplifier output is possible, as illustrated on Fig. 5.28. This is the best estimate of what is going into the ASIC after the preamplifier, and this signal is typically digitized during testbeams to be later used for timewalk correction. The preamplifier probe can be enabled only for one pixel at a time.

Occupancy

For LSB calibration it will be important how many pixels are injected. It only makes sense to do the calibration within the range of expected occupancy - shown on Fig. 5.20, where it can be seen that it can be as high as 10%.



6 - ALTIROC1 testbeam

The first results with ALTIROC1 in testbeam were published in [16], preceded by ALTIROC0 paper [17]. This section shows a more detailed analysis of the ALTIROC1 performance.

6.1 Campaign overview

ALTIROC1 testbeam measurements were performed in October 2021 with the ASIC bump-bonded to the LGAD (this object is called hybrid later in the text).

The goal of this testbeam was to determine the hybrid performance limit (time resolution of a single pixel) at the beginning of HGTD operation (before some of the sensors will be replaced) meaning before any irradiation as a result of which the deposit charge by a MIP will be decreased. The LGAD used is HPK2 W42 5×5-pad sensor produced by Hamamatsu Photonics; it is a second sensor prototype version from HPK [74] production focused on the research and development for the ATLAS and CMS timing detectors. The hybrid was exposed to a 120 GeV pion beam at CERN SPS (North Area, H6B beamline).

The testbeam setup is shown on Fig. 6.1. It consists of

- An ASIC+LGAD hybrid (the device we’re testing) mounted on a custom ASIC readout board - shown on Fig. 6.3, mounted on movable stage
- An FPGA board (not marked on the picture) used for controlling the chip and receiving the data from it and the FPGA-ASIC interface board (not marked on the picture), used to reduce the noise contributions of various powering and digital signals to the ASIC
- Two Cherenkov counters consisting of a 6×6 mm² quartz bar coupled to a 5×5 mm² Silicon photomultiplier (SiPM) is used for timing reference. Two are needed to extract the time resolution of the hybrid
- A Lecroy oscilloscope with a sampling rate of 20 GSamples/s and a bandwidth of 2.5 GHz, used to record ASIC preamplifier probe pulse, 40 MHz clock, and SiPMs
- EUDET telescope [82] (only used for the alignment) based on six MIMOSA pixel planes, combined with an FE-I4 [85] readout module (chip-based)
- A programmable Trigger Logic Unit (TLU) [60] which handles the trigger logic
- Power supplies
- Several computers to control the setup remotely and store the recorded data

A trigger was issued by ALTIROC1 when a hit was recorded, initiating the data acquisition of the oscilloscope. While the digital data acquisition was done continuously, the oscilloscope buffered the data until its memory was full. At this point, it was necessary to pause the data acquisition and transmit the oscilloscope data. Therefore, a “busy“ logic was implemented in the FPGA to stop the ASIC acquisition while the oscilloscope was read out. A common event number provided a unique mapping between the two data streams.

The testbeam period and equipment were shared between the hybrid tests and standalone LGAD sensor measurements (with custom non-HGTD readout) so that only at the end of the period hybrid data at cold were recorded.

The challenge with using SiPMs for reference was that their performance degrades significantly with beam irradiation as shown on Fig. 6.2. The vertical lines show the start of the dedicated periods of data recorded and used in analysis (Table 6.1). The SiPM2 shows worse degradation with more than 100 ps resolution during the first week of data taking, so it was decided to replace it with a single pad reference LGAD (LGA35) of size $1.1 \times 1.1 \text{ mm}^2$ after day 11. This sensor, readout by a custom electronics, had been used in measurement many times and was expected to have a time resolution of about 30 ps. Meanwhile, during the low-temperature data taking, the resolution of SiPM1 also reached 100 ps and special care had to be taken to extract results - low-temperature results will not be shown.

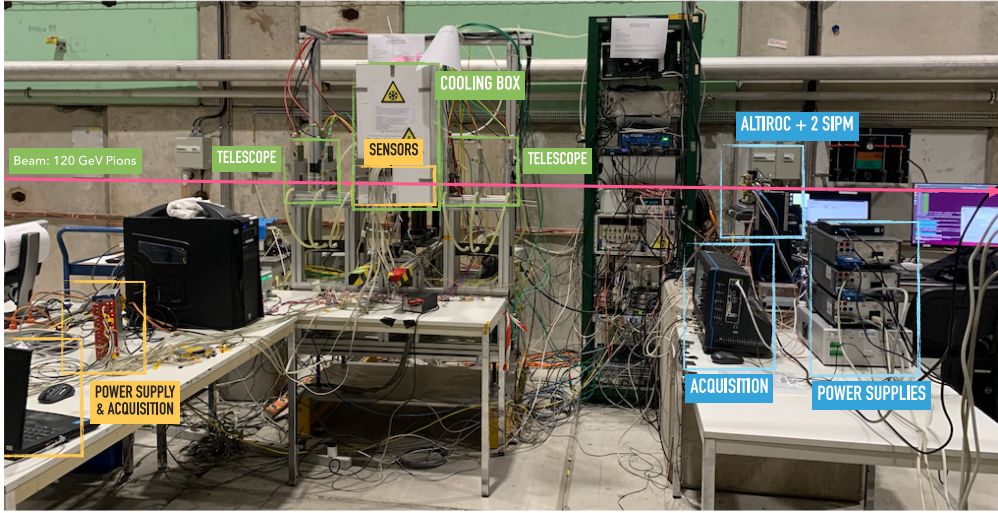


Figure 6.1: ALTIROC1+LGAD hybrid testbeam setup at CERN SPS. Not marked on the picture: FPGA, FPGA-ASIC interface board, Trigger Logic Unit[61].

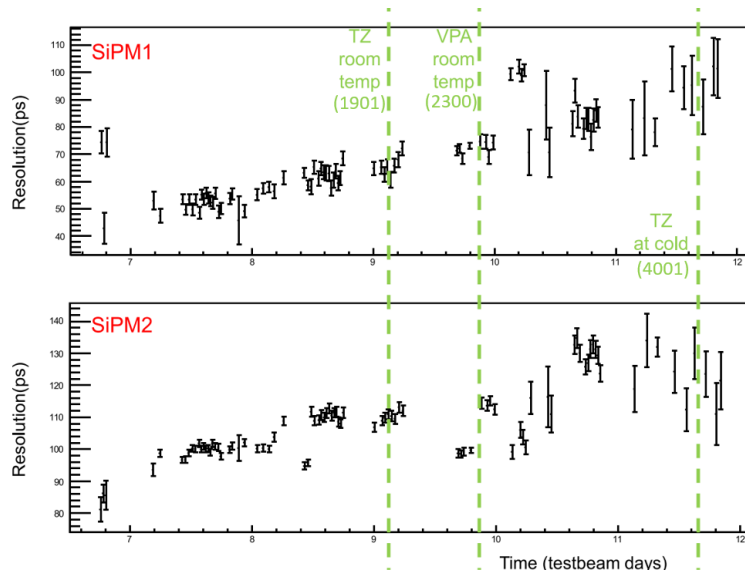


Figure 6.2: Degradation of reference SiPM time resolution during testbeam. The green vertical line shows the start of the data-taking periods for batches from Table 6.1. Resolution against testbeam days shown for (top) quartz+SiPM1 system (bottom) quartz+SiPM2 system

In this chapter, the results obtained at room temperature will be presented. Within two weeks, the total number of events recorded in various configurations is ≈ 18 million. At the time of this

| Batch number | num events | channel activated | preamp type | temperature | reference devices |
|--------------|--------------|-------------------|-------------|-------------|-------------------|
| 1901 | 1.86 million | 11 | TZ | room | SiPM1+SiPM2 |
| 2300 | 0.68 million | 15 | VPA | room | SiPM1+SiPM2 |

Table 6.1: Summary of data-taking conditions and parameters used to collect the data used for results presented in this chapter

testbeam, the preamplifier choice (TZ or VPA) was not made, so the data were taken with both. A run is the smallest data block taken with the same parameters (ASIC threshold, bias voltage, preamplifier probe output of which pixel is ON). The size of a run is typically taken around 100000 events (total across all pixels in the beam) - not too small (restart is done by shifter and humans tend to make mistakes while repeating similar operation many times, also restart takes time and doing this too often leads to larger fraction of beam time left unrecorded) but also not too large (simpler to deal with smaller files overall, particularly reject runs which ended up being bad for whatever reason). Runs are grouped into batches (unique identifier of configuration). The description of batches used in this chapter is given in Table 6.1. For all these runs, a preamplifier probe was always ON, and the sensor bias voltage was 265 V to have the maximal charge (about 15 fC) while staying safe with respect to the breakdown voltage. Finally, the ASIC discriminator threshold was set to about 5 fC, low enough to guarantee a good hit detection efficiency.

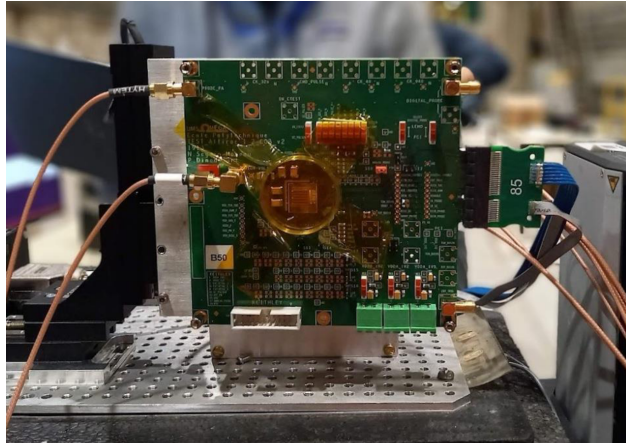


Figure 6.3: ALTIROC1+LGAD hybrid mounted on dedicated ASIC read-out board. The board is mounted on a movable stage.

6.2 Method of time resolution extraction

Having three devices (two reference SiPMs and ASIC+LGAD hybrid), we can extract the time resolution of each ($\sigma_0 \equiv \sigma_{SiPM1}, \sigma_1 \equiv \sigma_{SiPM2}, \sigma_2 \equiv \sigma_{hybrid}$) by assuming no correlation between each measurement and solving the 3x3 system shown in Eq. 6.1.

$$\begin{cases} \sigma_{\Delta T01} = \sigma_0 \oplus \sigma_1 \\ \sigma_{\Delta T02} = \sigma_0 \oplus \sigma_2 \\ \sigma_{\Delta T12} = \sigma_1 \oplus \sigma_2 \end{cases} \quad (6.1)$$

The main interest is σ_{hybrid} . However, knowing reference $\sigma_{SiPM1}, \sigma_{SiPM2}$ is also helpful for debugging, especially if it gets much larger than the target resolution σ_{hybrid} , then results are not

accurate. On the Left Hand Side (LHS) of Eq. 6.1 are the quantities we measure from data - they are the widths of three unique time differences between 3 devices. For example, to obtain ΔT_{01} , here the difference of times between SiPM1 and SiPM2, one starts from the time when each device was fired (what is meant by this is explained in Sec. 6.3). The distribution of the difference between these times is (hopefully) Gaussian. This distribution is fitted with Gaussian width obtained from fit is $\sigma_{\Delta T_{01}}$ and fit error on this parameter gives $\sigma_{\sigma_{\Delta T_{01}}}$. Uncertainties on $\sigma_0, \sigma_1, \sigma_2$ are expressed in terms of $\sigma_{\Delta T_{ij}}, \sigma_{\sigma_{\Delta T_{ij}}}$ by Eq. 6.2 - the equation is obtained using the usual uncertainty propagation rules.

$$\frac{1}{4\sigma_i} \sqrt{(2\sigma_{\Delta T_{01}}\sigma_{\sigma_{\Delta T_{01}}})^2 + (2\sigma_{\Delta T_{02}}\sigma_{\sigma_{\Delta T_{02}}})^2 + (2\sigma_{\Delta T_{12}}\sigma_{\sigma_{\Delta T_{12}}})^2} \text{ where } i = 1, 2, 3 \quad (6.2)$$

6.3 SiPM time reconstruction and it's matching with hybrid

ΔT_{01} , width of which is used in Eq. 6.1, is given by Eq. 6.3. Constant fraction discrimination (CFD) is used to determine the time when the individual device was fired and allows to suppress the timewalk effect. tCFD is a moment when a signal crosses a certain fraction of its amplitude. CFDs are obtained from the numerical calculation on SiPM signal digitized by an oscilloscope (Lecroy with 20 GSamples/s sampling rate), and the reference time axis is provided by the scope. This axis is used in tCFD calculation. The time of each SiPM device $tCFD$ is obtained with the software CFD, i.e. the time is computed event-by-event at a constant fraction of the amplitude, therefore insensitive to the timewalk effect. The time is extracted from scope data sampled at 20 Gsample/s and interpolated to the precise threshold. A 20% threshold is used later in the analysis (for both SiPMs), and ΔT_{01} is defined as Eq. 6.3. 20% fraction choice allows to get the best SiPM resolution while solving Eq. 6.1, which is shown in Fig. 6.4a (dependency obtained with batch 1901 data). CFD30 is comparable and also can be used. Both $tCFD_{20_{SiPM1}}$ and $tCFD_{20_{SiPM2}}$ are in picoseconds and referenced to a consistent time axis so that they can be subtracted from each other (contrary to the other two differences, where hybrid participates).

$$\Delta T_{01} = tCFD_{20_{SiPM1}} - tCFD_{20_{SiPM2}} \quad (6.3)$$

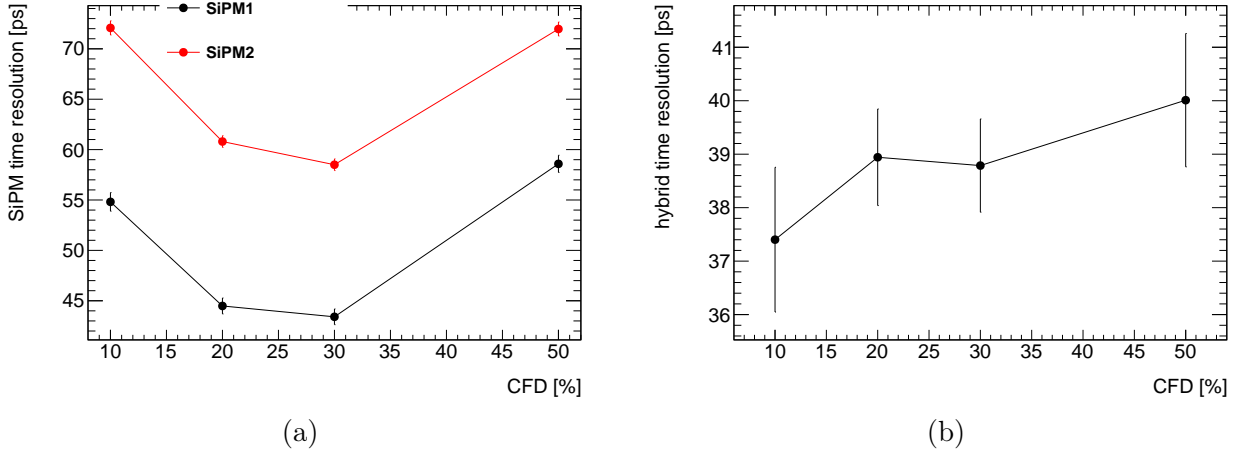


Figure 6.4: Effect of varying (a) SiPM's CFD[%] on quartz+SiPM1 and quartz+SiPM2 systems time resolution. (b) SiPM's CFD[%] on hybrid time resolution.

ΔT_{02} and ΔT_{12} , width of which is used in Eq. 6.1, is given by

$$\Delta T_{0(1)2} = -TOA \times TOALSB - tCFD_{20_{0(1)}} - t_{clock} \quad (6.4)$$

However, because the trigger was issued by ALTIROC when a hit was recorded, referencing to clock is done by construction and one can drop t_{clock} , giving

$$\Delta T_{0(1)2} = -TOA \times TOALSB - tCFD_{20_{0(1)}} \quad (6.5)$$

The time when the hybrid is fired is given by TOA measured by the ASIC (in raw TDC unit); it can be converted to picoseconds by multiplying TOA with TOA quantization step (also called TOALSB standing for TOA Least Significant Bit), which is obtained for each channel from testbench measurements and expected to be ≈ 20 ps. CFD for ASIC data is not used; instead, timewalk is corrected using measured TOT¹. TOA in picoseconds can be compared to the CFD of two reference devices. $tCFD_{20_{1(2)}}$ in principle should be $(tCFD_{20_{1(2)}} - t_{clock})$ (it is done in this way with ALTIROC2 where trigger setup was different), but it is not done because we trigger on ALTIROC and including t_{clock} will only give a constant shift (identical in every event) - what matters is a shape and width of ΔT , not the absolute value so t_{clock} contribution is dropped. The minus sign in front of TOA is because TOA measures time until the falling edge of the 40 MHz clock, not the rising edge.

As shown in Fig. 6.4b, and as a sanity check, the extracted hybrid resolution has little sensitivity to the SiPM CFD fraction.

6.4 Resolution obtained with TZ preamplifier

This section uses batch 1901; its parameters are shown in Table 6.1.

6.4.1 TOA-TOT coupling caveat

The TOT measured with the TDC is expected to be independent of its TOA as the energy deposition of the particles should be similar whenever the arrival time is with respect to the 40 MHz clock. However, the Fig. 6.5a shows a clear unexpected dependence. This S-shape variation depends on the ASIC discriminator threshold. The effect is attributed to a digital coupling synchronized with the 40 MHz clock. The digital activity at the channel level generates a 40 MHz digital noise that is partially injected through the ground of the preamplifier and amplified by it. The effect is also observed in testbench measurements but only with hybrid, not when the ASIC alone is used.

Another way to see the coupling is shown on Fig. 6.5b: average preamplifier probe pulse (each pulse is digitized and recorded by the oscilloscope, then 100000 pulses averaged) in three TOA bins. The time the pulse is over a certain threshold (fraction of amplitude) is not the same for different TOA values. While the rising edges are similar, the falling edges are clearly not - inducing a TOT dependence vs TOA.

6.4.2 Event selections

The common event selections for all correction variables are related to TOA and SiPM amplitudes. TOA of the pixel selected is non-saturated: the maximum value TOA can take is 127, so events with $TOA < 127$ are taken, which leaves us with 10% of events recorded since the measurement window of 2.5 ns is ten times smaller than the period of the 40MHz clock. Amplitude of both reference SiPMs should be above MPV of corresponding distribution, shown on Fig. 6.6, to get better SiPM resolution (as it is improving with amplitude). The downside of using tighter SiPM amplitude cuts is that statistics decrease. For SiPM1, amplitude also should be below 140 mV

¹CFD is complex to do at the ASIC level since it requires frequent signal sampling, and even if it is possible, power consumption is too large to be fitted within HGTD requirements. ZCD (Zero Crossing Discrimination) was considered as a timewalk correction method in earlier ASIC prototypes, and results obtained were insufficient - TOT correction is used instead

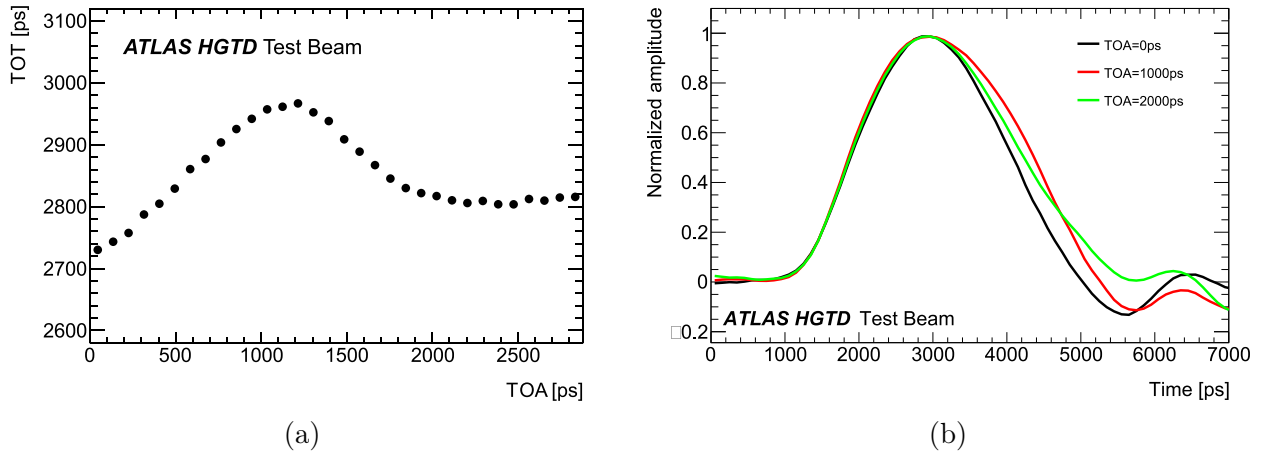


Figure 6.5: (a) TOT as a function of the TOA. (b) Preamplifier probe waveform for various TOA values.

since this is where the saturation peak appears (caused by misconfiguration of oscilloscope channel recording SiPM1)

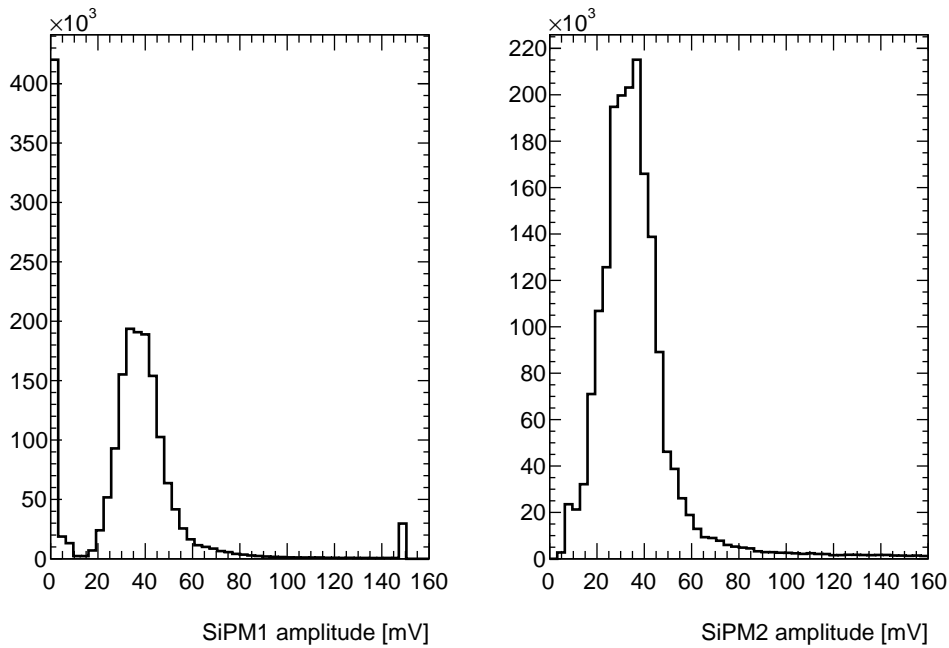


Figure 6.6: Pulse amplitude distribution of (left) SiPM1 (right) SiPM2.

6.4.3 Uncorrected resolution

An example of three ΔT s used in Eq. 6.1 is shown in Fig. 6.7 with black (batch 1901, before time-walk correction) together with their width obtained from Gaussian fit. Fit gives $\sigma_{\Delta T01}, \sigma_{\Delta T02}, \sigma_{\Delta T12}$ entering LHS of Eq. 6.1. The uncorrected σ_{hybrid} , before timewalk correction, is 73.5 ± 0.7 ps - only statistical uncertainty is considered.

6.4.4 Timewalk correction variables

The ASIC measures the TOT because the TOT is a proxy for the LGAD signal amplitude, and “amplitude“ is needed for timewalk correction. The timewalk correction can significantly improve

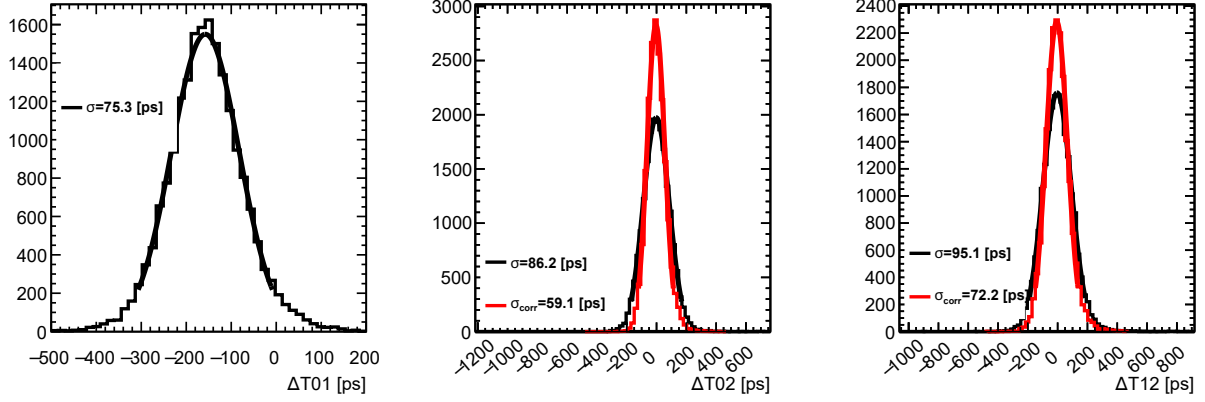


Figure 6.7: Three ΔT distributions used to extract hybrid time resolution: (left) time difference between the quartz+SiPM1 system ($\equiv 0$ in ΔT) and quartz+SiPM2 system ($\equiv 1$ in ΔT). (middle) time difference between the quartz+SiPM1 system and hybrid ($\equiv 2$ in ΔT) before (black) and after (red) timewalk correction with the preamplifier probe amplitude. (right) time difference between the quartz+SiPM2 system and hybrid before and after timewalk correction with preamplifier probe amplitude. For (middle) and (right), the black/red lines show Gaussian fits of timewalk uncorrected/corrected, and corresponding numbers are widths obtained from the fit.

time resolution. The complete list of variables used as TOT proxies for timewalk correction is: probe amplitude, probe TOT, corr probe TOT (those three will not be available in actual HGTD, derived from digitized preamplifier probe pulse) and ASIC TOT, corr ASIC TOT (those two would be available). Those that will not be available in actual HGTD are useful for debugging to obtain lower (best) limit on performance.

Probe amplitude

In testbeam, we can estimate the signal amplitude from the preamplifier probe, shown on Fig. 6.8a is a distribution of a per-event maximum of digitized preamplifier probe pulse. This is our best estimation of signal amplitude. The application of timewalk correction is shown in Fig. 6.9 (looks the same for $\Delta T12$, so only one plot is shown). The left figure shows the smooth dependence of the time difference with the preamplifier probe amplitude, called timewalk. The right figure presents the same time difference after a correction with polynomial fit (subtracting ΔT fit values in each amplitude bin). The procedure is applied for the two differences with the SiPM reference devices, but this is redundant as they are identical up to a constant shift. The timewalk correction for two SiPMs is not needed because it was already taken into account with CFD, so $\sigma_{\Delta T01}$ is used to solve for timewalk corrected σ_{hybrid} is the same as in the uncorrected case. $\sigma_{\Delta T02}^{corr}$ obtained by fitting with a Gaussian $\Delta T02$ distribution after correction. Similarly, for $\Delta T12$. After this correction, the contribution of the timewalk to the resolution is negligible.

Probe TOT

Probe TOT is shown on Fig. 6.8b - time during which probe signal is above a certain threshold which we choose during processing. The dependence of probe TOT against probe amplitude is shown in Fig. 6.10a. Probe TOT resolution in probe amplitude bins is shown in Fig. 6.12b.

Fig. 6.11 is showing timewalk dependence of $\Delta T02$ as function probe TOT on the left plot, together with residual timewalk dependence as function of the same variable, on middle plot.

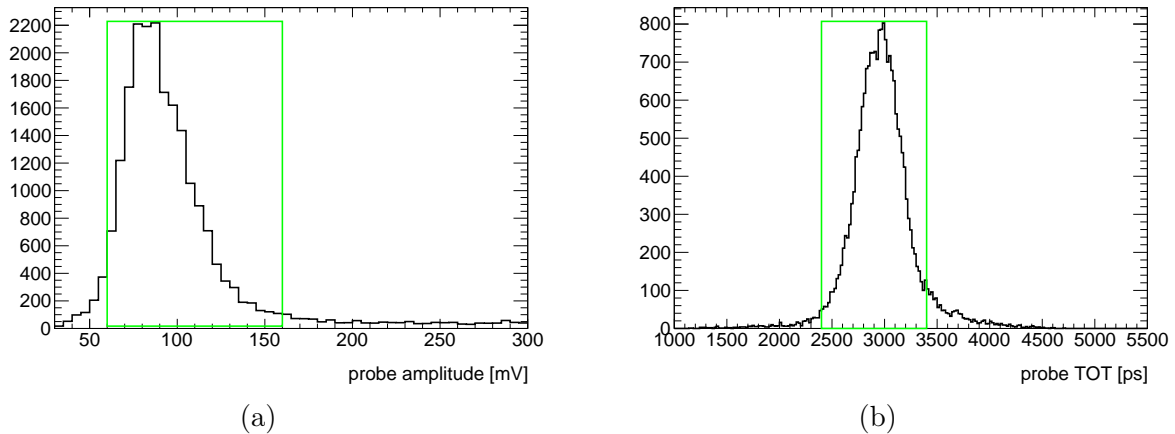


Figure 6.8: For a single TZ channel, room temperature: (a) preamplifier probe amplitude distribution. (b) Preamplifier probe TOT distribution (single TZ channel, room temperature). For both (a) and (b), the region marked with green is used to extract time resolution.

ASIC TOT

ASIC TOT is shown on Fig. 6.13 , composed of coarse TOT with nominal 160 ps quantization step (TOTC LSB) and fine TOT with 40 ps LSB as $TOT[ps] = TOTC * 160 - TOTF * 40$. Nominal values of TOT LSBs are used for simplicity, and because the resolution obtained is independent of absolute TOT value - only relation with TOA is relevant. The dependence of ASIC TOT on probe amplitude is shown in Fig. 6.15a , where the TOT plateau can be seen for a wide range of values in the probe tail. However, in a region where most events are, TOT is reasonably linear. TOTF is available, but it is probably not worth having it: Fig. 6.12a shows that TOT resolution is larger than TOTF bin (40ps)

Fig. 6.14 is showing timewalk dependence of ΔT_{02} as a function ASIC TOT on the left plot, together with residual timewalk dependence as function of the same variable, on middle plot.

TOA-TOT coupling correction and corr ASIC TOT

Sometimes, the result obtained after timewalk correction is not the best possible result because the TOA-TOT coupling mentioned above and shown in Fig. 6.5a is still contributing. It is possible to introduce a new variable, let us call it corr TOT (TOT corrected for coupling), which is flat as a function of TOA . Fig. 6.16 shows on the left TOA-TOT histogram together with the mean value of TOT in each TOA bin.

In ATLAS, correction of the timewalk only will be possible through the TOT information. However, as shown in Fig. 6.5a, the TOT is showing a variation with the TOA which will be a limitation to the timewalk correction. Consequently, this dependence should first be corrected and a new variable corr TOT is introduced. Fig. 6.16 show this dependence before and after a bin to bin correction. After correction a TOT value is centered around 0 in all TOA bins ² , as shown on the right plot of Fig. 6.16. corr TOT obtained in this way is then used to perform timewalk correction, just like it was done above with preamplifier probe amplitude. Fig. 6.17 is showing timewalk dependence of ΔT_{02} as a function corr ASIC TOT on the left plot, together with residual timewalk dependence as function of the same variable, on middle plot.

ASIC TOT corr resolution as a function of probe amplitude is improved compared to the original

²the value around which TOT is centered is irrelevant and can be anything; 0 used is a natural choice

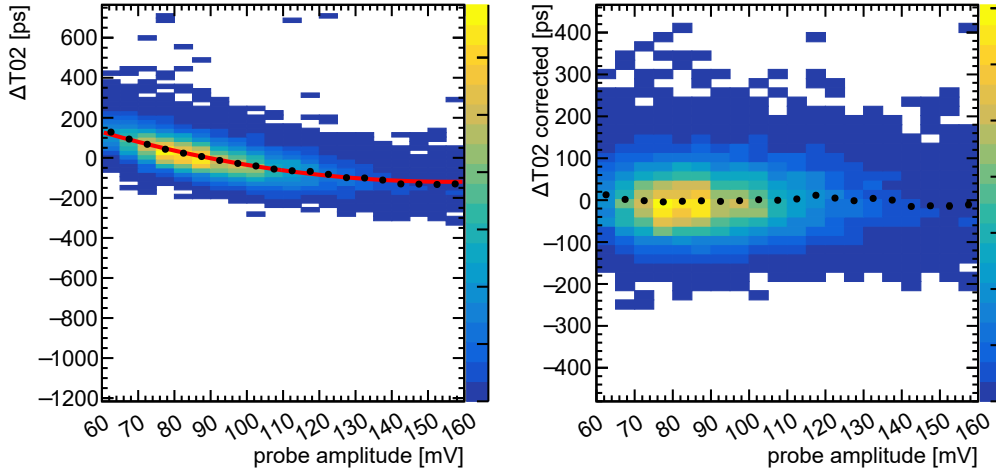


Figure 6.9: Distribution of the time difference (ΔT mean shifted to zero) between the quartz+SiPM system ($\equiv 0$ in ΔT) and hybrid ($\equiv 2$ in ΔT) as a function of the preamplifier probe amplitude (left) before timewalk correction, the red line is a fit used to perform the timewalk correction with probe amplitude (right) after timewalk correction using fit shown on (left). In both plots, the dots correspond to the mean value of the ΔT distribution.

ASIC TOT, as shown in Fig. 6.12a. The distribution from which resolution is obtained is shown in Fig. 6.15b.

Corr probeTOT

Corr probe TOT is the transformation of probe TOT, used because probe TOT, similarly to ASIC TOT, is not flat as a function of TOA (which is consistent). Comparison of corrected probe TOT and original probe TOT resolutions in probe amplitude bins is shown in Fig. 6.12b and corrected probe TOT resolution is better - distribution from which resolution is obtained is shown on Fig. 6.10b.

Fig. 6.18 is showing timewalk dependence of $\Delta T02$ as a function corr probeTOT on the left plot, together with residual timewalk dependence as function of the same variable, on middle plot.

Results

Three resulting corrected ΔT s with probe amplitude are shown in Fig. 6.7 together with their width in red. It can be seen that the width of both $\Delta T02$ and $\Delta T12$ are significantly reduced compared to uncorrected cases. Three corrected widths, as before, allow to obtain the individual device resolution through Eq. 6.1. For the correction using probe amplitude, $\sigma_{hybrid} = 38.9 \pm 0.9$ ps, so the quadratic improvement obtained from timewalk correction here is 63 ps (expressed in this way in order to obtain $\sigma^{timewalk}$ contribution from $\sigma^{uncor} = \sigma^{cor} \oplus \sigma^{timewalk}$). The gain will be smaller while using ASIC-only information. Correction with other variables will be below. The timewalk correction using the ASIC information (TOT) is not as efficient and will be discussed below.

The expectation is that probe amplitude correction will give the best result; ASIC TOT and probe TOT are hopefully similar (the same applies to corr ASIC TOT and corr probe TOT). Right plots of Fig. 6.11, Fig. 6.14, Fig. 6.17, Fig. 6.18 show a dependence of $\Delta T02$ after correction as a function of probe amplitude - this slope is an estimation of residual timewalk, which was not corrected away. It can be seen that residual timewalk is reduced on corr probe TOT compared to probe TOT correction and on corr ASICTOT compared to ASIC TOT correction. Also, the

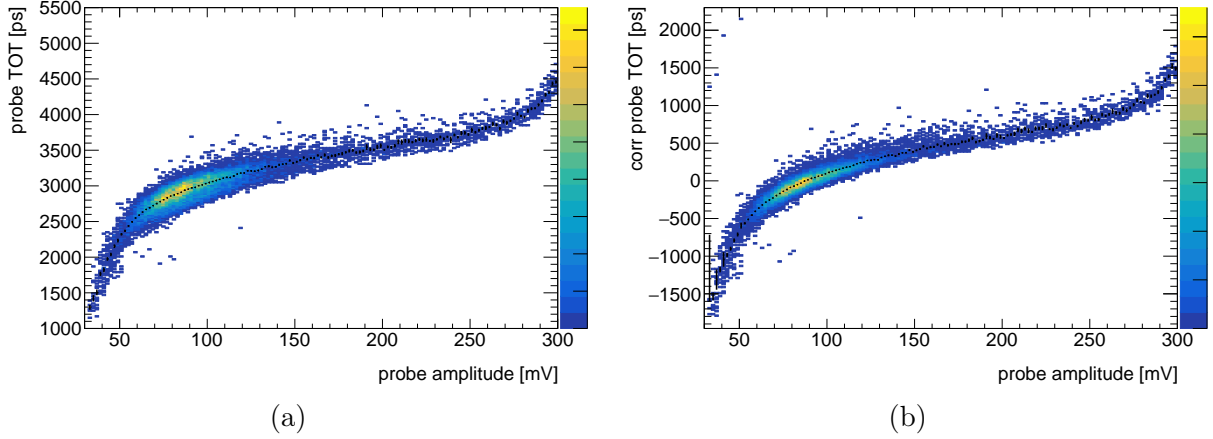


Figure 6.10: (a) probe TOT against preamplifier probe amplitude. The threshold used for probe TOT calculation is 27.7 mV. (b) corrected probe TOT against preamplifier probe amplitude.

residual slope is similar between probe TOT and ASIC TOT; and between corr probe TOT and corr ASIC TOT corrections.

Obtaining time resolution in a way described in Sec. 6.2 with different timewalk correction variables gives results shown in Table 6.2. For probe TOT, the threshold of 27.7 mV was used to compare with ASIC TOT. Event selection for particular variables does not rely on other timewalk correction variables; for example, in order to obtain resolution with ASIC TOT correction, cut is done by selecting the core of TOT distribution (marked by green box shown on Fig. 6.13) where it is roughly linear (shown on Fig. 6.15a) and plateau is rejected. The same is done with other “TOT” variables - the green box on Fig. 6.8a (Fig. 6.8b) shows the core of probe amplitude (probe TOT) distribution.

Looking at uncorrected and corrected resolution columns in Table 6.2, it can be seen that despite different selection cuts (selections for uncorrected resolutions are not relying on variables that will not be used later for correction), we start more or less from the same value. The biggest gain from timewalk correction is achieved with the probe amplitude, which is expected. The results of the two types of TOT (probe and ASIC) are similar, demonstrating that the TDC works well. Correcting for TOA-TOT dependence and using corr probe TOT and corr ASIC TOT gives similar gain for both probe and ASIC TOT and equals to in quadrature to ≈ 24 ps (75.9-51.3 for probe TOT).

The best resolution obtained with ASIC-only information (which we are mostly interested in) is 45.7 ps, obtained after timewalk correction with corr ASIC TOT. As a baseline, one can look at probe amplitude correction that gives 38.9 ps. Right plot of Fig. 6.17 displays residual slope, seen by probe but left uncorrected by corr ASIC TOT.

The $TOA > 1600$ column in Table 6.2 adds to selections described above one that selects region where TOA-TOT is flat, as shown on Fig. 6.5a. $TOA > 1600$ ps result for probe TOT correction is close to corr probe TOT result without $TOA > 1600$ ps cut, showing that correction for TOA-TOT dependence can partially compensate for TOA-TOT dependence. However, there is still a gain in going from probe TOT to corr probe TOT when the $TOA > 80$ cut is applied in both cases. The same is observed for ASIC TOT, corr ASIC TOT. Both corr ASIC TOT and corr probe TOT with $TOA > 1600$ ps cut cannot reach probe amplitude correction result.

Once data is taken, we cannot check the resolution after ASIC TOT correction with different ASIC thresholds. However, with comparable thresholds, ASIC TOT and probe TOT corrections give similar results, as was shown in Table 6.2. In this way, we can simulate the result with a different threshold by using probe TOT and varying threshold for its calculation. Probe TOT threshold used

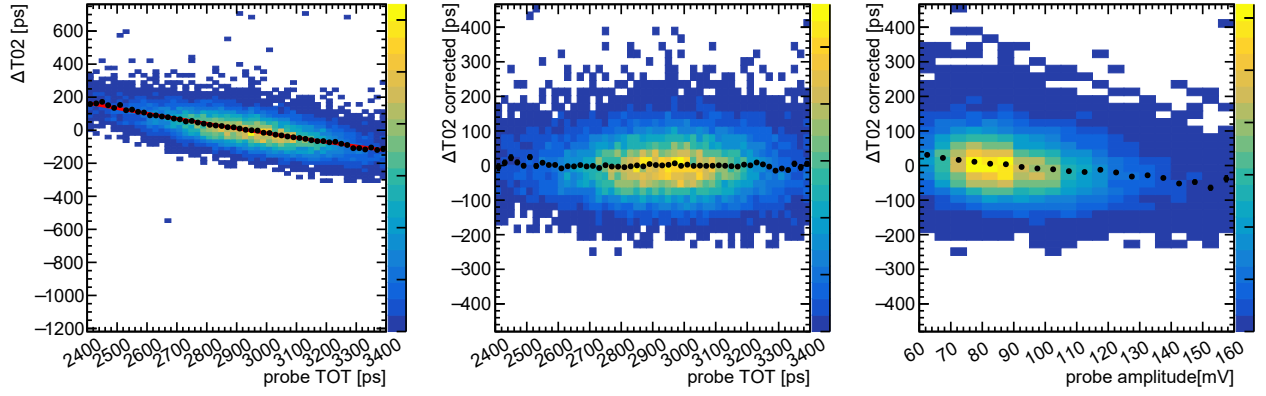


Figure 6.11: Distribution of the time difference (ΔT mean shifted to zero) between the quartz+SiPM system ($\equiv 0$ in ΔT) and hybrid ($\equiv 2$ in ΔT) (left) as a function of the preamplifier probe TOT, before timewalk correction, the red line is a fit used to perform the timewalk correction with preamplifier probe TOT (middle) as a function of the preamplifier probe TOT, after timewalk correction with preamplifier probe TOT (fit shown on (left) is used) (right) as a function of the preamplifier probe amplitude after timewalk correction with preamplifier probe TOT.

| Timewalk correction variable | Uncorrected resolution [ps] | Corrected resolution [ps] | Corrected resolution [ps], TOA>1600 ps |
|------------------------------|-----------------------------|---------------------------|--|
| probe amplitude | 73.5 | 38.9 | 37.0 |
| probe TOT | 75.9 | 51.3 | 46.6 |
| corr probe TOT | 75.9 | 45.7 | 42.3 |
| ASIC TOT | 76.7 | 51.8 | 44.1 |
| corr ASIC TOT | 76.7 | 45.7 | 42.8 |

Table 6.2: ALTIROC1+LGAD hybrid time resolutions obtained after timewalk correction with different variables, with one TZ ASIC channel (number 11) of batch 1901.

Uncertainty on all resolutions is ≈ 1 ps (statistical). Selections to obtain uncorrected resolution is not relying on variables that will not be used for timewalk correction.

is to be compared with MPV of probe amplitude distribution (≈ 80 mV). Resolution (after probe TOT timewalk correction) depending on threshold is shown on Fig. 6.19 together with result of one measurement with ASIC TOT correction - two timewalk correction methods agree if same threshold is used. Also, in Fig. 6.20, a possible explanation is shown as to why resolution increases with a lower threshold: amplitude (difference between maximum of Y axis appearing near $TOA \approx 70$ and minimum appearing near $TOA \approx 0$) of TOA-TOT coupling “wave“ (seen with probe TOT where it’s easy to vary threshold in software) decreases.

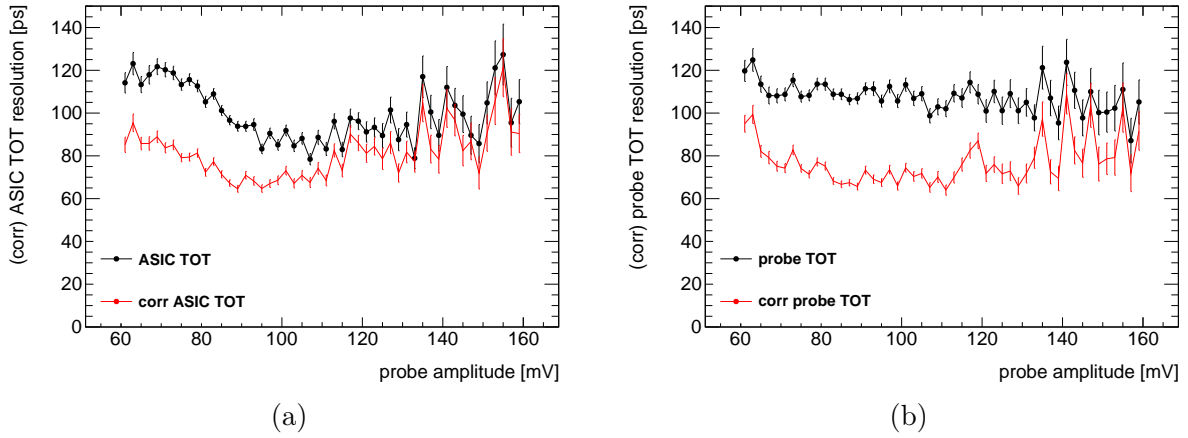


Figure 6.12: (a) ASIC TOT and corr ASIC TOT resolutions as a function of probe amplitude (b) probe TOT and corr probe TOT resolutions as a function of probe amplitude. Threshold used for probe TOT is 27.7 mV. Both (a) and (b) obtained from RMS of their distributions in corresponding preamplifier probe amplitude bin.

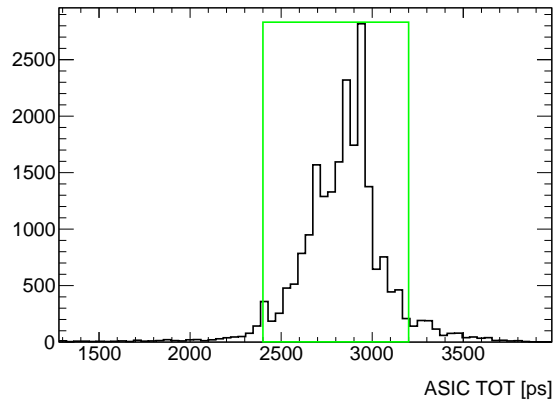


Figure 6.13: ASIC TOT distribution (single TZ channel, room temperature). The region marked with green is used to extract time resolution.

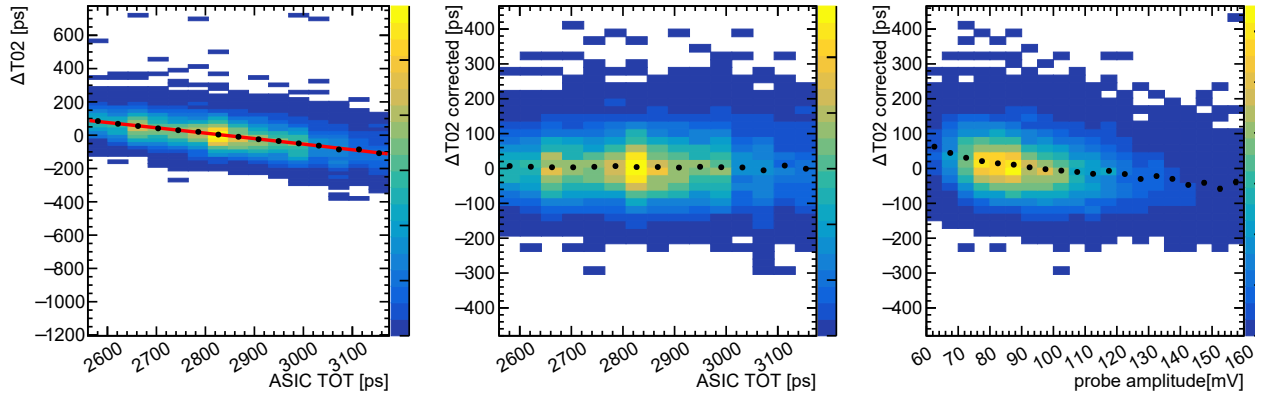


Figure 6.14: Distribution of the time difference (ΔT mean shifted to zero) between the quartz+SiPM system ($\equiv 0$ in ΔT) and hybrid ($\equiv 2$ in ΔT) (left) as a function of the ASIC TOT, before timewalk correction, the red line is a fit used to perform the timewalk correction with ASIC TOT (middle) as a function of the ASIC TOT, after timewalk correction with ASIC TOT (fit shown on (left) is used) (right) as a function of the preamplifier probe amplitude after timewalk correction with ASIC TOT.

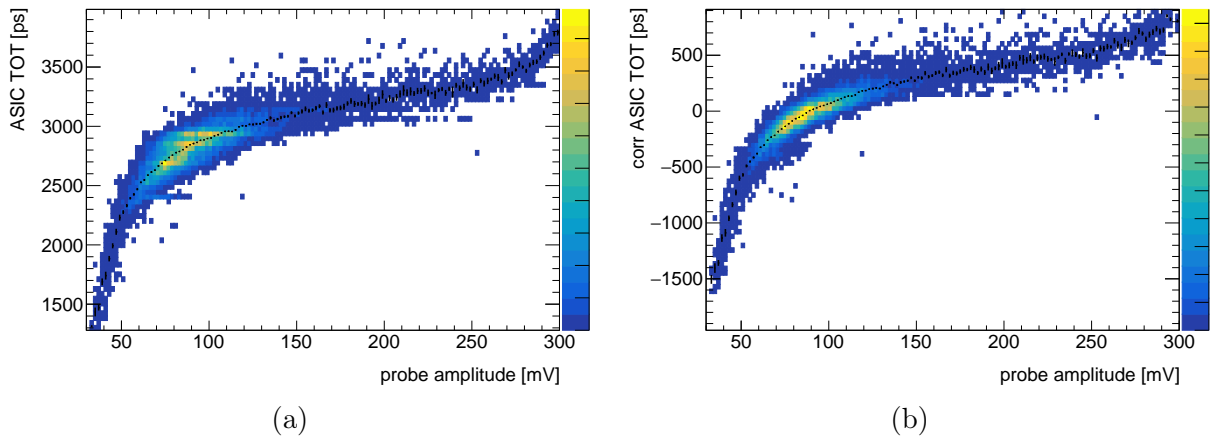


Figure 6.15: (a) ASIC TOT against preamplifier probe amplitude (b) corrected ASIC TOT against preamplifier probe amplitude.

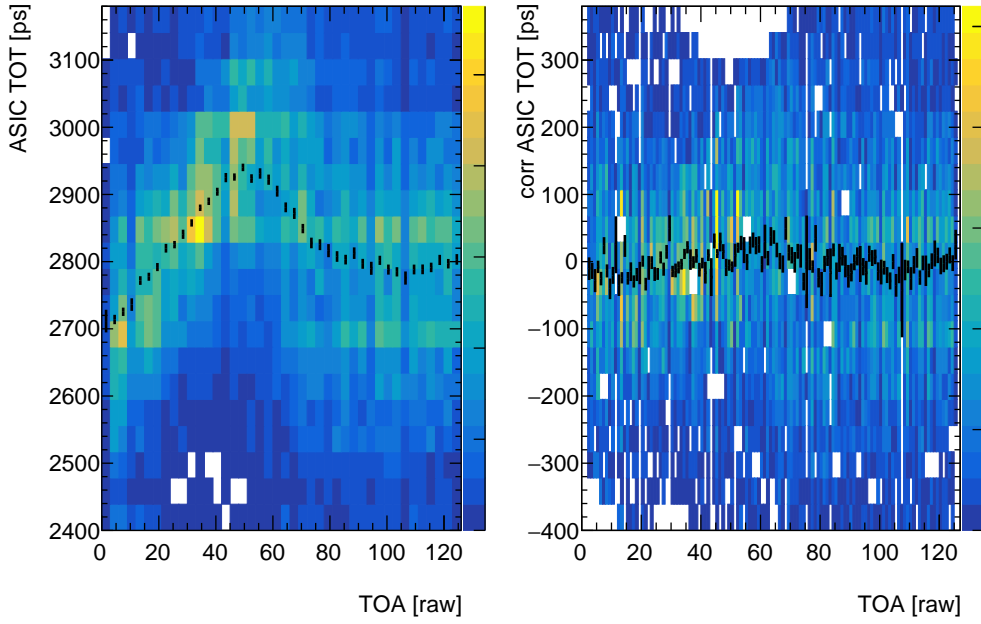


Figure 6.16: (left) ASIC TOT dependence on TOA. (right) corr ASIC TOT as a function of TOA, obtained with subtraction of average ASIC TOT in each TOA bin from ASIC TOT shown in (left).

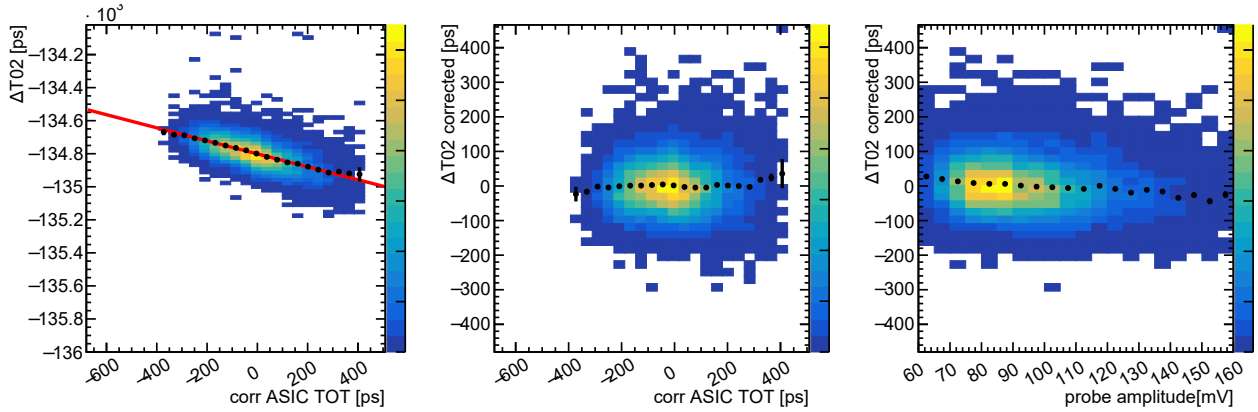


Figure 6.17: Distribution of the time difference (ΔT mean shifted to zero) between the quartz+SiPM system ($\equiv 0$ in ΔT) and hybrid ($\equiv 2$ in ΔT) (left) as a function of the corr ASIC TOT, before timewalk correction, the red line is a fit used to perform the timewalk correction with corr ASIC TOT (middle) as a function of the corr ASIC TOT, after timewalk correction with corr ASIC TOT (fit shown on (left) is used) (right) as a function of the preamplifier probe amplitude after timewalk correction with corr ASIC TOT.

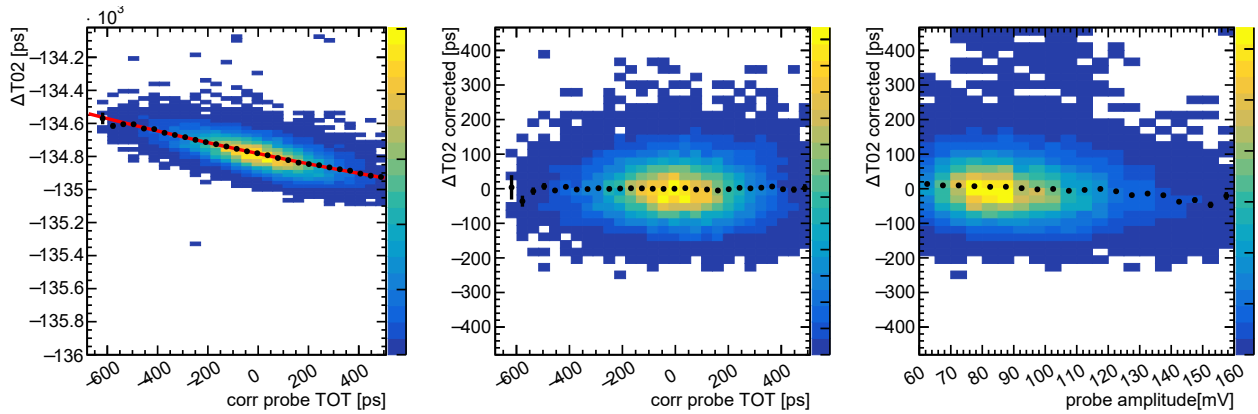


Figure 6.18: Distribution of the time difference (ΔT mean shifted to zero) between the quartz+SiPM system ($\equiv 0$ in ΔT) and hybrid ($\equiv 2$ in ΔT) (left) as a function of the corr Probe TOT, before timewalk correction, the red line is a fit used to perform the timewalk correction with corr Probe TOT (middle) as a function of the corr Probe TOT, after timewalk correction with corr Probe TOT (fit shown on (left) is used) (right) as a function of the preamplifier probe amplitude after timewalk correction with corr Probe TOT.

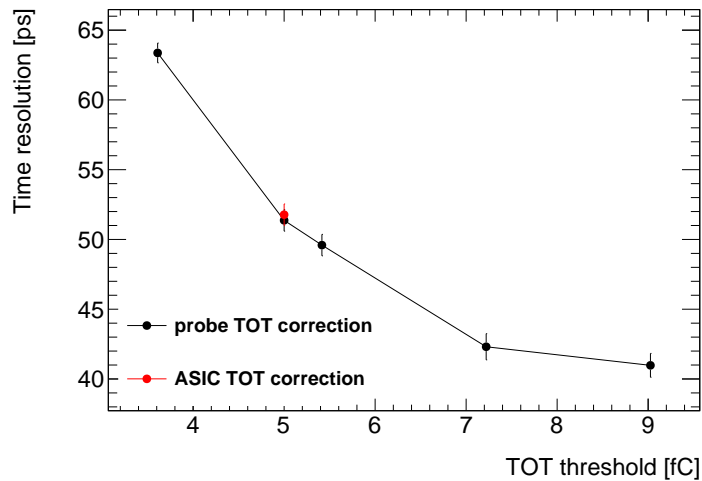


Figure 6.19: Time resolutions obtained with probe TOT correction and different thresholds to calculate probe TOT. ASIC TOT correction result with a threshold of batch 1901 is shown for comparison.

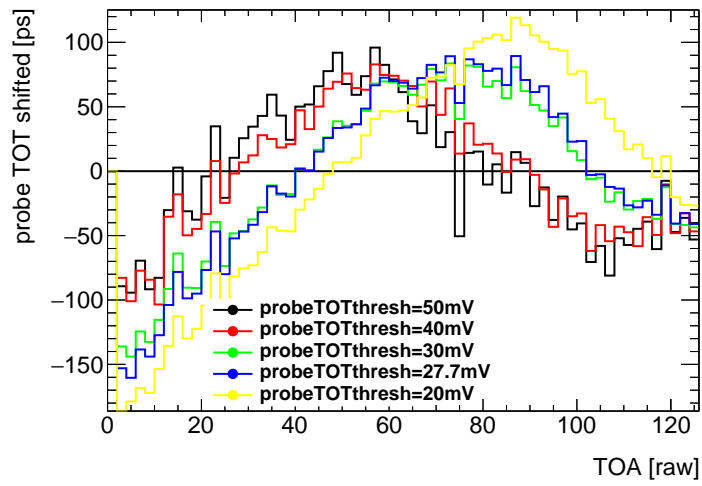


Figure 6.20: Mean preamplifier probe TOT (shifted to be centered around 0) against ASIC TOA shown for different probe TOT thresholds (values used are written in legend).

6.4.5 Amplitude dependence

The time resolution is expected to depend on the signal amplitude. Fig. 6.21 shows this dependence (after timewalk correction with probe amplitude) as a function of the probe amplitude. It can be seen that the resolution has a minimum where the probe amplitude is near its MPV, and the resolution is degraded when going away from MPV. This behavior comes from the LGAD itself (not from ASIC and not from the connection between the ASIC and the LGAD, not from trigger setup) as explained in [26],[100]: “The events in the high tail of the Landau are mostly due to the presence of localized clusters of ionization. Given that the ionization is very non-uniform for these events, their temporal resolution is worse than that of signals with an amplitude around the Landau most probable value“. In low tail $\sigma_{jitter} = \frac{t_{rise}}{S/N}$ is also contributing to degradation since S (amplitude) is lower. Similar dependence is observed when correcting with two types of TOT available in bins of TOT, as shown in Fig. 6.22a and Fig. 6.22b. The minimum doesn't precisely coincide with the minimum of the amplitude proxy because relation between amplitude and probe TOT, ASIC TOT is not precisely linear (see Fig. 6.10a, Fig. 6.15a) - e.g. higher ASIC TOT value contains a mixture of probe amplitude values and establishing direct correspondence from probe amplitude distribution maximum to probe/ASIC TOT distribution maximum is not possible. Finally, Fig. 6.21 also shows the time resolution obtained with the probe amplitude and two types of TOT where all are plotted in bins of the probe amplitude: it can be seen if we select the probe amplitude peak, all corrections give similar result. However, this is not the test to compare the timewalk correction methods because in each bin, especially in small bins near the amplitude peak: the timewalk effect envelope is small, and the correction does not bring much difference.

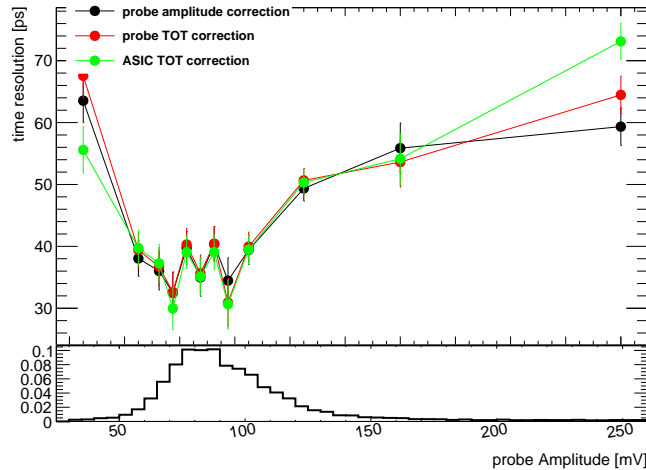
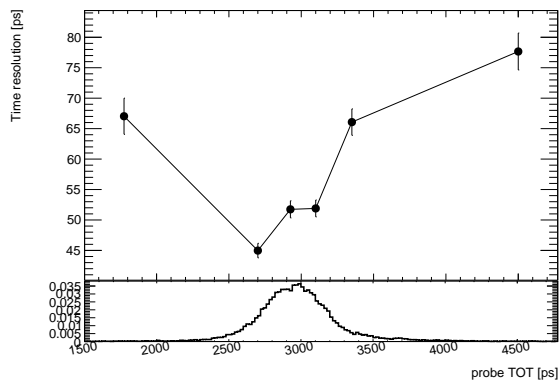
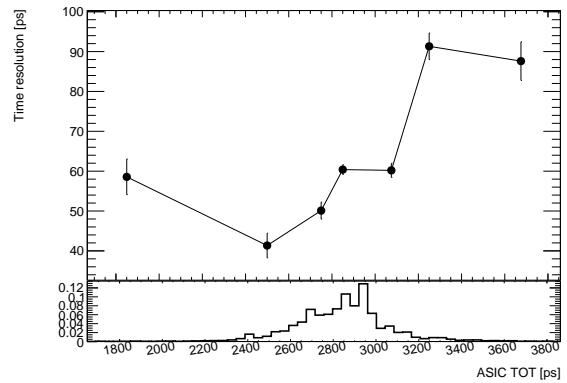


Figure 6.21: (top) Time resolution obtained after correction with preamplifier probe amplitude, preamplifier probe TOT (with a 27.7 mV threshold), and ASIC TOT, all plotted against preamplifier probe amplitude. (bottom) Normalized preamplifier probe amplitude distribution.



(a)



(b)

Figure 6.22: Time resolution obtained (a) after correction with preamplifier probe TOT (27.7 mV threshold) plotted against preamplifier probe TOT. On the bottom, the normalized preamplifier probe TOT distribution is shown. (b) after correction with ASIC TOT plotted against ASIC TOT. On the bottom, the normalized ASIC TOT distribution is shown.

6.4.6 Impact of TDC DNL

It was observed during testbeam that the TOA distribution shown in Fig. 6.23 is not uniform. It is expected to be uniform because the beam is not synchronized with the data taking, and particles can hit the hybrid at any time within the measurement window with equal probability. Then, the TOA non-uniformity is interpreted as a variation of the TOALSB value in each bin of TOA - instead of nominal ≈ 20 ps LSB, we have in each bin different LSB (this is due to the differential non-linearity of the TDC and also seen in the testbench). The bin with a population larger (smaller) than the average means the LSB is larger (smaller) than the average LSB .

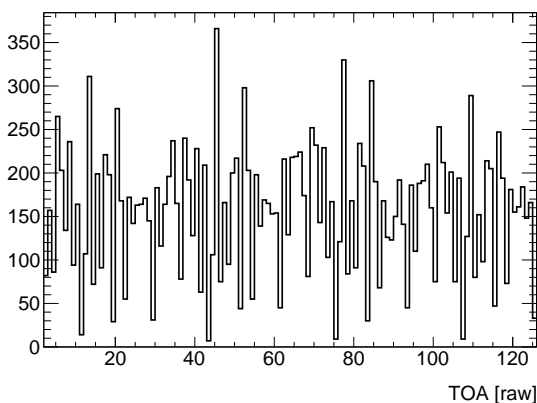


Figure 6.23: TOA distribution (single TZ channel, room temperature), non-uniformity of which is attributed to non-uniform TOA LSB.

The impact of having non-uniform LSB on time resolution was investigated. To obtain TOALSB in each TOA bin, it is assumed that the mean TOA value corresponds to TOALSB measured in testbench (for the configuration and the pixel considered, it is 22.5 ps), then LSB_i is obtained by the ratio of the number of events in a particular bin to the mean TOA value. The resulting TOALSB distribution is shown in Fig. 6.24a. Instead of using a uniform LSB for each bin as done previously (multiplying TOA [raw] count i by TOALSB value measured in testbench: $TOA_{uniform}[ps] = i \times TOALSB$), the TOA can be computed using the real bin size as $TOA_{non-uniform}[ps] = \sum_{i=1}^{TOA} TOALSB_i$. Fig. 6.24a shows real bin sizes. Fig. 6.24b shows this new TOA corrected from the differential non-linearity as a function of the TOA assuming a constant LSB . Applying the timewalk correction with the probe preamplifier amplitude as explained before and using the corrected TOA, the extracted hybrid time resolution is 39.2 ps, quite similar to the time resolution obtained assuming a constant TOALSB, demonstrating that in ALTIROC1 the differential non-linearity has a negligible impact on the final resolution.

6.5 Resolution obtained with VPA preamplifier

Some data were taken with the VPA preamplifier to compare it with TZ; however, it was known already from testbench measurements and [17] that VPA TOT is problematic: TOT does not scale proportionally with the injected charge, which is shown with testbeam data (batch 2300 from Table 6.1) on Fig. 6.25. Also, Fig. 6.26 shows VPA TOT distribution. The TOT measurements are perturbed by the couplings at the input of the preamplifiers, and the VPA TOT is more sensitive since the VPA pulse is longer than the TZ pulse. VPA TOT cannot be used to correct the time-walk effect, but this is the only reason to measure TOT. VPA TOT (Fig. 6.25) has a core of distribution at ≈ 10000 ps (value depends on the threshold), but in addition, several other peaks are present at ≈ 6000 ps, ≈ 11000 , ≈ 12000 ps which was not the case for TZ TOT (Fig. 6.15a)

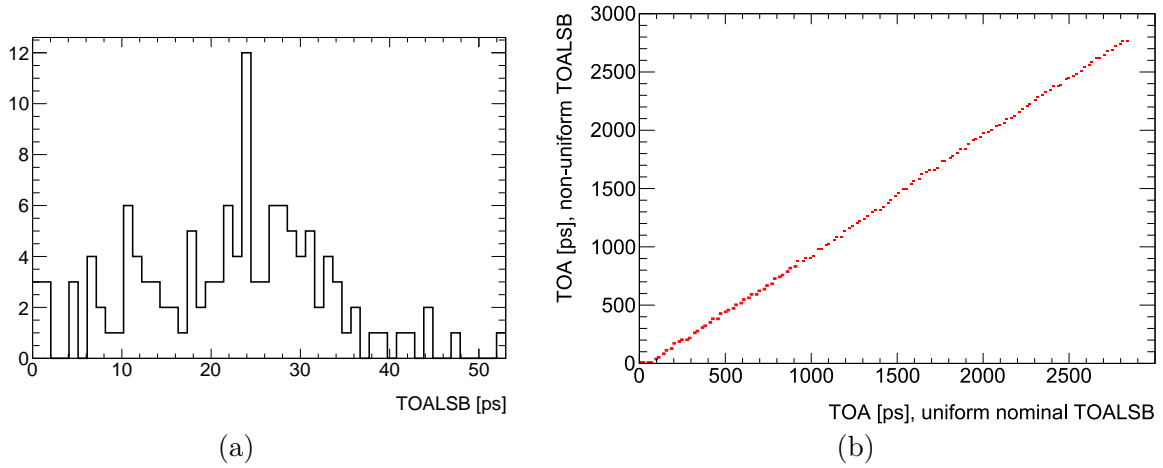


Figure 6.24: (a) Bin TOALSB values obtained from TOA non-flatness (Fig. 6.23). (b) TOA obtained with non-uniform LSB against usual TOA obtained under the uniform TOALSB value assumption.

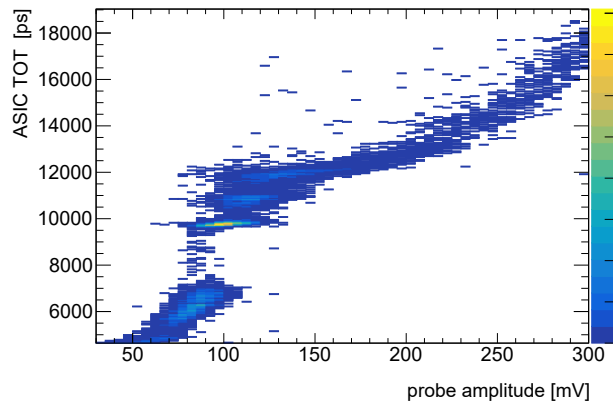


Figure 6.25: VPA ASIC TOT as a function of probe amplitude.

Due to a problem with VPA TOT, only timewalk correction with probe amplitude was performed in two TOT regions shown with green and red boxes in Fig. 6.26 - results are shown in Table 6.3, and they are worse than the TZ result, even worse than the TZ correction with ASIC TOT.

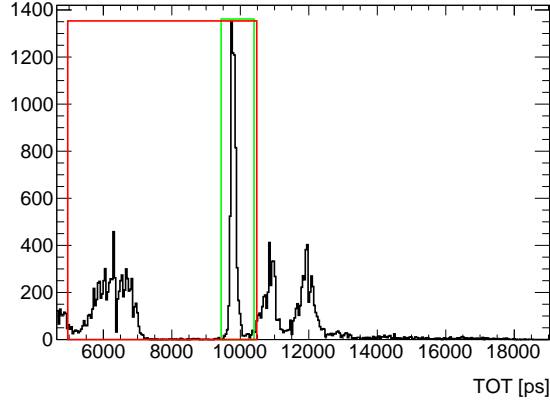


Figure 6.26: VPA ASIC TOT distribution (projection of Fig. 6.25) . The regions marked with green and red boxes are used to extract time resolution.

| TOT selection | Uncorrected resolution [ps] | Corrected resolution [ps] |
|--|-----------------------------|---------------------------|
| $4640 \leq TOT \leq 10400$ (core and second largest peak) | 113.9 | 87.9 |
| $9440 \leq TOT \leq 10400$ (core) | 81.6 | 76.1 |

Table 6.3: Time resolution obtained with VPA preamplifier after timewalk correction with probe amplitude. Uncertainty on all resolutions is ≈ 1 ps.

7 - ALTIROC2 testbench

ALTIROC2 ASIC, first full-size prototype, was produced in 2021 and went through an intensive series of testbench measurements to characterize it - they are summarized in this chapter.

7.1 LSB calibration

ALTIROC2 is equipped with the TOA and TOT TDC, each providing results of their measurements in binary and having some LSB (see Sec. 5.5.5). Therefore, the (in)accuracy of the knowledge of the LSB can directly influence the timing performance. It will be shown later how mismeasured TOA LSB significantly degrades the timing performance in testbeam. The TOT LSB is of the least importance as TOT is only used for timewalk correction - TOT is, therefore, required to be a good proxy for amplitude, however, the value of the proportionality constant between the amplitude and TOT is of less importance. Nevertheless, for TOT LSB, just as for TOA LSB, it's good to check that the value is roughly in an expected range, which is 160 ps for TOT (coarse ¹) and 20 ps for TOA. For TOT, the focus has been mainly on the TOT coarse calibration, as it was observed in the previous analysis that the addition of TOT fine does not improve timewalk significantly.

7.1.1 Methodology

There are two methods to calibrate the TOA LSB and one for TOT LSB .

Using external trigger ² both TOA and TOT LSB can be measured. The signal is injected directly at the input of the TDC, bypassing the preamplifier and discriminator. The injected signal is a square signal with both the start time (indirectly, though changing TDC clock delay) and width of this signal can be varied accurately (at each step, the output of the TDC is saved), allowing to scan both the TOA and TOT range. Delay is obtained by combining coarse (step of 1562 picoseconds) and fine (step of 97 ps) steps. Width can be selected in steps of 1562 picoseconds. Fig. 7.1a shows the measured TOT as a function of the injected pulse width for one of the pixels (step of scan is larger than the minimum possible to have the faster scan). As expected, the behavior is linear, and the TOT LSB can be extracted. An inverse of slope of the linear fit gives the LSB. Similarly, the measured TOA is shown in Fig. 7.1b as a function of TDC clock delay. Saturated values (127 for TOA and 255 for TOTC) are removed. The requirement is to have a set of at least three widths or delay values; otherwise, the fit is not performed. Points with anomalously high jitter have been removed, which has not happened often. The size of the measurement window is 3000 ps starting from the first good point - size of the window chosen to safely cover ASIC's ≈ 2.5 ns measurement window ³ and points outside of this window are removed.

TOA calibration with "pulser" is the second way for TOA LSB calibration. With this method, the whole pixel chain is used instead of going directly to TDC: a certain charge is injected (high enough to avoid being close to the threshold) at the entrance of the TDC, and the TDC clock delay is varied. The comparison between two ways of obtaining TOA LSB is shown on Fig. 7.2 where it can be seen that the two methods give similar results up to a shift in the mean.

All three types of LSB measurements can be done differently regarding pixel activation pattern and into which pixels injection is done. Typical injection patterns are per column or row (meaning 15 pixels simultaneously receiving external trigger or pulser signal) and per pixel (used less often

¹There are two TOT TDCs: coarse (larger LSB) and fine (LSB ≈ 40 ps)

²External relative to the preamplifier and discriminator, not the ASIC - the signal comes from within the ASIC

³Obtained from the product of maximum TOA value (127) and expected TOA LSB value (20 [ps])

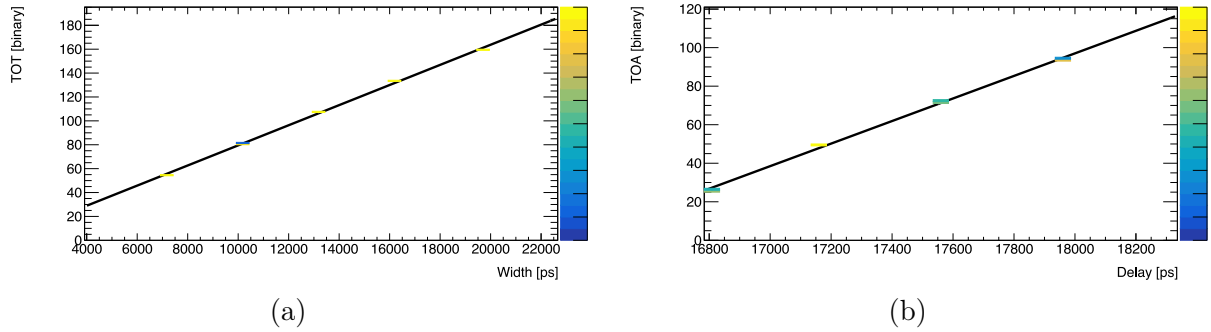


Figure 7.1: (a) Example of TOT LSB extraction in testbench, one of the pixels: distribution of TOT vs injected width together with the fitted mean of the distribution. X bins of distribution are enlarged for visual purposes. The TOT LSB is given by $1/\text{slope}$. (b) Example of TOA LSB extraction in testbench, one of the pixels: distribution of TOA vs TDC clock delay together with the fitted mean of the distribution. The TOA LSB is given by $1/\text{slope}$.

than the other two because it takes too long to obtain results for all 225 channels). Pixel into which injection is done should also be activated: typically, the whole matrix is activated (all preamplifiers, discriminators, and TDCs), but there is a possibility in the software⁴ developed to activate per column or some selected number of columns if there is a need to do so.

7.1.2 General trends observed

The resulting TOA and TOTC LSBs with an external trigger, measured with whole matrix activated and with injection per column, for one board, are summarized in Fig. 7.3 and Fig. 7.4 respectively. The number written in each cell is an LSB of the corresponding pixel. For the board and configuration shown (similar behavior for the other boards) it can be seen that LSB grows along the column. The overall mean value can be tuned, but the trend stays the same. Per-pixel LSB also can be tuned in principle but this was not used as one would measure the value per-pixel anyway. Not a problem if LSBs are different in different parts of the chip as long as one knows the value. No general trend is seen for LSB along the row. TOA and TOT LSB more or less grow together, which is shown on Fig. 7.5: one point corresponds to one pixel, which gives TOTC and TOA LSB.

The activation pattern doesn't matter much for LSB values, as it can be seen from slope ≈ 1 on Fig. 7.6. As mentioned above, different numbers of pixels can be "turned on", which is separate from the injection pattern. Different pixel electronic read-out blocks can be chosen for the pixels selected to be activated. The plot shows the correlation of TOA LSBs injected per column, comparing the cases with

- All preamplifiers are turned on and the case with all pixels turned on
- All preamplifiers are turned on and only one column (the one into which injection is done) is turned on.

The conclusion is the same for TOTC LSB and other boards.

Doing similar measurements, now varying injection pattern instead of activation shows that, on the contrary, the injection pattern typically does matter for the LSB value, as can be seen from Fig. 7.7. Comparing slopes of correlations obtained per row, column, and pixel injection shows that only (row, pixel) combination gives the same result while others do not - suggesting that not only the number of pixels into which injection is done one at a time but also into which pixels injection

⁴FADA: <https://gitlab.cern.ch/atlas-hgtd/Electronics/FADA/-/tree/master/software>

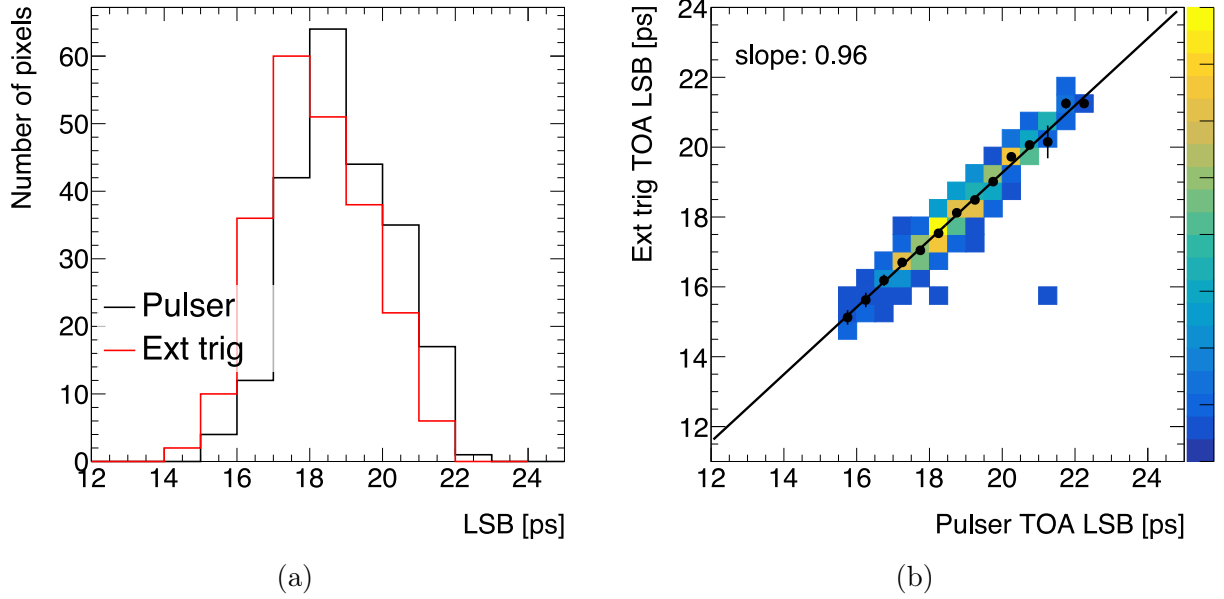


Figure 7.2: TOA LSB obtained in the same configuration but in two ways: external trigger and pulser (a) TOA LSB distributions (b) correlation of the two measurements

is done can change the outcome of the measurement. In the future HGTD typical occupancy will reach 10% in some $|\eta|$ regions, and LSB calibration process should replicate detector conditions ().

Based on measurements shown, modification to next chip iteration (ALTIROC3) were done. Latest ALTIROC3 measurements show weaker dependence of LSB on number of pixels injected.

7.1.3 More on LSB dependence on injection

A more detailed investigation on LSB, depending on pixel injection, was done. Two additional types of measurement were done.

First is LSB dependence with a number of pixels from the same column that are injected: one picks one pixel to monitor, and as a reference and injection is done into only this one pixel. In the next step, injection is done into two pixels: one being the monitor and another one, which can be the pixel just nearby or on another end of the column. Then, injection is done into three pixels: one being monitored and two nearby or two on the other end of the column. More pixels are added until the whole column is full. This was done for several pixels at the bottom of the column, each pixel giving two curves. They are shown on Fig. 7.8. Overall, the change for both TOA and TOT LSB is related to voltage drops along the column (effect was simulated and reproduced by OMEGA engineers). For the TOT case, both ways of adding pixels result in the same starting value (injection into a single pixel that is being monitored) and full column value - showing the closure of the procedure. What happens between endpoint values is similar in having a kink at half of the pixels (seven-eight) and a bigger slope after the kink; the exact values within the trend are different, though. TOT LSB value changes by $\approx 4\%$ between the endpoints. TOA LSB dependence measurement shows less stability because the full column value does not precisely agree between two ways of adding more pixels (same as the starting value but to a smaller degree) - there each value in between can be assumed to be different by maximum $19.4/19 = 2\%$ (comparing values obtain from two patterns at maximum occupancy). Nevertheless, the overall trend, although less clean compared to the TOT case, is conserved and gives about $\approx 7\%$ increase of LSB value between injection into 1 pixel and the whole column.

Another type of measurement is the LSB dependence as a function of the number of columns

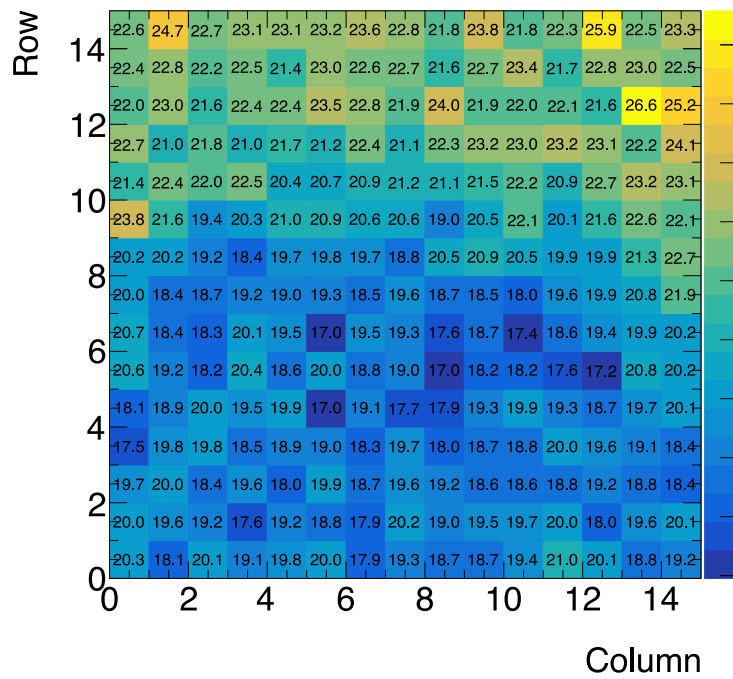


Figure 7.3: ALTIROC2 15x15 pixel matrix of TOA LSB values

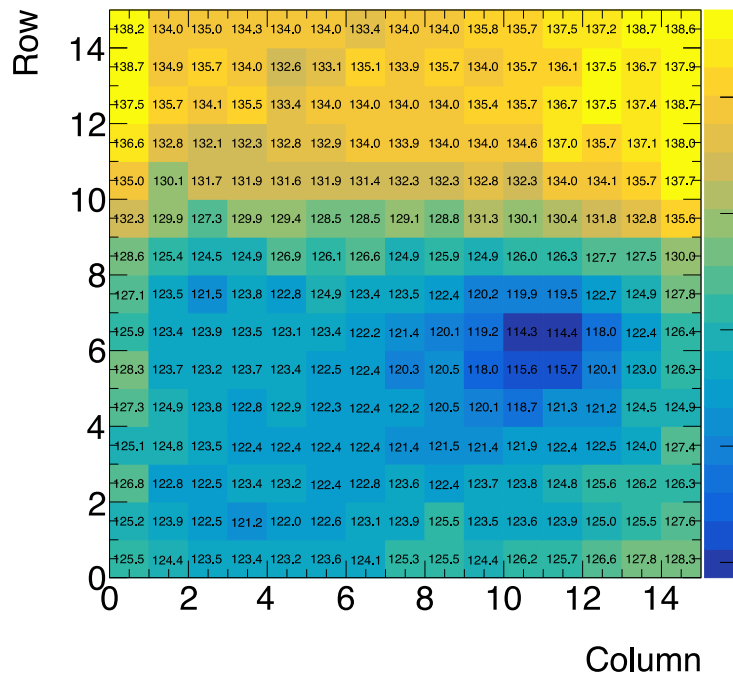


Figure 7.4: ALTIROC2 15x15 pixel matrix of TOTC LSB values

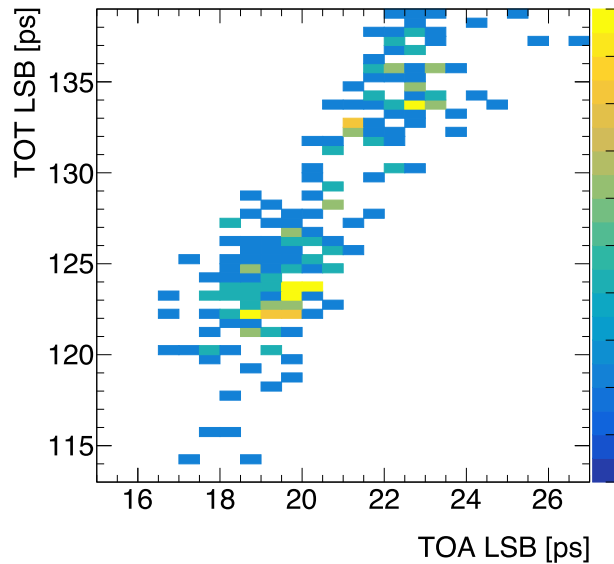


Figure 7.5: Correlation of the TOTC LSB vs TOA LSB

into which injection is done. As before, nearby or faraway columns can be added. In case we monitor column 0 for the point with injection into three columns, this gives: (col0, col1, col2) and (col0, col14, col13) contributing. Fig. 7.9 shows TOTC LSB dependence. In the case of TOT, it's visible that the slope is larger when for the first \approx half of the columns when neighboring columns are being added - contrary to the case of faraway columns being added, which gives a higher slope after eight columns are injected simultaneously. This suggests that not only the number of columns into which injection is simultaneously done, but also that they are close by. Similar Fig. 7.10 shows TOA LSB dependence, where the overall endpoint-endpoint change is smaller than in the case of TOT, and it's harder to see the slope change. As a side note, this is too much of a stress test for the system, as the typical expected occupancy is below 10%, and under normal conditions, even half of the pixels should not be hit simultaneously.

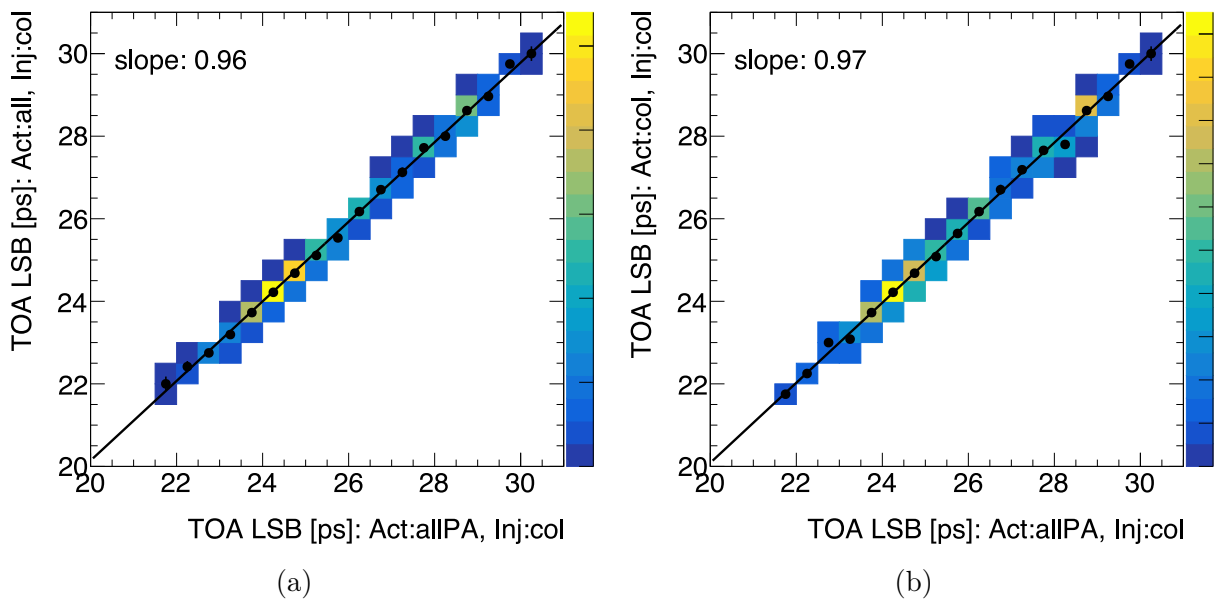


Figure 7.6: Correlation of TOA LSBs with different activation patterns (a) whole matrix activated vs only preamplifiers activated (b) only one column activated vs only preamplifiers activated

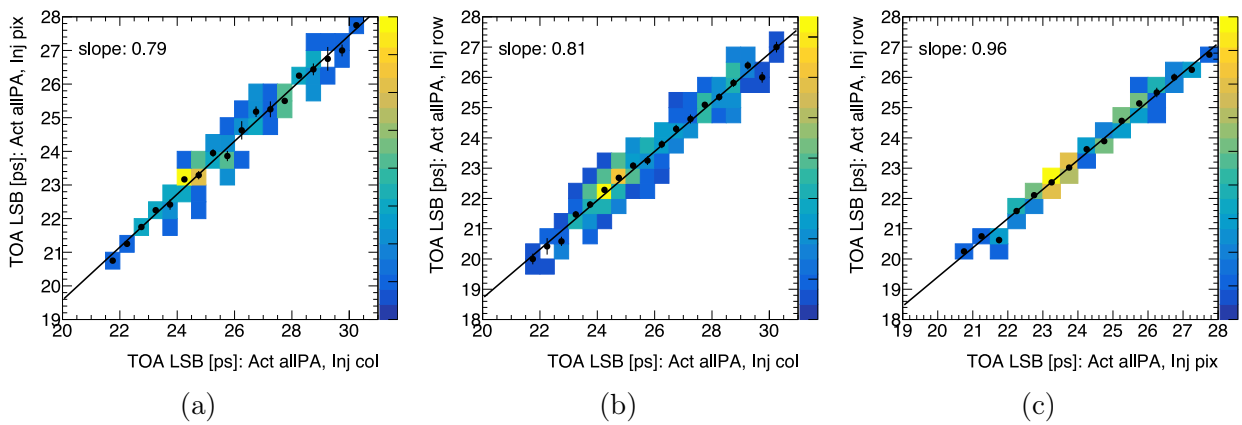
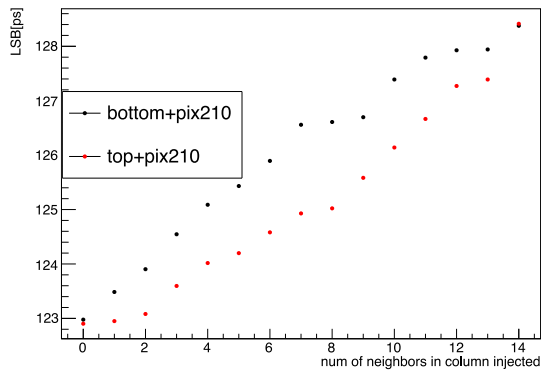
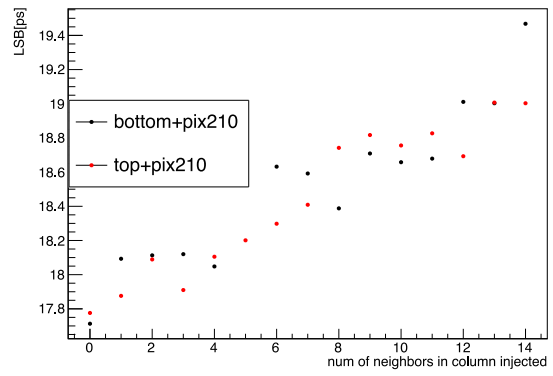


Figure 7.7: Correlation of TOA LSBs with different injection patterns (a) per pixel vs per column (b) per row and vs. per column (c) per pixel vs. per row

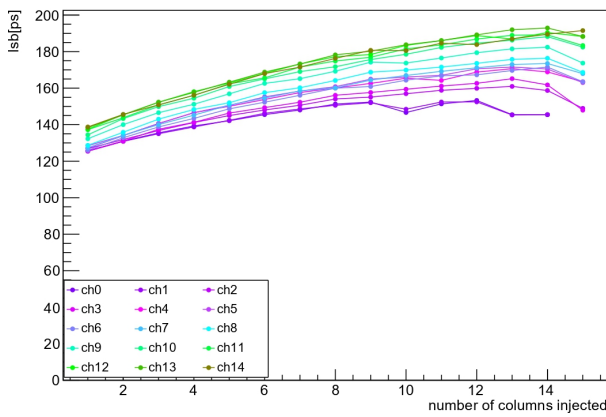


(a)

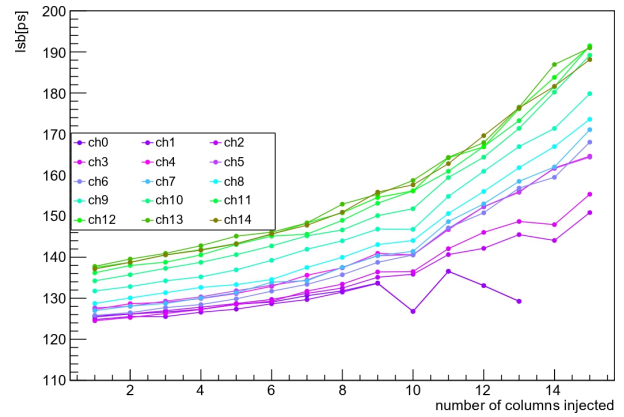


(b)

Figure 7.8: LSB for one of the pixels depending on the number of pixels in the same column injected, starting from the bottom (black dots) or top (red dots) of the column (a) TOT (b) TOA

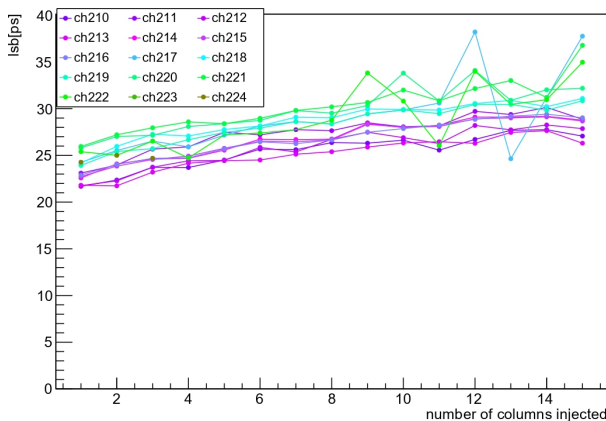


(a)

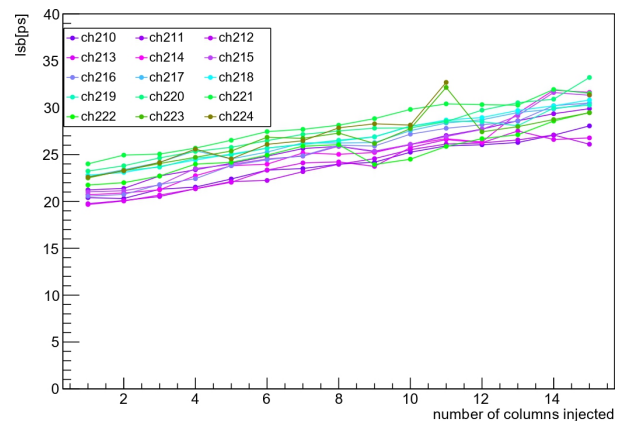


(b)

Figure 7.9: LSB TOT for column 0 (a) adding nearby columns first (b) adding faraway columns first



(a)



(b)

Figure 7.10: LSB TOA for column 14 (a) adding nearby columns first (b) adding faraway columns first

7.2 Lowest detectable charge and associated jitter

According to TDR requirements, ALTIROC should be able to set a threshold as low as 2 fC. This value was chosen to work comfortably with an LGAD signal of 4 fC (LGAD output charge after irradiation and before replacement, as expected when writing the TDR). The tests shown in this section were done while having TDR sensor-driven requirement in mind; however, by the moment of writing, this requirement was relaxed.

First, the threshold must be tuned to measure the lowest detectable charge. There are two types of thresholds: global per chip and individual per pixel. The total threshold used by pixel combines the per-pixel threshold applied on top of the per-ASIC threshold. Both thresholds are determined by varying the threshold for a fixed injected charge. With both thresholds known as a consistency check, the reverse is done: the injected charge is varied for the determined lowest threshold. The resulting charge should be close to the charge which gave the threshold.

Two thresholds (global and per-pixel) and the minimal charge are determined through the S-curve turn-on⁵. One set of such curves for the global threshold is shown on Fig. 7.11, where each line represents one pixel. Efficiency is the ratio between the number of pulses sent of a fixed charge and the number of pulses seen by ASIC. For the low threshold, the ASIC pixel is triggered by noise events, and the efficiency is 100%. When increasing the threshold, the efficiency stays at 100% and starts to decrease to 0 when the threshold is higher than the preamplifier output for this injected charge. The preamplifier noise gives the slope of this efficiency. Two populations can be observed below and above threshold ≈ 650 DAC, corresponding respectively to the columns equipped with VPA or TZ preamplifier. The value that gives 50% efficiency gives threshold value per pixel and among them, because there should be only one value per board, median value is chosen (not average to be less sensitive for outliers)

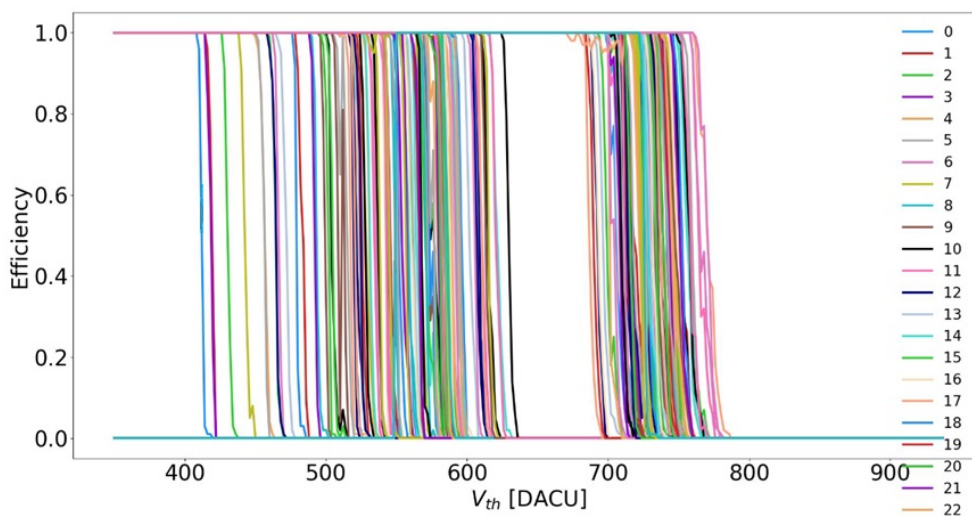


Figure 7.11: Efficiency as a function of the per-ASIC threshold. Each curve represents one pixel.

With the global threshold, the S-curves are quite dispersed, and to be able to trigger with each pixel at the same lowest charge, they need to be aligned with the in-pixel threshold.

Fig. 7.12 shows the S-curve as a function of the in-pixel threshold for the global ASIC threshold 560. Tuning values obtained for each pixel are shown in the same picture.

Finally, the lowest detectable charge was obtained. The requirement for the threshold to be qualified as the lowest is that

⁵probably should be called turn-off curves for per-ASIC thresholds

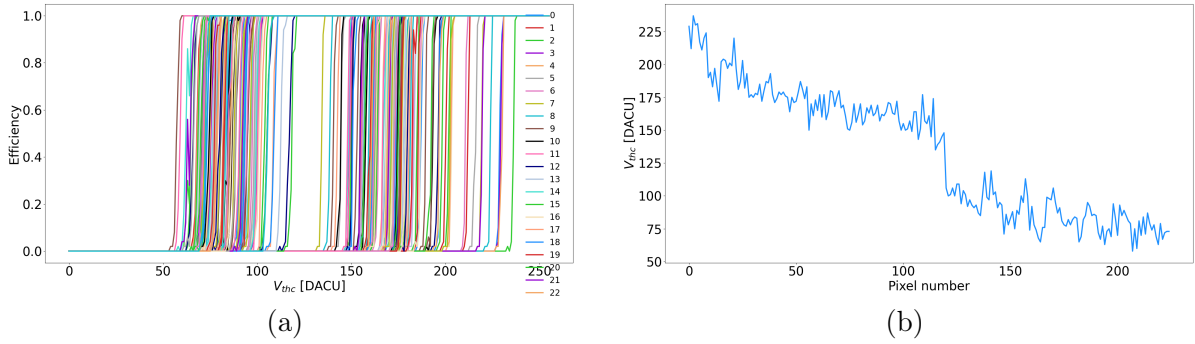


Figure 7.12: (a) Per-pixel threshold S-curves (b) resulting threshold values per pixel

1. Efficiency at zero charge is zero - otherwise, we're triggering on noise
2. There is no large spread between pixels or spikiness of each
3. The slope is reasonably steep.

Example charge s-curves (obtained by fixing the threshold and varying the charge) are shown on Fig. 7.13, where it can be seen that requirements 1) and 2) are satisfied. Typically, the lowest detectable charge on this plot is ≈ 6 fC. Requirement 3) is also visible to be good on the same plot, but additionally shown on Fig. 7.14 - to obtain it, turn-on curves are fitted with an error function whose $\sigma \equiv$ noise. All pixels noise has small values, and the difference is visible in values between first eight columns and last seven columns corresponding to VPA and TZ columns, respectively.

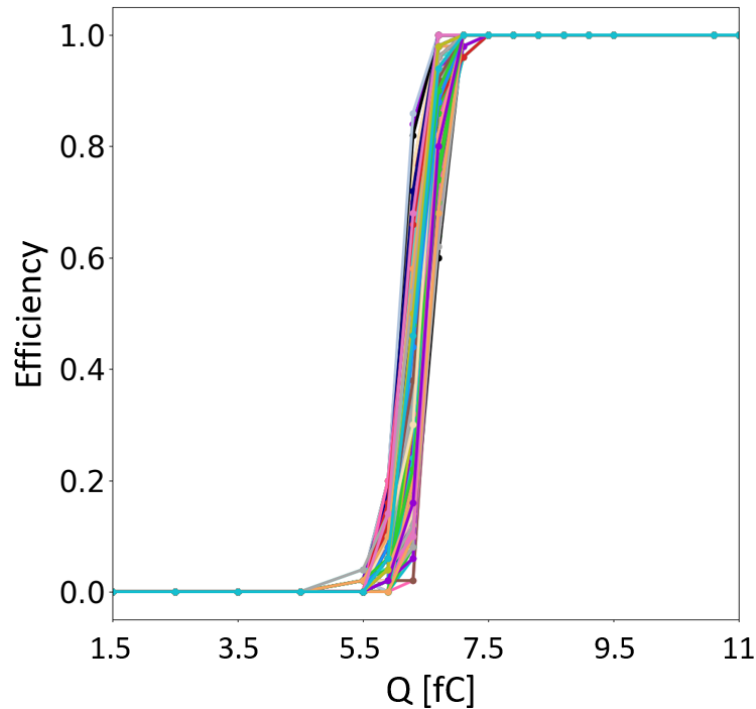


Figure 7.13: Example of lowest detectable charge S-curves. Each line correspond to one pixel. Obtained from varying the charge on top of fixed threshold (combination of per-pixel and global ones).

The lowest charge measurements were repeated for different boards in different configurations - a summary of them is given in Table 7.1. It can be seen that the target 2 fC threshold was

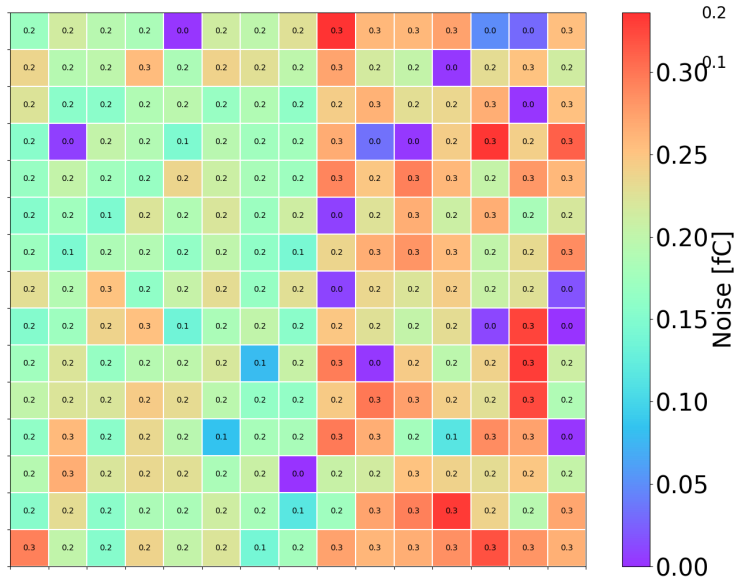


Figure 7.14: Table of noise (fit function width) seen in charge scan

| Board | Sensor | Whole matrix ON | One column ON |
|-------|--------|-----------------|---------------|
| 8 | No | 4.3 fC | 3 fC |
| 108 | No | 4.3 fC | 3 fC |
| 16 | Yes | 6 fC | 3.8 fC |
| 17 | Yes | 5.5 fC | 3.8 fC |

Table 7.1: Summary of lowest charge measurements

unreachable with ALTIROC2. Between two boards without a sensor and two boards with a sensor, the results are compatible. The higher (worst) the lowest charge with the sensor indicates that the combination of sensor and ASIC degrades performance. In all cases, injection is done per column (15 at the time), and when only one, same column, is activated, a better result is obtained compared to the whole matrix turned ON: 3.8 fC with the sensor. As was mentioned above, the ALTIROC threshold requirement changed compared to TDR due to progress in sensor design: it turned out in sensor testing that after irradiation, the charge obtained is higher than 4 fC expected before - therefore, the threshold doable by ALTIROC can also be higher.

Having a low enough (or not) minimum charge is not enough for ASIC to be considered operational in this configuration: the jitter requirements for the HGTD are defined in the TDR by the TOA jitter ⁶ of the ASIC at 10 fC (expected charge before irradiation) and at 4 fC (after irradiation). The same dataset for the lowest charge is used to determine jitter because TOA and TOT values are always saved in the measurement. Jitters have been extracted from the TOA dispersion at a given charge, multiplied by the TOALSB to convert to picoseconds, and are summarized in Table 7.2. At large charge when the electronics noise is negligible, both the ASIC alone and the boards with the sensor give about 30–35 ps jitter (no specific threshold optimization was done). At 4 fC jitter increase to 52 ps (respectively 99 ps) for the ASIC alone (respectively with sensor) due to the noise increases, and the minimal threshold is too high for a good time resolution. Doing jitter measurement at 4 fC only makes sense if the lowest detectable charge was lower than 4 fC - which, from Table 7.1 is only valid for non-sensor boards with one column activated, right at the boundary for sensor boards with one column; maybe it can work for no-sensor with all matrices,

⁶Also, the TOT jitter should be low for TOTC to be usable in timewalk correction

| Board | Sensor | 10 fC Whole matrix ON | 10 fC One column ON | 4 fC Whole matrix ON | 4 fC One column ON |
|-------|--------|--------------------------|------------------------|-------------------------|-----------------------|
| 8 | No | 35 ps | 30 ps | 75 ps | 52 ps |
| 108 | No | 30 ps | 32 ps | 80 ps | 52 ps |
| 16 | Yes | 35 ps | 32 ps | x | 99 ps |
| 17 | Yes | 35 ps | 31 ps | x | 96 ps |

Table 7.2: Summary of jitter at lowest threshold

but that is not the case for sensor boards and all matrices activated. Therefore, boards 16,17 jitter measurements are exploding at 4 fC jitter; With no sensor boards at 4 fC, the requirement is almost satisfied with the whole matrix and good enough with one column.

Based on the measurements taken, engineers made modifications to the design of ALTIROC3. Typically, pixels at the top of the column had a higher lowest charge, which was attributed to voltage drop along the column, due to which the injected signal appeared smaller than the one seen by pixels lower in the column. Re-routing improved this behavior. Also, high voltage decoupling was optimized (for the capacitor mounted on the board, specific value was chosen), giving lower noise. The latest testbench measurements show ALTIROC3 having a 2.5 fC threshold at cold.

7.3 TID test

ALTIROC2 board 7 (one without a sensor) underwent a Total Ionizing Dose (TID) test: goal is to irradiate with a dose that the chip will receive during HGTD operation before the foreseen replacement (200 Mrad). To cover uncertainty on dose rate delivered, chip was irradiated with 225 Mrad dose. During irradiation all the key quantities, part of them was shown above, were monitored. The hope for this test was that the chip would be able to maintain the initial or close-to level of performance, compared to unirradiated.

Tests were done at CERN with X-ray. The setup is shown on Fig. 7.15. The chip is mounted on the board (used for the rest of the measurements) and put inside the X-ray “box“. The board is positioned under the beam (whose diameter is 5.1 cm) in the center. The distance from the board chip to the source is chosen so that the whole chip receives the dose as uniformly as possible. This distance is 10.2 ± 0.1 cm. The dose rate is chosen to be 2.99 ± 0.05 Mrad/h to get the needed dose within the time setup was available for us (less than one week). The numbers were optimized through software provided by the X-ray facility ⁷. The temperature was stabilized at 22 degrees via chiller. The board inside of the X-ray setup is shielded and connected to the rest of the setup (through long cables) located outside: the oscilloscope, multimeters, power supplies, and computer to control everything.

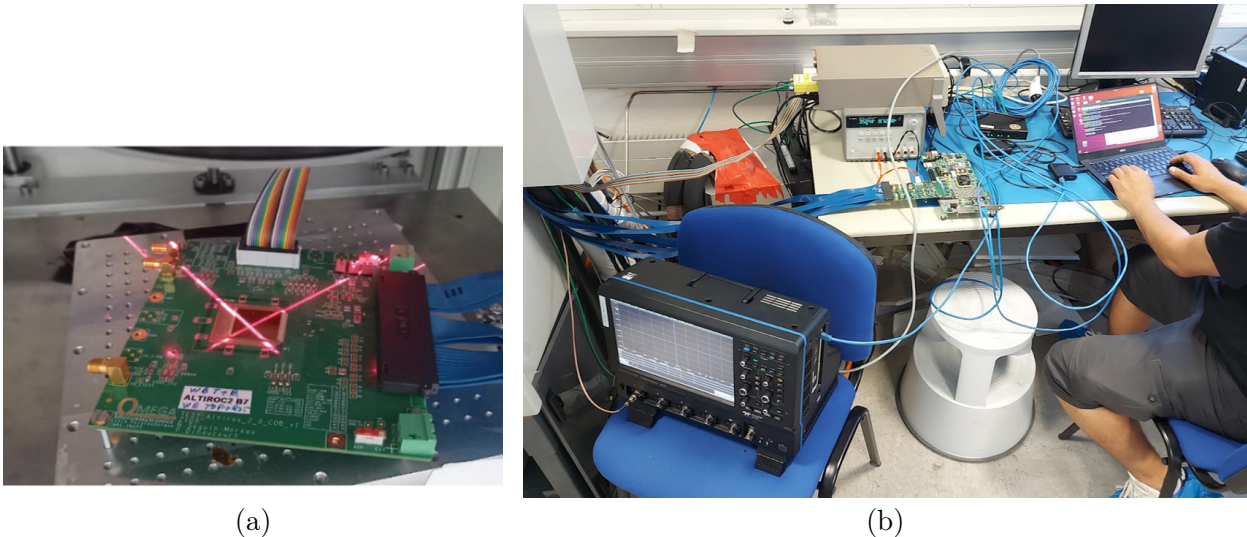


Figure 7.15: (a) Board 7 positioning under X-ray (b) setup outside of X-ray box to control/read the chip

To capture any potential anomaly, measurements should be continuously repeated. As measuring all columns takes time, it was decided to measure only one VPA and one TZ column (at the time VPA rejection was not finalized). The plots shown in this chapter are for TZ (15 pixels from column 8). All preamplifiers, discriminators, and TDCs in the column were turned ON (but not the whole matrix). The injection was made into the entire column simultaneously to measure the global threshold at two charges ($Q = 4.8$ fC, 9.6 fC), the per-pixel thresholds at two charges ($Q = 2.4$ fC, 4 fC), and the corresponding lowest charge, TOA and TOT LSB. From charge and TOA LSB measurements combined, jitter vs time dependence in picoseconds was obtained. Keithley multi-meter was used to monitor chip internal voltage parameters like v_{dda} (supply voltage for the ASIC analog part) v_{ddd} (supply voltage for the ASIC digital part). An oscilloscope was used to measure

⁷<https://ade-pixel-group.web.cern.ch/xray/>

the amplitude and noise from the preamplifier probe.

Fig. 7.16 shows the ASIC current and `vddd` values as monitored during the entire period. At about 150 Mrad, both an increase of the current and a decrease of the `vddd` have been observed. After power resets, the measurements returned to the nominal value and stayed stable, showing that this effect is probably not due to the irradiation itself. Such a behavior had already been observed over long measurements also on the testbench and attributed to instability in the firmware of the data-taking board. Therefore, `vddd` drop is not qualified as a problem caused by the dose received. TID measurements were repeated later with ALTIROC3 chip, and no `vddd` drop was observed. A short period of instability will be rejected later for the analysis (as it is unrelated to the test being done), except for the noise plot.

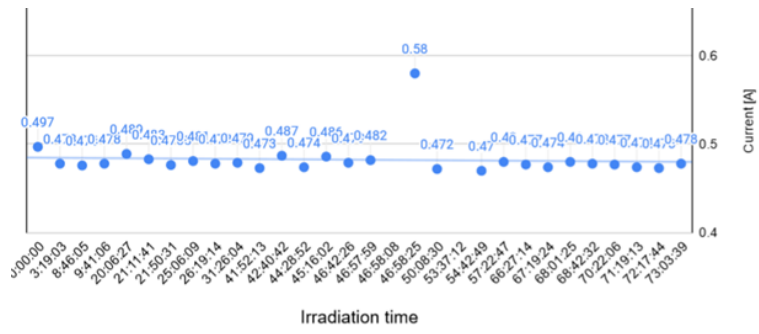
On most plots below, the first red vertical line marks the moment when a sudden `vddd` change happened. The green vertical line marks the moment of irradiation start, and the measurements were taken before that with an unirradiated board for reference. Each colored point corresponds to one pixel, the number of which is indicated in the legend, and the black line is the average over pixels at a given dose. The gap in data points at around 150 Mrad is related to data cleaning.

The main quantities being monitored are:

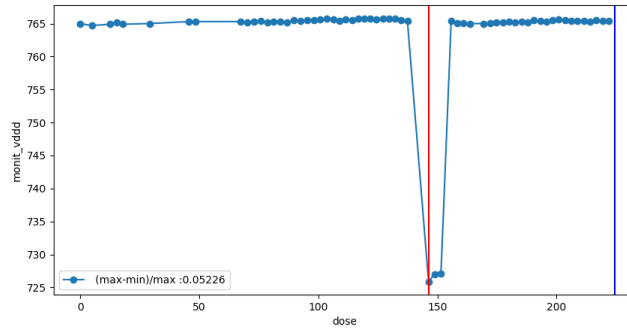
- Noise extracted from the width of S-curve ($Q=2.4$ fC) fit - Fig. 7.17. The drop at 150 Mrad is correlated to the abovementioned problem, but there is no noise increase under irradiation. Later, noise recovers and stays stable at the previous value (about 0.25 fC)
- Amplitude, as obtained from the difference between the global thresholds at $Q = 9.6$ fC and $Q = 4.8$ fC. A global threshold instead of a per-pixel was chosen because of finer granularity. Dependence is shown on Fig. 7.18, and a negligible decrease is observed
- Per-pixel threshold (Fig. 7.19a) is shown only for one of the charges because the other one behaves similarly. A slight increase in the pixel threshold is observed
- The lowest threshold (Fig. 7.19b) is also shown only for one of the charges. No variation is observed, which is compatible with the fact that the noise and the amplitude are not seen to vary.
- TOA LSB measured with the pulser (Fig. 7.20a) is well stable as is the respective jitter at 4 fC or 10 fC, shown in Fig. 7.21

Measurement with the external trigger has shown some variations in dose of TOT LSB (as it is illustrated on Fig. 7.20b - the absolute value of the TOTLSB is irrelevant for the timewalk correction, and this is not a significant problem) and completely failed for TOA LSB (therefore not shown).

Globally, this first ASIC full-size version has shown satisfactory results against TID irradiation. Given that later similar measurements were repeated with a different board, and there was no problem with an external trigger - board 7 external trigger behavior is interpreted as bad luck.



(a)



(b)

Figure 7.16: Observed during TID but not related to it (a) Voltage drop (b) Corresponding current drop

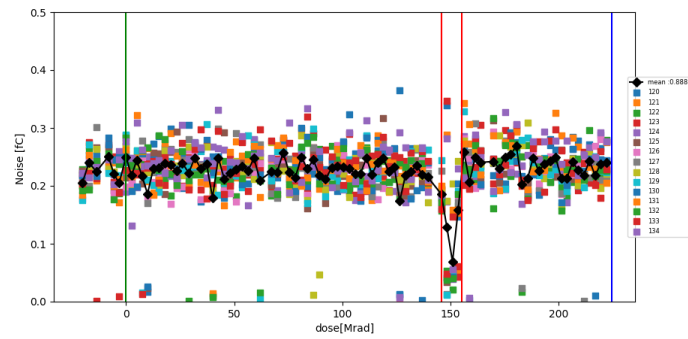


Figure 7.17: Effect of voltage drop shown in Fig. 7.16 on noise seen in charge scan

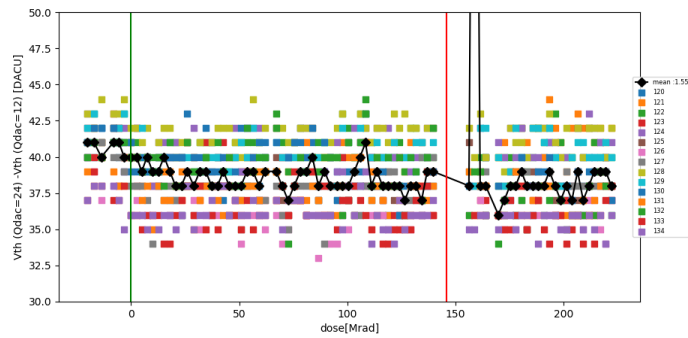


Figure 7.18: Amplitude proxy as function of dose

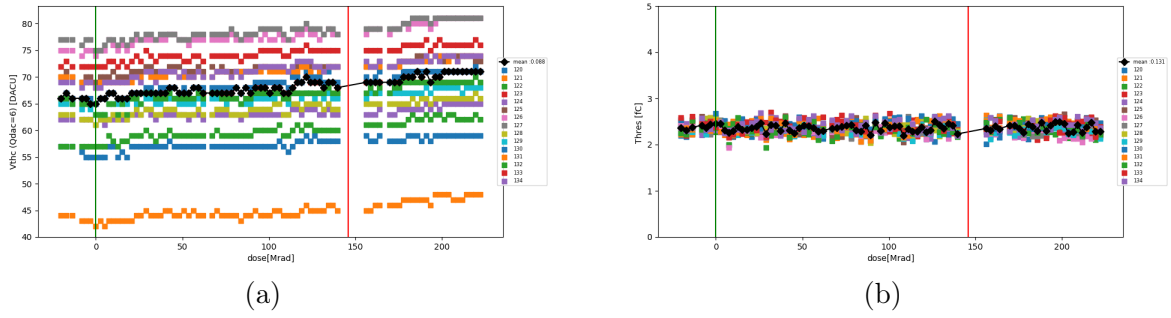


Figure 7.19: (a) Per-pixel threshold as a function of dose (b) Charge scan with threshold determined in Fig. 7.19a as function of dose

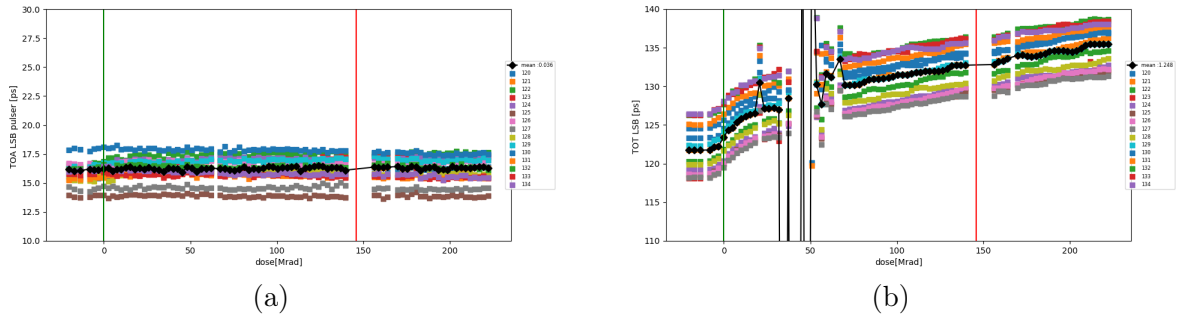


Figure 7.20: (a) TOA LSB (pulser) as a function of dose (b) TOT LSB as a function of dose

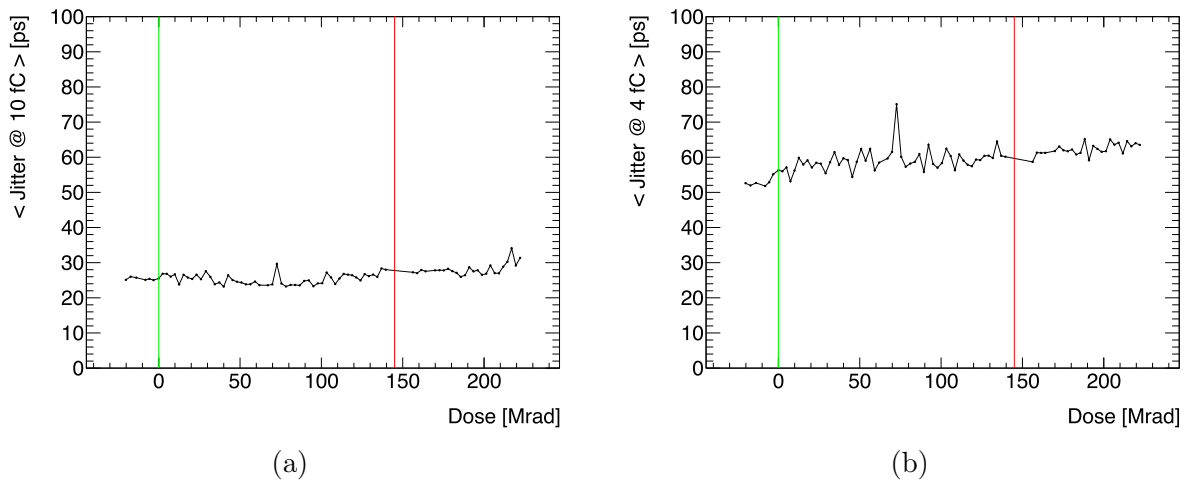


Figure 7.21: Average TOA jitter (over pixels) as function of dose (a) 10fC (b) 4fC

7.4 Low temperature test

In the future HGTD, the ASICs, among everything else, would be located in the cold vessel and operated at a temperature ≈ -30 °C. Consequently, the performance of the ASIC was measured at cold temperatures.

The climate chamber at OMEGA was used, shown in Fig. 7.22. The board inside is also partially visible. The rest of the setup is the same as in other tests: the FPGA is visible on top of the climate chamber connected with a long cable to a board that goes through a “gap” in a climate chamber. A computer with FADA (see Footnote 4) software controls the FPGA, which in turn controls the chip. The ASIC board and FPGA are powered by power supplies, as also shown in the picture. Keithley multimeter is also connected and constantly recorded.

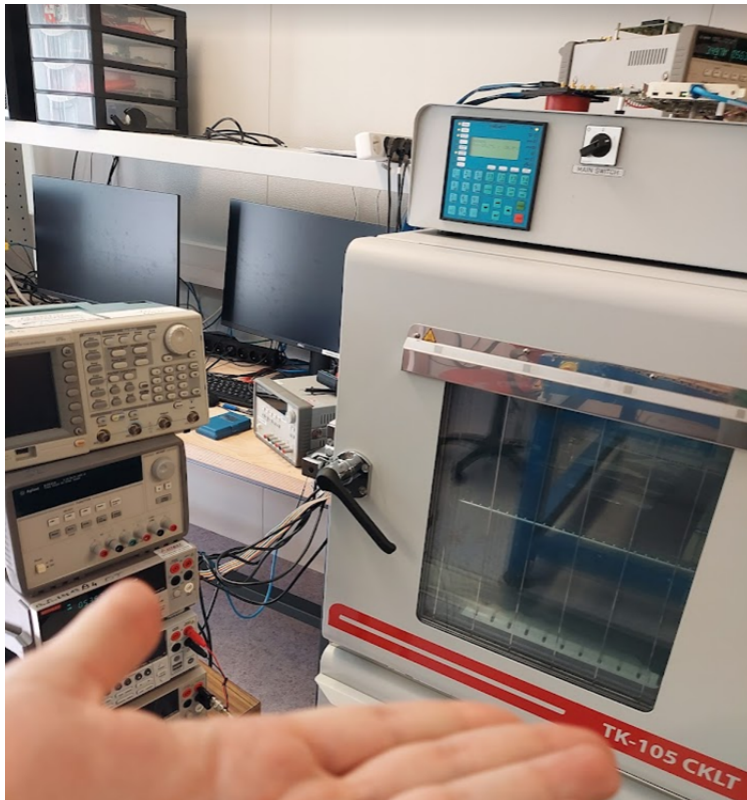


Figure 7.22: Climate chamber at OMEGA and the rest of the low-temperature setup

Two ASICs (both without a sensor) were operated under different temperatures up to as low as the target -30 °C. Results from only one will be shown because they are similar. Another board in another climate chamber was tested by a different group with the same conclusion and will not be shown here. After putting the board into the climate chamber, one needs to wait sometime before measuring for the chip temperature to stabilize, which is not instantaneous, and a chip internal temperature monitor can be used for monitoring: `vtemp` voltage is seen to be linear with temperature, as expected, shown on Fig. 7.23.

The injection was done into one column (TZ) simultaneously, and the whole column was activated. The same quantities as in the case of the TID test are shown on Fig. 7.24–Fig. 7.27b as a function of the temperature. Each temperature point is an average over several “batches” (same configuration taken multiple times), separately per pixel. Most quantities are reasonably stable. One exception is the per-pixel threshold drifting - this is expected⁸ and compensated by the output

⁸not surprising overall as the transistor threshold voltage is known to vary with temperature

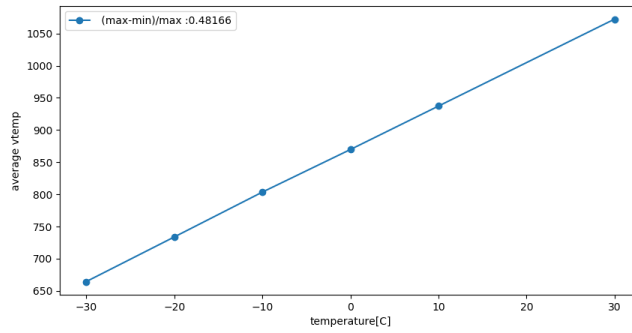


Figure 7.23: Vtemp against temperature

DC level of the preamplifier also drifting, but also that calibration derived at room temperature should be re-done at low temperatures like $-30\text{ }^{\circ}\text{C}$. There is also some increase of TOA jitter at a lower charge, only at hot room temperature ($30\text{ }^{\circ}\text{C}$), that drops to plateau already at $10\text{ }^{\circ}\text{C}$. Also, a small TOTLSB dependence is seen.

The performance of the ASIC at $-30\text{ }^{\circ}\text{C}$ is expected to be quite similar to that at room temperature.

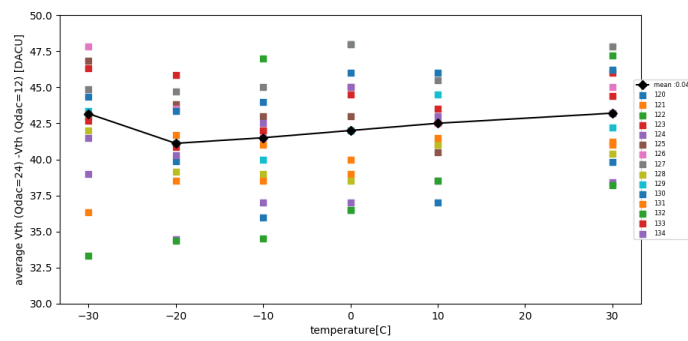


Figure 7.24: Amplitude proxy as a function of temperature

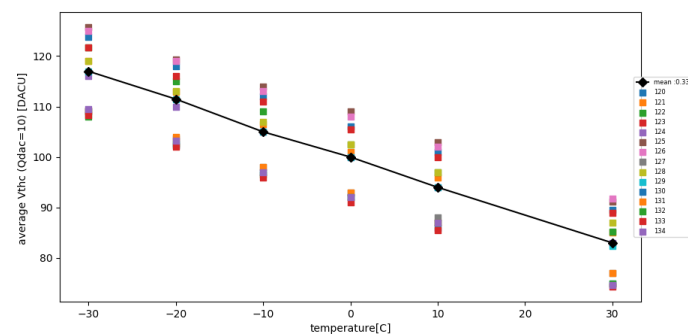


Figure 7.25: Per-pixel threshold as a function of temperature

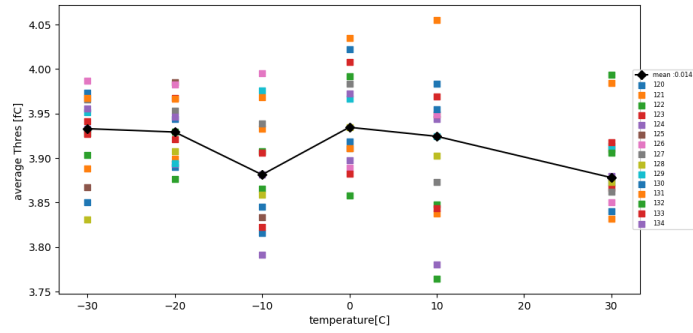
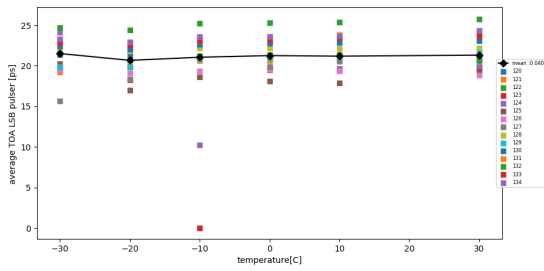
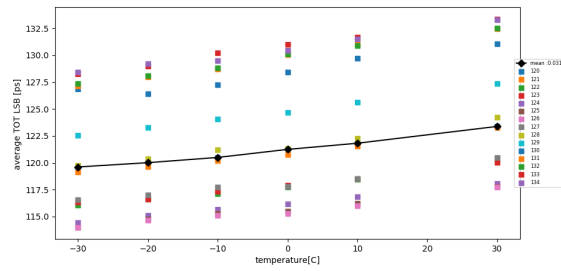


Figure 7.26: Charge scan with threshold determined in Fig. 7.25 as function of temperature

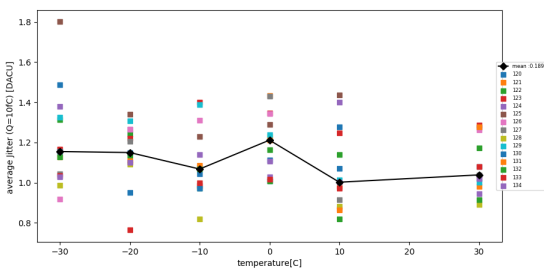


(a)

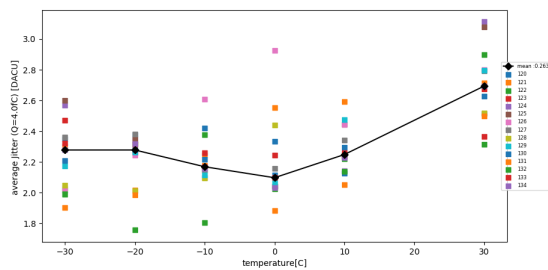


(b)

Figure 7.27: (a) TOA LSB (pulser) as a function of temperature (b) TOT LSB as a function of temperature



(a)



(b)

Figure 7.28: TOA jitter as a function of temperature at charge (a) 10 fC (b) 4 fC



8 - ALTIROC2/3 testbeam

8.1 Setup

ALTIROC2, the first full-scale chip prototype, had a new DAQ system (compared to ALTIROC1), developed at IJCLab (Orsay) and Omega (Palaiseau) - this also meant that the testbeam setup needed to be adjusted. Testbeam-specific DAQ development was done by IFAE Barcelona. Sensor is the same as in ALTIROC1. The setup used at CERN SPS (pion beam) is shown on Fig. 8.1 and key components are labeled - this setup is also used for measurements shown in Sec. 8.2. ALTIROC3 timing measurements (Sec. 8.4) were done in DESY with an electron beam, but the setup is mostly the same. An additional component is a trigger interface board (developed at IFAE) that receives a trigger from TLU and tells ASIC to save data. ASIC data taking is done through Alvin¹, integrated into the EUDAQ framework. Alvin output format is a text file with output from several (typically five) bunch crossings, recorded at each trigger. If there were a pixel hit at a given bunch crossing, in output it's represented with a line containing number of pixel, TOA and TOT. The converter was written to translate this text file in ROOT ntuple, compatible with the software written for ALTIROC analysis. As in the ALTIROC1 case, the ASIC+LGAD hybrid, telescope, and time reference device are the main components.

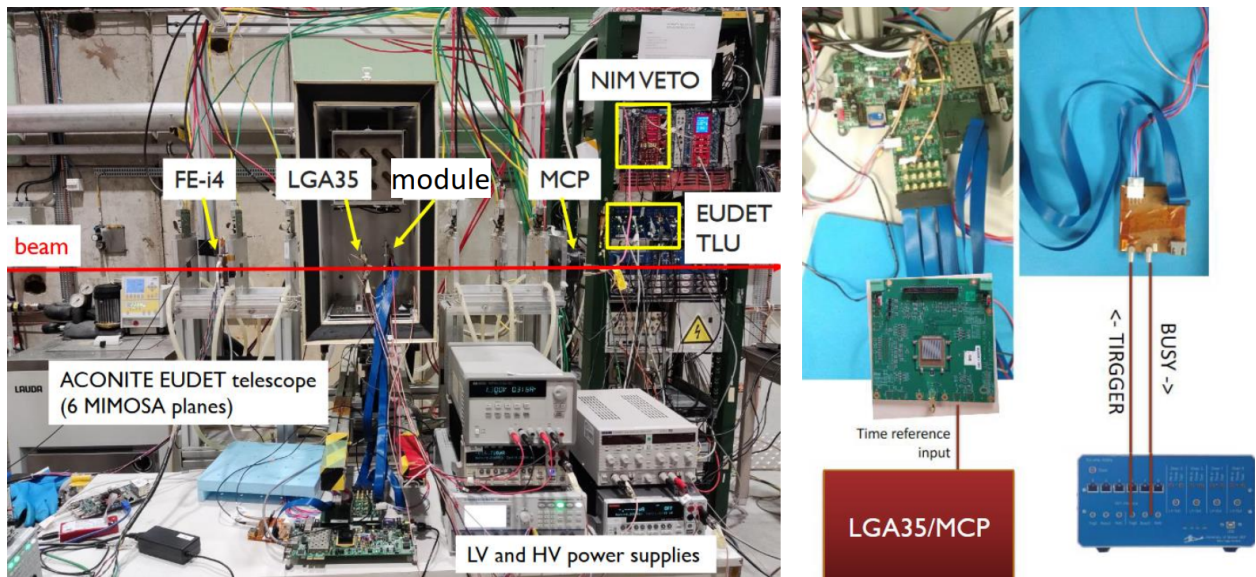


Figure 8.1: ALTIROC 2/3 SPS testbeam setup

The telescope is the same as for the ALTIROC1 case, it is an EUDET telescope consisting of 6 planes (sometimes not all of them are used if one turns out to be noisy), each with pixel side of $18.5\mu m$. Positions of plane hits are fitted with a straight line, this line is then extrapolated to hybrid plain providing position where ASIC was hit.

Time reference is new compared to the previous setup - here it's MicroChannel Plate (MCP) Photomultiplier Tube with negligible time resolution compared to hybrid's, therefore instead of solving a system of equations, one can just take and fit the difference in the form

$$\Delta T = \underbrace{-TOA \times LSB_{TOA}}_{t_{ASIC}} - \underbrace{t_{MCP}^{trig,CFD} - t_{clock}}_{t_{MCP}} \quad (8.1)$$

¹<https://gitlab.cern.ch/ifaepix/alvin>

The minus sign in front of TOA is due to falling edge reference used by the TDC . The LSB is taken from calibration measurements, similarly to Sec. 7.1.1 where FADA is used, but for testbeam done with Alvin for consistency with Alvin data taking. Clock is implicitly always there for TOA and inserted explicitly for t_{MCP}^{trig} reference to do an apple-to-apple comparison. Contrary to ALTIROC1 setup, the scope trigger is not issued from the ASIC and is not synchronous with the 40 MHz clock, so the MCP time should be referenced to the clock. The trigger is based on a region of interest in the FEI4 plane and is handled by the Trigger Logic Unit (TLU). When triggered, the TLU sends commands to the ASIC (through custom trigger board) to save the timing data (through FPGA), oscilloscope to save full waveforms of the MCP and analogue ASIC probe and telescope to save the tracking data. Both t_{MCP}^{trig} and t_{clock} are obtained from digitized by oscilloscope MCP and clock pulses, respectively. The recorded pulse is analyzed with PyAna ² , giving $t_{MCP}^{trig,CFD}$ the moment where MCP pulses cross certain amplitude fraction and t_{clock} is the moment when the clock pulse crosses zero voltage (for which clock pulses are shifted such amplitude oscillates around zero). Resulting ΔT distribution is looking Gaussian, and the sigma of its Gaussian fit gives the hybrid time resolution.

MCP resolution was checked in 3 ways, all methods giving 3–7 ps $\lll \sigma_{hybrid}$:

- Directly by solving the time resolution system as before with a third device being LGA35 (time resolution comparable to ASIC)
- Looking at resolution of time difference between LGA35 and MCP - which is close to the resolution of LGA alone that would be impossible with large MCP resolution
- Using the slope of the average (over many events) digitized MCP pulse, jitter is expected to be given by $N/\frac{dV}{dt} = t_r/A/N$ with N (noise) and A (amplitude), also measured from the oscilloscope data

With MCP resolution checked, CFD was selected by solving for MCP resolution with different CFD values. Resulting in choice of CFD at 50% of the amplitude (denoted as CFD50) for Eq. 8.1, consistent with the fact that MCP amplitude derivative is maximal near half of the amplitude. However, CFD optimization does not bring much because MCP pulse is very sharp.

An example of testbeam event, seen by the oscilloscope, is shown on Fig. 8.2. The periodic green line is the clock, in black - MCP pulse, in blue - preamplifier pulse (also digitized by the scope). On trigger, all the event data is saved to the PC controlling the setup. Event data includes three independent streams: ASIC output, telescope output (not shown in the picture), and oscilloscope information.

Both ASIC and oscilloscope information are needed to find the ΔT shown in Eq. 8.1, and they need to be synchronized for the difference to work: the event labeled N from the ASIC stream should also be event number N from the oscilloscope stream - due to the complexity of the software chain and hardware setup, possible unintentional re-configuration between different runs, nothing guarantees synchronization. It can be checked in two ways: with TOA and TOT information, results of which are shown on Fig. 8.3. Comparison of TOA as provided by ASIC and t_{MCP} should give linear dependence, which is the case. Comparing TOT (from ASIC) and probe amplitude (from oscilloscope) should give a known linear dependence at the beginning and then reach a plateau, as seen before in ALTIROC1. Both were observed, except for missynchronization for small part of data as seen on TOT-amplitude correlation via “blob“ at low probe amplitude values and TOT around 20. Those TOT values really belong to the core of distribution. It only happens at the end of the runs. No correction was needed in ALTIROC2, “blob“ was removed by probe amplitude selection. However, it will not be the case for ALTIROC3 setup (see Sec. 8.4). To obtain the tracking results,

²<https://gitlab.cern.ch/atlas-hgtd/TestBeam/PyAna>

the telescope and the ASIC streams should be synchronized, and the oscilloscope is not used. As ASIC and oscilloscope synchronization was confirmed and ASIC and telescope information follow the same “data path“, ASIC and telescope are assumed to be synchronized.

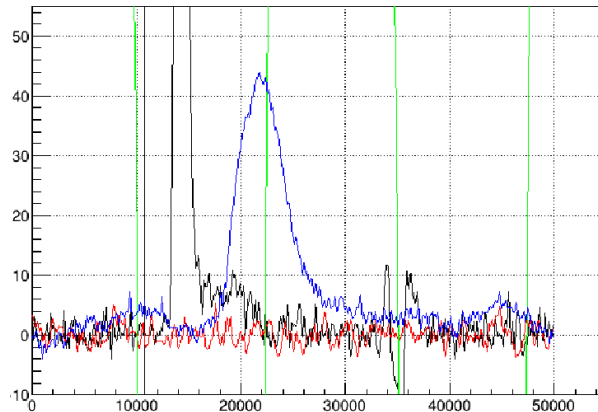


Figure 8.2: One testbeam event. MCP is shown in black, premplifier probe in blue. Green lines are half-periods of 40 MHz clock with much larger amplitude.

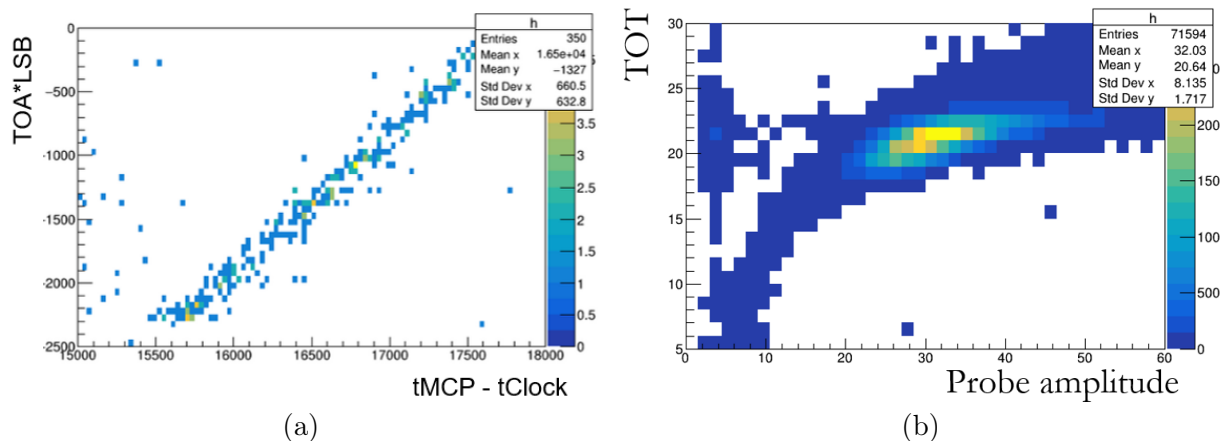


Figure 8.3: ASIC-oscilloscope data streams synchronization with (a) TOA (b) TOT

Therefore, the updated testbeam setup (hardware and software) was verified, and one can move on to measurements with it.

8.2 ALTIROC2 timing

The hope for ALTIROC2 time resolution is that it should not degrade much compared to ALTIROC1, and overall behavior should be similar. It has been observed that the TOA-TOT coupling is still there, similar to ALTIROC1 (Fig. 8.4). It was also observed that “amplitude“ of coupling depends on the threshold: the difference between the minimum and maximum of the S-shape is larger for a lower threshold, as shown on Fig. 8.4.

The starting point for time resolution extraction has changed, as described above: two reference SiPMs were replaced by MCP, and therefore, there is no need to solve the system. The timewalk correction is done in the same way. A summary of the configurations tested at room temperature is given in Table 8.1. The bias voltage is chosen to be as high as possible without creating noise.

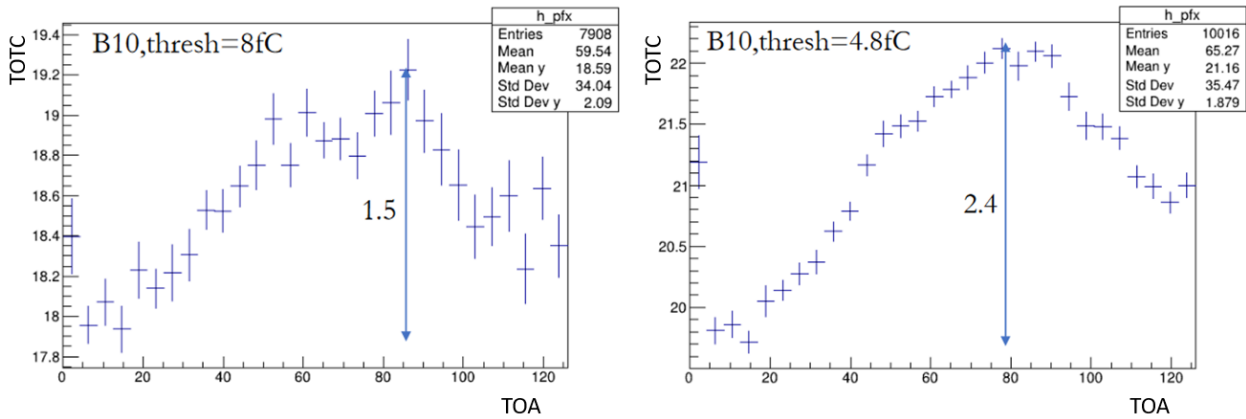


Figure 8.4: TOA-TOT mean with (a) 8 fC threshold (b) 4.8 fC threshold

All TZ pixels are activated (half of all the pixels), and the beam was positioned (by moving the ASIC relative to it) to be roughly in the center of TZ pixels. Two thresholds of 8 and 4.8 fC were tested. The preamplifier probe was activated and connected to pixel 156. Despite ALTIROC2 having many more pixels than ALTIROC1, at the time, the focus was on measuring resolution in one pixel - the one from which the preamplifier probe was outputted³. As a validation of the new prototype, measurements were re-done similarly to ALTIROC1. Measurements of many pixels were done in ALTIROC3 (which doesn't have major modifications compared to ALTIROC2), and shown in Sec. 8.4.

| Batch | Board | Bias voltage | Pixels activated | ASIC threshold | Probe pixel |
|-------|-------|--------------|------------------|----------------|-------------|
| 301 | B10 | -200 V | all TZ | 4.8 fC | 156 |
| 302 | B10 | -200 V | all TZ | 8 fC | 156 |

Table 8.1: Summary of ALTIROC2 testbeam batches

For organizational reasons, TOA LSB was not known during the data-taking, and workaround was introduced to find the right value: scanning over LSB values and assuming that the right LSB value is the one that minimized the resolution. The variation of ΔT distributions (before timewalk correction) with different LSBs is shown on Fig. 8.5. From set of LSBs on figure nominal LSB turns to be the one that minimizes the resolution. Using instead value smaller by 1.1 ps, resolution degrades by 13 ps. Using the LSB value larger by 1.1 ps gives resolution 3.5 ps larger and taking even larger LSB values degrades resolution even more, until the point when distribution becomes non-Gaussian. Later, when the calibration became available, it was checked that the LSB obtained from the minimization is the same as the calibration value. The overall idea is that one cannot minimize the resolution lower than what it is; however, the approach should be used with care (it was only used because no other alternative was available) : in future HGTD, there would be no reference devices to calibrate LSB in that way; one should be able to obtain the right value from the calibration (it will turn out to be difficult, as will be shown in ALTIROC3 section) and a poor knowledge of the LSB translates into systematic uncertainty on time resolution.

A summary of the time resolutions obtained with different timewalk correction methods is shown in Table 8.2, and it can be seen that they are similar to ALTIROC1. Correction for TOA-TOT non-uniformity was applied but did not improve the resolution. As before, time resolution dependence

³It was pixel 156

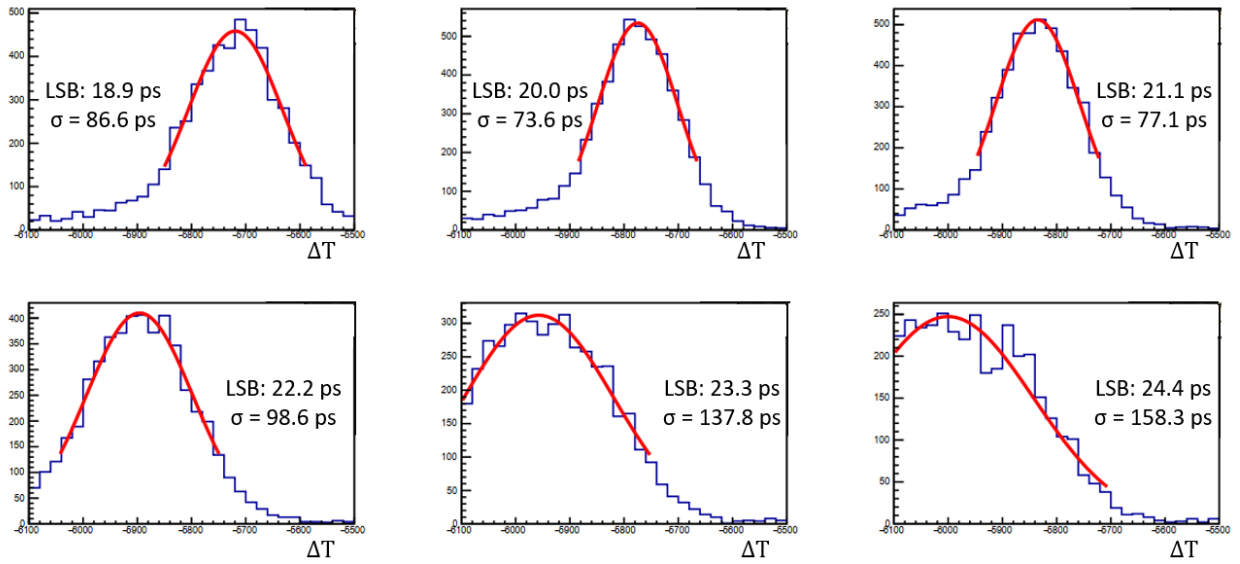


Figure 8.5: change of ΔT with LSB

on amplitude is seen, as indicated by improvement in “Probe amplitude, distribution core“ column.

| Batch | TW-uncorrected | Probe amplitude TW | Probe amplitude TW, distribution core | ASIC TOT TW | probe TOT TW |
|-------|----------------|--------------------|---------------------------------------|-------------|--------------|
| 301 | 77 ps | 49 ps | 45 ps | 50 ps | 51 ps |
| 302 | 64 ps | 45 ps | 42 ps | 53 ps | 46 ps |

Table 8.2: Summary of ALTIROC2 testbeam results with Table 8.1 batches

8.3 Tracking, efficiency and interpad

The tracking efficiency of the ALTIROC2 hybrid device have been measured using the telescope information. Hit efficiency is

$$\varepsilon_{hit} = \frac{N_{tracks}^{ASIC\,fired}}{N_{tracks}} \quad (8.2)$$

For this measurement, a MIMOSA telescope is used, with around 10 microns spatial resolution of extrapolated to ASIC plane track position. From each plane of MIMOSA, a straight line is fitted using the PaTrack ⁴ software and extrapolated at the hybrid front face. Only events with a single track reconstructed are kept in analysis to avoid any potential ambiguities. If the track matched the hybrid, a hit associated with a TOA and TOT should be recorded in the ASIC data stream.

The resulting efficiency, defined with Eq. 8.2, is shown on Fig. 8.6. This map is obtained as the ratio of the other two maps: distribution of tracks going through the ASIC with hit registered divided by just distribution of tracks. The color code shows the efficiency from 0 to 1. Each square (in yellow with 100% efficiency) corresponds to an ASIC pixel with an expected side size of roughly 1.3 mm. Between the pixels is the interpad region, which is a no-gain region, and when the particle is going through the hit is typically not registered - this is expected. Only 20 ASIC pixels are shown corresponding to the size of the tracking device used for the trigger.

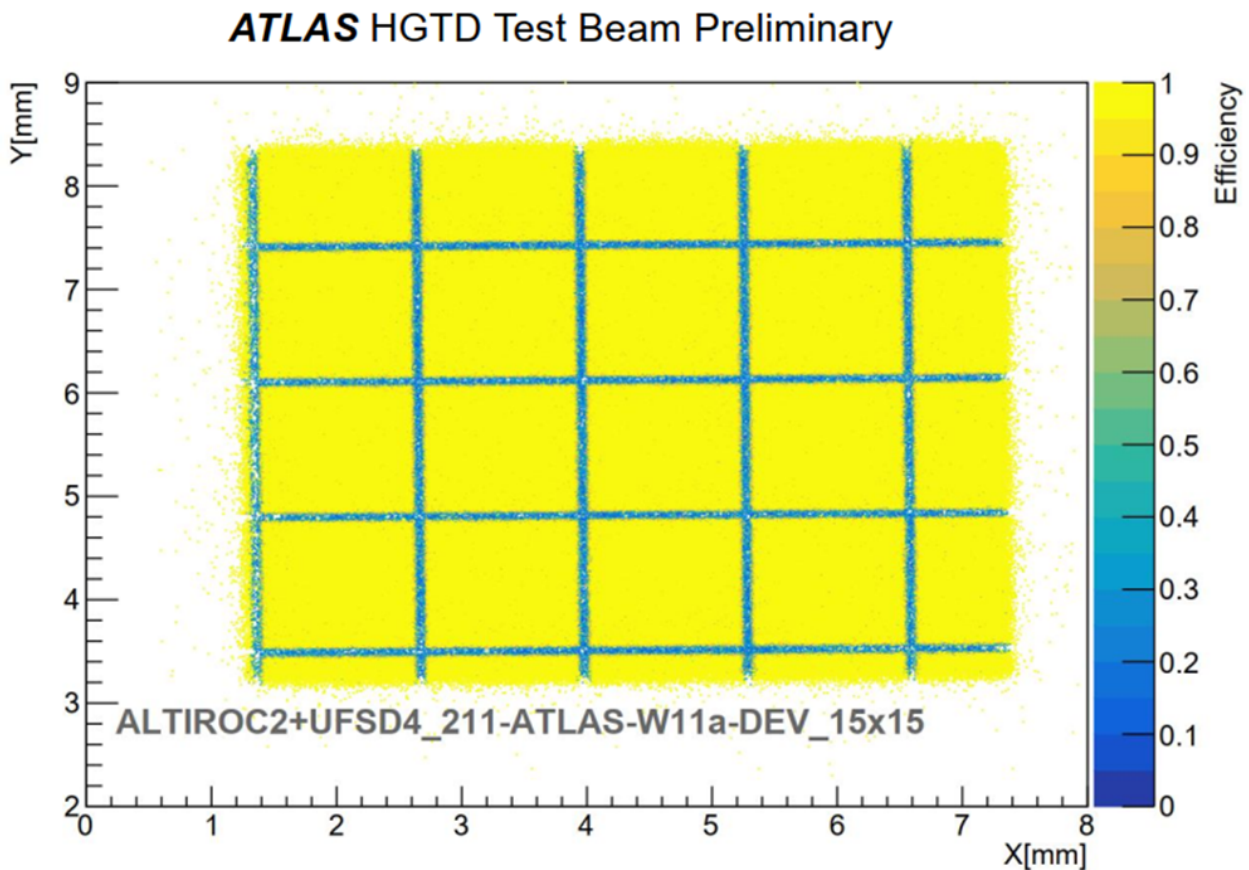


Figure 8.6: Efficiency map of ALTIROC2+LGAD measured as ratio of the reconstructed tracks with a hit seen in ALTIROC to all the reconstructed tracks penetrating the module area. 100% efficiency was achieved outside of inter- pad region. Only fraction of 15x15 pixel matrix is visible because of triggering on smaller pre-defined area.

⁴<https://gitlab.cern.ch/atlas-hgtd/TestBeam/PaTrack/-/tree/master>

A near 100% efficiency is obtained in the core of the pixel, but it's also important to check that the area on which efficiency is high is as large as it should be - determined by the size of the interpad region. It can be seen already on Fig. 8.6 that interpad size is uniform (there are no columns/rows that are much larger than others) and that the size of interpad is smaller than 100 microns. A more detailed investigation was done. For gaps seen to be parallel to the Y axis, each gap can be looked at separately by taking the relevant slice and projecting it into the X axis. For example, to obtain the distribution for a vertical gap in the top-right corner, one would make the selections $Y > 7.5$ and $X > 6$ to isolate that one gap and project it into X . The resulting efficiency for one gap is shown on Fig. 8.7a. Drop corresponds to the center of interpad where if the track is going through, the hit never gets registered. Efficiency is around one near the edges because those are pixels (only part of their 1.3 mm size is shown). All the other individual gaps are obtained the same way, with one difference being for horizontal gaps - they are projected in Y .

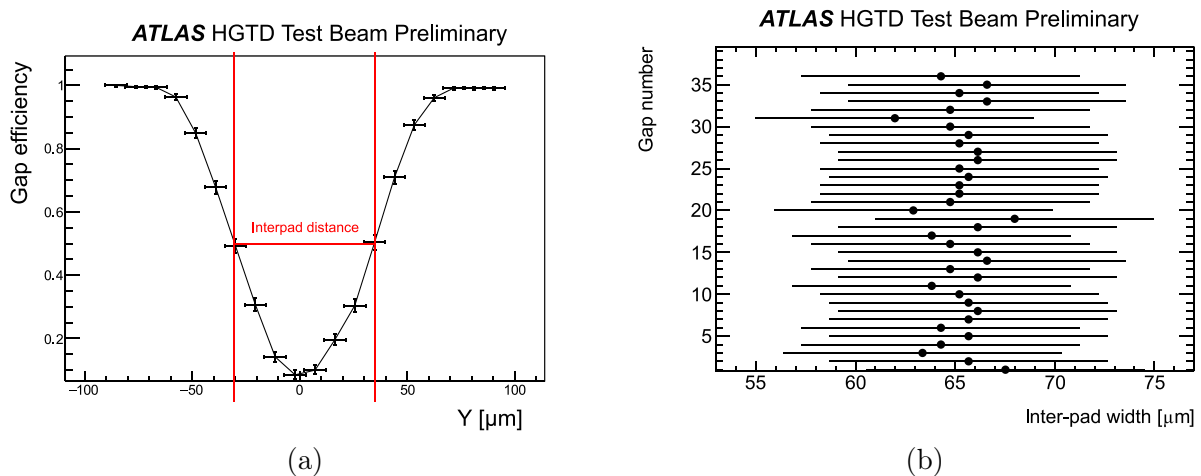


Figure 8.7: (a) Efficiency versus y of ALTIROC2+LGAD zoomed around an interpad region. Vertical lines mark 50% efficiency obtained with linear interpolation, difference in their positions is taken as the interpad distance. (b) ALTIROC2+LGAD : gaps widths taken from 50%-50% efficiency, obtained from linear interpolation, shown for each gap from 2D efficiency map, together with uncertainty. Vertical and horizontal gap widths are combined in this plot.

The gap size is defined as width at 50 percent efficiency and is obtained from a linear interpolation⁵. Interpolation is visible on Fig. 8.7a. For that one gap shown, the gap size is 67.5 microns. All the gap sizes are shown on Fig. 8.7b. Each gap visible in Fig. 8.6 is assigned a unique number (Y axis) and plotted against its width. How the gap number is assigned is irrelevant because all of them are seen to have a similar width of roughly 65 microns, well overlapping within uncertainty. The gap size obtained is within the sensor requirements. With the gap size known, one can obtain the fill factor, which is defined as the ratio of the gain area (where hit can be registered) to the total. The dependence of the fill factor on gap size is shown on Fig. 8.8, where it can be seen that the measured gap size corresponds to the fill factor around 90%, satisfying the requirement.

⁵Alternative is making S-curve fit similar to Fig. 7.13 but given the tracking resolution it will not change anything

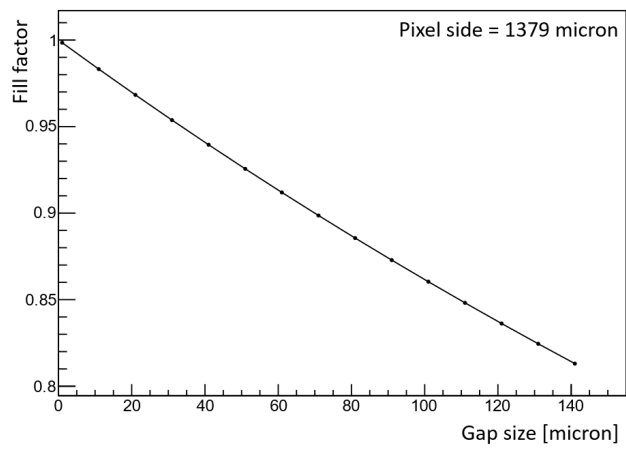


Figure 8.8: Hybrid fill factor depending on gap size (given by sensor)

8.4 ALTIROC3 timing

First ALTIROC3 testbeams were done at DESY in September, November 2023 and the setup together with the board 27 are shown in Fig. 8.9. At DESY, there is an electron beam instead of a pion, with 5 GeV energy. Tracks reconstructed in the telescope are no longer straight lines due to multiple scattering⁶. Another difference compared to the SPS setup is the usage of a digitizer instead of the oscilloscope to digitize analog signals like a clock and preamplifier probe amplitude - the advantage of a digitizer is that it has more channels, which is convenient to test multiple sensors in parallel to ASIC, but for ASIC itself no advantage is gained. The software was adjusted to use a digitizer with a new output format. The software was adjusted to use EUDAQv2, as previously used EUDAQv1 had already become obsolete. Contrary to ALTIROC2, missynchronization was seen for large fraction of the data (unlike Fig. 8.3) and was corrected by a dedicated algorithm.

Results shown in this section are mostly obtained with batch 1103 (board 27, IME-IHEPv3 sensor without carbon, bias voltage 149 V, all 225 pixel activated, threshold 10.8 fC, -30 °C) data of the November testbeam - except the last section (Sec. 8.4.5) where summary is given.

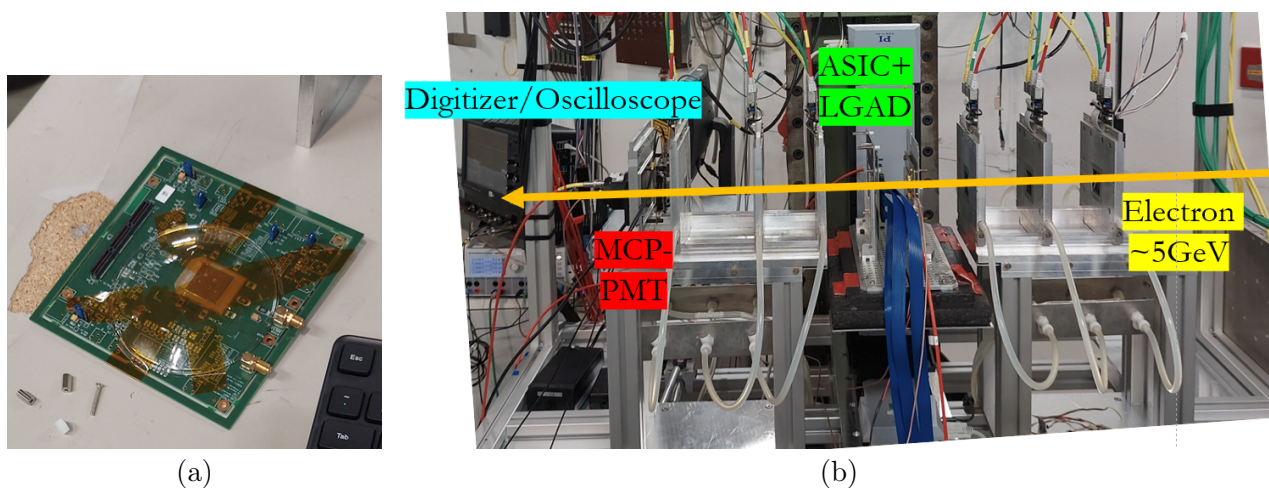


Figure 8.9: (a) ALTIROC3 board tested at DESY (b) DESY testbeam setup

MCP is still used as a time reference, and the resolution is extracted according to Eq. 8.1. This time, measurements were done for many pixels. For each pixel, LSB from calibration was used. Resulting timewalk-uncorrected time resolutions are shown in Fig. 8.10. It can be seen that they are outside of the HGTD requirement and much above⁷ the ones seen in ALTIROC1,2.

Investigation showed that there are two problems:

- LSB from calibration does not give the correct value (overall scale problem)
- There is not just one LSB valid for the whole TOA range (0-127), but at least two LSB values that should be used. Once overall LSB scale is fixed, tuning is still needed to have the correct value, depending on the TOA sub-region

8.4.1 LSBs from resolution minimization

Overall scale can be found by minimizing time resolution as a function of LSB, which was introduced in ALTIROC2 (see Fig. 8.5). The resulting dependence of resolution on LSB is shown on Fig. 8.11 for one of the pixels for TOA $0 < TOA < 127$ (inclusive) on the green curve. The

⁶tracking results are not used for timing measurements shown in this section

⁷part of the discrepancy, as was found later, is due to bug in calibration software

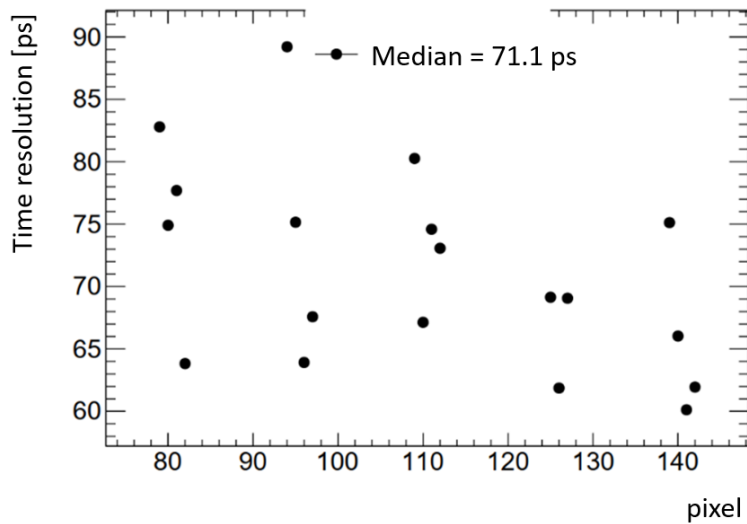


Figure 8.10: ALTIROC3 time resolutions without timewalk correction and using LSB obtained from calibraton

minimum of parabola obtained shows the right TOA LSB ballpark, in this case at around 17.5 ps, with a resolution of around 55 ps. The parabola is quite sharp, showing that LSB mismeasured by ± 1 ps can lead to resolution degradation of up to 10 ps.

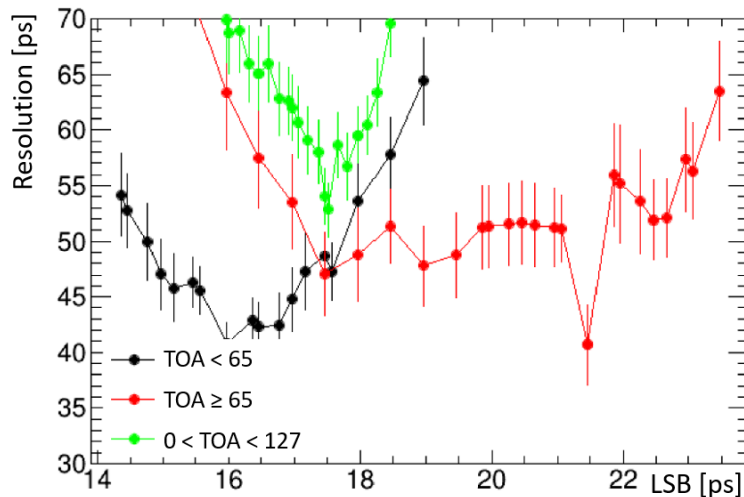


Figure 8.11: ALTIROC3 time resolution dependence on TOA LSB. Green curve curve obtained for $0 < TOA < 127$. Black (red) curve obtained for $TOA < 65$ ($TOA \geq 65$).

In Fig. 8.11 black and red curves show LSB minimization done separately for $TOA < 65$ (later called left (L) TOA sub-region with L LSB) and $TOA \geq 65$ (later called right (R) TOA sub-region with R LSB), respectively. The division is done at 65 because it was observed by looking at TOA distribution, showed on Fig. 8.12a, that the mean count clearly changes around that value. This would not be the case if all TOA bins had the same size in time units, but this observation suggests LSB non-uniformity with a larger value in the second TOA half-range. Sub-range parabolas on Fig. 8.11 shows that

- LSB of lowest sub-range is lower compared to higher sub-range
- The width of the sub-range parabola is wider than the full range, making sub-ranges less sensitive to having a wrong LSB . LSB of two sub-ranges are different by 2–3 ps

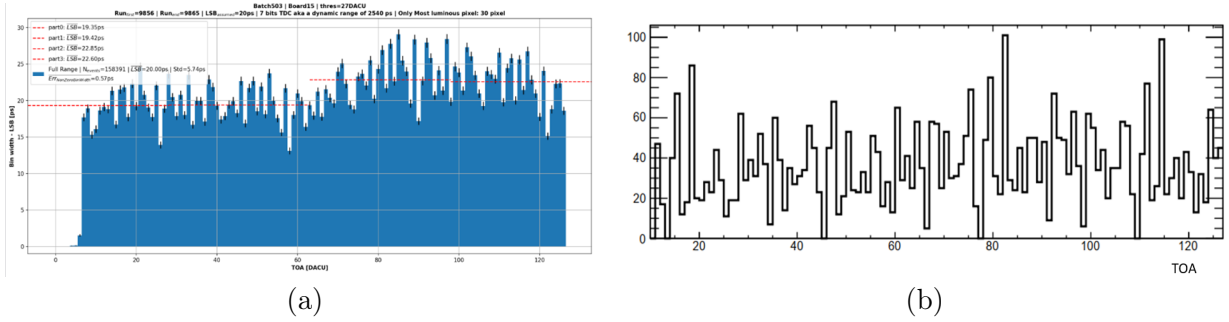


Figure 8.12: (a) ALTIROC3 testbeam TOA distribution, mixed from many pixels [78]
 (b) ALTIROC3 testbeam one pixel initial TOA distribution

In the way minimization method was used, it is subject to instability: significant downward fluctuations can be created during manipulation of ΔT through LSB adjustment: two (lowest in resolution) points in the scan are very close to neighbors in terms of LSB but better in resolution by 5 ps. It can be improved though, by, for example, fitting the parabola and taking the minimum of fit - in order to smooth the dependence.

8.4.2 LSBs from $t_{MCP} : TOA$ fit

To avoid LSB extraction from spiky unstable dependence shown above, another method was introduced, relying on linearity between time of the MCP measured by digitizer⁸ and TOA of ASIC - it is shown on Fig. 8.13. Focusing on the black line for a moment: it is a fit of correlation, assuming that LSB is the same in the whole TOA range. Its value is 16 ps. This method of getting the LSB is more stable than the one shown on Fig. 8.11 and will be used to obtain final numbers for the resolutions.

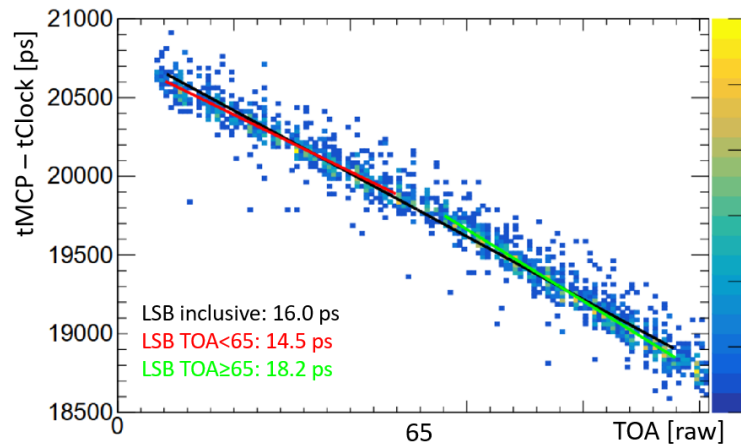


Figure 8.13: ALTIROC3 time of the MCP(digitizer) vs TOA (ASIC) linearity used for TOA LSB extraction

Comparison between LSB obtained from calibration and the one obtained from fit using digitizer information gives different results by up to 2 ps. Same applies to method shown in Sec. 8.4.1 for TOA inclusive case. This is part of the reason why the first attempt of LSB extraction shown in Fig. 8.10 gives bad results - overall LSB scale is wrong.

With the overall scale being fixed, one can look again at Fig. 8.13 focusing now on TOA sub-range dependence. Sub-range fits are shown in red and green, and values obtained⁹ are written in

⁸now used instead of the oscilloscope

⁹this is a different pixel from the one shown on Fig. 8.11

legend - L,R LSBs are different by ≈ 4 ps. At the moment of writing, it is not possible to reproduce the same behavior in testbench ¹⁰ - as shown on Fig. 8.14 (obtained by mixing TOA distributions of many pixels). Inclusive LSB is between the left (L), right (R) LSBs - using inclusive TOA LSB does not give the minimum of either sub-range, which is why the resolution is worse when using only one LSB .

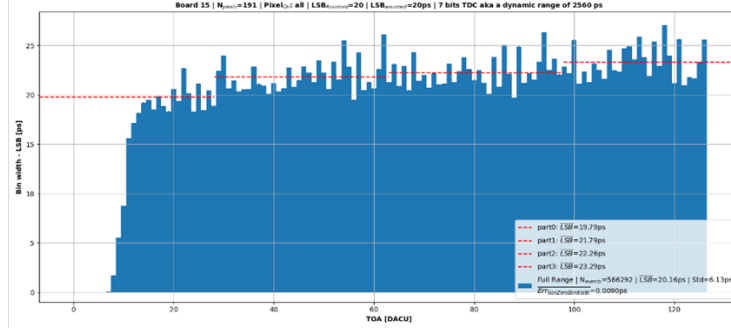


Figure 8.14: ALTIROC3 testbench TOA distribution, mixed from many pixels [78]

8.4.3 Correction for DNL

It would be convenient to bring left and right TOA sub-ranges on equal footing by using the same LSB in both of them. LSB uniformization was introduced for this purpose. It was already used in Sec. 6.4.6 but no large impact was seen, unlike ALTIROC3. The disadvantage of the method is that it's unclear whether it can be used in future HGTD or not, but in any case, it allows us to see the magnitude of double-slope by removing it. Starting point of uniformization is TOA distribution per pixel, as seen in testbeam ¹¹ - an example of such distribution is shown on Fig. 8.12b. Non-uniformity is a proxy for Differential Non-Linearity (DNL). The y-axis is the number of counts observed per batch per pixel before any cuts. Uniformization is done before applying event selections (like TOTC, number of hits etc.) as they can modify the shape of the TOA distribution. It can be seen again that the L average count is lower, and the goal is to correct that: for this count in each TOA bin (integer) is divided by the average count across all TOA bins (around 30 in this example). The average count here sets the overall LSB scale and the uniformization corrects for deviations from it. In this way, one corrects for DNL and obtains instead the original TOA_i another variable denoted $uniTOA_i$ (short-hand for uniformized TOA)

$$uniTOA_i = \frac{\int_0^{TOA_i} dTOA}{\langle \#TOA \rangle_{0-127}} \quad (8.3)$$

Distribution $uniTOA_i$ is shown on Fig. 8.12b. It's expected to be TOA corrected for DNL . It's no longer supposed to be an integer because of the division from which it is obtained. Relationship between original and uniformized TOA is shown on Fig. 8.15, showing deviation from starting line after half-range, showing that correction is happening. With uniformized TOA derived, selections are applied, and they are minimal: only one pixel is fired (to avoid noisy events), TOT value above 14 (for the same purpose), MCP amplitude above 30 mV (to have a clean time reference signal), removal events with saturated TOA (values above 126).

As mentioned, the uniformization corrects the relative deviation from the overall LSB, but it does not give the absolute value of it. To find new proportionality constant ¹² between time and

¹⁰testbench partially reproduces absence of hits at low TOA values - but this is a separate issue

¹¹same can be done in principle with testbench TOA, however, it was seen not to reproduce testbeam TOA and therefore not used

¹²words discretization step or LSB are avoided because the variable is not an integer anymore

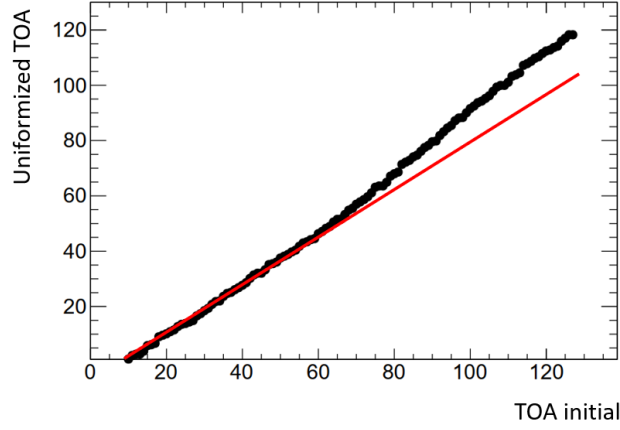


Figure 8.15: Uniformized TOA against original TOA. Red line is a “fit“ on $TOA < 65$ and extrapolated to whole TOA range.

binary TDC same approach as shown in Fig. 8.13 is used, this time on uniformized TOA instead of the original one. Example is shown on Fig. 8.16, where single line is describing well the whole uniTOA range - this was the goal. While in the previous case, the double-line is visible by comparing with sub-range fits, and the whole range fit is overshooting the mean near $TOA=0$ and overshooting near $TOA=127$ as a consequence.

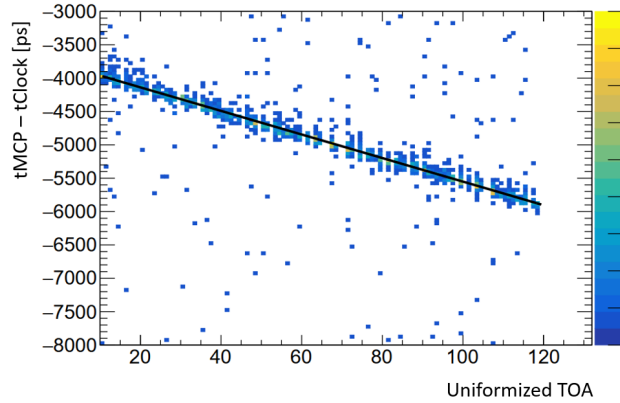


Figure 8.16: Extraction of proportionality constant between uniformized TOA and time

With uniformized TOA and associated LSB obtained, the remainder of time resolution extraction is similar to Eq. 8.1 but now with new variables. Familiar ΔT gaussian is obtained, shown for one pixel in Fig. 8.17 ¹³.

$$\Delta T = \underbrace{-uniTOA \times LSB_{uniTOA}}_{t_{ASIC}^{uni}} - \underbrace{t_{MCP}^{trig,CFD} - t_{clock}}_{t_{MCP}} \quad (8.4)$$

8.4.4 TOT-inclusive timewalk correction

Lastly, timewalk correction is applied, shown on Fig. 8.18a. Contrary to previous studies, upper TOT cut is not applied to avoid possible under-estimation of resolution (event in the tail is known to have a worse resolution, but the tail is included which degraded the resolution by ≈ 1 ps). The timewalk correction, however, is not giving much improvement because, as can be seen from the

¹³Dedicated study is planned concerning events in tail

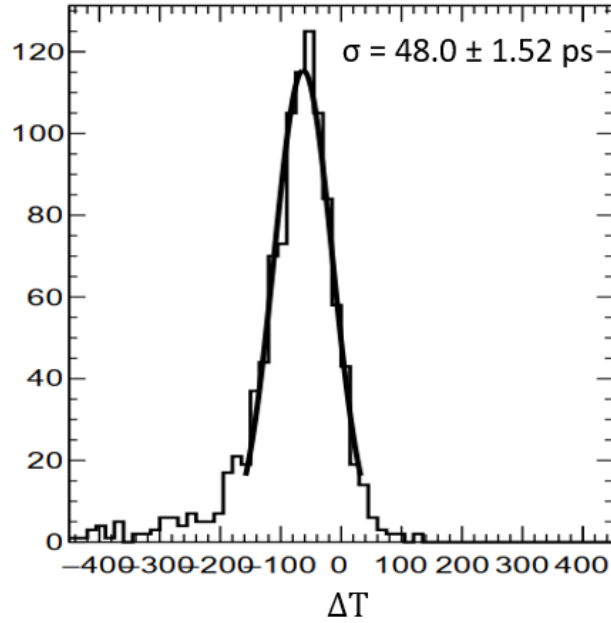


Figure 8.17: Uniformized ΔT together with fit used in time resolution, before timewalk correction

distribution, dominating fraction of events is concentrated in small ASIC TOT slice - width of projection into Y (time resolution) has a small contribution from the timewalk slope - there is not much to correct in the first place because of the high bias voltage used and high amplitude as a consequence. Resulting ΔT is shown on Fig. 8.18b

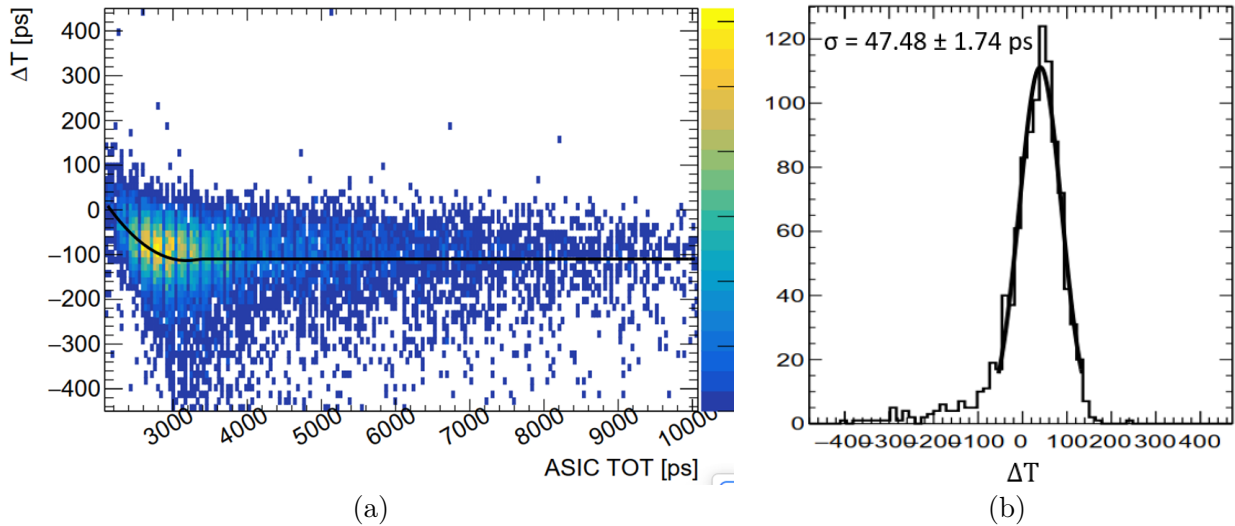


Figure 8.18: (a) ASIC TOT timewalk correction (b) Uniformized ΔT together with fit used in time resolution after timewalk correction with ASIC TOT

With uniformization and timewalk correction applied, one can compare results with separate sub-ranges. Four sub-ranges result is shown on Fig. 8.19, showing that all four sub-ranges have comparable time resolution at the level of 43ps. This result can be compared to the uniformized time resolution shown in Fig. 8.20. Without uniformization, the average is 48.4 ps; therefore, the quadratic contribution of the non-linearity is ≈ 20 ps.

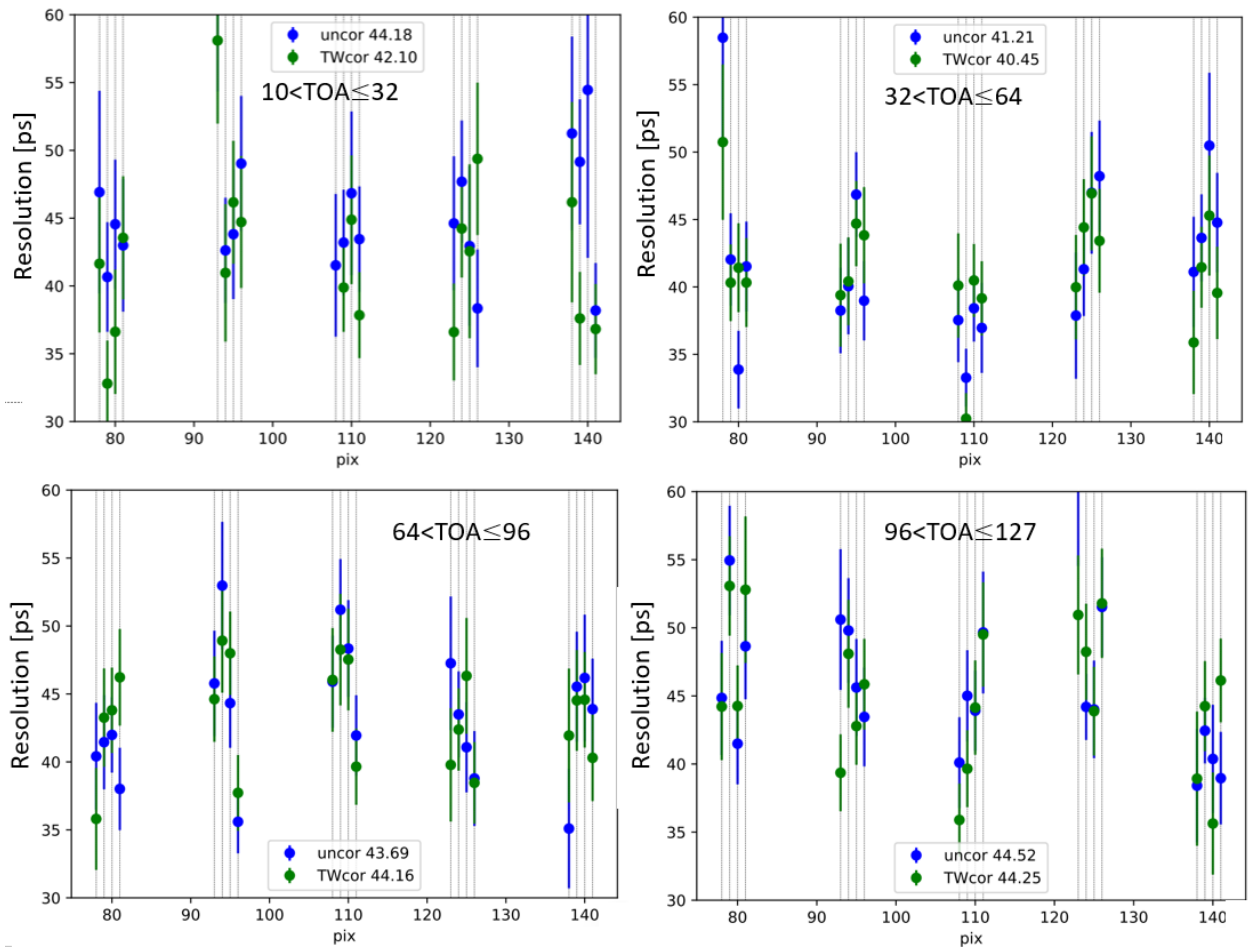


Figure 8.19: ALTIROC3 time resolution before and after timewalk correction in four TOA sub-ranges, without uniformization

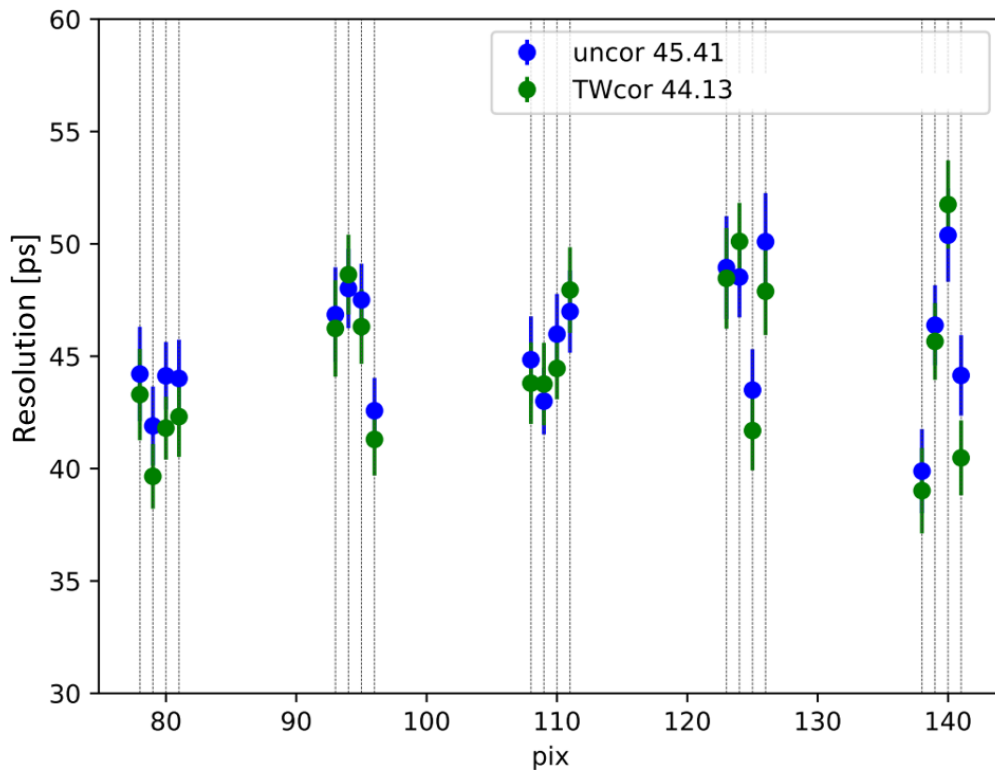


Figure 8.20: ALTIROC3 time resolution before and after timewalk correction, after uniformization

8.4.5 Summary of different configurations

Measurements were done for two boards in different configurations, summarized in Table 8.3, also including measurements at low temperatures. For all batches the threshold is 10.8 fC (with expected signal, 20 fC, being much larger) and all pixels are activated. Temperature listed was not stabilized, as in DESY dry ice is used for cooling. Time resolutions obtained are summarized in Table 8.4, showing average resolution over typically ≈ 20 pixels. Uncertainty is at the level of 0.5 ps. No upper amplitude (TOT) cut is applied. For both TOA and uniTOA, whole range of values is used. The timewalk correction, done with ASIC TOTC+TOTF, is only helpful at lower voltages as shown in “TW corr gain in quadrature“ column. The TOA uniformization gain is at the level of 19–30 ps in quadrature - see “uniTOA gain in quadrature“ column.

| Batch | Board | Temp | Voltage |
|-------|-------|------|---------|
| 300 | B27 | room | 200 V |
| 314 | B27 | room | 193 V |
| 1103 | B27 | -30 | 146 V |
| 502 | B15 | room | 200 V |
| 504 | B15 | room | 195 V |
| 506 | B15 | room | 203 V |

Table 8.3: Summary of ALTIROC3 testbeam batches

| Batch | TOA | TOA, TW corr | uniTOA | uniTOA, TW corr | uniTOA gain in quadra- ture | TW corr gain in quadra- ture |
|-------|-------|-----------------|--------|--------------------|--------------------------------------|---------------------------------------|
| 300 | 55.1 | 55.0 | 48.4 | 48.8 | 25.0 | 10.8 |
| 314 | 60.18 | 59.0 | 53.0 | 50.2 | 30.1 | 17.0 |
| 1103 | 48.8 | 48.4 | 45.4 | 44.1 | 19.8 | - |
| 502 | 58.4 | 59.0 | 53.5 | 49.9 | 31.5 | 19.3 |
| 504 | 58.5 | 59.0 | 56.7 | 50.2 | 30.1 | 26.3 |
| 506 | 57.6 | 55.2 | 52.1 | 47.6 | 27.8 | 21.2 |

Table 8.4: Summary of ALTIROC3 testbeam results with Table 8.3 batches

Conclusion

This thesis describes my work on three projects, starting from anomalous Quartic Gauge Coupling Vector Boson Scattering statistical combination of ATLAS Run-2 analyses. The other two are related to VBS: forward Jet Vertex Tagger in (currently ongoing) Run-3 and (preparing for High Luminosity LHC) High Granularity Timing Detector front-end electronics characterization.

anomalous Quartic Gauge Couplings (aQGC) are described through the 18 Eboli operators, divided into three “families“. Each operator can contribute to the SM+EFT cross-section via interference term with Standard Model, pure EFT quadratic term, or being in pair with another operator, giving rise to the EFT cross-term. I have estimated the significance of cross-terms in simulations, demonstrating that these terms cannot be ignored when both pair members belong to the same family. Unfortunately, many analyses did not initially include cross-terms. To address this, I developed a method to insert these missing cross-terms by leveraging experimental degeneracy between certain operators. This method has been generalized in cases where other operators are missing. The insertion method was validated, typically showing less than 10% non-closure. Partial combination (not all the building blocks were available at the time of writing) results are shown. One-dimensional combined limits display the power of combination as they are better than the best individual (from one analysis) limit by up to $\approx 30\%$. The limits obtained are also meaningful in the sense that they are below the unitarity bound. Because of previous work done on completing the missing EFT terms, particularly cross-term, it was possible to obtain two-dimensional limits. The correlation of limits is coming solely from cross-term. 2D limits also show magnitude improvement compared to the best individual one.

ATLAS forward jet vertex tagger (fJVT) migration to the updated ATLAS software initially resulted in up to 15% performance degradation, which I fixed. Additionally, I calibrated the fJVT using Run-2 and Run-3 (2022-2023) data. This calibration quantified the differences in fJVT efficiency between simulations and real data, resulting in a set of scale factors. These scale factors, now available for use by the entire collaboration, need to be applied to Monte Carlo (MC) simulations based on jet transverse momentum and the number of simultaneous proton-proton interactions in the event. I also investigated the effects of systematic uncertainties, including those arising from different generators, the specific forward sub-detector where the jet is detected, variations in pileup profiles depending on the year, and the final state of the calibration. The calibration was conducted for three working points, with the differences between simulation and real data generally being below 5%.

For HL-LHC, a new sub-detector, the High Granularity Timing Detector (HGTD), will be installed in the forward region to provide high-resolution timing information. Achieving this requires front-end electronics with excellent time performance called ALTIROC. I have participated in the characterization of various prototypes. In this context, I analyzed test beam data for ALTIROC1 (small-size prototype), demonstrating a time resolution of 45 ± 1 ps with a TZ preamplifier (results published in paper: 2023 JINST 18 P08019). VPA preamplifier was rejected, as its Time Over Threshold vs amplitude dependence makes this architecture unusable for timewalk correction. With ALTIROC1 showing good results, I moved on to ALTIROC2 (full-scale prototype). I contributed to the development of ALTIROC2 software for laboratory and charged particle tests, conducting multiple evaluations, particularly of the Time of Arrival LSB, the lowest possible threshold, and test beam analysis. My measurements showed the dependence of LSB on occupancy, constituting important feedback for chip designers who made modifications and dependence was improved in the next iterations of the chip. Also, I’ve found that LSB depended on the position of the pixel inside the chip, based on what chip designers made modifications to the floor plan. My measure-

ments of the lowest possible charge showed that the TDR requirement was not reached at the time, but the information obtained, again, allowed to make modifications and improve results for the next iteration of the chip. I also checked that chip performance doesn't degrade at the necessary radiation and temperature regime. With ALTIROC2 in testbeam i obtained time resolution (similar to ALTIROC1) and hit efficiency - 100% within pixel core. Looking at gaps between pixels allowed to measure their size - $65 \mu\text{m}$. Both hit efficiency and gap size satisfy the requirement. Furthermore, I analyzed test beam data for ALTIROC3, discovering that calibration performed in the laboratory could not be directly applied to the test beam environment, leading to performance degradation. I identified a method to overcome this miscalibration only applicable to testbeam, ultimately achieving an average time resolution of 44 ± 0.2 ps across many pixels, which is close to the TDR requirement.

A - $Z(\rightarrow \bar{\nu}\nu)\gamma$ replacements

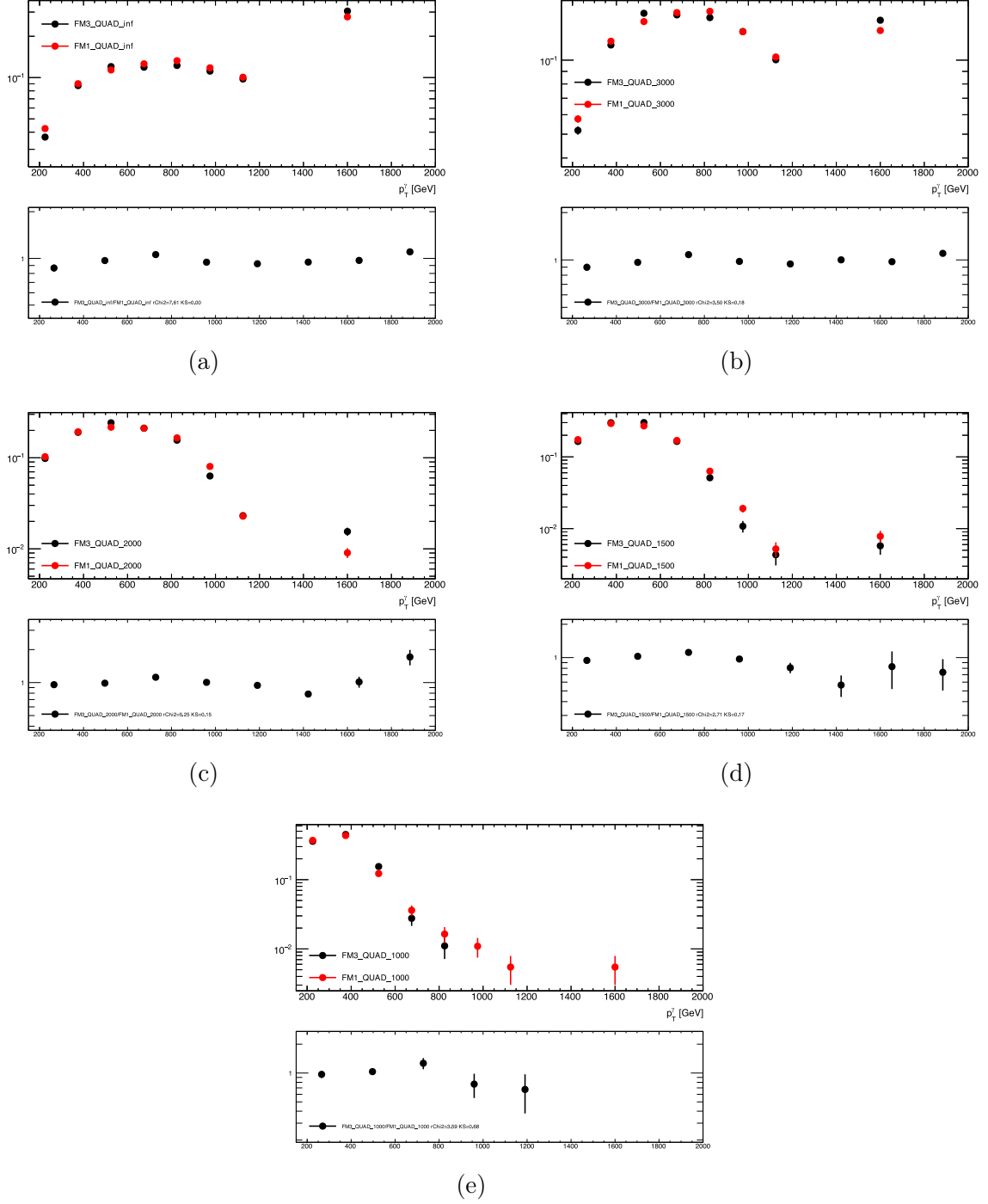


Figure A.1: FM3vsFM1 shape comparison obtained in $Z(\rightarrow \bar{\nu}\nu)\gamma$ sample, replicating analysis selections. Bins match those used in the analysis. The bottom pad is the ratio between two operator shapes (a) without clipping (b) clipping=3000 (c) clipping=2000 (d) clipping=1500 (e) clipping=1000.

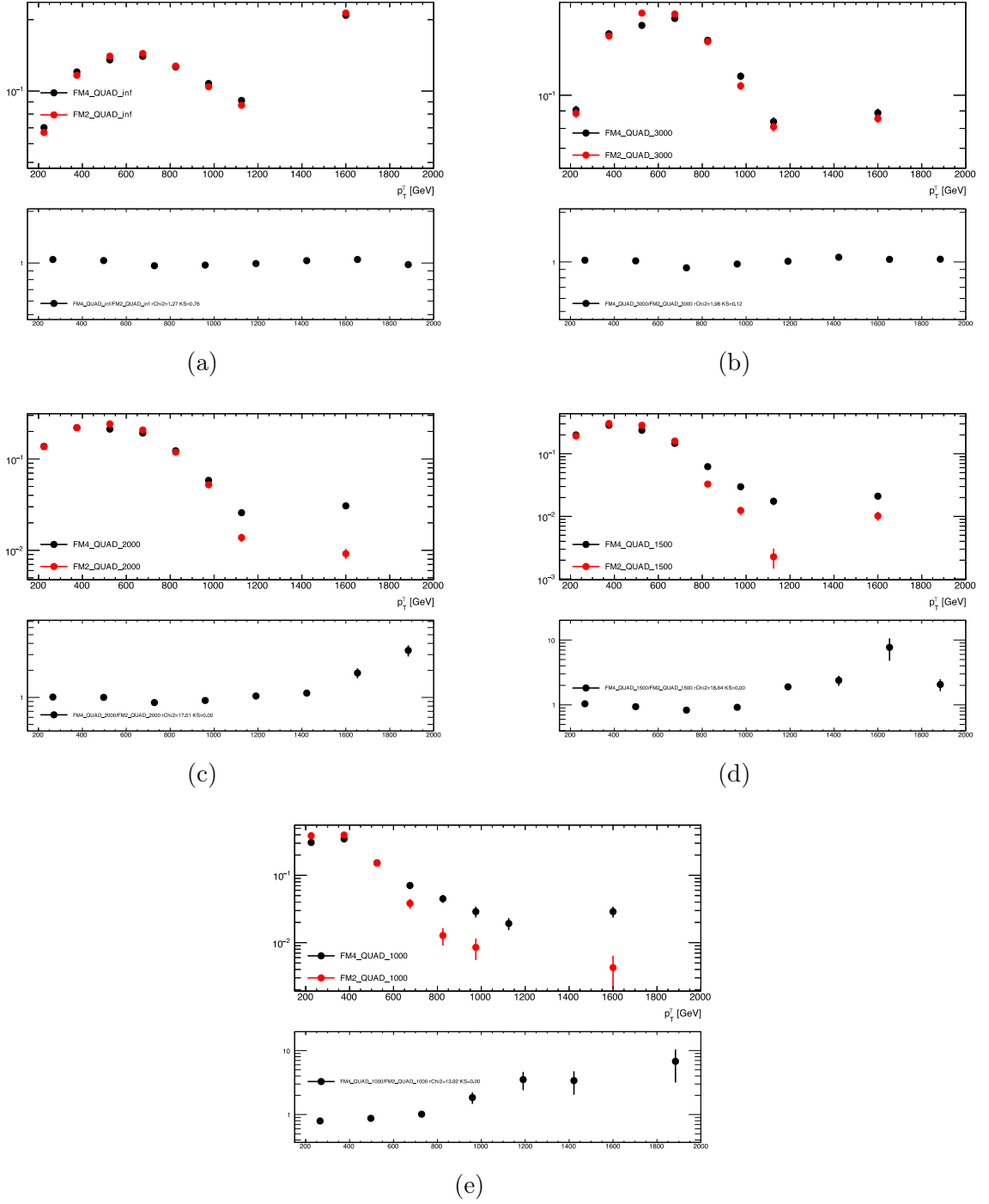


Figure A.2: FM4vsFM2 shape comparison obtained in $Z(\rightarrow \bar{\nu}\nu)\gamma$ sample, replicating analysis selections. Bins match those used in the analysis. The bottom pad is the ratio between two operator shapes (a) without clipping (b) clipping=3000 (c) clipping=2000 (d) clipping=1500 (e) clipping=1000.

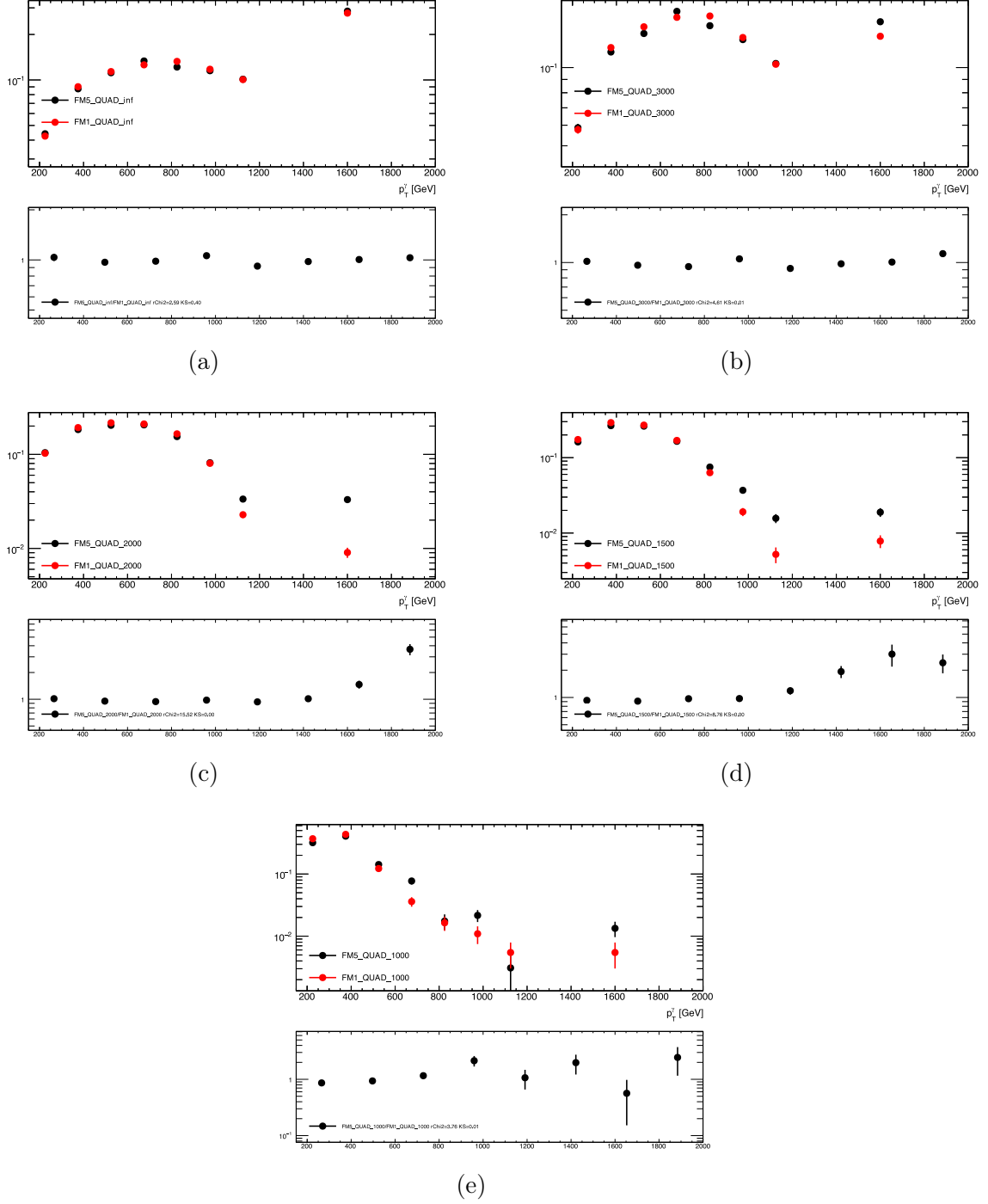


Figure A.3: FM5vsFM1 shape comparison obtained in $Z(\rightarrow \bar{\nu}\nu)\gamma$ sample, replicating analysis selections. Bins match those used in the analysis. The bottom pad is the ratio between two operator shapes (a) without clipping (b) clipping=3000 (c) clipping=2000 (d) clipping=1500 (e) clipping=1000.

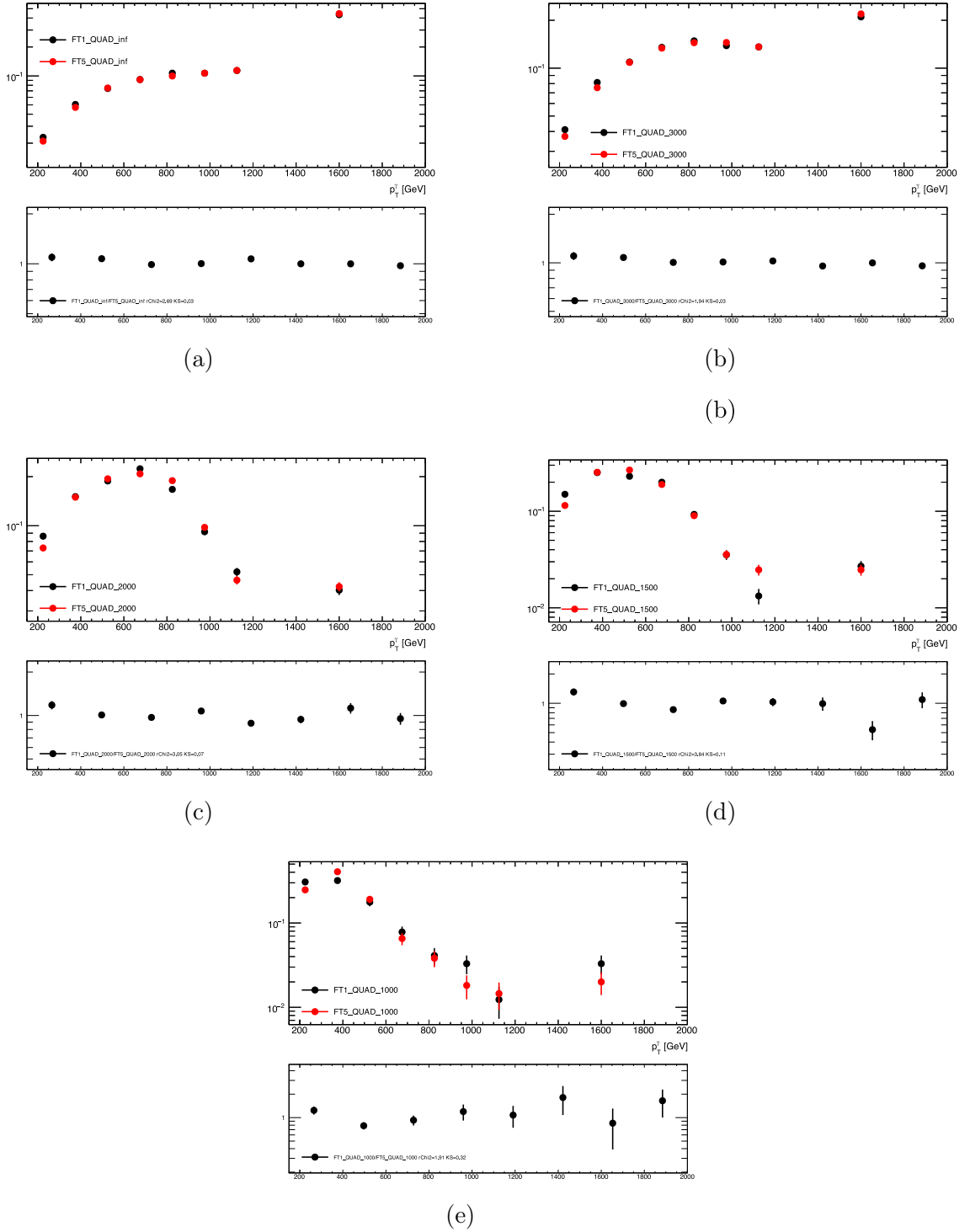


Figure A.4: FT1vsFT5 shape comparison obtained in $Z(\rightarrow \bar{\nu}\nu)\gamma$ sample, replicating analysis selections. Bins match those used in the analysis. The bottom pad is the ratio between two operator shapes (a) without clipping (b) clipping=3000 (c) clipping=2000 (d) clipping=1500 (e) clipping=1000.

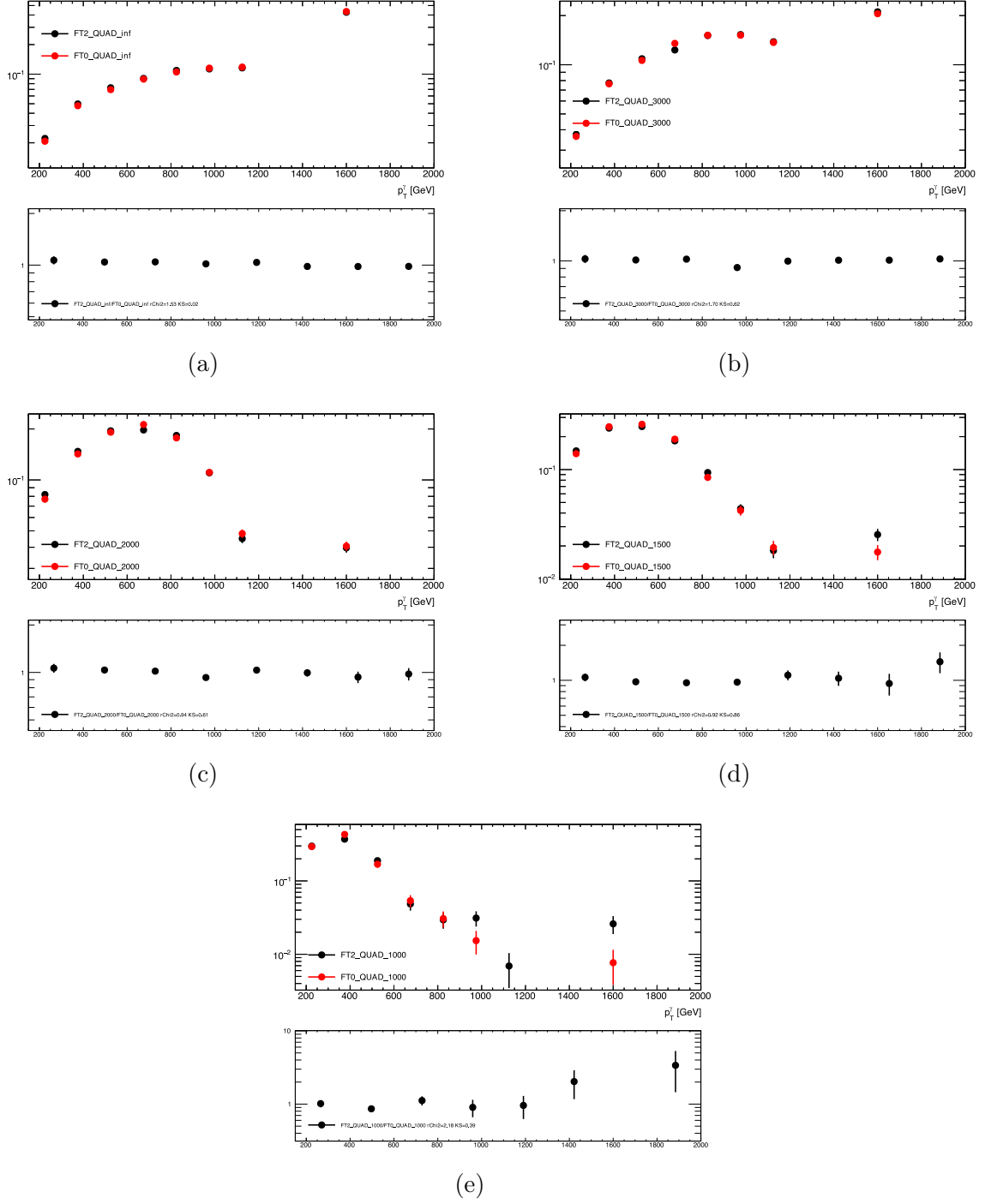


Figure A.5: FT2vsFT0 shape comparison obtained in $Z(\rightarrow \bar{\nu}\nu)\gamma$ sample, replicating analysis selections. Bins match those used in the analysis. The bottom pad is the ratio between two operator shapes (a) without clipping (b) clipping=3000 (c) clipping=2000 (d) clipping=1500 (e) clipping=1000.

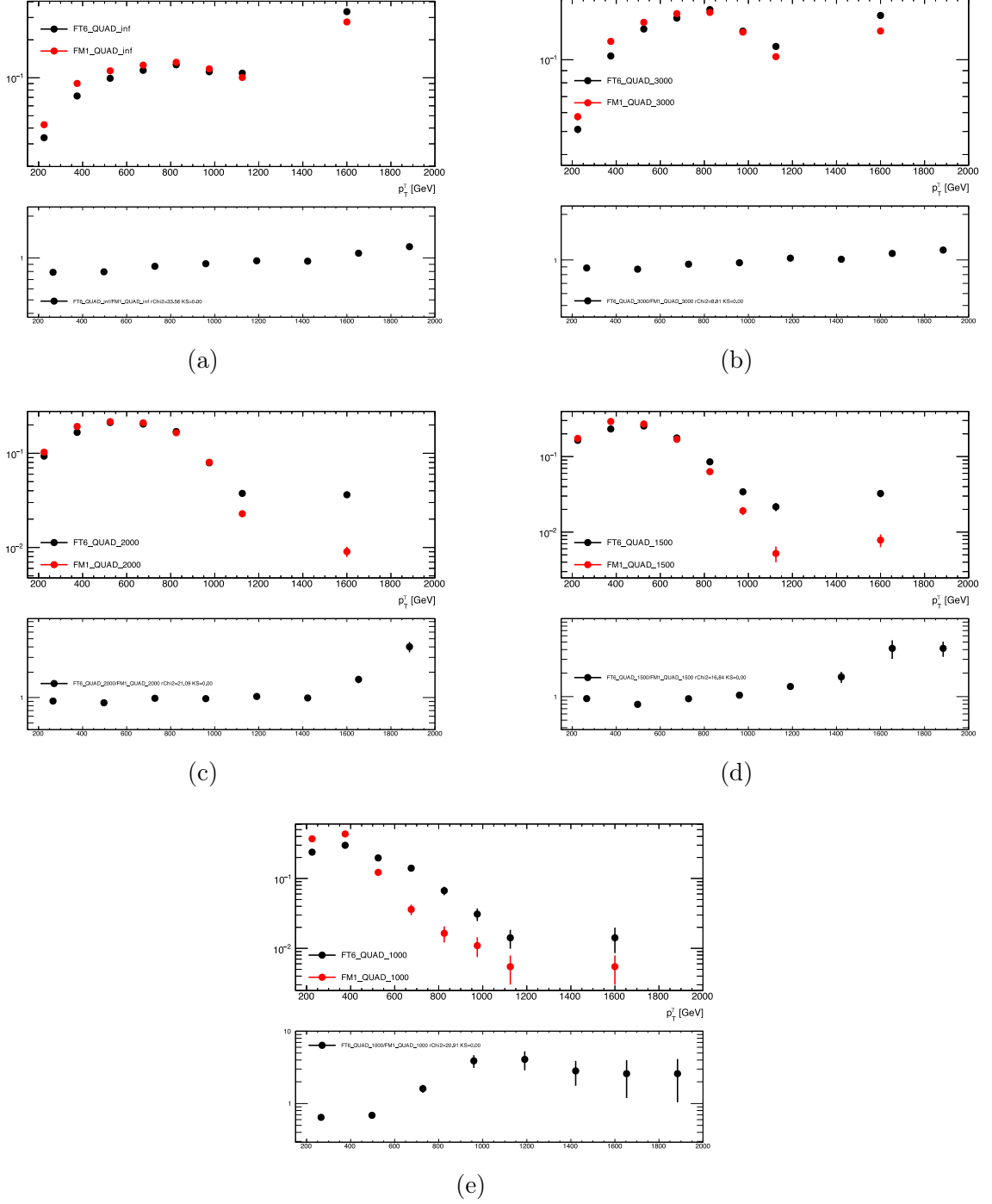


Figure A.6: FT6vsFM1 shape comparison obtained in $Z(\rightarrow \bar{\nu}\nu)\gamma$ sample, replicating analysis selections. Bins match those used in the analysis. The bottom pad is the ratio between two operator shapes (a) without clipping (b) clipping=3000 (c) clipping=2000 (d) clipping=1500 (e) clipping=1000.

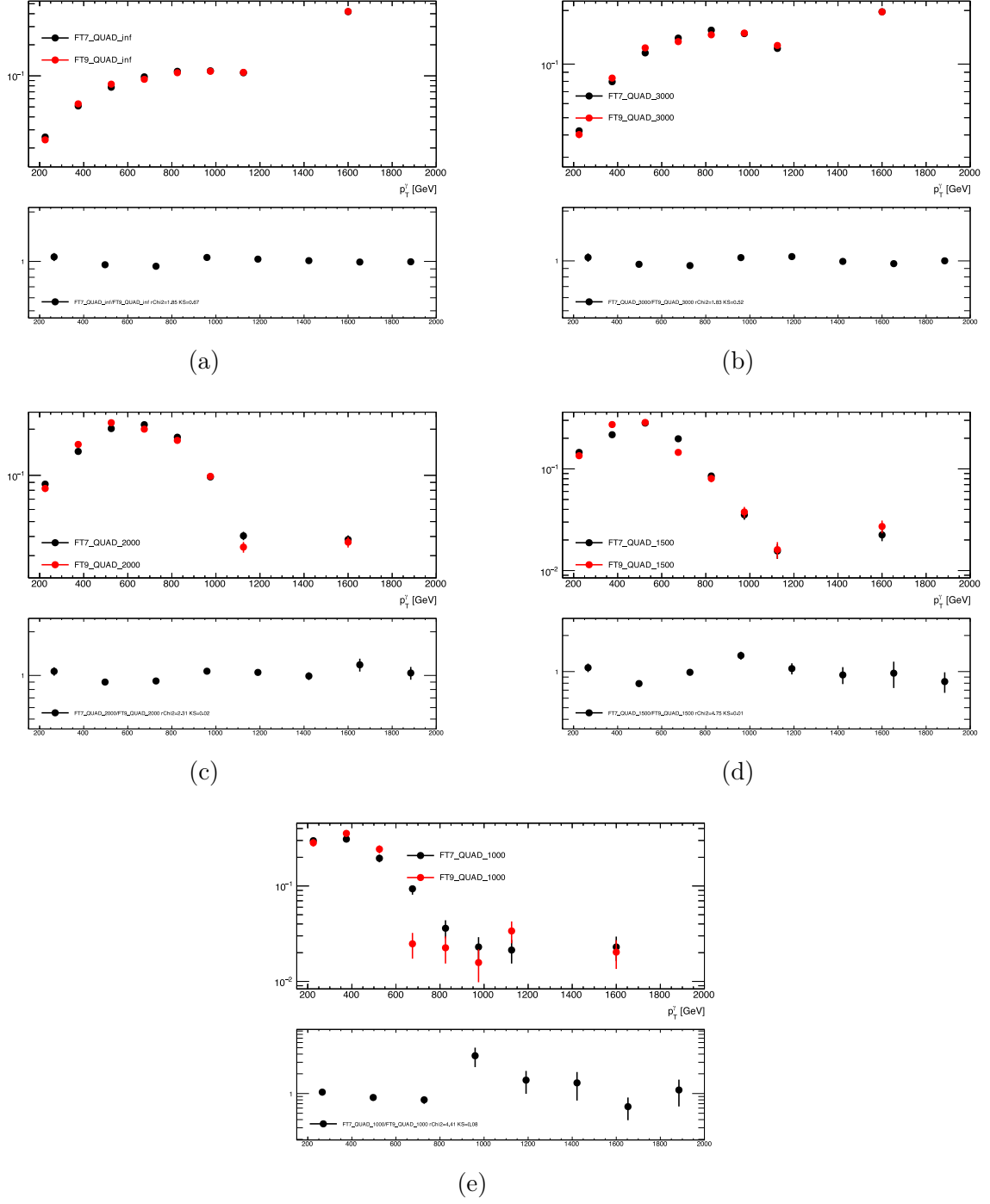


Figure A.7: FT7vsFT9 shape comparison obtained in $Z(\rightarrow \bar{\nu}\nu)\gamma$ sample, replicating analysis selections. Bins match those used in the analysis. The bottom pad is the ratio between two operator shapes (a) without clipping (b) clipping=3000 (c) clipping=2000 (d) clipping=1500 (e) clipping=1000.

B - $Z(\rightarrow \bar{\nu}\nu)\gamma$ replacements validation fits

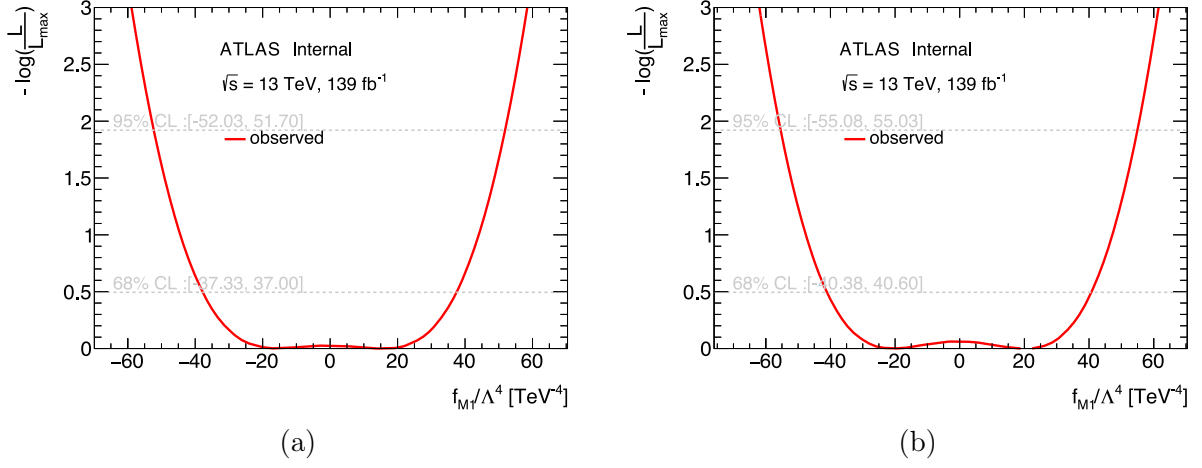


Figure B.1: $Z(\rightarrow \bar{\nu}\nu)\gamma$ analysis replacement validation: comparison between M1 (a) original limit (b) replaced limit

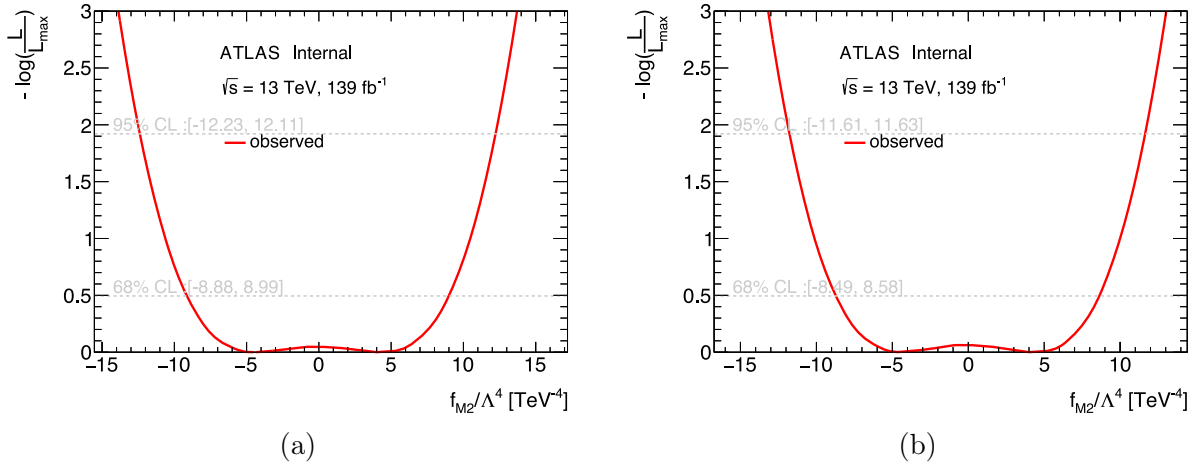
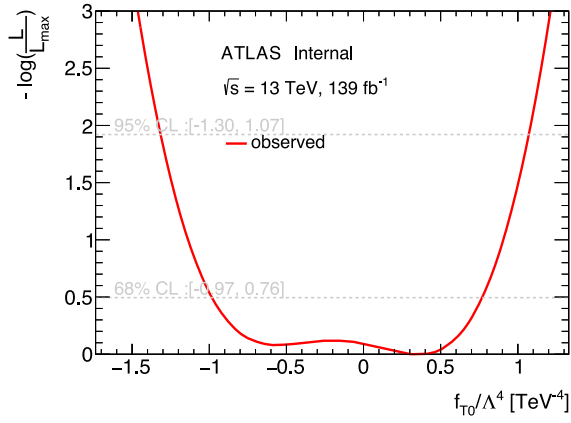
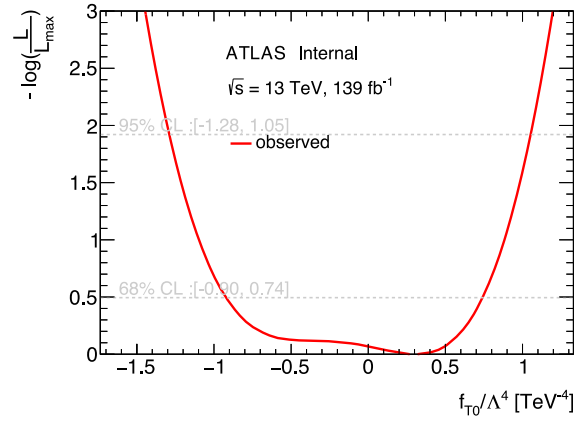


Figure B.2: $Z(\rightarrow \bar{\nu}\nu)\gamma$ analysis replacement validation: comparison between M2 (a) original limit (b) replaced limit

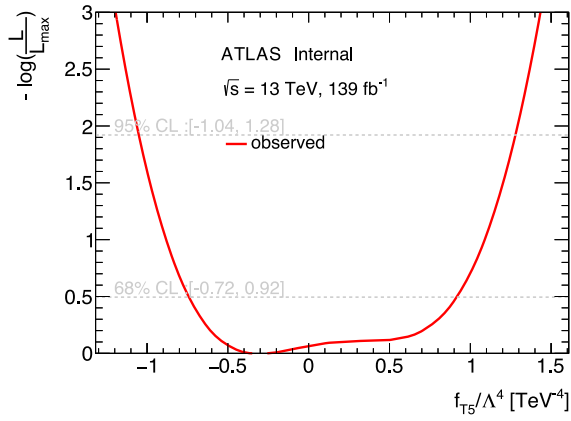


(a)

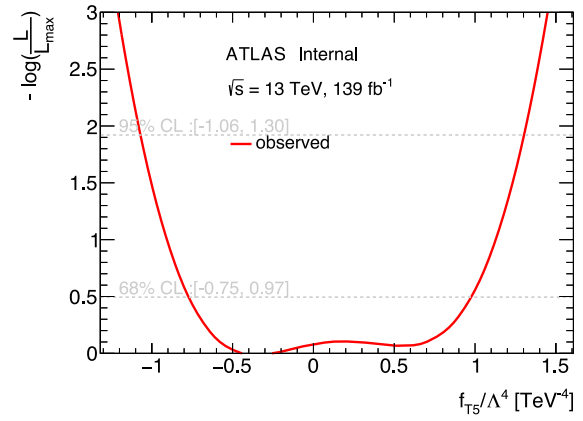


(b)

Figure B.3: $Z(\rightarrow \bar{\nu}\nu)\gamma$ analysis replacement validation: comparison between T0 (a) original limit (b) replaced limit

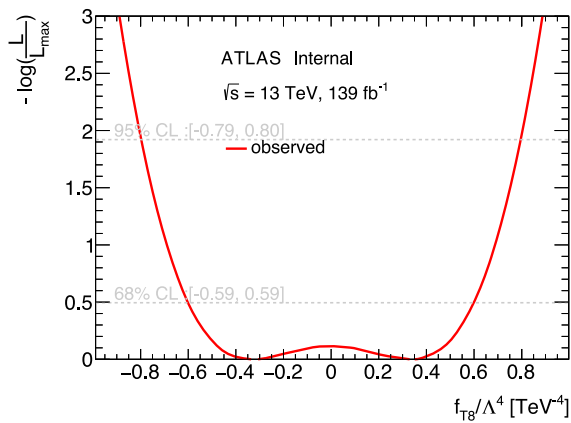


(a)

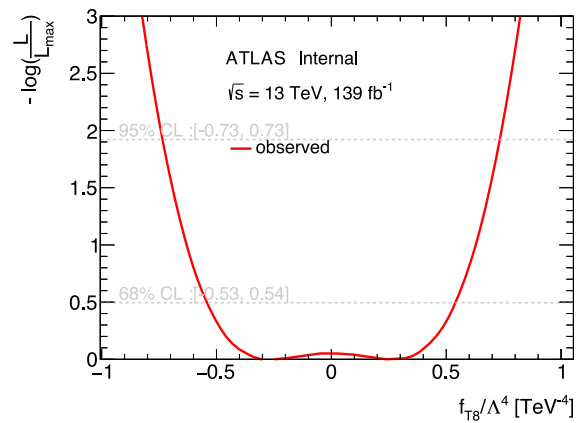


(b)

Figure B.4: $Z(\rightarrow \bar{\nu}\nu)\gamma$ analysis replacement validation: comparison between T5 (a) original limit (b) replaced limit

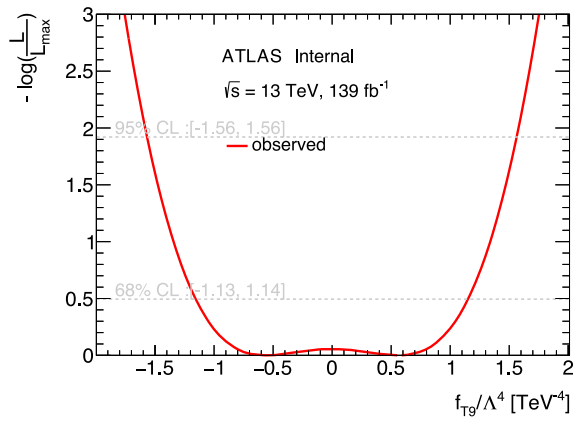


(a)

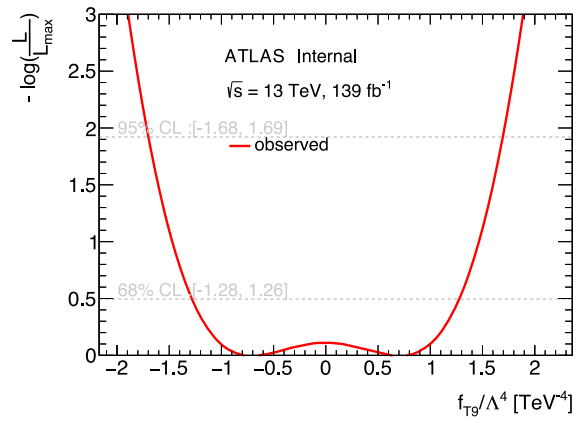


(b)

Figure B.5: $Z(\rightarrow \bar{\nu}\nu)\gamma$ analysis replacement validation: comparison between T8 (a) original limit (b) replaced limit



(a)



(b)

Figure B.6: $Z(\rightarrow \bar{\nu}\nu)\gamma$ analysis replacement validation: comparison between T9 (a) original limit (b) replaced limit

C - $Z \rightarrow \ell\bar{\ell} + \text{jets}$ basic distributions

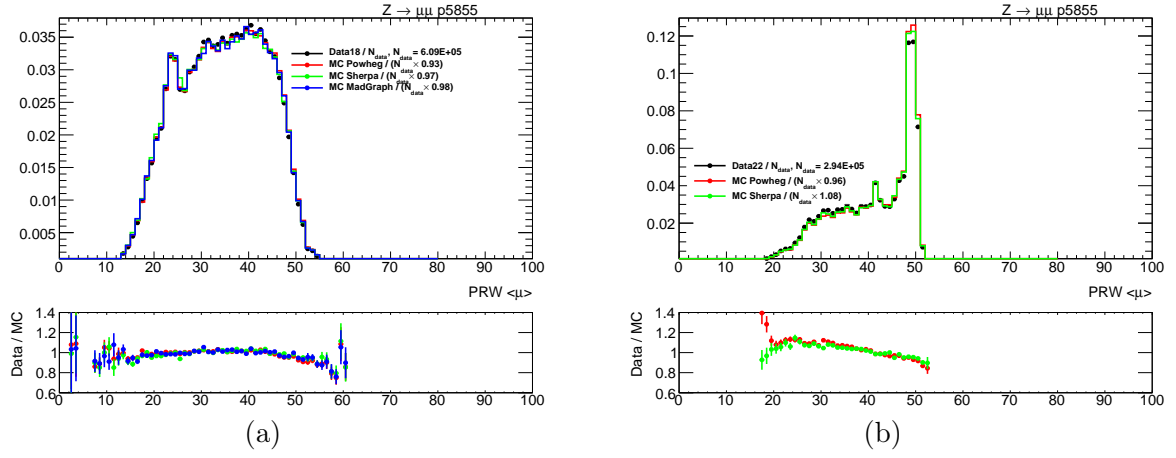


Figure C.1: Data/MC comparison of Pileup Reweighted $\bar{\mu}$, fJVT calibration selections (a) Run-2: 2018 $Z \rightarrow \mu\bar{\mu}$ (b) Run-3: 2022 $Z \rightarrow \mu\bar{\mu}$.

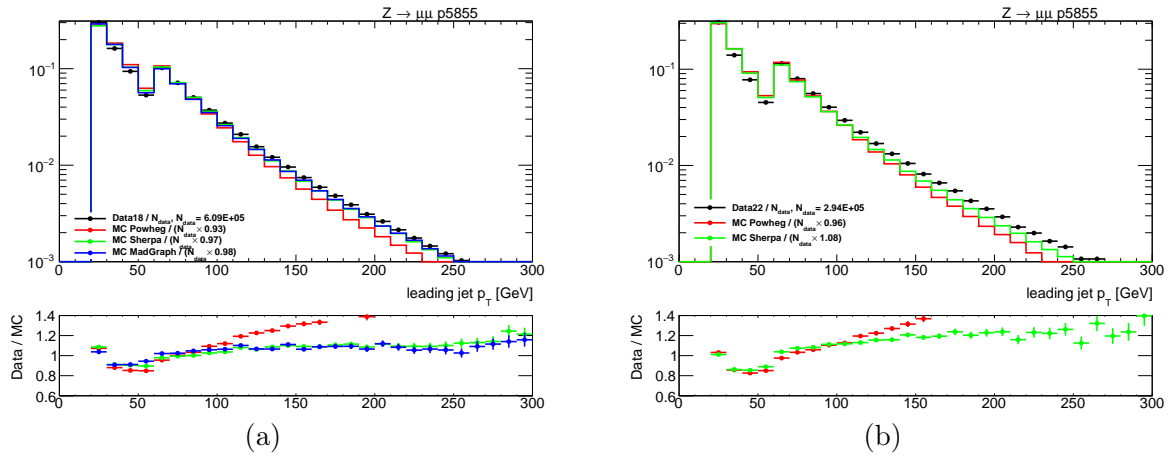


Figure C.2: Data/MC comparison of p_T -leading jet p_T , fJVT calibration selections (a) Run-2: 2018 $Z \rightarrow \mu\bar{\mu}$ (b) Run-3: 2022 $Z \rightarrow \mu\bar{\mu}$.

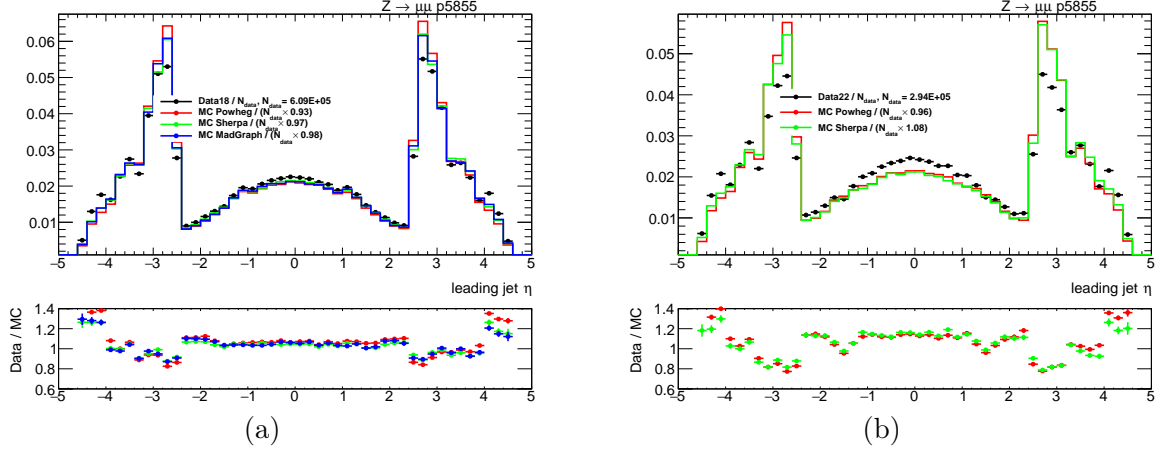


Figure C.3: Data/MC comparison of p_T -leading jet η , fJVT calibration selections (a) Run-2: 2018 $Z \rightarrow \mu\bar{\mu}$ (b) Run-3: 2022 $Z \rightarrow \mu\bar{\mu}$.

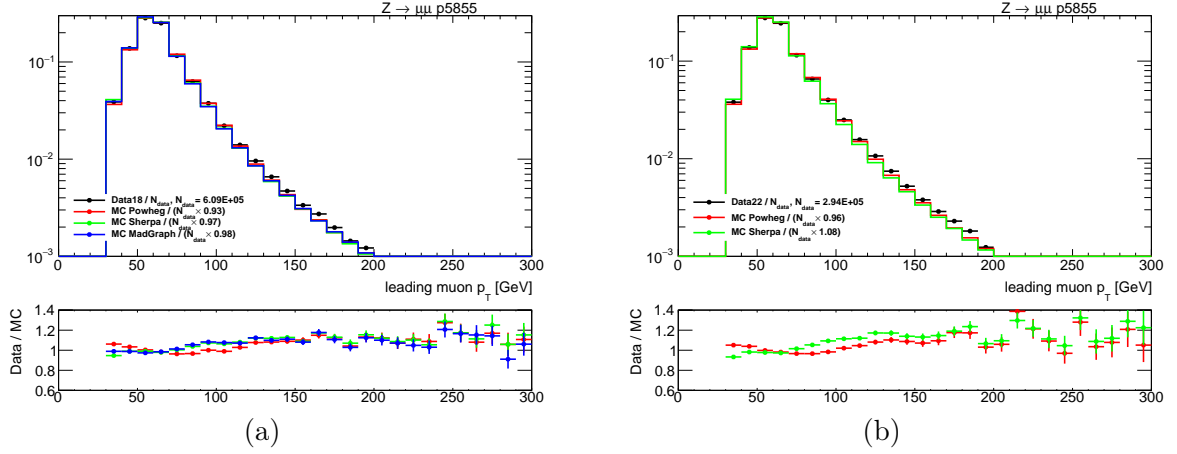


Figure C.4: Data/MC comparison of p_T -leading muon p_T , fJVT calibration selections (a) Run-2: 2018 $Z \rightarrow \mu\bar{\mu}$ (b) Run-3: 2022 $Z \rightarrow \mu\bar{\mu}$.

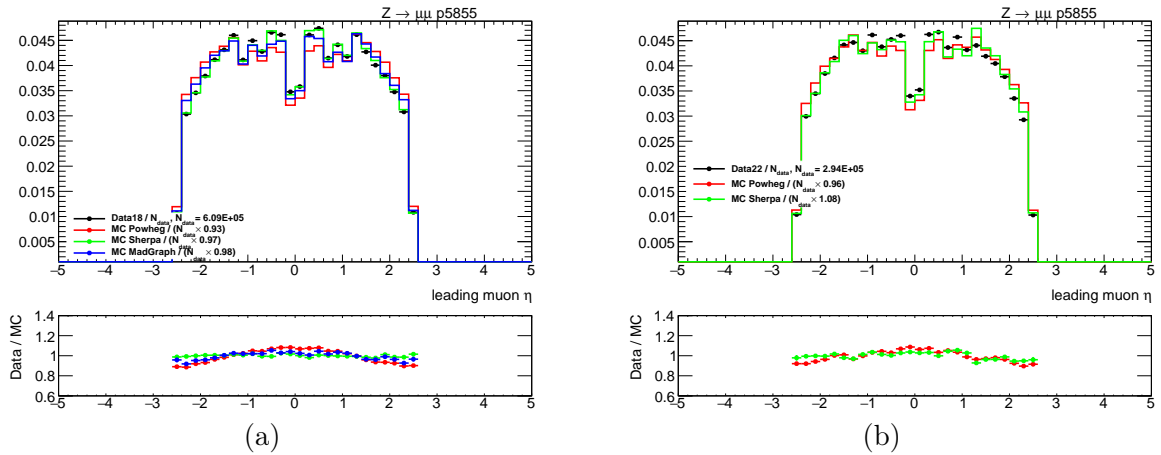


Figure C.5: Data/MC comparison of p_T -leading muon η , fJVT calibration selections (a) Run-2: 2018 $Z \rightarrow \mu\bar{\mu}$ (b) Run-3: 2022 $Z \rightarrow \mu\bar{\mu}$.

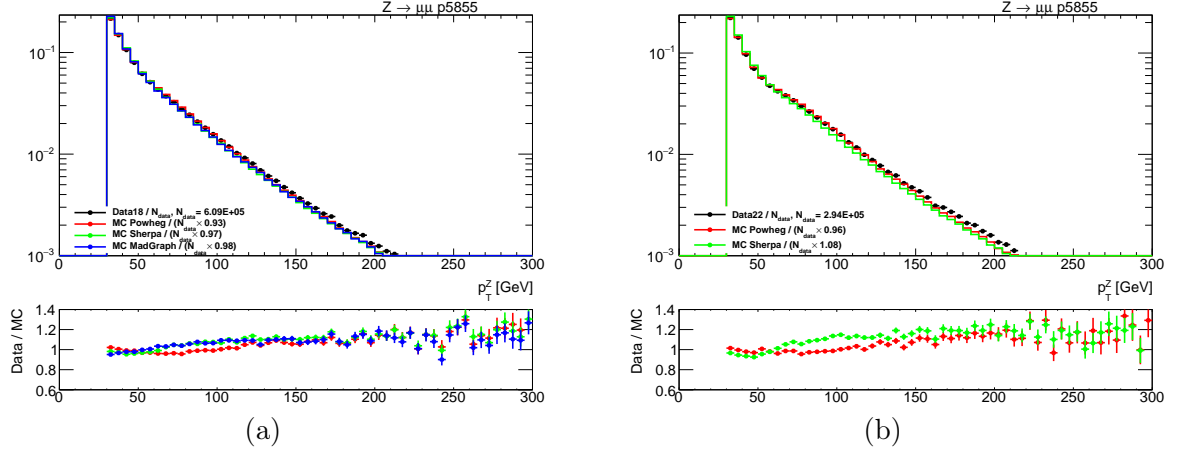


Figure C.6: Data/MC comparison of pt_Z of Z reconstructed from two leptons, fJVT calibration selections (a) Run-2: 2018 $Z \rightarrow \mu\bar{\mu}$ (b) Run-3: 2022 $Z \rightarrow \mu\bar{\mu}$.

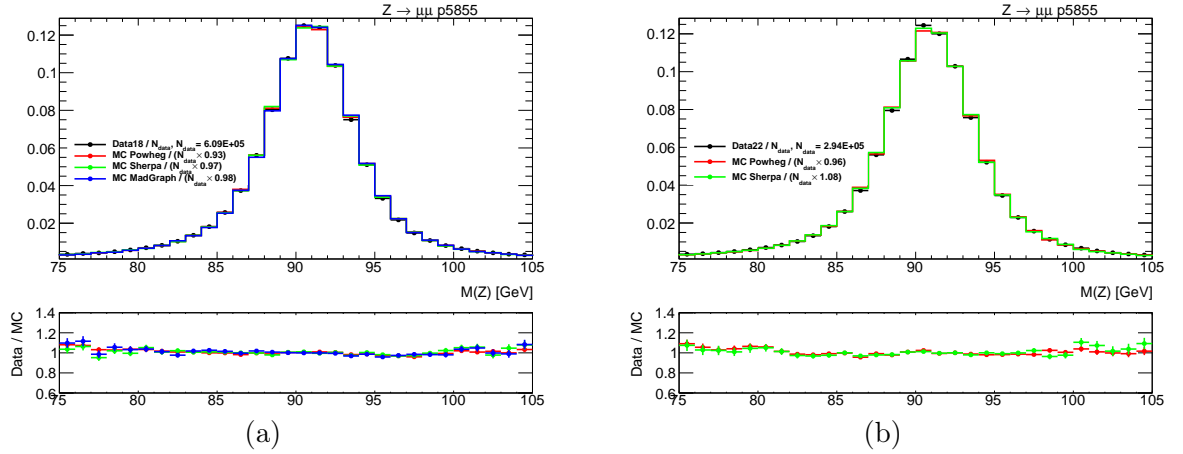


Figure C.7: Data/MC comparison of m_Z of Z reconstructed from two leptons, fJVT calibration selections (a) Run-2: 2018 $Z \rightarrow \mu\bar{\mu}$ (b) Run-3: 2022 $Z \rightarrow \mu\bar{\mu}$.

D - ε_{HS} , SF, σ_{SF} for Tighter WP

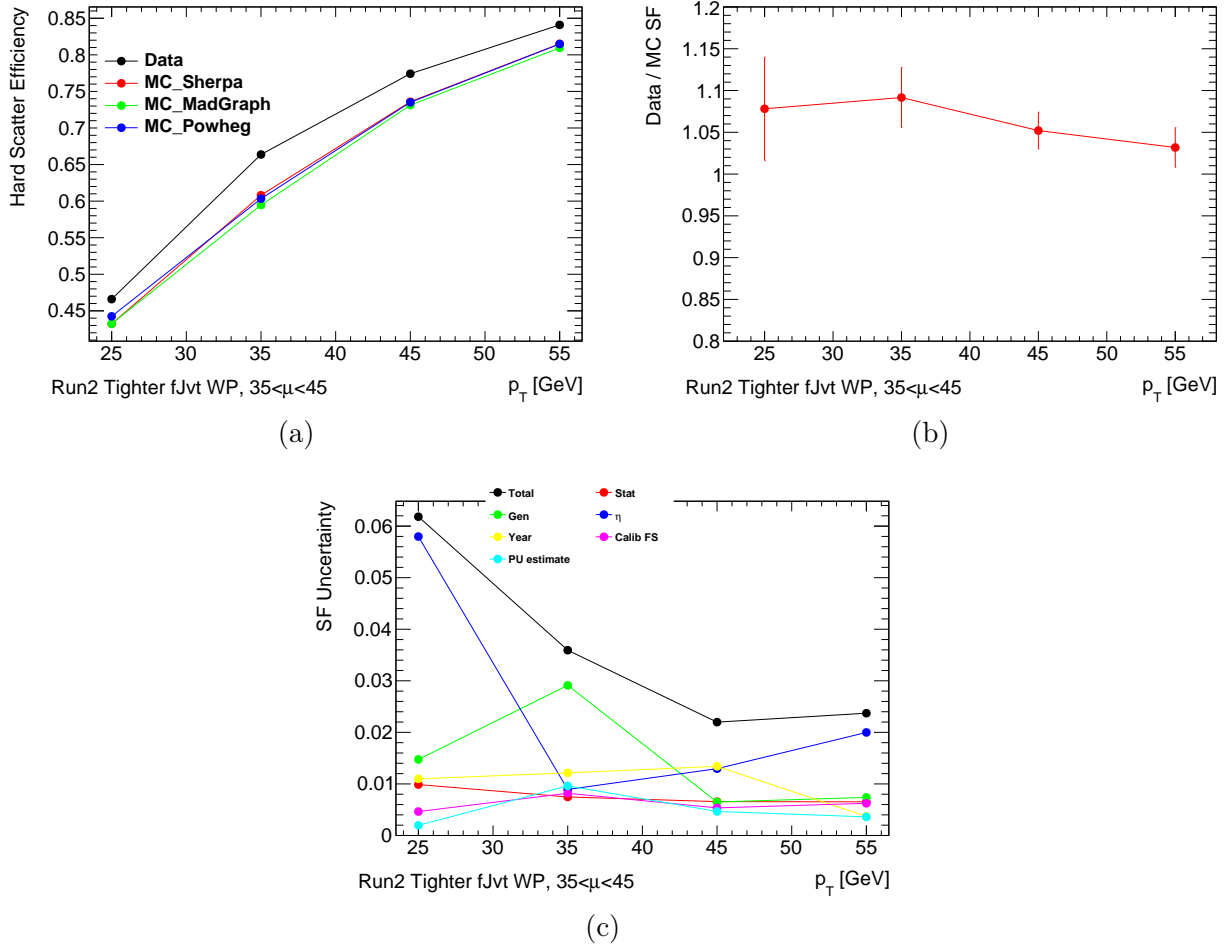
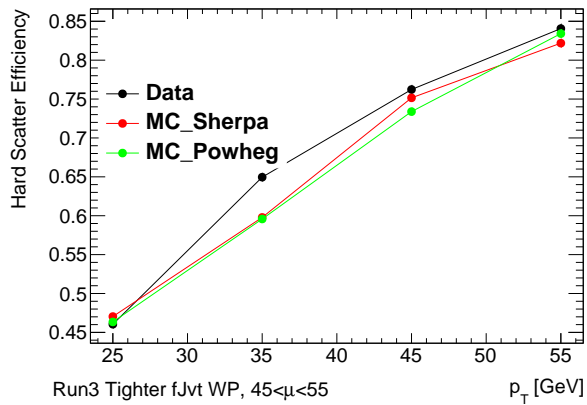
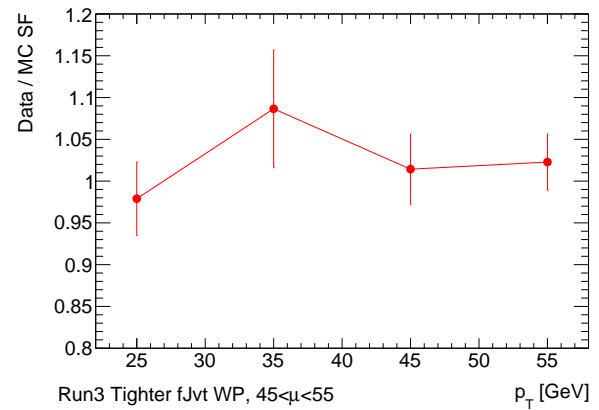


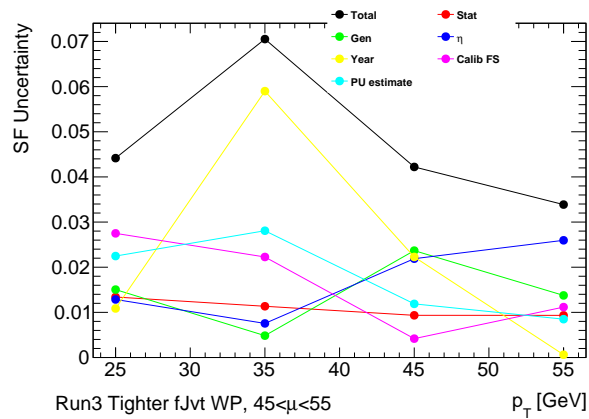
Figure D.1: Run2 calibration results in $35 < \bar{\mu} \leq 45$, Tighter working point (a) Hard-Scatter efficiency (b) Scale Factor (c) Scale Factor uncertainty breakdown.



(a)



(b)



(c)

Figure D.2: Run3 calibration results in $45 < \bar{\mu} \leq 55$, Tighter working point (a) Hard-Scatter efficiency (b) Scale Factor (c) Scale Factor uncertainty breakdown.

E - ϵ_{HS} , SF, σ_{SF} for Loose WP

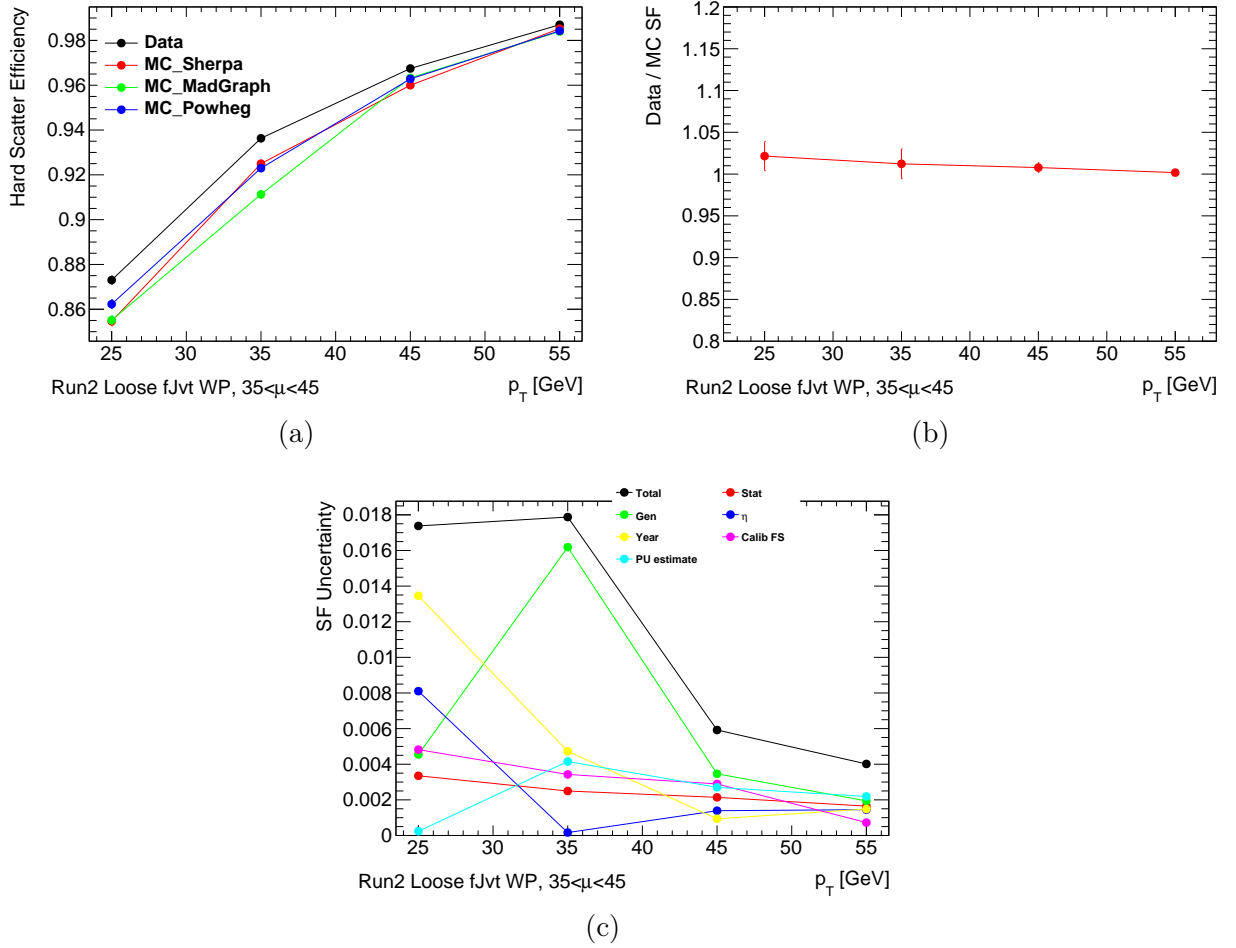
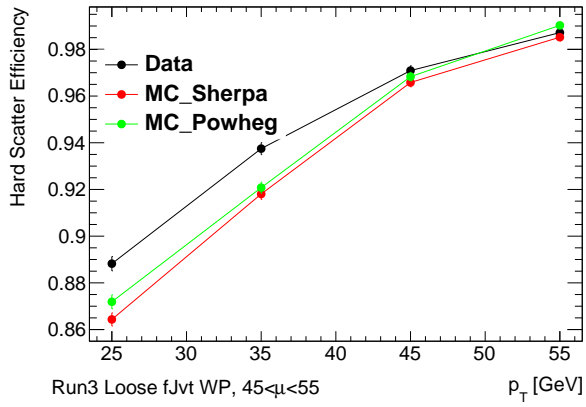
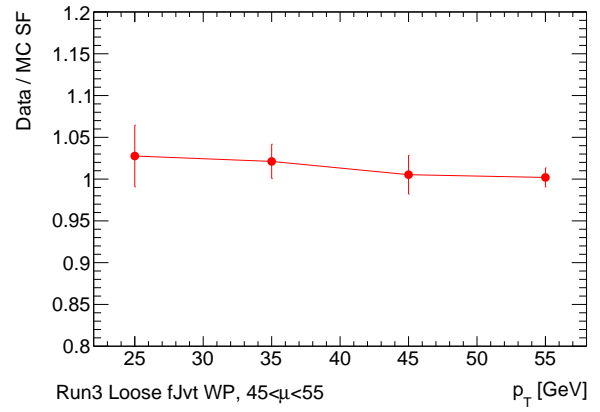


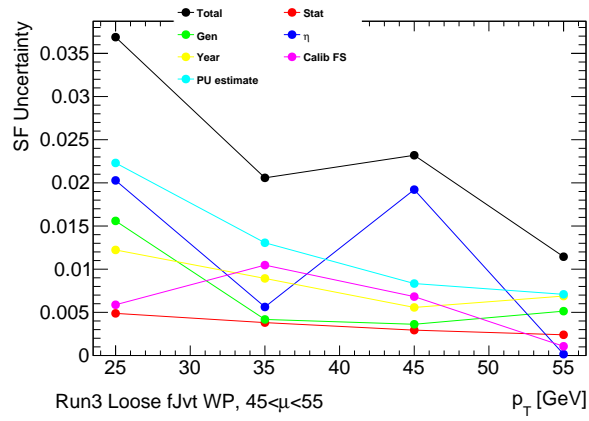
Figure E.1: Run2 calibration results in $35 < \mu \le 45$, Loose working point (a) Hard-Scatter efficiency (b) Scale Factor (c) Scale Factor uncertainty breakdown.



(a)



(b)



(c)

Figure E.2: Run3 calibration results in $45 < \bar{\mu} \leq 55$, Loose working point (a) Hard-Scatter efficiency (b) Scale Factor (c) Scale Factor uncertainty breakdown.

F - Synthèse en français

Le modèle standard (SM) est connu pour être incomplet, et l’approche de la théorie effective des champs (EFT) permet de paramétrer des déviations potentielles subtiles du modèle standard. La TEF pertinente pour cette thèse implique la description des couplages de jauge quartiques anormaux (aQGC) par des opérateurs d’Eboli. Ils sont mieux contraints dans la diffusion de bosons vectoriels (VBS). Cette thèse décrit mon travail sur trois projets, en commençant par la combinaison statistique des analyses du Run-2 d’ATLAS sur le couplage de jauge quartique anormal et la diffusion du boson vecteur. Les deux autres sont liés au VBS : forward Jet Vertex Tagger dans le Run-3 (actuellement en cours) et (préparation du LHC à haute luminosité) caractérisation de l’électronique frontale du détecteur de timing à haute granularité.

F.1 Les couplages de jauge quartiques anormaux

Les couplages de jauge quartiques anormaux (aQGC) sont décrits à travers les 18 opérateurs d’Eboli, divisés en trois “familles“. Chaque opérateur peut contribuer à la section efficace SM+EFT via un terme d’interférence avec le modèle standard, un terme quadratique EFT pur, ou en étant en paire avec un autre opérateur, donnant lieu au terme croisé EFT. J’ai estimé l’importance des termes croisés dans les simulations (Fig. F.1), démontrant que ces termes ne peuvent être ignorés lorsque les deux membres de la paire appartiennent à la même famille. Malheureusement, de nombreuses analyses n’incluaient pas initialement les termes croisés. Pour remédier à ce problème, j’ai mis au point une méthode permettant d’insérer ces termes croisés manquants en tirant parti de la dégénérescence expérimentale entre certains membres de la paire (Fig. F.2). Cette méthode a été généralisée dans les cas où d’autres opérateurs sont manquants. La méthode d’insertion a été validée, montrant généralement moins de 10% de non-fermeture. Les résultats de la combinaison partielle (tous les éléments constitutifs n’étaient pas disponibles au moment de la rédaction) sont présentés. Les limites combinées unidimensionnelles démontrent la puissance de la combinaison, car elles sont meilleures que la meilleure limite individuelle (provenant d’une seule analyse) jusqu’à environ 30% (Fig. F.3). Les limites obtenues sont également significatives dans le sens où elles sont inférieures à la limite d’unitarité. Grâce à des travaux antérieurs effectués pour compléter les termes EFT manquants, en particulier les termes croisés, il a été possible d’obtenir des limites bidimensionnelles. d’obtenir des limites bidimensionnelles. La corrélation (Fig. F.4) des limites provient uniquement du terme transversal. Les limites 2D montrent également une amélioration de la magnitude par rapport à la meilleure limite individuelle.

F.2 Forward jet vertex tagger

Migration de Forward jet vertex tagger (fJVT) de l’ATLAS vers le logiciel ATLAS mis à jour a initialement entraîné une dégradation des performances allant jusqu’à 15%, que j’ai corrigée. En outre, j’ai calibré le fJVT en utilisant les données du Run-2, Run-3 (2022-2023). Cet étalonnage a permis de quantifier les différences d’efficacité du fJVT entre les simulations et les données réelles (Fig. F.5a), ce qui a donné lieu à un ensemble de facteurs d’échelle (Fig. F.5b). Ces facteurs d’échelle, désormais disponibles pour l’ensemble de la collaboration, doivent être appliqués aux simulations de Monte Carlo (MC) basés sur le moment transverse du jet et le nombre d’interactions proton-proton simultanées dans l’événement. J’ai également étudié les effets des incertitudes systématiques, y compris celles provenant de différents générateurs, du sous-détecteur avant spécifique où le jet est détecté, des variations des profils de pile-up en fonction de l’année, et de l’état final de l’étalonnage.

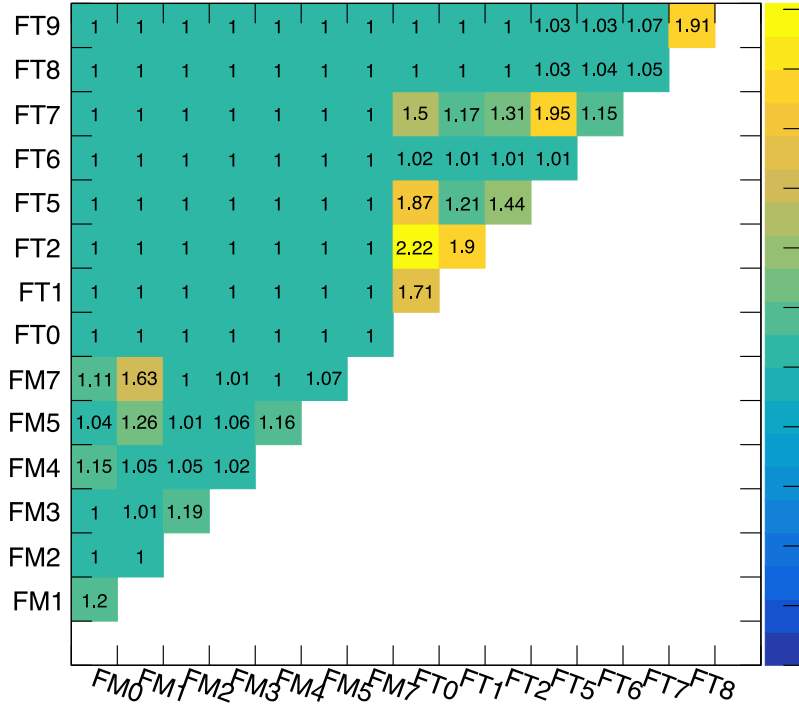


Figure F.1: $S_{cross}/S_{no-cross}$ Matrice d'analyse $Z(\rightarrow \bar{\nu}\nu)\gamma$

L'étalonnage a été réalisé pour trois points de travail, les différences entre la simulation et les données réelles étant généralement inférieures à 5%.

F.3 High Granularity Timing Detector

Pour le HL-LHC, un nouveau sous-détecteur, le High Granularity Timing Detector (HGTD), sera installé dans la région avant afin de fournir des informations temporelles à haute résolution. Pour ce faire, il faut une électronique frontale dotée d'excellentes performances temporelles, appelée ALTIROC. J'ai participé à la caractérisation de divers prototypes. Dans ce contexte, J'ai analysé les données du faisceau d'essai pour ALTIROC1 (prototype de petite taille), démontrant une résolution temporelle de 45 ± 1 ps avec un préamplificateur TZ (résultats publiés dans l'article : 2023 JINST 18 P08019). Le préamplificateur VPA a été rejeté, car sa dépendance du temps sur le seuil par rapport à l'amplitude rend cette architecture inutilisable pour la correction du décalage temporel. ALTIROC1 ayant donné de bons résultats, je suis passé à ALTIROC2 (prototype grandeur nature). J'ai contribué au développement du logiciel ALTIROC2 pour les tests de laboratoire et de particules chargées, j'ai effectué de nombreuses évaluations, en particulier du temps d'arrivée LSB, le seuil le plus bas possible, et de l'analyse du faisceau d'essai. Mes mesures ont montré la dépendance du LSB par rapport à l'occupation (Fig. F.6), ce qui a constitué un retour d'information important pour les concepteurs de puces qui ont apporté des modifications et la dépendance a été améliorée dans les itérations suivantes. ont apporté des modifications et la dépendance a été améliorée dans les itérations suivantes de la puce. J'ai également constaté que le LSB dépendait de la position du pixel à l'intérieur de la puce, en fonction des modifications apportées par les concepteurs de la puce au

plan d'étage. Mes mesures de la charge la plus faible possible ont montré que l'exigence TDR n'était pas atteinte à l'époque, mais les informations obtenues, une fois de plus, ont permis d'apporter des modifications et d'améliorer les résultats pour la prochaine itération de la puce. J'ai également vérifié que les performances de la puce ne se dégradent pas dans les conditions de rayonnement et de température requises. Avec ALTIROC2 dans le faisceau d'essai, j'ai obtenu une résolution temporelle (similaire à celle d'ALTIROC1) et une efficacité de frappe de 100% dans le cœur du pixel (Fig. F.7a) au cœur des pixels. L'observation des espaces entre les pixels (Fig. F.7b) a permis de mesurer leur taille - $65 \mu\text{m}$. L'efficacité de l'impact et la taille de l'espace satisfont toutes deux aux exigences. En outre, j'ai analysé les données du faisceau d'essai pour ALTIROC3, découvrant que l'étalonnage effectué en laboratoire ne pouvait pas être directement appliqué à l'environnement du faisceau d'essai, ce qui entraînait une dégradation des performances, J'ai identifié une méthode pour surmonter cette erreur d'étalonnage, applicable uniquement au faisceau d'essai, J'ai finalement obtenu une résolution temporelle moyenne de 44 ± 0.2 ps (Fig. F.8) sur de nombreux pixels, ce qui est proche de l'exigence du TDR.

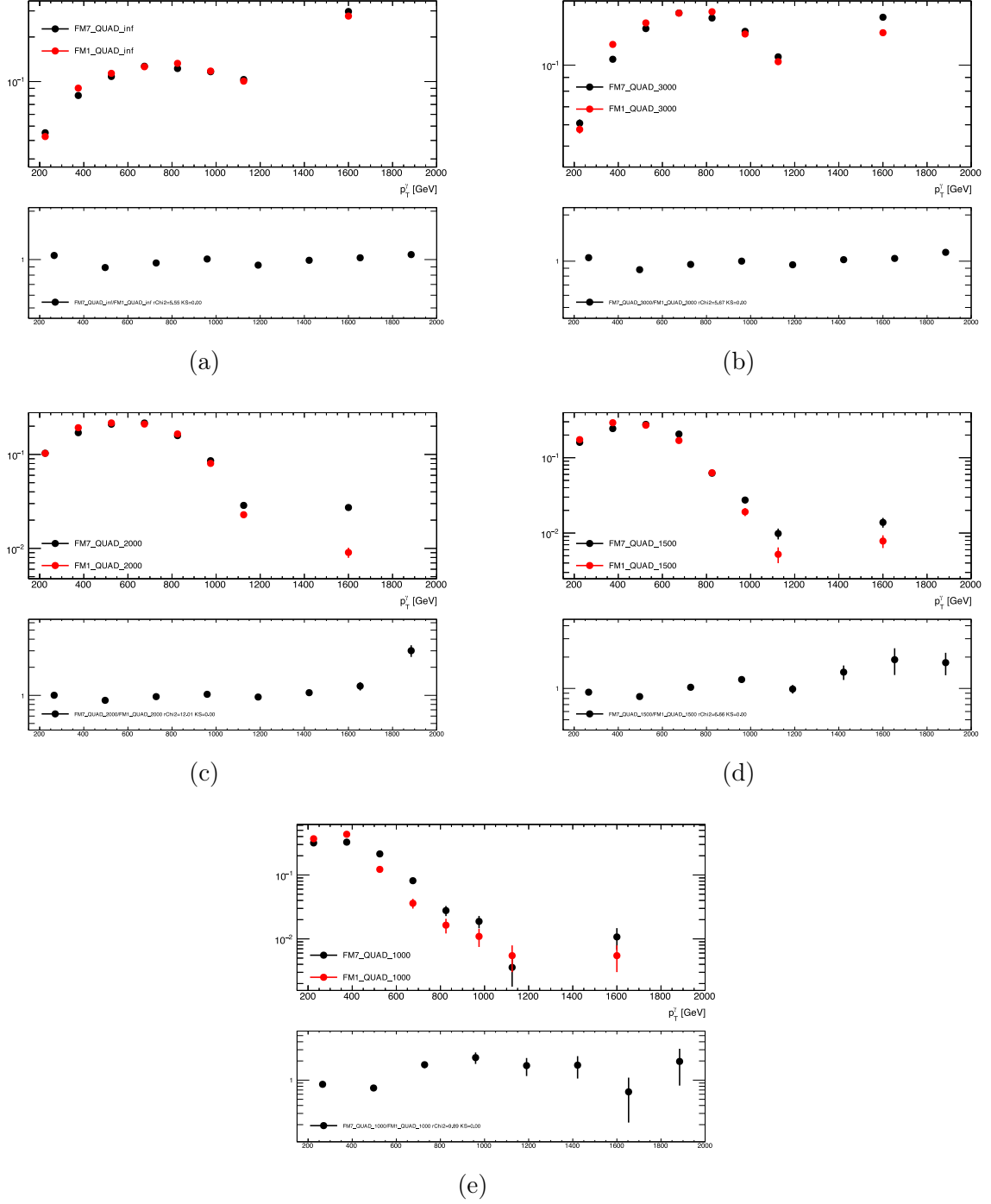


Figure F.2: Comparaison de la forme FM7vsFM1 obtenue dans $Z(\rightarrow \bar{\nu}\nu)\gamma$, reproduisant les sélctions de l'analyse. Les bins de l'histogramme correspondent à celles utilisées dans l'analyse. Le pavé du bas est le rapport entre deux formes d'opérateurs (a) sans clipping (b) clipping=3000 (c) clipping=2000 (d) clipping=1500 (e) clipping=1000

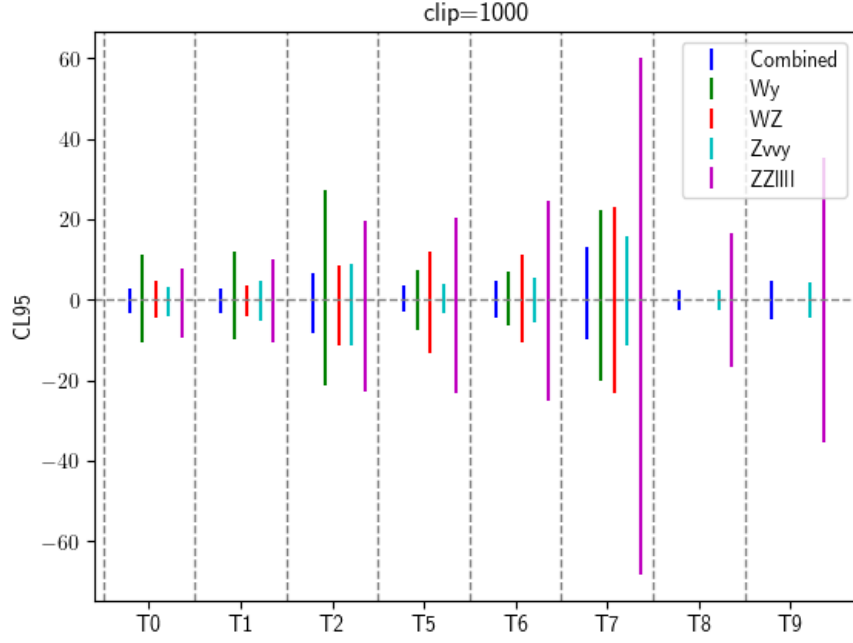


Figure F.3: Limites individuelles de $Z(\rightarrow \bar{\nu}\nu)\gamma$, $W^\pm Z$, $W\gamma$, $ZZ \rightarrow 4\ell$ et limites de la famille T unidimensionnelle combinée pour clipping=1000

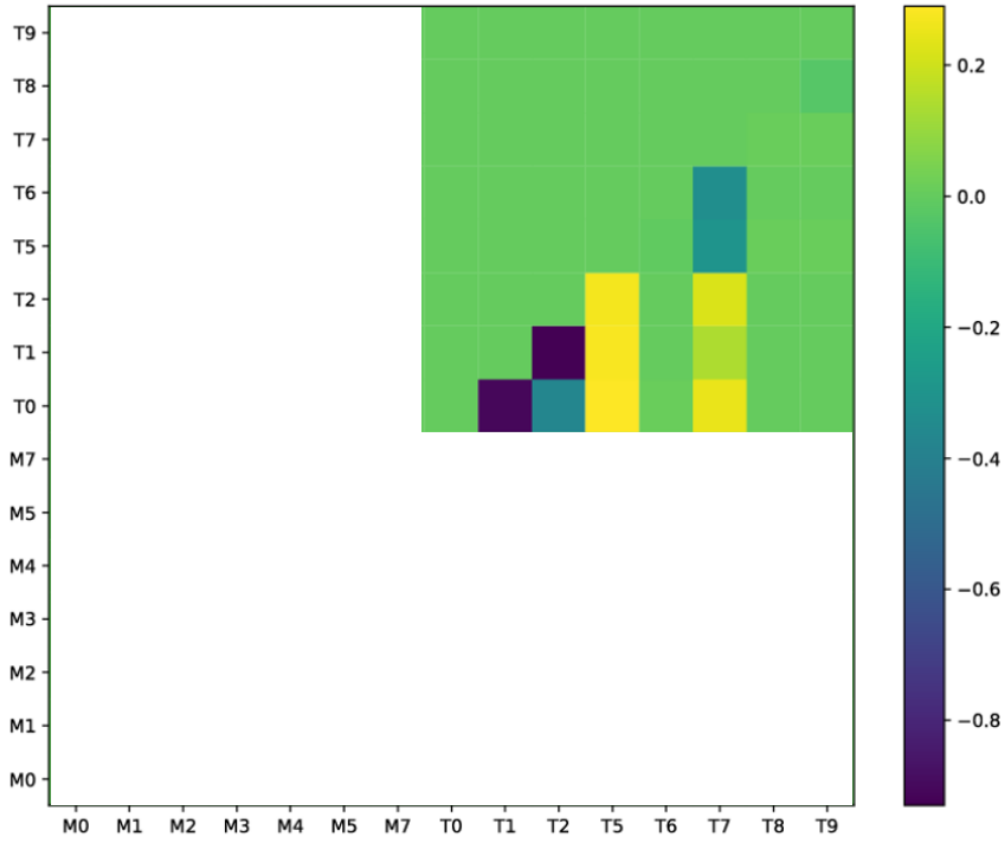


Figure F.4: Résumé des corrélations limites des paires 2D T (combinées)

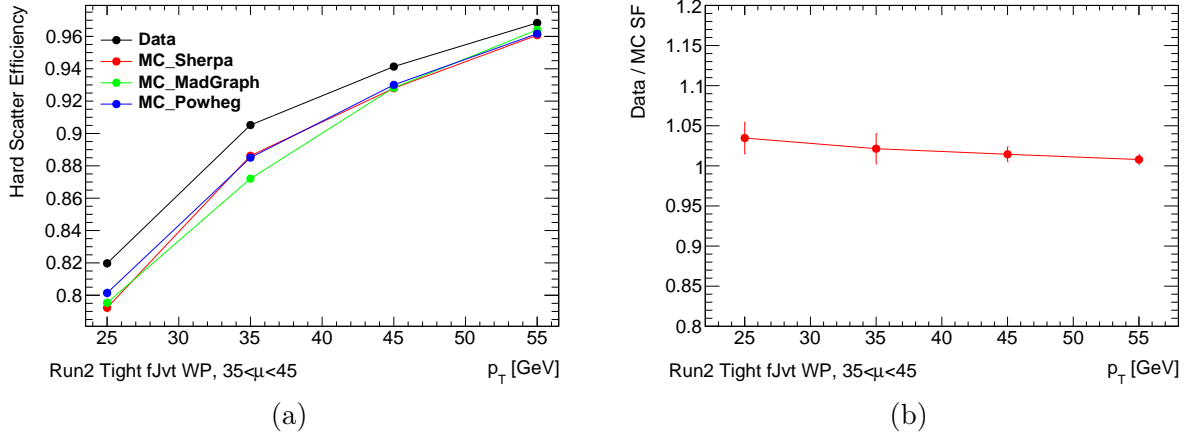


Figure F.5: Résultats de l'étalonnage Run2 en $35 < \bar{\mu} \leq 45$, point de travail Tight (a) Efficacité Hard-Scatter (b) Scale Factor

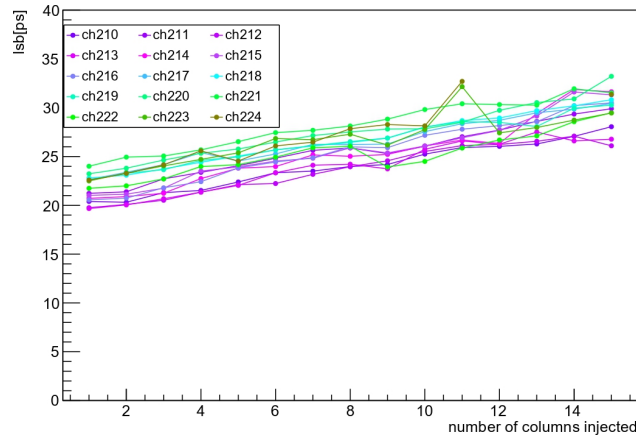


Figure F.6: LSB TOA pour la colonne 14 obtenue en additionnant d'abord les colonnes éloignées

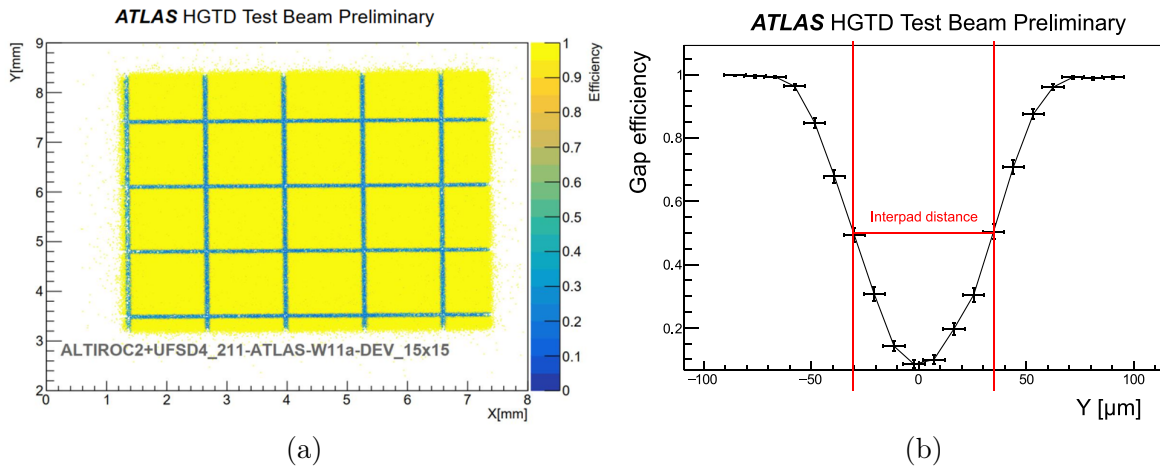


Figure F.7: (a) Carte d'efficacité de ALTIROC2+LGAD mesurée par rapport entre les pistes reconstruites avec un résultat visible dans ALTIROC et toutes les pistes reconstituées pénétrant dans la zone du module. (b) Efficacité en fonction de y de ALTIROC2+LGAD zoomé autour d'une région interpad. Les lignes verticales marquent l'efficacité de 50% obtenue par interpolation linéaire, La différence entre leurs positions est considérée comme la distance interpad.

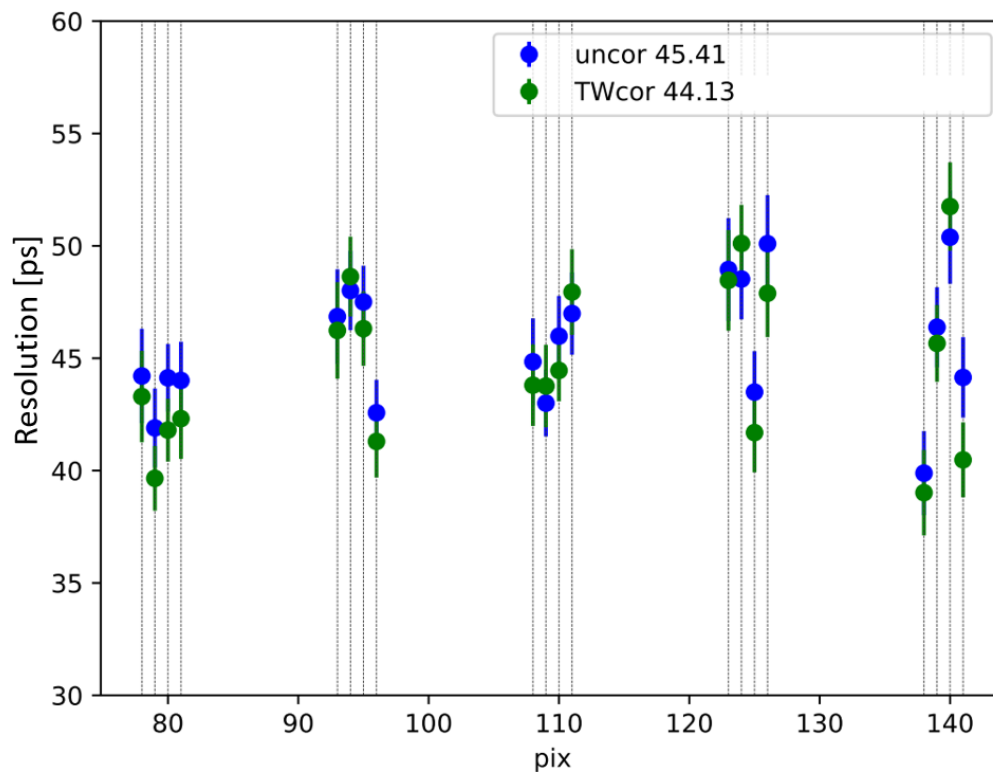


Figure F.8: Résolution temporelle ALTIROC3

Bibliography

- [1] Metperfhistogramming. <https://gitlab.cern.ch/atlas-jetmiss/etmiss/metperformancestudies/metperfhistogramming>. GitLab repository.
- [2] Metperformance. https://gitlab.cern.ch/atlas-jetmiss/etmiss/metperformancestudies/metperformance/-/tree/master?ref_type=heads. GitLab repository.
- [3] ATLAS: letter of intent for a general-purpose pp experiment at the large hadron collider at CERN. 1992.
- [4] *ATLAS: technical proposal for a general-purpose pp experiment at the Large Hadron Collider at CERN*. LHC technical proposal. CERN, Geneva, 1994.
- [5] Expected pileup values at the HL-LHC. Technical report, CERN, Geneva, 2013. All figures including auxiliary figures are available at <https://atlas.web.cern.ch/Atlas/GROUPS/PHYSICS/PUBNOTES/ATL-UPGRADE-PUB-2013-014>.
- [6] Performance of pile-up mitigation techniques for jets in pp collisions at $\sqrt{s} = \text{TeV}$ using the atlas detector. *The European Physical Journal C*, 76(11), October 2016.
- [7] Jet reconstruction and performance using particle flow with the atlas detector. *The European Physical Journal C*, 77(7), July 2017.
- [8] Topological cell clustering in the atlas calorimeters and its performance in lhc run 1. *The European Physical Journal C*, 77(7), July 2017.
- [9] *ATLAS – A 25 Year Insider Story of the LHC Experiment*. WORLD SCIENTIFIC, 2019.
- [10] Observation of electroweak production of a same-sign w boson pair in association with two jets in pp collisions at $\sqrt{s} = 13 \text{ TeV}$ with the atlas detector. *Physical Review Letters*, 123(16), October 2019.
- [11] Observation of electroweak $W^\pm Z$ boson pair production in association with two jets in pp collisions at $\sqrt{s} = 13 \text{ TeV}$ with the atlas detector. *Physics Letters B*, 793:469–492, June 2019.
- [12] Jet energy scale and resolution measured in proton–proton collisions at $\sqrt{s} = 13 \text{ TeV}$ with the atlas detector. *The European Physical Journal C*, 81(8), August 2021.
- [13] Observation of electroweak production of two jets in association with an isolated photon and missing transverse momentum, and search for a higgs boson decaying into invisible particles at $\sqrt{s} = 13 \text{ TeV}$ with the atlas detector. *The European Physical Journal C*, 82(2), February 2022.
- [14] Combined effective field theory interpretation of $W^\pm Zjj$ and $W^\pm W^\pm jj$ measurements using ATLAS 13 TeV data. Technical report, CERN, Geneva, 2023.
- [15] New techniques for jet calibration with the atlas detector. *The European Physical Journal C*, 83(8), August 2023.
- [16] Christina Agapopoulou. *Search for supersymmetry with the ATLAS detector and development of the High Granularity Timing Detector*. PhD thesis, universit  Paris-Saclay, 2020.

- [17] Christina Agapopoulou, S Blin, A Blot, L Castillo Garcia, M Chmeissani, S Conforti Di Lorenzo, C de La Taille, P Dinaucourt, A Fallou, J Garcia Rodriguez, et al. Performance of a front end prototype ASIC for picosecond precision time measurements with lgad sensors. *Journal of Instrumentation*, 15(07):P07007, 2020.
- [18] Ana Alboteanu, Wolfgang Kilian, and Jürgen Reuter. Resonances and unitarity in weak boson scattering at the LHC. *Journal of High Energy Physics*, 2008(11):010–010, nov 2008.
- [19] Adam Alloul, Neil D. Christensen, Céline Degrande, Claude Duhr, and Benjamin Fuks. Feynrules 2.0 - a complete toolbox for tree-level phenomenology. *Computer Physics Communications*, 185(8):2250–2300, August 2014.
- [20] J. et al. Alwall. The automated computation of tree-level and next-to-leading order differential cross sections, and their matching to parton shower simulations. [https://doi.org/10.1007/JHEP07\(2014\)079](https://doi.org/10.1007/JHEP07(2014)079), 2014.
- [21] The ATLAS and CMS Collaborations. Expected pile-up values at the HL-LHC. <https://twiki.cern.ch/twiki/bin/view/AtlasPublic/UpgradeEventDisplays>. ATLAS EXPERIMENT - PUBLIC RESULTS.
- [22] The ATLAS and CMS Collaborations. Snowmass white paper contribution: Physics with the phase-2 ATLAS and CMS detectors, 2022. ATL-PHYS-PUB-2022-018, CMS PAS FTR-22-001.
- [23] Fabrice Balli. Copying new empflow r22 run2+run3 nnjvt/fjvt config files. <https://its.cern.ch/jira/browse/ATLASG-2711>, 2024. JIRA ticket.
- [24] Benedikt Biedermann, Ansgar Denner, and Mathieu Pellen. Complete NLO corrections to w^+w^+ scattering and its irreducible background at the LHC. *Journal of High Energy Physics*, 2017(10), 2017.
- [25] Matteo Cacciari, Gavin P Salam, and Gregory Soyez. The anti-ktjet clustering algorithm. *Journal of High Energy Physics*, 2008(04):063–063, April 2008.
- [26] N Cartiglia, R Arcidiacono, M Costa, M Ferrero, G Gioachin, M Mandurrino, L Menzio, F Siviero, V Sola, and M Tornago. 4d tracking: present status and perspectives. *Nuclear Instruments and Methods in Physics Research Section A: Accelerators, Spectrometers, Detectors and Associated Equipment*, 1040:167228, 2022.
- [27] ATLAS collaboration. Public ATLAS luminosity results for run-2 of the LHC. <https://twiki.cern.ch/twiki/bin/view/AtlasPublic/LuminosityPublicResultsRun2>. Twiki.
- [28] ATLAS collaboration. Public ATLAS luminosity results for run-3 of the LHC. <https://twiki.cern.ch/twiki/bin/view/AtlasPublic/LuminosityPublicResultsRun3>. Twiki.
- [29] ATLAS collaboration. Standard model summary plots June 2024. <https://atlas.web.cern.ch/Atlas/GROUPS/PHYSICS/PUBNOTES/ATL-PHYS-PUB-2024-011/>.
- [30] ATLAS Collaboration. Observation of a new particle in the search for the standard model Higgs boson with the ATLAS detector at the LHC. <https://doi.org/10.1016/j.physletb.2012.08.020>, 2012.
- [31] ATLAS Collaboration. Fiducial and differential cross-section measurements of electroweak $w\gamma jj$ production in pp collisions at $\sqrt{s} = 13$ TeV with the ATLAS detector, 2024.

- [32] CMS Collaboration. Observation of a new boson at a mass of 125 gev with the cms experiment at the lhc. <https://doi.org/10.1016/j.physletb.2012.08.021>, 2012.
- [33] The ATLAS collaboration. Atlas liquid argon calorimeter phase-ii upgrade : Technical design report. <https://cds.cern.ch/record/2285582?ln=en>, 2017. 10.17181/CERN.6QIO.YGHO.
- [34] The ATLAS collaboration. Identification and rejection of pile-up jets at high pseudorapidity with the atlas detector. <https://doi.org/10.1140/epjc/s10052-017-5081-5>, 2017.
- [35] The ATLAS Collaboration. Measurement of $W^\pm W^\pm$ vector-boson scattering and limits on anomalous quartic gauge couplings with the atlas detector. *Physical Review D*, 96(1), July 2017.
- [36] The ATLAS Collaboration. Studies of $z\gamma$ production in association with a high-mass dijet system in pp collisions at $\sqrt{s} = 8$ tev with the atlas detector. *Journal of High Energy Physics*, 2017(7), July 2017.
- [37] The ATLAS collaboration. Technical design report for the atlas inner tracker pixel detector. <https://cds.cern.ch/record/2285585?ln=en>, 2017. 10.17181/CERN.FOZZ.ZP3Q.
- [38] The ATLAS collaboration. Technical design report for the phase-ii upgrade of the atlas muon spectrometer. <https://cds.cern.ch/record/2285580?ln=en>, 2017.
- [39] The ATLAS collaboration. Technical design report for the phase-ii upgrade of the atlas tdaq system. <https://cds.cern.ch/record/2285584?ln=fr>, 2017. 10.17181/CERN.2LBB.4IAL.
- [40] The ATLAS collaboration. Technical design report for the phase-ii upgrade of the atlas tile calorimeter. <https://cds.cern.ch/record/2285583?ln=en>, 2017.
- [41] The ATLAS collaboration. Prospect study of electroweak production of a z boson pair plus two jets at the hl-lhc. <http://cds.cern.ch/record/2647219>, 2018. ATL-PHYS-PUB-2018-029.
- [42] The ATLAS collaboration. Prospective study of vector boson scattering in wz fully leptonic final state at hl-lhc. <http://cds.cern.ch/record/2645271>, 2018. ATL-PHYS-PUB-2018-023.
- [43] The ATLAS collaboration. Prospects for the measurement of the $W^\pm W^\pm$ scattering cross section and extraction of the longitudinal scattering component in pp collisions at the high-luminosity lhc with the atlas experiment. <https://cds.cern.ch/record/2652447>, 2018. ATL-PHYS-PUB-2018-052.
- [44] The ATLAS collaboration. Forward jet vertex tagging using the particle flow algorithm. ATL-PHYS-PUB-2019-026, 2019.
- [45] The ATLAS collaboration. Atlas hl-lhc computing conceptual design report. <http://cds.cern.ch/record/2729668>, 2020.
- [46] The ATLAS collaboration. Technical design report: A high-granularity timing detector for the atlas phase-ii upgrade. <https://cds.cern.ch/record/2719855?ln=en>, 2020.
- [47] The ATLAS Collaboration. Muon reconstruction and identification efficiency in atlas using the full run 2 pp collision data set at $\sqrt{s} = 13$ tev. <https://doi.org/10.1140/epjc/s10052-021-09233-2>, 2021.

- [48] The ATLAS Collaboration. Measurement of electroweak $z(\nu\bar{\nu})\gamma jj$ production and limits on anomalous quartic gauge couplings in pp collisions at $\sqrt{s} = 13$ tev with the atlas detector. *Journal of High Energy Physics*, 2023(6), jun 2023.
- [49] The ATLAS Collaboration. Measurement of the cross-sections of the electroweak and total production of a $z\gamma$ pair in association with two jets in pp collisions at $\sqrt{s} = 13$ tev with the atlas detector, 2023.
- [50] The ATLAS collaboration. Observation of electroweak production of two jets and a z-boson pair. <https://doi.org/10.1038/s41567-022-01757-y>, 2023.
- [51] The ATLAS Collaboration. The atlas experiment at the cern large hadron collider: a description of the detector configuration for run-3. *Journal of Instrumentation*, 19(05):P05063, may 2024.
- [52] The ATLAS Collaboration. Differential cross-section measurements of the production of four charged leptons in association with two jets using the atlas detector. *Journal of High Energy Physics*, 2024(1), jan 2024.
- [53] The ATLAS Collaboration. Electron and photon energy calibration with the atlas detector using lhcb run 2 data. <https://doi.org/10.1088/1748-0221/19/02/P02009>, 2024.
- [54] The ATLAS collaboration. Improving topological cluster reconstruction using calorimeter cell timing in atlas. <https://doi.org/10.1140/epjc/s10052-024-12657-1>, 2024.
- [55] The ATLAS collaboration. Measurement and interpretation of same-sign w boson pair production in association with two jets in pp collisions at $\sqrt{s} = 13$ tev with the atlas detector. [https://doi.org/10.1007/JHEP04\(2024\)026](https://doi.org/10.1007/JHEP04(2024)026), 2024.
- [56] The ATLAS collaboration. Measurements of electroweak $W^\pm Z$ boson pair production in association with two jets in pp collisions at $\sqrt{s} = 13$ tev with the atlas detector. [https://doi.org/10.1007/JHEP06\(2024\)192](https://doi.org/10.1007/JHEP06(2024)192), 2024.
- [57] The CMS collaboration. Measurement of electroweak wz production and search for new physics in pp collisions at $\sqrt{s} = 13$ tev. <http://cds.cern.ch/record/2629457>, 2018. ATLAS-SMP-18-001.
- [58] The CMS collaboration. Vector boson scattering prospective studies in the zz fully leptonic decay channel for the high-luminosity and high-energy lhcb upgrades. <http://cds.cern.ch/record/2650915>, 2018. CMS-PAS-FTR-18-014.
- [59] TOTEM Collaboration. *Luminosity-Independent Measurement of the Proton-Proton Total Cross Section at $\sqrt{s}=8$ TeV*. American Physical Society, 2013. PRL 111, 012001 (2013).
- [60] D. Cussans. Description of the jral trigger logic unit (tlu), v0.2c. <https://www.eudet.org/e26/e28/e42441/e57298/EUDET-MEMO-2009-04.pdf>, 2009. Accessed: 2023-14-08.
- [61] L. CASTILLO GARCÍA D. BOUMEDIENE. Overview of october sps test beam. <https://indico.cern.ch/event/968948/contributions/4608807/attachments/2343653/3995967/SPS-TB-HGTD-10-2021-overview.pdf>, 2021. Accessed: 2023-14-08.
- [62] Eduardo da Silva Almeida and O. J. P. Éboli. Unitarity constraints on anomalous quartic couplings. *PHYSICAL REVIEW D* 101, 113003 (2020), 2020.

- [63] A. Denner and T. Hahn. Radiative corrections to $w^+w^- \rightarrow w^+w^-$ in the electroweak standard model. *Nuclear Physics B*, 525(1–2):27–50, aug 1998.
- [64] eds. O. Brüning and L. Rossi. The high luminosity large hadron collider - new machine for illuminating the mysteries of the universe, second edition, <https://cds.cern.ch/record/2690118?ln=en>. ADVANCED SERIES ON DIRECTIONS IN HIGH ENERGY PHYSICS, Vol.31.
- [65] S. Farry et al. eds. P. Azzi. Standard model physics at the hl-lhc and he-lhc. report from working group 1 on the physics of the hl-lhc, and perspectives at the he-lhc, 2018. CERN-LPCC-2018-03.
- [66] C.J. Baker et al. E.K. Anderson. Observation of the effect of gravity on the motion of antimatter. <https://doi.org/10.1038/s41586-023-06527-1>, 2023.
- [67] F. Englert and R. Brout. Broken symmetry and the mass of gauge vector mesons. *Phys. Rev. Lett.*, 13:321–323, Aug 1964.
- [68] A. Bocci et al. Recommendations from the anomalous gauge coupling taskforce. <https://cds.cern.ch/record/2261444/files/ATL-COM-PHYS-2017-433.pdf>, 2017.
- [69] G. Arnison et al. Experimental observation of lepton pairs of invariant mass around 95 gev/c² at the cern sps collider. [https://doi.org/10.1016/0370-2693\(83\)90188-0](https://doi.org/10.1016/0370-2693(83)90188-0), 1983.
- [70] G. Durieux et al. Lhc eft wg note: Basis for anomalous quartic gauge couplings. https://indico.cern.ch/event/1433939/contributions/6032971/attachments/2888812/5063744/aQGCs_2024-06-19.pdf, 2024.
- [71] M. Banner et al. Observation of single isolated electrons of high transverse momentum in events with missing transverse energy at the cern pp collider. [https://doi.org/10.1016/0370-2693\(83\)91605-2](https://doi.org/10.1016/0370-2693(83)91605-2), 1983.
- [72] O. Arbele et al. High-luminosity large hadron collider (hl-lhc) technical design report. <https://cds.cern.ch/record/2749422>. CERN-2020-010.
- [73] R. Casanova et al. Altiroc2 datasheet. https://twiki.cern.ch/twiki/pub/Atlas/Altiroc2Board/ALTIROC2_DATASHEET_15March2022.pdf, 2022.
- [74] Marco Ferrero, Roberta Arcidiacono, Marco Mandurrino, Valentina Sola, and Nicolò Cartiglia. *An Introduction to Ultra-Fast Silicon Detectors*. CRC Press, 2021.
- [75] European Strategy for Particle Physics Preparatory Group. Strategy brochure 2006. <https://cds.cern.ch/record/2690118?ln=en>. CERN-ESU-001.
- [76] Christian Gumpert. Measurement of electroweak gauge boson scattering in the channel $pp \rightarrow w^\pm w^\pm jj$ with the atlas detector at the large hadron collider, 2014. Presented 27 Feb 2015.
- [77] G. S. Guralnik, C. R. Hagen, and T. W. B. Kibble. Global conservation laws and massless particles. *Phys. Rev. Lett.*, 13:585–587, Nov 1964.
- [78] Salah El Dine HAMMOUD. Toa lsb – fitting different ranges of toa bins – boards 15 - 47 : Delay scan vs rpg. <https://indico.cern.ch/event/1360548/#2-updates-from-omegaijclab>, 2024.

- [79] Peter W. Higgs. Broken symmetries and the masses of gauge bosons. *Phys. Rev. Lett.*, 13:508–509, Oct 1964.
- [80] Michael Holzbock. fjvt performance. <https://indico.cern.ch/event/1223581/contributions/5147742/attachments/2555453/4403422/ETmissPU-2022-11-28-R22-fJvt-Study.pdf>, 2023. slides from ETmiss + PU subgroup meeting.
- [81] Michael Holzbock. fjvt,jvt in r22 recommendation software update. https://gitlab.cern.ch/atlas/athena/-/merge_requests/70961, 2024. GitLab Merge Request.
- [82] Hendrik Jansen, Simon Spannagel, Jörg Behr, Antonio Bulgheroni, Gilles Claus, Emlyn Corrin, David Cussans, Jan Dreyling-Eschweiler, Doris Eckstein, Thomas Eichhorn, et al. Performance of the eudet-type beam telescopes. *EPJ Techniques and Instrumentation*, 3:1–20, 2016.
- [83] Peter Jenni. EAGLE : Experiment for Accurate Gamma, Lepton and Energy measurements: expression of interest. 1992. Conference : Towards the LHC experimental programme : General Meeting on LHC Physics and Detectors, Evian-les-Bains, France, 5 - 8 Mar 1992.
- [84] L. Moneta et al" K. Cranmer, G. Lewis. HistFactory: A tool for creating statistical models for use with RooFit and RooStats. Technical report, New York U., New York, 2012.
- [85] R. U. Koetz. User manual: Atlas fe-i4a pixel module as a trigger plane for the beam telescope. <https://www.desy.de/f/students/2013/reports/bisanz.pdf.gz>, 2013. Accessed: 2023–14-08.
- [86] Anastasia KOTSOKECHAGIA. Fvjt pflow algorithm. https://gitlab.cern.ch:8443/atlas/athena/-/blob/main/Reconstruction/Jet/JetMomentTools/JetMomentTools/JetForwardPFlowJvtTool.h?ref_type=heads. ATLAS Athena.
- [87] Anastasia KOTSOKECHAGIA. Search for vector boson scattering in semi-leptonic final states with the atlas detector. contribution to the inner tracker upgrade in view of the high-luminosity lhc. Thèse de doctorat, 2022.
- [88] Oleksii Kurdysch. fjvt in r22. https://gitlab.cern.ch/atlas/athena/-/merge_requests/64339, 2023. GitLab Merge Request.
- [89] Mathieu Markovitch. Full run-2 aqgc combination status. https://indico.cern.ch/event/1353688/contributions/5699756/attachments/2768423/4822783/Mathieu_081223.pdf, 2023.
- [90] Mathieu Markovitch. Fit updates. https://indico.cern.ch/event/1448186/contributions/6097771/attachments/2914320/5114021/Mathieu_220824.pdf, 2024.
- [91] Mathieu Markovitch. Fit updates. https://indico.cern.ch/event/1448186/contributions/6097771/attachments/2914320/5114021/Mathieu_220824.pdf, 2024.
- [92] Mathieu Markovitch. Sm closure: Semi-leptonic vbs. https://indico.cern.ch/event/1423251/contributions/5986144/attachments/2872111/5028695/Mathieu_SM.pdf, 2024. slides from Standard Model Plenary Meeting.
- [93] Esma Mobs. The CERN accelerator complex - August 2018. Complexe des accélérateurs du CERN - Août 2018. 2018. General Photo.

- [94] Peter R Norton. The ASCOT detector at the LHC: expression of interest. 1992. Conference : Towards the LHC experimental programme : General Meeting on LHC Physics and Detectors, Evian-les-Bains, France, 5 - 8 Mar 1992.
- [95] Aleksandr Petukhov. Zllvv editorial board request follow-up. <https://indico.cern.ch/event/1342027/contributions/5649518/attachments/2745972/4778036/2023.11.03%20ZZ%20212v%20Status%20Report.pdf>, 2023. slides from SM Electroweak group meeting.
- [96] Louis PORTALES. Observation of electroweak wzjj production, and studies on pile-up mitigation with the atlas detector. Thèse de doctorat, 2020.
- [97] DILIA MARÍA PORTILLO QUINTERO. Introduction: jet inputs and mc calibration. 2024. slides from HCW2024.
- [98] H.Arnold et al. S. Ali. Performance in beam tests of carbon-enriched irradiated low gain avalanche detectors for the atlas high granularity timing detector. *JINST*, 18, 2023.
- [99] Gavin Salam. Jet reconstruction theory. <https://indico.cern.ch/event/817757/contributions/3712514/attachments/1999205/3336281/hamburg-jets-1.pdf>, 2020. slides from PREFIT school.
- [100] Federico Siviero, Roberta Arcidiacono, Giacomo Borghi, Maurizio Boscardin, Nicolo Cartiglia, M Centis Vignali, Marco Costa, G-F Dalla Betta, Marco Ferrero, Francesco Ficorella, et al. Optimization of the gain layer design of ultra-fast silicon detectors. *Nuclear Instruments and Methods in Physics Research Section A: Accelerators, Spectrometers, Detectors and Associated Equipment*, 1033:166739, 2022.
- [101] Stefanie Todt. The $W^{\pm}W^{\pm}$ Scattering Process – Theoretical Studies, Observation, Cross-section Measurement, and EFT Reinterpretation at $\sqrt{s} = 13$ TeV with the ATLAS Detector, 2022. Presented 02 Dec 2022.
- [102] Georges Trad. The cern accelerator complex. <https://indico.cern.ch/event/1418290/>, 2024.
- [103] Corentin Allaire et al. Xiaocong Ai. A common tracking software project. <https://doi.org/10.1007/s41781-021-00078-8>, 2022.
- [104] Antonino Zichichi. ECFA-LEP working group: 1979 progress report. The LEP-White Book, 1980. Repr. 2004.
- [105] O.J.P. Éboli and M.C. Gonzalez–Garcia. Classifying the bosonic quartic couplings. *Phys. Rev. D* 93, 093013, 2016.